Thermal Ignition Using Moving Hot Particles

Thesis by

Stephanie Alexandra Coronel

In Partial Fulfillment of the Requirements

for the Degree of

Doctor of Philosophy

California Institute of Technology

Pasadena, California

2016

Defended April 26 , 2016

To Adam, Betty, Alex, Karol, and Marco

Acknowledgements

I am incredibly grateful to my thesis advisor, Professor Joe Shepherd, for his guidance and unwavering support over the past years. He has shaped who I am both as a scientist and a person. By allowing, and even encouraging, me to work independently in the laboratory I was able to hone my skills as an experimentalist, but, of course, he also knew when to step in and provide useful counsel. Although he had other commitments, previously as Dean of Graduate Studies and currently as Vice President of Student Affairs, he always made time to advise and meet with me, including during more evenings and weekends than I can remember. I cannot express enough how thankful I am for his countless hours of help during this process, without which I am certain I would not have successfully completed my PhD. I was extremely fortunate to have had Professor Shepherd as an advisor and will always value his mentorship and friendship.

I would like to thank the members of my thesis committee, Professors Joanna Austin, Guillaume Blanquart, and Beverley McKeon, and also Professor Ravi Ravichandran, who was part of my candidacy committee. I would especially like to thank Ravi for his support and encouragement during my time at GALCIT.

I owe a debt of gratitude to past and present members of the Explosion Dynamics Lab. I am thankful to Dr. Sally Bane, who mentored me when I came to Caltech for an undergraduate summer internship in 2008 and later when I joined the research group as a graduate student. She taught me the ins and outs of the laboratory, and also provided words of encouragement when my research was not going so well. She became a great friend and has been a source of inspiration throughout my time at Caltech. I hope someday to be as accomplished of a researcher and mentor as

Dr. Bane. I would also like to thank Drs. Philipp Boettcher and Jason Damazo. They helped make my transition to the laboratory a smooth one and remain my good friends. I also want to thank the current group members, Drs. Josué Melguizo-Gavilanes and Rémy Mével. They are supremely skilled researchers who have become good friends and have helped to make my experience in the group so rewarding. Their knowledge of chemistry and reactive flow simulations has been invaluable to my work. I am grateful for their support and will truly miss our time together after leaving Caltech. Finally, I will be eager to learn of the many accomplishments of Jean-Christophe Veilleux as he continues his graduate studies and Bryan Schmidt as he starts his career following commencement.

To the first year group of 2009, it was a pleasure to have shared the ups and downs of the Master's year. We formed friendships that year that remain strong to this day. This group made the first year at Caltech incredibly fun; of course, the fun came after all the problem sets were completed. Thank you especially to Jomela Meng, Ignacio Maqueda, and Siddharta Verma; we had so many great times together and so many laughs.

I am grateful to my mother, Betty Manno, her husband, Paul Manno, and my siblings, Karol Trojacek and Alex and Marco Coronel, for their loving support. I could not have done this without them. My mother was my inspiration for pursuing graduate studies and through her endless encouragement and love I have been able to complete this magnificent journey.

Finally, a loving thank you to Adam Wright. He is an incredible human being and I am lucky to have met him. Thank you Adam for your patience, support, and love throughout these years. I look forward to building our future together.

This work was supported by the Boeing Company through a Strategic Research and Development Relationship Agreement CT-BA-GTA-1.

Abstract

In this work, ignition of n-hexane-air mixtures was investigated using moving hot spheres of various diameters and surface temperatures. Alumina spheres of $1.8 - 6$ mm diameter were heated using a high power CO_2 laser and injected with an average velocity of 2.4 m/s into a premixed n-hexane-air mixture at a nominal initial temperature and pressure of 298 K and 100 kPa, respectively. The 90% probability of ignition using a 6 mm diameter sphere was 1224 K. High-speed experimental visualizations using interferometry indicated that ignition occurred in the vicinity of the separation point in the boundary layer of the sphere when the sphere surface temperature was near the ignition threshold. Additionally, the ignition threshold was found to be insensitive to the mixture composition and showed little variation with sphere diameter.

Numerical simulations of a transient one-dimensional boundary layer using detailed chemistry in a gas a layer adjacent to a hot wall indicated that ignition takes place away from the hot surface; the igniting gas that is a distance away from the surface can overcome diffusive heat losses back to the wall when there is heat release due to chemical activity. The use of fluid parcel tracking indicated that in a n-hexane-air mixture at $\Phi = 0.9$, it was a fluid parcel located a distance of $0.15\delta_T$ normal to the wall that first ignited, where δ_T is the thermal boundary layer thickness. Finally, a simple approximation of the thermal and momentum boundary layer profiles indicated that the residence time within a boundary layer varies drastically, for example, a fluid parcel originating at $0.05\delta_T$ normal to the wall has a residence time that is $65\times$ longer than the residence time of a fluid parcel traveling along the edge of the momentum boundary layer.

A non-linear methodology was developed for the extraction of laminar flame properties from synthetic spherically expanding flames. The results indicated that for accurate measurements of the flame speed and Markstein length, a minimum of 50 points is needed in the data set (flame radius vs. time) and a minimum range of 48 mm in the flame radius. The non-linear methodology was applied to experimental n-hexane-air spherically expanding flames. The measured flame speed was insensitive to the mixture initial pressure from 50 to 100 kPa and increased with increasing mixture initial temperature. One-dimensional freely-propagating flame calculations showed excellent agreement with the experimental flame speeds using the JetSurF and CaltechMech chemical mechanisms.

Published Content and Contributions

Publications

J. Melguizo-Gavilanes, A. Nové-Josserand, S. Coronel, R. Mével, and J. E. Shepherd. Hot surface ignition of n-hexane mixtures using simplified kinetics. *Combustion Science and Technology*, 2016c. Accepted for publication

J. Melguizo-Gavilanes, S. Coronel, R. Mével, and J. E. Shepherd. Dynamics of ignition of stoichiometric hydrogen-air mixtures by moving heated particles. *International Journal of Hydrogen Energy*, 2016b. Accepted for publication

R. Mével, J. Melguizo-Gavilanes, U. Niedzielska, S. Coronel, and J. E. Shepherd. Chemical kinetics of n-hexane-air atmospheres in the boundary layer of a moving hot sphere. *Combustion Science and Technology*, 2016. Accepted for publication

Conference Proceedings

S. A. Coronel, S. Menon, R. Mével, G. Blanquart, and J. E. Shepherd. Ignition of nitrogen diluted hexane-oxygen mixtures by moving heated particles. In *24th International Colloquium on the Dynamics of Explosions and Reactive Systems (ICDERS 2013)*, Taipei, Taiwan, 28 July-2 August 2013b

S. A. Coronel, R. Mével, P. Vervish, P. A. Boettcher, V. Thomas, N. Chaumeix, N. Darabiha, and J. E. Shepherd. Laminar burning speed of n-hexane-air mixtures. In *8th US National Combustion Meeting*, University of Utah, May 19-22 2013c. Paper 070LT-0383

S. A. Coronel, V. Bitter, N. Thomas, R. Mével, and J. E. Shepherd. Non-linear extrapolation of laminar flame properties from spherically expanding flames. In *Spring*

Meeting, Western States Section of the Combustion Institute, California Institute of Technology, March 24-25 2014. Paper 087LF-0020

S. A. Coronel, J. Melguizo-Gavilanes, and J. E. Shepherd. Ignition of n-hexane-air by moving hot particles: effect of particle diameter. In *9th US National Combustion Meeeting*, Cincinnati OH, May 17-20 2015. Paper 0114RK-0452

R. Mével, J. Melguizo-Gavilanes, S. A. Coronel, and J. E. Shepherd. Chemical kinetics of ignition of n-hexane by a moving hot sphere. In *25th International Colloquium on the Dynamics of Explosions and Reactive Systems (ICDERS 2015)*, Leeds, UK, August 2-7 2015

S. A. Coronel and J. E. Shepherd. Effect of equivalence ratio on ignition and flame propagation of n-hexane-air mixtures using moving hot particles. In *25th International Colloquium on the Dynamics of Explosions and Reactive Systems (ICDERS 2015)*, Leeks, UK, August 2-7 2015

Stephanie Coronel designed, constructed and carried out the experiments described in Chapters 2, 3, 4 and 7. Stephanie Coronel developed the software and analyzed all experimental data presented in all Chapters. Josué Melguizo-Gavilanes performed the 2D simulations presented in Chapters 3 and 4. Stephanie Coronel performed the 1D numerical simulations presented in Chapter 5 with the assistance of Simon Lapointe. The analysis in Chapter 6 was initiated by Rémy Mével and Vaugh Thomas; Stephanie Coronel developed the software, performed the simulations and analyzed the results. The experiments and data analysis in Chapter 7 were performed by Stephanie Coronel, the flame speed calculations were performed by Simon Lapointe. Stephanie Coronel was the sole author of all chapters in this thesis and prepared all the original graphics.

Contents

List of Figures

List of Tables

Chapter 1

Introduction

1.1 Motivation

Hot particle hazards are present in the manufacturing, aviation, nuclear, and mining sectors. In the manufacturing, nuclear, and mining sectors, hot particles are generated during welding, cutting, grinding, and soldering, among other applications (Mikkelsen, 2014). An example of hot particles and hot spots generated during a low speed grinding process performed by Hawksworth et al. (2004) is shown in Fig. 1.1. The streaks of yellow/orange correspond to particles ejected from the specimen subjected to the grinding, and the color of the particles is indicative of the high temperatures reached. According to Hawksworth et al. (2004), for a stainless steel specimen, the temperature at the contact spot varied from approximately 1100 to 1500 K for a coefficient of friction of 0.1.

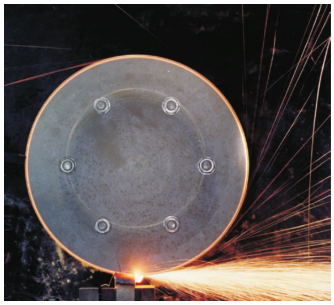

Figure 1.1: Photograph showing frictional sparks and hot spots produced during a grinding test (Hawksworth et al., 2004).

In aviation, heated particles can be generated during a lightning strike on composite aircraft structures; hot particles can be ejected from the surface that is struck due to resistive heating. Feraboli and Miller (2009) subjected unnotched and filled-hole CFRP (Carbon Fiber Reinforced Polymers) specimens to simulated lightning strikes and determined that for the filled-hole specimens, the damage was confined to the fastener and surrounding region. Figure 1.2 shows a post-mortem micrograph of a specimen subjected to a 30 kA simulated lightning strike that destroyed the resin and fibers on the back-face of the laminate (close to the fastener collar). Resistive heating of the material leads to pyrolysis of the resin and fiber which can result in an explosive release of the heated material due to gases developing from the burning resin (Feraboli and Miller, 2009).

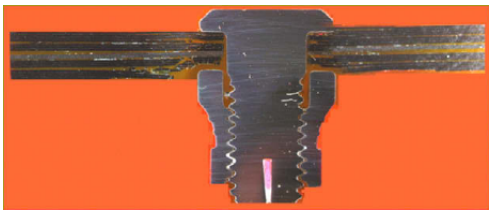

Figure 1.2: Micrograph of filled-hole specimen subjected to 30 kA simulated lightning strike, reprinted with permission from Feraboli and Miller (2009).

The motivation to study hot particle hazards stems from the possibility that hot particles can make their way into a flammable environment and cause an unwanted explosion that could possibly lead to damage to the surroundings, unsafe conditions, and most importantly, loss of life. Therefore, it is important to understand the underlying physics behind hot particle ignition, in particular, moving hot particle ignition. As indicated by Figs. 1.1 and 1.2, the hot particles that are generated are in motion. Additionally, the flammable mixture of interest in the present study is *n*-hexane-air; *n*-hexane is used as a surrogate for kerosene based fuels (see Appendix A for analysis of surrogate choice).

Hot particles come in all shapes and sizes, are made of a wide range of materials, and can produce different flow configurations depending on whether the particle is stationary or moving. The following section provides an overview of the hot particle

configurations that are possible and the resulting ignition behavior; the hot particles are approximated as spheres.

1.2 Hot Particle Configurations

The ignition behavior of reactive mixtures in the presence of a hot particle is dependent on several factors such as the particle temperature, diameter, velocity, material, and heating method. Based on these factors, hot particles can have the following characteristics:

1. The hot particle can be stationary or moving.
2. The particle can be heated impulsively or via a finite heating rate.
3. The hot particle size can be sub-millimeter (focus of experimental studies on stationary hot particle ignition, see Fig. 1.12), or ~ 1 mm (focus of experimental studies on moving hot particle ignition, see Fig. 1.12)
4. The hot particle can travel through a reactive mixture or travel through an inert environment and subsequently enter a reactive mixture.
5. The hot particle material can be metallic, ceramic, glass, or a composite made from artificial materials or cellulose fibers, i.e. reactive or inert.

These configurations do not cover non-ideal parameters such as surface temperature inhomogeneities and particle non-sphericity.

The natural or forced convection flow over a sphere is characterized by non-dimensional parameters such as the Froude number, Fr, Reynolds number, Re, and Grashof number, Gr. The ignition behavior of the reactive mixture is characterized by the Damköhler number, Da, which is the ratio of the flow time scale to the chemical time scale. The non-dimensional numbers are given in Eq. 1.1.

$$\mathrm{Fr} = \frac{U_\infty}{\sqrt{gd\frac{\Delta\rho}{\rho}}} \ , \ \mathrm{Re} = \frac{U_\infty d}{\nu} \ , \ \mathrm{Gr} = g\frac{\Delta\rho}{\rho}\frac{d^3}{\nu^2} \ , \ \mathrm{Gr} = \left(\frac{\mathrm{Re}}{\mathrm{Fr}}\right)^2 \tag{1.1}$$

U_∞ is the sphere or freestream velocity (sphere fixed reference frame), d is the sphere diameter, ν and ρ are the kinematic viscosity and density of the gas, respectively, and g is the gravitational acceleration. The Froude number represents the ratio of inertial forces to gravitational forces, whereas the Reynolds number is the ratio of inertial to viscous forces and the Grashof number is the ratio of buoyant to viscous forces. Finally, the Damköhler number is defined as,

$$\mathrm{Da} = \frac{t_{\mathrm{flow}}}{t_{\mathrm{chemical}}}, \tag{1.2}$$

where

$$\begin{aligned} t_{\mathrm{flow}} &\sim \frac{d}{U}: \quad \text{forced convection} \\ t_{\mathrm{flow}} &\sim \frac{\delta_T^2}{\alpha}: \quad \text{diffusion.} \end{aligned} \tag{1.3}$$

In Eq. 1.3, δ_T is the thermal boundary layer thickness and α is the thermal diffusivity which is written as,

$$\alpha = \lambda / \rho c_p, \tag{1.4}$$

where λ and c_p are the thermal conductivity and specific heat of the gas, respectively. The chemical time scale is typically defined by an ignition delay time or induction period. During this period, the radical pool formation is increasing however depletion of the fuel is not significant; when the pool is sufficiently large to consume the fuel, a rapid ignition takes place (Warnatz et al., 2013).

Figure 1.3 shows a schematic of laminar flow over a sphere and parameters which are frequently mentioned in the following sections. The sphere parameters (in the reference frame of the sphere) are based on a positive incoming freestream velocity U_∞ and freestream temperature T_∞. The sphere has a wall temperature of T_{wall} and radius R. The front and rear stagnation points are labeled along with the angle at which flow separation occurs, θ_s. The momentum boundary layer is delineated by the blue dashed line on the left side of the sphere and has thickness δ that grows with increasing angle θ. The thermal boundary layer is delineated by the red dashed line and is shown on the right side of the sphere; the thickness δ_T grows as θ increases.

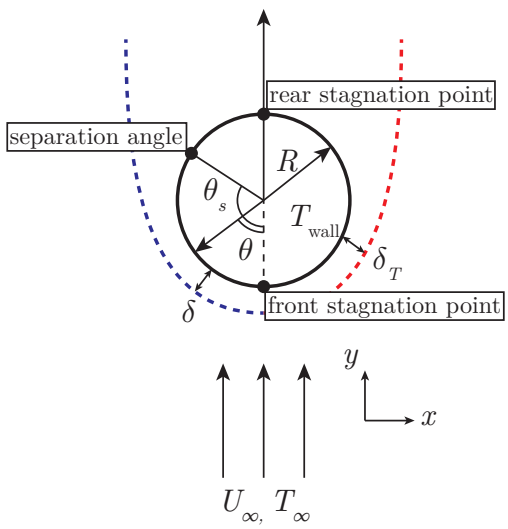

Figure 1.3: Schematic of laminar flow with separation around a sphere.

The ratio of δ/δ_T varies according to the square root of the Prandtl number, where $\mathrm{Pr} = \nu/\alpha$. The ratio is less than 1 for $\mathrm{Pr} < 1$ and is greater than 1 for $\mathrm{Pr} > 1$. Prandtl values as a function of gas temperature are shown in Fig. 1.4 for n-hexane-air at various compositions. The values of Prandtl number indicate that the thermal boundary layer should be expected to be slightly thicker $(8 - 15\%)$ than its corresponding momentum boundary layer over a wide range of mixture compositions and gas temperatures.

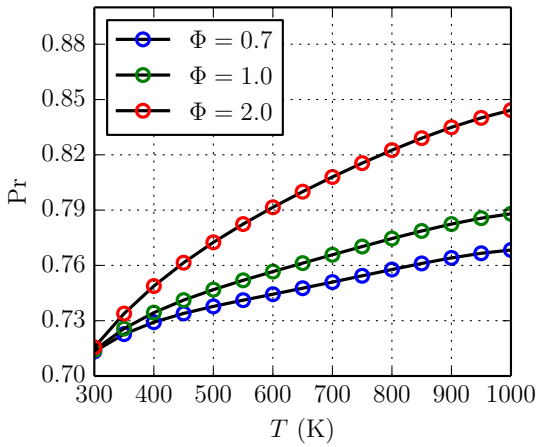

Figure 1.4: Prandtl number as a function of temperature for n-hexane-air mixtures.

In the present study, laminar flows with separation around a sphere are considered, i.e. $60 < \mathrm{Re} < 210$. The corresponding Froude and Grashof numbers are ~ 10 and $\sim 10 - 10^2$, respectively. Flows with values of $\mathrm{Gr}/\mathrm{Re}^2 \geq 1.67$ are considered to have buoyant force effects that dominate over forced convection (Chen and Mucoglu, 1977); however, for the flows considered in the present study, $\mathrm{Gr}/\mathrm{Re}^2 << 1$.

1.2.1 Stationary and Moving Hot Particles

The difference between stationary and moving hot particles is in the manner by which the fluid surrounding the hot particle is transported, either through natural or forced convection. Natural convection occurs when a density gradient exists in the fluid that leads to an induced fluid velocity. Examples of streamlines in forced convection of increasing Reynolds number flows around a sphere are shown in Fig. 1.5. At $1 < \mathrm{Re} < 20$, the flow around the sphere is attached and axisymmetric, shown in Fig. 1.5 (a). The onset of flow separation occurs at $\mathrm{Re} = 20$ and is marked by a change in the sign of vorticity downstream of the separation point (Clift et al., 2005). At $20 < \mathrm{Re} < 210$, the flow has separated and is steady and axisymmetric; the separation location moves forward along the sphere leading to wider and longer wakes as the Reynolds number increases, shown in Fig. 1.5 (b) and (c).

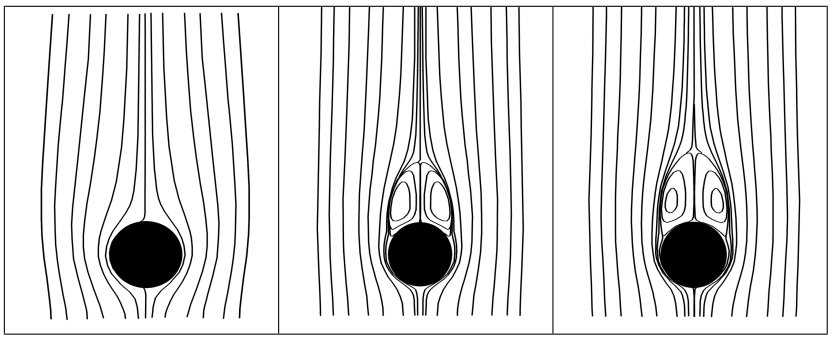

(a) Re = 1 (b) Re = 150 (c) Re = 200

Figure 1.5: Streamlines surrounding sphere for increasing Re flows, from left to right; adapted from Bhattacharyya and Singh (2008) and Johnson and Patel (1999).

Figure 1.6 shows the evolution of the momentum boundary around a sphere for

separated flow. The flow decelerates to zero velocity at the front of the sphere, reaching a maximum pressure at this location; the flow then accelerates as it travels around the sphere until it reaches a maximum velocity where the pressure is minimum at $\theta = 90°$. Past $\theta = 90°$, the flow starts decelerating until it encounters an adverse pressure gradient leading to reversal of the flow and separation. An empirical relationship of the separation angle as a function of Reynolds number is given by Eq. 1.5 (Clift et al., 2005), the relation is valid for $20 < \mathrm{Re} \leq 400$.

$$\theta_s = 180 - 42.5 \left[\ln\left(\mathrm{Re}/20\right)\right]^{0.483} \tag{1.5}$$

At $\mathrm{Re} = 210$, the flow becomes asymmetric but still maintains its steady behavior. The onset of unsteadiness occurs at $270 < \mathrm{Re} < 300$ when diffusion and convection of vorticity can no longer keep up with vorticity generation (Johnson and Patel, 1999).

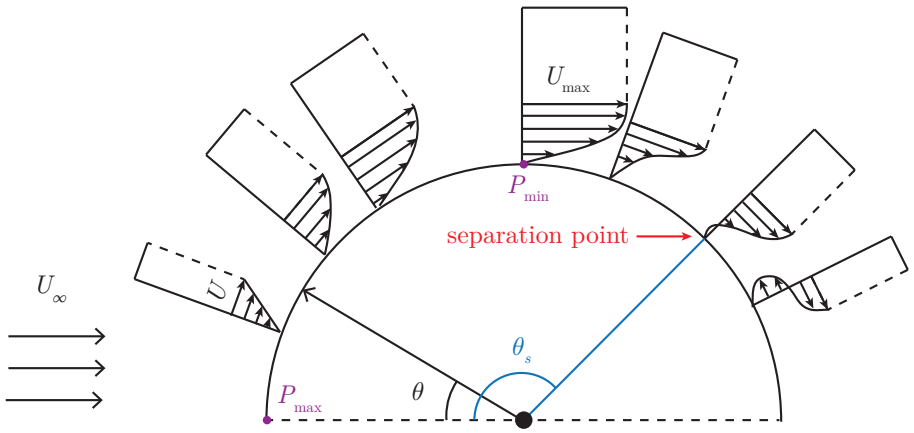

Figure 1.6: Evolution of the momentum boundary layer around sphere for separated flow.

The corresponding temperature contours for the flows in Fig. 1.5 are shown in Fig. 1.7. At small Reynolds numbers the heat transfer to the fluid is primarily through conduction in the gas, indicated by the wide thermal boundary layer in Fig. 1.7 (a). As the Reynolds number increases, the heat transfer is dominated by convection, indicated by the thinner and more elongated thermal boundary layers in Fig. 1.7 (b) and (c).

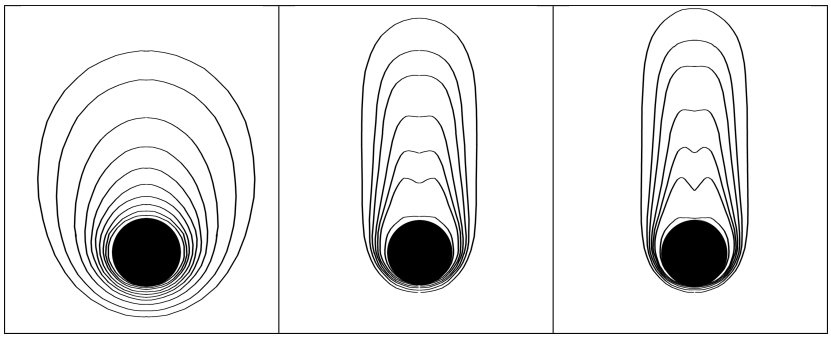

(a) Re = 1 (b) Re = 150 (c) Re = 200

Figure 1.7: Isotherms surrounding sphere for increasing Re flows, from left to right; adapted from Bhattacharyya and Singh (2008) and Johnson and Patel (1999).

The highest density of isotherms is at the front stagnation point of the sphere for the cases shown in Fig. 1.7, corresponding to a large temperature gradient; the thickness of the thermal boundary layer grows from the front stagnation point to the rear stagnation point or forward of the rear stagnation point when the flow is attached or separated, respectively. The large variation in the temperature within the thermal boundary layer, due to a hot sphere and cold freestream, results in a non-unique Reynolds number. The Reynolds number can be defined by the cold flow gas properties or the properties of the gas immediately next to the hot sphere surface or properties based on the average of the freestream and hot sphere temperatures, i.e. T_∞, T_{wall} or $T_{\text{film}} = (T_\infty + T_{\text{wall}})/2$.

In reactive mixtures with low Reynolds numbers (Re ~ 1), the shape and thickness of the isotherms (see Fig. 1.7 (a)) suggests that ignition is possible anywhere in the thermal boundary layer from heat release due to chemical reactions. At higher Reynolds numbers and in separated flows, stagnation regions are created that are likely locations for ignition when nearing the ignition threshold, i.e. the minimum sphere surface temperature required for ignition. The ignition can be characterized using a critical Damköhler number (see Eq. 1.2), i.e. Da $\geq$ Da*, usually Da$^* = \mathcal{O}(1)$. In low Reynolds number flows, corresponding to a stationary or very slow moving sphere with almost circular isotherms, the flow time scale is defined by the thermal

boundary layer thickness and thermal diffusivity. The thermal boundary layer has to be sufficiently thick to overcome heat losses back to the wall when there is heat release due to chemical reactions; this also applies to higher Reynolds number flows. In high Reynolds number separated flows, the flow time scale is governed by the sphere diameter and freestream velocity. Fluid parcels that are entrained in the thermal boundary layer experience a temperature increase as they travel from the front stagnation point to the separation region; as they move past the separation region, the fluid parcels begin to cool down as they travel within the recirculation region (wake). For ignition to take place, a fluid parcel must ignite prior to the start of the cooling process.

1.2.2 Particle Heating Method

A stationary particle can be impulsively heated or heated via a finite temperature ramp. An impulsively heated particle will ignite the surrounding gas when heat has diffused sufficiently to establish a thick enough thermal boundary layer; as noted earlier, the thermal boundary layer has to be thick enough to prevent diffusive losses back to the wall when there is heat release due to chemical reactions. When a temperature ramp is imposed on a particle, the thermal boundary layer development is dependent on the magnitude of the heating rate. For low heating rates, the thermal boundary layer will develop more slowly than the thermal boundary layer of an impulsively heated surface and the time to ignition will be longer than in the impulsively heated case.

1.2.3 Particle Size

Increasing particle size for a fixed freestream velocity and particle temperature results in an increasing Reynolds number. This corresponds to decreasing values of θ_s (according to Eq. 1.5), resulting in wider and longer wakes. Examples of isotherms of increasing particle size are shown in Fig. 1.8. A fluid parcel that travels from the front stagnation point to the separation region needs to travel longer distances for in-

creasing sphere diameters, resulting in longer flow time scales. The ignition threshold is defined as the minimum sphere surface temperature required for ignition; in terms of a critical Damköhler number Da^*, the ignition threshold corresponds to $Da \geq Da^*$, corresponding to a sphere surface temperature at which the flow time scale is sufficiently large compared to the chemical time scale. The chemical time scale is usually defined by an ignition delay time. Ignition delay times, measured with a shock tube over a range of gas temperatures and fuels, are shown in Fig. 1.9. The logarithm of the ignition delay time is inversely proportional to the gas temperature away from NTC (negative temperature coefficient) region. In the NTC region (not shown in Fig. 1.9), the ignition delay time decreases with increasing temperature.

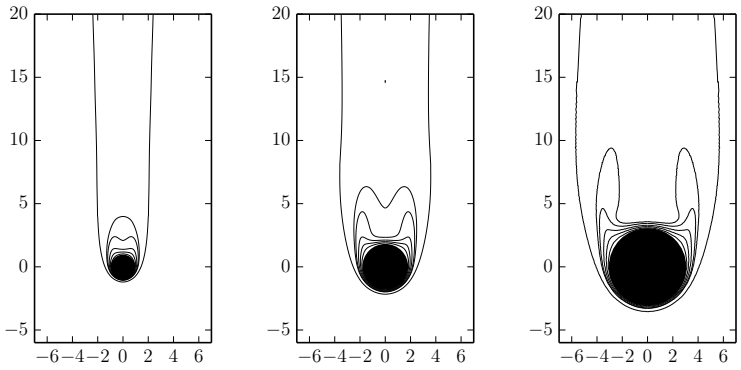

(a) Re = 90 (b) Re = 170 (c) Re > 200

Figure 1.8: Isotherms surrounding sphere for increasing particle size from left to right.[1]

For a fixed freestream velocity and increasing sphere diameter, the flow time scale increases. If the ignition conditions correspond to a fixed value of critical Damköhler number, the chemical time scale must increase a corresponding amount to maintain critical conditions. For chemical reactions in the normal (non-NTC) regime, for the chemical time scale to increase, the gas temperature and corresponding sphere surface temperature will also decrease. Therefore, the minimum ignition temperature decreases with increasing sphere diameter; this is demonstrated by previous experi-

[1]The isotherms were obtained from 2D numerical simulations of flow past a hot sphere performed by Josué Melguizo-Gavilanes

mental studies presented in Section 1.3. There are temperature variations within the thermal boundary layer of the sphere, indicated by the multiple isotherms in Fig. 1.8, making it difficult to characterize the chemical time scale using a unique gas temperature. In the above analysis, the chemical time scale is defined by assuming that the gas temperature is at the sphere surface temperature.

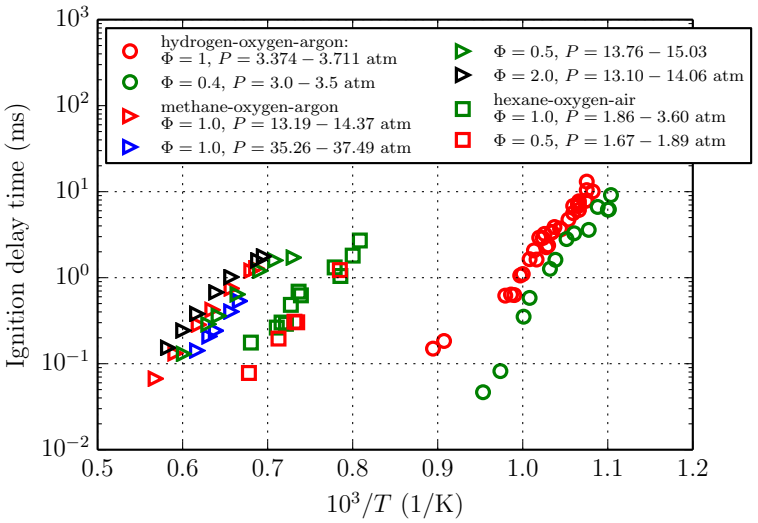

Figure 1.9: Ignition delay time measurements as a function of gas temperature taken from Vasu et al. (2011) (hydrogen-oxygen-argon), Davidson et al. (2012) (methane-oxygen-argon) and Davidson et al. (2010); Lam (2013) (*n*-hexane-oxygen-argon).

1.2.4 Inert/Reactive Environments

In the current study, the experimental setup was designed such that the particle is heated in an inert environment, accelerated, and then injected into a reactive mixture. Such a design ensures that ignition occurs while the particle is moving and not during the heating phase when the particle is stationary. Due to the abrupt transition from an inert environment to a reactive one, the inert gas has to be flushed from the boundary layer and replaced with the reactive mixture for ignition to take place. The flushing procedure time is on the order of the time required for a fluid parcel to travel from the front stagnation point to the separation region or rear stagnation point; the time is longer for fluid parcels close to the wall that have velocities close to zero

and shorter close the edge of the momentum boundary layer where a fluid parcel is traveling at or close to the freestream velocity (sphere fixed reference frame).

1.2.5 Particle Material/Surface

Lewis and von Elbe (1961) provided a brief summary of the effect of catalytic surfaces on ignition. They stated that ignition occurs more readily over a noncatalytic surface compared to a catalytic surface. A difference in the ignition behavior over catalytic and noncatalytic surfaces exists due to radical quenching at the catalytic surface. Coward and Guest (1927) heated metal strips to study the effect of surface material on ignition of natural gas-air mixtures. They found that over a wide range of materials, platinum yielded higher ignition temperatures compared to other materials such as copper, gold, nickel, stainless steel, tungsten, etc. More recently, Roth et al. (2014) quantified the effect of the surface material on the minimum ignition temperature. Tungsten carbide surfaces resulted in higher ignition thresholds than silicon nitride surfaces.

The hydroxyl radical (OH*) is an important radical species during an ignition event of various reactive mixtures. The radical is created during branching chain reactions in the thermally neutral induction period and its concentration further increases as the temperature of the gas increases. The accumulation of radicals leads to accelerated chemical activity, resulting in an ignition event. Suh et al. (2000) measured the reactivity of OH* over titanium dioxide (TiO_2), silicon dioxide (SiO_2), alumina (Al_2O_3), and gold surfaces. The reactivity was defined as the ratio of OH* radicals that reacted on the surface to the total flux of OH* incident on the surface. Suh et al. (2000) determined that gold was the most efficient at removal of OH*, whereas alumina was the second most efficient and TiO_2 was the least efficient. Given that the loss of OH* depends on the surface material, ignition could potentially be delayed for the material that showed the highest OH* reactivity: gold. Suh's study was performed at gas temperatures below 350 K, making it difficult to extrapolate the findings to temperatures plausible for ignition.

1.2.6 Particle Temperature Spatial and Temporal Variations

The previous subsections covering particle configurations assume that the sphere has a homogeneous isothermal temperature distribution. This subsection provides a brief discussion on the validity of the temperature homogeneity assumption and variation of temperature with time after heating for the specific particle configuration used in the present study.

Chapter 2 has a detailed description of the experimental setup used in this study along with the experimental procedure. In summary, a stationary sphere suspended by supports is heated for $100 - 300$ s inside an inert environment until the desired surface temperature is achieved, the sphere is then released and falls for 250 ms through the inert environment before entering the reactive mixture; the sphere falls through the reactive mixture for less than 100 ms (ignition can occur within this time).

To ensure that the temperature is spatially uniform, heating takes place over a much longer time scale than the characteristic time for heat conduction within the sphere. For example, a 1.8 mm diameter sphere will reach a temperature of approximately 1200 K in > 100 s, this is a factor of 10^3 larger than the conduction time scale (~ 0.1 s) assuming material properties of titanium alloy. The heat conduction time scale, τ_{cond}, is,

$$\tau_{\text{cond}} = \frac{r^2}{\alpha}, \tag{1.6}$$

where r is the sphere radius and α is the thermal diffusivity of the solid. For a titanium alloy sphere with a temperature of 1200 K, $\alpha = 5.5 \times 10^{-6}$ m^2/s (material properties obtained from Figs. 2.9 and 2.10); for a $r = 1$ mm sphere, $\tau_{\text{cond}} = 0.2$ s. For an alumina sphere, $\alpha = 2 \times 10^{-6}$ m^2/s and $\tau_{\text{cond}} = 0.5$ s. The combination of slow heating time and fast heat conduction within the sphere ensures that a sphere has a uniform temperature distribution when it is released.

Temperature non-uniformities can also arise while the sphere is falling; the variation in edge velocity of the momentum boundary layer around the sphere results in a distribution of the convective heat transfer coefficient, h, (Bhattacharyya and Singh,

2008) which can lead to temperature non-uniformities on the surface of the sphere (Salleh et al., 2010). However, the heat transfer to the gas from the sphere occurs over a slower time scale than heat conduction within the sphere; this is explained using a Biot number approach. The Biot number, Bi, is defined as

$$\mathrm{Bi} = hL_c/\lambda_s, \tag{1.7}$$

where h is the convective heat transfer coefficient, L_c is a characteristic length scale defined as $L_c = V/A_s$, where V and A_s are the volume and surface area of a sphere, respectively, and λ_s is the thermal conductivity of the sphere material. The Biot number is the ratio of convective heat transfer from the sphere to the surrounding gas to heat conduction within a solid, a value less than 0.1 indicates that heat conduction within the sphere occurs much faster that heat transfer to the surrounding gas (Baehr and Stephan, 2011). For a titanium sphere with a diameter of 4 mm traveling at 2.4 m/s and surface temperatures of $1000 - 1500$ K, the Biot number is $0.003 - 0.005$. Baehr and Stephan (2011) state that for a Biot number of 0.1, the variations in temperature within a solid body are less than 2%.

Finally, the sphere surface temperature changes with time after it is released. The change in temperature can be estimated using engineering heat transfer relationships for the Nusselt number (Clift et al., 2005) during the time from sphere release to entering the reactive mixture. Figure 1.10 shows the estimated temperature drop as a function of sphere temperature for different sphere diameters. The temperature drop is calculated by using a lumped model, i.e. the heat conduction within the sphere occurs sufficiently rapidly that the solid is assumed to have a homogeneous temperature (based on the Biot number analysis). Using a lumped model takes into account the convective and radiative losses from the sphere surface. The largest temperature drop is observed for the smallest sphere diameter of 1 mm; diameters smaller than 1.8 mm are not used in the present study. Over the range of diameters used in the present study, the largest temperature drop would be close to 7.5% (2 mm diameter sphere with initial surface temperature of 1400 K)

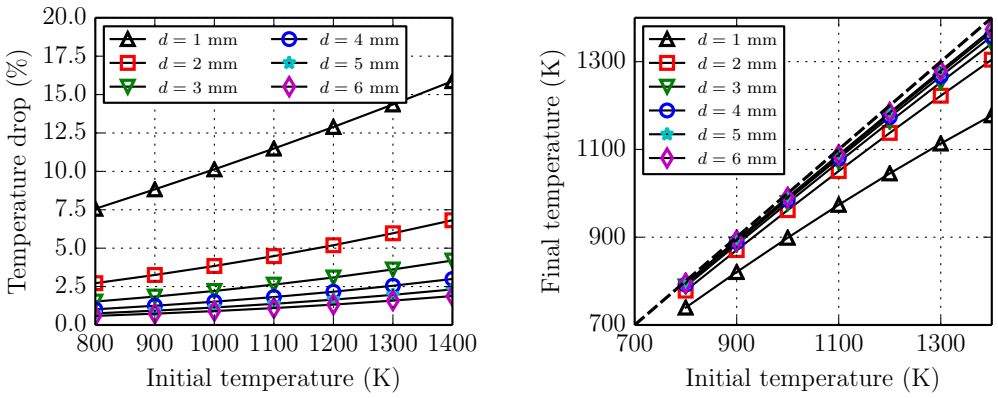

(a) Percent temperature drop (b) Final temperature

Figure 1.10: Temperature drop calculations during sphere falling time of 250 ms as a function of initial sphere surface temperature for different sphere diameters; (a) percent temperature drop and (b) final sphere temperature, the black dashed line corresponds to no temperature drop.

Although a temperature drop of less than 10% is expected over the range of experiment conditions presented in this study, what is of greater importance is the temperature drop during the time the sphere enters the reactive mixture to when ignition occurs, this corresponds to less than 50 ms. Experimentally in the present study, the last temperature measurement of the sphere surface is made prior to the sphere entering the reactive mixture. Therefore, the ignition temperature measurements are based on that particular measurement and not on the actual surface temperature of the sphere when ignition occurs. Figure 1.11 shows that for a 2 mm diameter sphere, the temperature drop is slightly over 1%; the larger sphere diameters are expected to have even smaller temperature drops. Therefore it is valid to assume that at ignition, the sphere surface temperature is approximately equal to the temperature at the final measurement location.

1.3 Previous Experimental Investigations

Previous experiments on hot particle ignition include a particle heated in a furnace and then injected into an explosive atmosphere, as well as a stationary particle placed

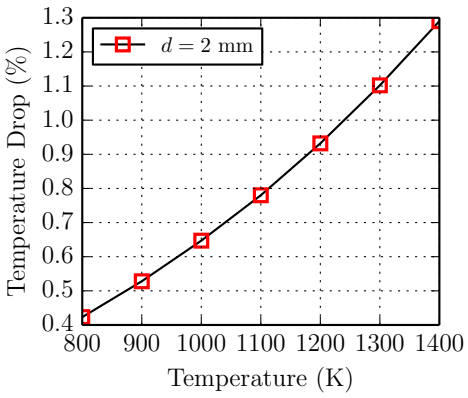

Figure 1.11: Temperature drop calculations for a 2 mm diameter sphere over 50 ms (time interval between sphere entering the reactive mixture to ignition taking place.

in an explosive atmosphere and heated via laser light. A selection of previous experimental data using hydrogen-air mixtures are shown in Fig. 1.12. Note that the figure shows a wide range of hydrogen-air mixture compositions (figure displays percent by volume of H_2 values in the caption): $5 - 25\%$ from Beyer and Markus (2012), 15% from Roth et al. (2014), 20% from Silver (1937), and 10% from Paterson (1940). Additionally, different sphere materials are displayed, ranging from metals, glass, and highly catalytic materials such as platinum.

The experiments performed by Silver (1937) used two different particle materials, quartz and platinum. Varying the particle material had minimal effect on the minimum ignition temperature of three different flammable mixtures: a 10% coal-gas-air mixture (coal-gas is composed of CO_2, CO, CH_4, and H_2), a 3% pentane-air mixture, and a 20% hydrogen-air mixture. For a fixed gas mixture, the results suggest that the size and temperature of a particle were the most important factors in determining whether ignition occurs. The data indicate that as particle size increases, the minimum temperature required for ignition decreases. The experiments performed by Silver were done with particle speeds of $2 - 5$ m/s; however, the effect of particle speed was not investigated systematically.

Beyer and Markus (2012) performed studies using "inert" particles suspended in an explosive atmosphere and heated via laser light. The combustible mixtures used in

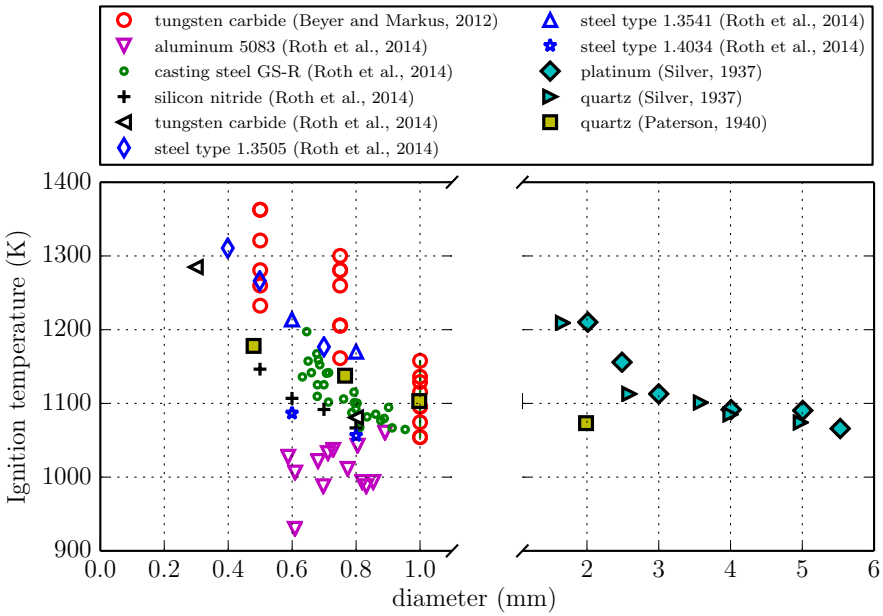

Figure 1.12: Experimental results from Beyer and Markus (2012) ($5 - 25$%-vol H_2), Roth et al. (2014) (15%-vol H_2), Silver (1937) (20%-vol H_2) and Paterson (1940) (20%-vol H_2) using hydrogen-air mixtures; the open and filled markers correspond to stationary and moving spheres, respectively.

the experiments were pentane-air, propane-air, ethylene-air, and hydrogen-air. The studies showed that the minimum ignition temperature was weakly dependent on the mixture composition but was highly dependent on which combustible gas was used. The minimum ignition temperature was also highly dependent on the particle diameter.

More recently, Roth et al. (2014) studied the ignition of hydrogen-air mixtures by sub-millimeter-sized particles and determined that the particle material (silicon nitride, tungsten carbide, steel, casting steel, and aluminum results shown in Fig. 1.12) had an effect on the minimum ignition temperature for a fixed mixture composition. For example, the aluminum particles had the lowest ignition thresholds over a wide range of diameters and the steel type 1.3505 and 1.3541 had the highest ignition thresholds.

Additional work on stationary hot particle ignition via laser light was performed by Beyrau et al. (2013), Bothe et al. (1999), Dubaniewicz et al. (2000, 2003), Dubaniewicz

(2006), and Homan (1981).

A comparison of the experimental data of Beyer and Markus (2012) and Silver (1937) for a pentane-air mixture suggests that controlling for the diameter of the particle, a moving particle will have a higher minimum ignition temperature than a stationary particle (see Fig. 1.13). Paterson (1939) saw a 300 K increase in the ignition threshold for a 2 mm diameter sphere injected into a 9% coal-gas-air mixture at 10 m/s vs. 65 m/s. In addition, Paterson (1940) performed experiments, similar to Silver (1937), in coal-gas-air, pentane-air, and hydrogen-air, at particle speeds of 1.2 m/s compared to Silver's speeds of $2 - 5$ m/s. At 1.2 m/s, the minimum ignition temperature of a 3% pentane-air mixture in Paterson's study was 100 K lower than the temperature required in Silver's study with higher particle velocities.

Additional experimental results are shown in Fig. 1.13 for pentane-air mixtures. It should be noted that the ignition thresholds obtained by Silver (1937) over the same range of sphere diameters are higher than those obtained by Paterson (1940) due to the difference in sphere speeds. Additionally, the results obtained by Beyer and Markus (2012) using stationary spheres yields ignition thresholds comparable to the moving sphere results of Paterson (1940) extrapolated to a 1 mm sphere diameter. It is important to note that the use of different materials can lead to significant variations in the ignition threshold for a fixed mixture composition and sphere diameter. Platinum in particular is known to have a strong catalytic activity that delays ignition (Coward and Guest, 1927; Griffin and Pfefferle, 1990; Kim et al., 1997; Lewis and von Elbe, 1961).

The previous work presented in this section indicates that the minimum ignition temperature is highly dependent on particle temperature, material, size, and velocity. It is unclear how different materials lead to variations in the ignition threshold; for example, Coward and Guest (1927), Griffin and Pfefferle (1990), and Kim et al. (1997) obtained higher ignition thresholds (hot surface geometries are metal strips) for the platinum surfaces than the nickel surfaces. The nickel surface is assumed to be inert since a layer of oxide is created while the material is heated. However, the study by Silver (1937) showed no significant differences in the ignition threshold

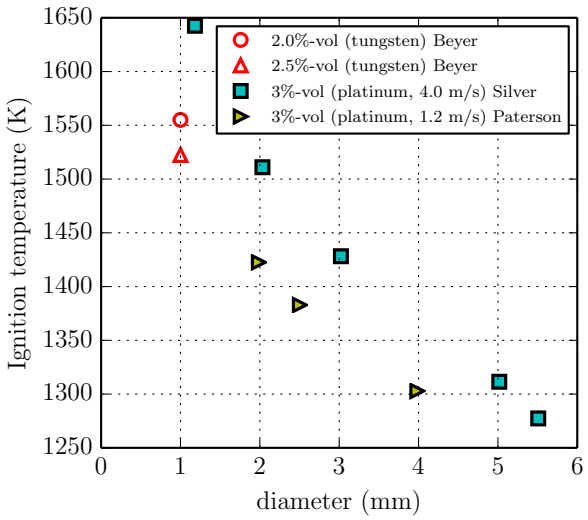

Figure 1.13: Experimental results from Beyer and Markus (2012) (red), Silver (1937) (cyan) and Paterson (1940) (yellow) using n-pentane-air mixtures; the open and filled markers correspond to stationary and moving spheres, respectively.

using platinum and quartz moving hot particles. Particle velocity plays an important role in determining the minimum ignition temperature. For example, in one study a 6.5× increase in particle velocity led to a 30% increase in the minimum ignition temperature (Paterson, 1939). Particle size is important in determining the minimum ignition temperature; however, large variations of the minimum ignition temperature can only be observed for particles of less than 1 mm in diameter. Even though extensive studies have been performed on hot particle ignition, an in-depth study of the behavior of the surrounding gas prior to and during ignition has not been performed. The main focus of the previous works cited was the parametric study of hot particle ignition with the goal of determining an ignition threshold. In addition, systematic data on moving hot particle ignition is limited and the mechanism of ignition has been largely unexplained.

1.4 Laminar Flame Propagation

If ignition takes place using a moving hot particle, a flame is created that can propagate away from the particle. The flame can be characterized using properties such as the laminar burning speed and Markstein length. The Markstein length is a measure of flame response to strain or curvature. In this work, experimental spherically expanding flames are used to measure the laminar burning speed and Markstein length in n-hexane-air at conditions characteristic of aircraft fuel tanks. Additionally, a methodology developed for accurately extracting flame properties from spherically expanding flames is applied to the experimental results of flame radius versus time.

1.5 Goal of the Investigation

A review of previous work on hot particle ignition indicates that the processes in the gas adjacent to the particle prior to and after ignition have not been thoroughly studied experimentally. Studies on moving hot particle ignition have limited to ignition threshold measurements.

The specific objectives of the present investigation are as follows:

1. Experimentally study the ignition of n-hexane-air mixtures by moving hot particles.
   (a) Develop an experimental technique for creating a well-defined moving hot particle.
   (b) Measure ignition temperature thresholds for particle diameters of $1.8 - 6$ mm.
   (c) Make detailed optical observations of events in the gas near the particle surface at the ignition threshold.
2. Obtain insight into the physical, chemical, and energy transport processes by numerically studying the ignition behavior within laminar thermal boundary layers of a one-dimensional transient model problem.

3. Characterize the flame properties such as the laminar burning speed and Markstein length of n-hexane air mixtures.

1.6 Thesis Outline

Chapter 1 discusses the motivation for studying moving hot particle ignition as well as background on previous experimental investigations of stationary and moving hot particle ignition. Chapter 2 provides a description of the experimental setup used to generate moving hot particles that are then injected into a flammable environment. The diagnostics used during each experiment are described; these are two-color pyrometry and interferometry. Chapter 3 provides an analysis of the interferograms of an unreacted wake. A step-by-step description is provided on how the raw interferograms are converted to gas temperature. Chapter 4 presents the ignition results as a function of the mixture composition and particle size. The results are presented in terms of probability of ignition versus the particle surface temperature. An analysis of the interferograms is used to pinpoint the ignition time and location. Chapter 5 describes a simplified modeling approach for ignition of the gas adjacent to a hot surface. Hydrogen-air and n-hexane-air are used as the reactive mixtures to understand the processes leading to ignition within a thermal boundary layer. Chapters 6 and 7 provide analysis on spherical flame propagation of n-hexane-air mixtures, including a methodology for extracting important flame parameters and results from spherical flame propagation experiments. Chapter 8 provides summaries and conclusions of the study as well as ideas for improvements on the current experimental setup and analysis.

Chapter 2

Experimental Setup and Diagnostics

2.1 Combustion Vessel and Heating Chamber

The ignition experiments were performed in a closed, cylindrical, stainless steel combustion vessel with a volume of approximately 22 L, shown in Fig. 2.1. The combustion vessel has a height of 37.5 cm and an inner diameter of 30.2 cm. Two parallel flanges are used to mount windows for visualization, the windows have a diameter of approximately 12 mm. Above the vessel sits a cylindrical aluminum chamber with a volume of approximately 0.1 L, also shown in Fig. 2.1. The small chamber has an inner diameter of 4 cm and a height of 8.9 cm. At the bottom of the small chamber is an opening that has a hollow cylinder attached to it; the cylinder protrudes into the inside of the combustion vessel and can be closed off with a remotely controlled actuated shutter.

The aluminum chamber is used to contain the heated spheres; it has two parallel flanges that are used to mount supports using three different configurations (further details in Section. 2.2) shown in Fig. 2.2. The other two sides of the chamber hold ZnSe (Zinc-Selenide) windows with a field of view of approximately 1.9 cm.

Figure 2.2 (a) shows two electrodes, which are linearly actuated through single acting pneumatic actuators. The electrode tips are made out of tungsten with a base diameter of 7.4 mm, cone angle of 25°, and a tip diameter of 1.3 mm. The

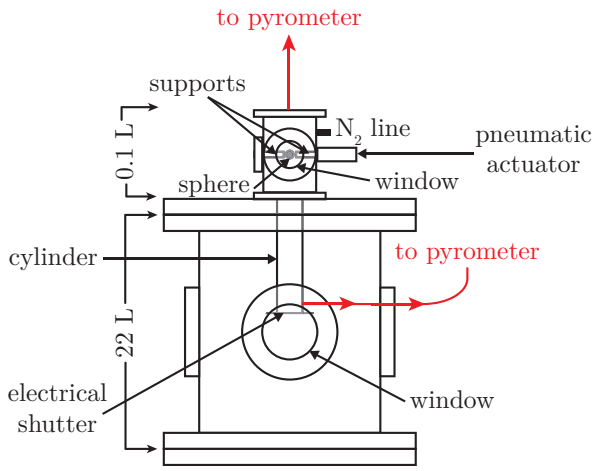

Figure 2.1: Combustion vessel and small chamber with components labeled, the red lines correspond to locations where temperature measurements are made using a two-color pyrometer.

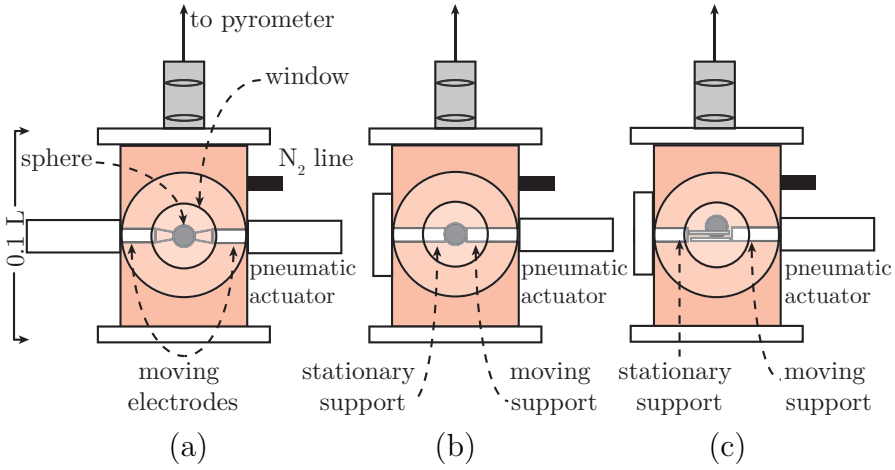

Figure 2.2: Configurations for heating spheres using: (a) electrical current and, (b) and (c) a high power laser.

electrodes hold the sphere in place and are contoured to maximize contact with the sphere, shown in Fig. 2.3 (a). Figure 2.2 (b) shows two titanium alloy supports, one of which is actuated linearly through a double acting pneumatic actuator. The titanium supports make contact with the sphere on opposite sides, holding it in place, shown in Fig. 2.3 (b). Figure 2.2 (c) shows two titanium alloy supports; however, the tip of each support is designed for particles with diameters of $1-2$ mm. The fixed support has a horizontal plate tip with a hole wide enough to allow the sphere to pass through,

and the moving support (actuated through a double acting pneumatic actuator) has a horizontal plate tip that is wide enough for the sphere to rest on, shown in Fig. 2.3 (c).

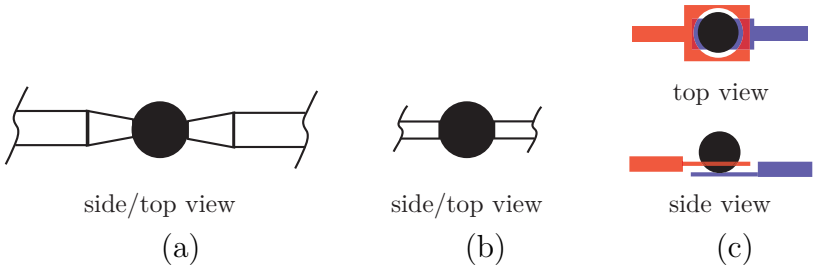

Figure 2.3: Sphere supports based on the configurations shown in Fig. 2.2: (a) two electrodes supporting sphere, (b) two titanium rods supporting sphere and (b) sphere resting on flat surface and surrounded by a plate with a hole.

The configuration shown in Fig. 2.2 (a) is used along with an electrical circuit to heat a sphere using high current (electrical heating configuration), and the configurations shown in Fig. 2.2 (b) and (c) are used along a high power laser to heat spheres using electromagnetic radiation (laser heating configuration).

Once a sphere is in place, a remotely controlled plumbing system is used to evacuate the combustion vessel to less than 50 mtorr and accurately fill it with the reactive mixture using the method of partial pressures (the reactive mixture is shown in blue in Fig. 2.4 (a)). A Heise manometer with a precise digital readout measures the static pressure so the gases can be filled to within 0.01 kPa of the desired gas pressure, providing control over the mixture composition. The aluminum chamber and attached cylinder, shown in Fig. 2.4 (b), are filled with nitrogen (shown by the red shaded region) through a port on the chamber labeled "N_2 line" (see Fig. 2.1). The bottom end of the cylinder has an electrical shutter designed for optical systems that is closed once the chamber and cylinder are completely filled with nitrogen. This ensures that during heating, the sphere is in an inert environment and there is minimal diffusion of the nitrogen from the chamber into the reactive mixture. The bottom end of the cylinder is vertically aligned with the top of the combustion vessel windows (see Fig. 2.1)

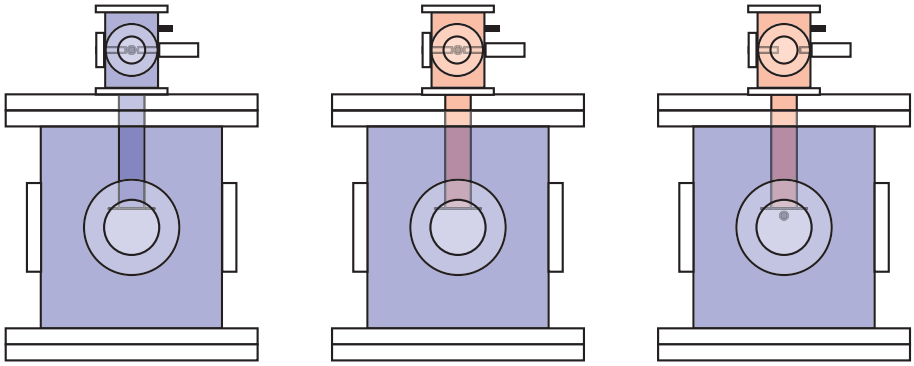

(a) Reactive mixture (b) N_2 addition (c) Sphere drop

Figure 2.4: Experimental procedure for igniting a reactive mixture using a moving hot sphere (a) fill combustion vessel and small chamber with reactive mixture (blue), then (b) fill small chamber with N_2 (red), and then (c) drop sphere into reactive mixture (blue).

In the laser heating configuration cases, a PID (Proportional, Integral, Derivative) feedback controller uses a pyrometer output to adjust the laser, thereby allowing precise control of the sphere surface temperature during heating. Once the desired sphere surface temperature is reached, one of the titanium supports retracts (laser heating configuration) or both electrodes retract (electrical heating configuration), allowing the sphere to fall; this process is shown in Fig. 2.4 (c). The sphere travels through the cylinder (containing nitrogen) and then exits through the now open optical shutter into the combustion vessel (containing the reactive mixture) and comes into the field of view of the windows. A two-color pyrometer (details in Fig. 2.3.1) measures the sphere surface temperature during heating and records it prior to the sphere entering the reactive mixture as indicated in Fig. 2.1.

Four different methods are used for ignition detection. First, the pressure rise from the combustion is measured using a pressure transducer. This measurement is used to determine the peak pressure rise in the vessel. Second, the temperature rise is detected using a K-type thermocouple located inside the vessel, approximately 30 mm normal to the inner vessel cylindrical wall. Third, the flame emission in the infrared is observed using the two-color pyrometer photodetectors. The fourth method is a shearing interferometer that uses Wollaston prisms and a 532 nm single mode laser.

This method is used to visualize the ignition and flame propagation using a high-speed camera at $10,000$ frames per second and a field of view of approximately 30 mm. Further details on the shearing interferometer are found in Section 2.3.2

2.2 Sphere Heating Configurations

2.2.1 Electrical Current Resistive Heating

As previously mentioned, two heating mechanisms are considered. In the initial phase of the study, metallic spheres are heated using electrical current. A circuit capable of producing high heating rates (> 100 K/s) using a low resistance resistor in series with a 12 V Bosch battery (CCA 850 A) is used, shown in Fig. 2.5. A sphere is connected to the circuit using two conical tungsten electrodes that are contoured to maximize contact with the sphere to ensure minimal contact resistance, and uniform heating. Different sets of resistance values ($3.8\,\Omega$, $8.1\,\Omega$, $12.8\,\Omega$, $17.8\,\Omega$) are used to obtain a wide range of currents to flow through a sphere. The voltage drop across the resistor is measured to calculate the current in the circuit. Initially the circuit connecting the sphere to the battery is open, and a Gigavac GX110 contactor is then used to close the circuit. The contactor requires 12 VDC to close, which is provided by a lab power supply and a Grayhill 70-ODC5 solid-state relay mounted on a Grayhill 70RCK4 rack.

A timing diagram illustrating the triggering of the devices and the closing of the contactor is shown in Fig. 2.6. A PCI-MIO-16E-1 12-bit data acquisition card interfacing with LabVIEW sends out a rising TTL signal that triggers a delay generator with four output channels (CHA,CHB,CHC,CHD). A 12 V power supply and a delay generator are used to provide the logic inputs to the contactor; the 12 V signal and TTL from CHA close the contactor so that the current, I, in the circuit is greater than zero. The contactor stays closed for a duration of time τ that is varied depending on the diameter of the sphere and the desired final surface temperature. After time τ, CHB from the delay generator sends out a TTL that triggers the camera to

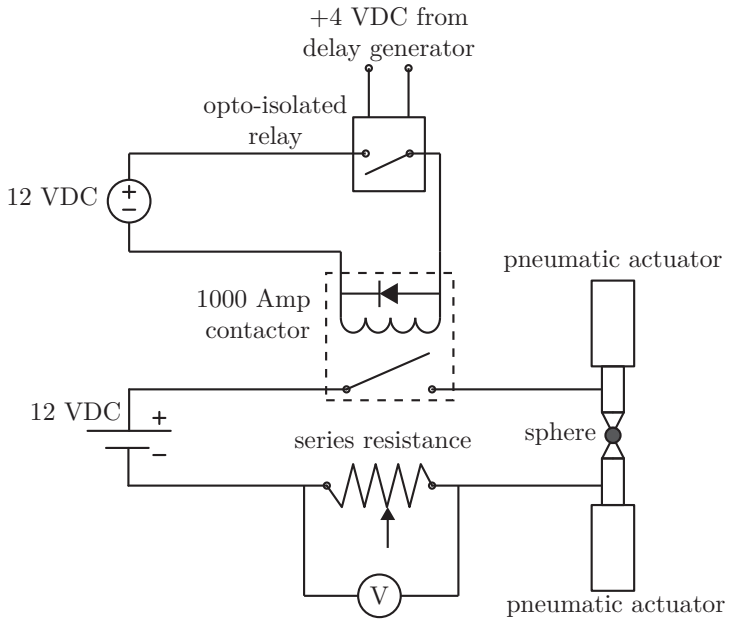

Figure 2.5: Circuit schematic for resistively heating small metallic spheres.

start recording, and a 12 V signal and TTL from CHC allow the electrodes to retract, thereby dropping the sphere.

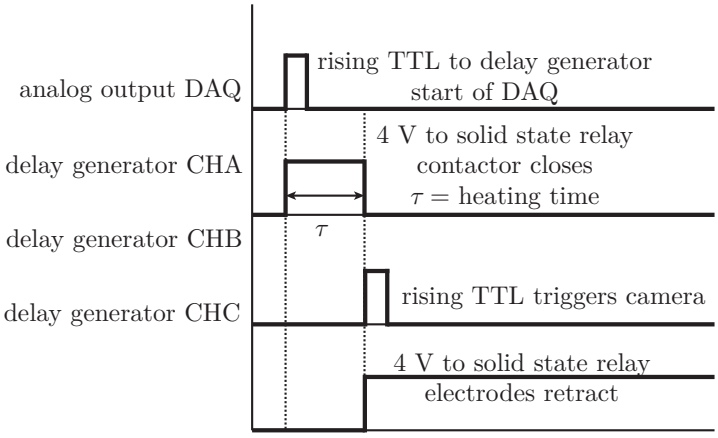

Figure 2.6: Timing diagram illustrating the experiment time and electrode retraction.

Several metals (302 stainless steel, copper, low carbon steel, alloy steel, titanium) were tested and it was concluded that a titanium alloy (Ti-6Al-4V) had a sufficiently rapid heating rate ($\sim$ 700 K/s), and due to its high melting temperature ($\approx$ 1900 K) could be heated to temperatures plausible for ignition ($>$ 1100 K). An example

of temperature-time histories for various metals tested is shown in Fig. 2.7; titanium reaches the highest temperature and also has a high signal to noise ratio due to its high emissivity, leading to a temperature time history with low noise.

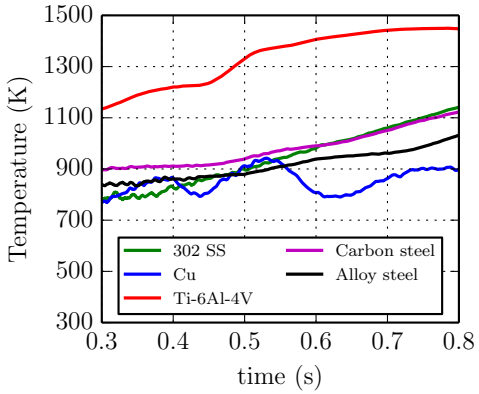

Figure 2.7: Surface temperature of various resistively heated metal spheres measured with two-color pyrometer.

Images taken during the electrical heating of a titanium sphere 4 mm in diameter are shown in Fig. 2.8. At 0.2 s, hot spots on the sphere are observed near regions that make contact with the electrodes, and the sphere continues to heat at 0.79 s; however, the regions near the electrodes remain hotter than the rest of the sphere. Finally at 1 s, the entire sphere is heated to a uniform temperature.

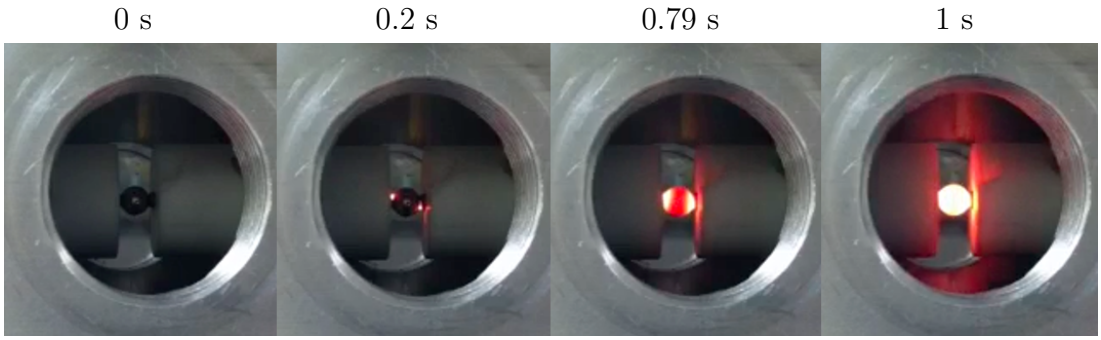

Figure 2.8: Electrical heating of titanium alloy 4 mm diameter sphere in air at room temperature and pressure.

Various material properties, i.e. thermal conductivity λ, electrical resistivity ρ_e, and specific heat c_p, are shown in Figs. 2.9 and 2.10 for stainless steel (Matula, 1979;

White and Collocott, 1984; Abu-Eishah, 2001), copper (Ho and Chu, 1977; IAE, 1997), and titanium (Maglic and Pavicic, 2001; Abu-Eishah, 2001).

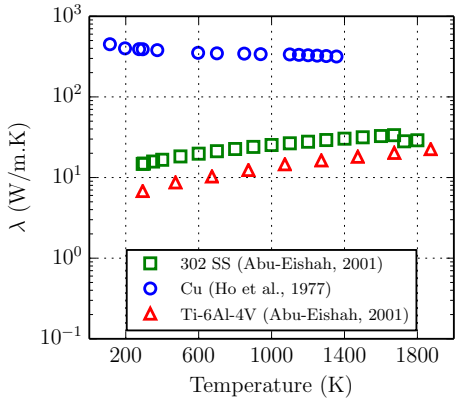

Figure 2.9: Thermal conductivity as a function of solid temperature.

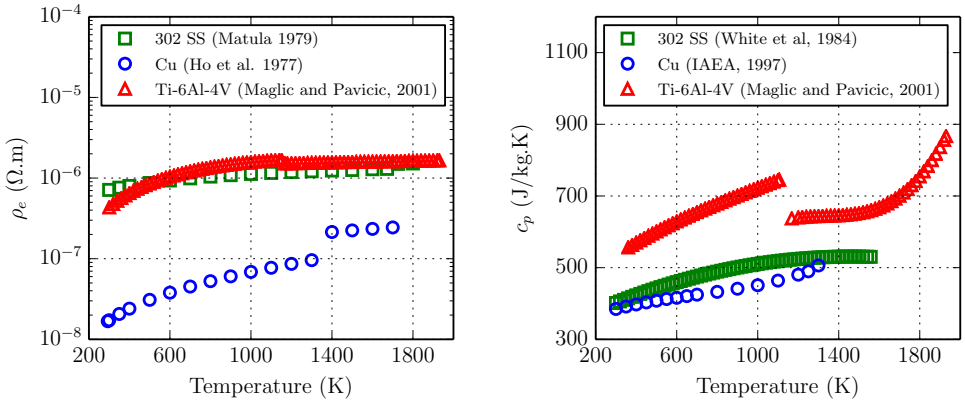

(a) Electrical resistivity (b) Specific heat

Figure 2.10: Material properties as a function of solid temperature: (a) electrical resistivity and (b) specific heat.

Additionally, the densities of the materials are 8940, 8027, and 4511 kg/m^3 for copper, 302 stainless steel and titanium, respectively. Titanium experiences a discontinuity at approximately 1200 K, shown in Figs. 2.7 and 2.9, due to a transformation of $\alpha \rightarrow \beta$, i.e. a phase change from hexagonal closed packed to body centered cubic (Maglic and Pavicic, 2001). The electrical heating method can be only be used with materials that are good electrical conductors, thereby excluding other materials such

as glass, ceramics, and plastics.

2.2.2 Infrared Laser Heating

The second method used for heating spheres is laser illumination. The sphere surface is irradiated on opposite sides with a continuous-wave (cw) CO_2 laser (Synrad) that has a maximum power output of 80 W with an emission wavelength of 10.6 μm. The optical setup, Fig. 2.11, consists of a 50/50 ZnSe beamsplitter that divides the incident beam into two beams that are perpendicular to each other; one beam is turned three times using Silicon (Si) single crystal mirrors so that it is incident on a ZnSe plano-convex lens with a 127 mm focal length (FL) and the other beam is incident on another 127 mm FL ZnSe plano-convex lens. The two beams are focused onto the sphere, inside the aluminum chamber, through ZnSe windows. The lenses allow for control of the spot size incident on the sphere.

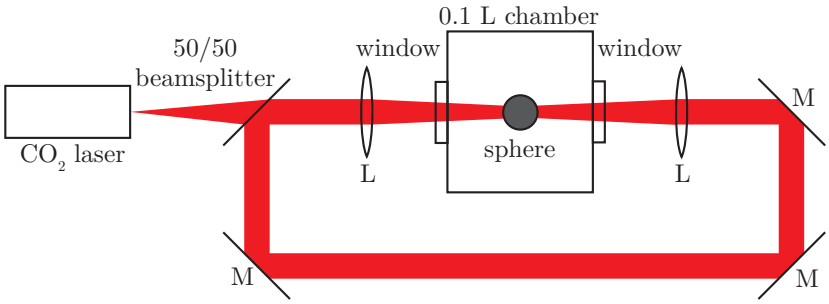

Figure 2.11: Beam splitting of CO_2 laser beam, shown in red; lenses are used to vary the beam spot size on the sphere surface (M: turning mirrors, L: 127 mm FL ZnSe lens).

The sphere surface temperature is set by using a software PID controller that interfaces with the laser controller. A timing diagram illustrating the triggering of the devices is shown in Fig. 2.12. An NI USB-6009 device interfacing with LabVIEW sends out an analog output, which varies according to the PID controller, to the laser controller modulating the laser power. The two-color pyrometer measures the temperature of the sphere as it is heated; the PID controller uses the temperature signal to control the analog output going into the laser controller. Once the desired

temperature is reached, the user activates a switch that sends a TTL signal to the delay generator. A 12 V signal and TTL from CHA allows one of the supports to retract, thereby dropping the sphere; CHB from the delay generator sends out a TTL that triggers the camera to start recording and a PCI-MIO-16E-1 12-bit data acquisition card to acquire the data from the sensors.

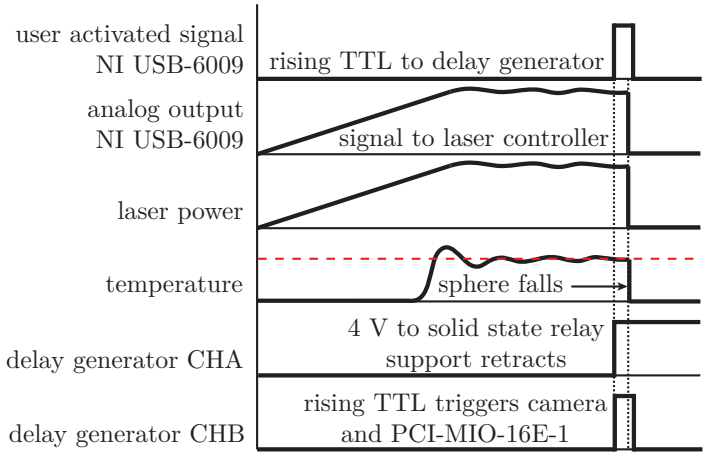

Figure 2.12: Timing diagram illustrating the laser controller and support retraction.

The parameters for the PID controller are shown in Table 2.1. These parameters are used as part of Eq. 2.1, where e is the error between the desired temperature and the temperature at t, and u is the new analog input into the laser controller.

$$u\left(t\right) = K_p e\left(t\right) + K_i \int_0^t e\left(\tau\right)\,\mathrm{d}\tau + K_d \frac{\mathrm{d}e\left(t\right)}{\mathrm{d}t}, \tag{2.1}$$

Parameter	Values
Proportional gain (K_p)	0.001
Integral gain (K_i)	0.110
Derivative gain (K_d)	0

Table 2.1: PID parameters.

Using the laser heating configuration requires materials with high emissivity at 10.6 μm; however, the metals shown in Fig. 2.7 reflect most of the incident light. Alumina is chosen as the sphere material since it has a high emissivity in the infrared

as indicated by Fig. 2.13. Additional information on the samples used to obtained the spectral emissivity such as temperature, T, surface roughness, R_a, thickness, t, purity, and heating methods are shown in Table 2.2. Figure 2.13 shows that at 10.6 μm, the spectral emissivity is roughly $0.9-1.0$, corresponding to a material with high absorption of light at the infrared wavelength.

Reference	T (K)	R_a (μm)	t (mm)	Purity (%)	Method
Ishii and Ono (2001)	373	0.62	1	-	Substrate heating
Teodorescu and Jones (2008)	823	1	6	99.5	Substrate heating
Birch and Clarke (1995)	1275	0.8	2	99.8	Cooling down after gas torching
Rozenbaum et al. (1999)	1470	-	1	-	Laser heating

Table 2.2: Specifications of samples for spectral emissivity measurements.

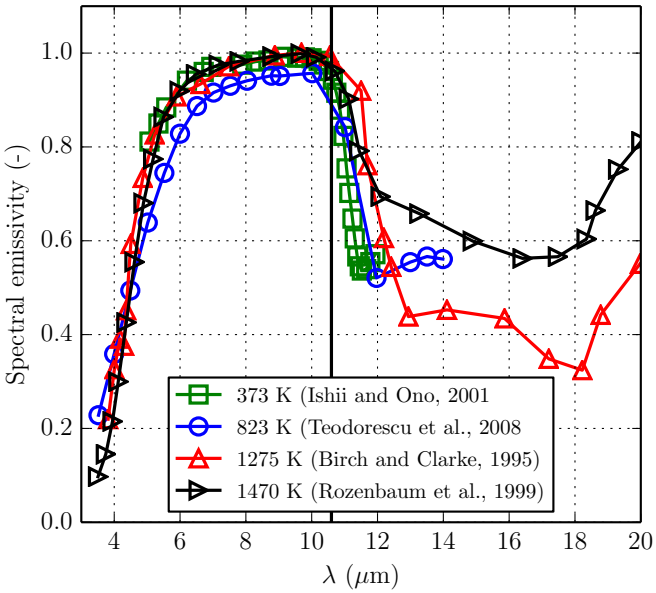

Figure 2.13: Alumina spectral emissivity obtained from Ishii and Ono (2001); Teodorescu and Jones (2008); Birch and Clarke (1995); Rozenbaum et al. (1999) for various temperatures; the vertical black line is at $\lambda = 10.6$ μm.

2.3 Optical Diagnostics

2.3.1 Two-Color Pyrometer

Several factors prevent the use of a thermocouple to measure the temperature of a sphere during heating and prior to entering the reactive mixture, the main one being that the sphere is not stationary. Therefore, a two-color pyrometer is used to perform non-contact temperature measurements of the sphere during heating and prior to entering the reactive mixture. The aim of the two-color pyrometer development is to have temperature measurements of metallic and non-metallic surfaces with temperatures ranging from 800 to 1600 K, and high speed measurements ($\sim 1\,\mu$s).

2.3.1.1 Theory

Planck's law, Eq. 2.2, gives a relationship between the spectral irradiance of a blackbody, $L_{\lambda,b}$, temperature, T, and wavelength, λ. The Planck constants are given by $C_1 = 1.496 \times 10^{-15}$ W·m^2 and $C_2 = 0.0144$ m·K. The constants are calculated by using Eq. 2.3, where h is Planck's constant, c is the speed of light in a vacuum, and k_B is Boltzmann's constant.

$$L_{\lambda,b}\left(T\right) = \frac{C_1}{\lambda^5\left[\exp\left(C_2/\lambda T\right) - 1\right]} \tag{2.2}$$

$$C_1 = 8\pi hc^2 \quad \text{and} \quad C_2 = hc/k_B. \tag{2.3}$$

Figure 2.14 shows the spectral irradiance of a blackbody at temperatures ranging from 800 to 1600 K; the maximum irradiance occurs at wavelengths between 1 μm and 4 μm. The black lines indicate the wavelengths chosen for the two-color pyrometer.

The relation in Eq. 2.2 is only valid for blackbodies which emit radiation perfectly; a correction factor called the spectral emissivity, ϵ_λ, is introduced for non-ideal bodies such that,

$$L_\lambda\left(T\right) = \epsilon_\lambda \frac{C_1}{\lambda^5\left[\exp\left(C_2/\lambda T\right) - 1\right]}. \tag{2.4}$$

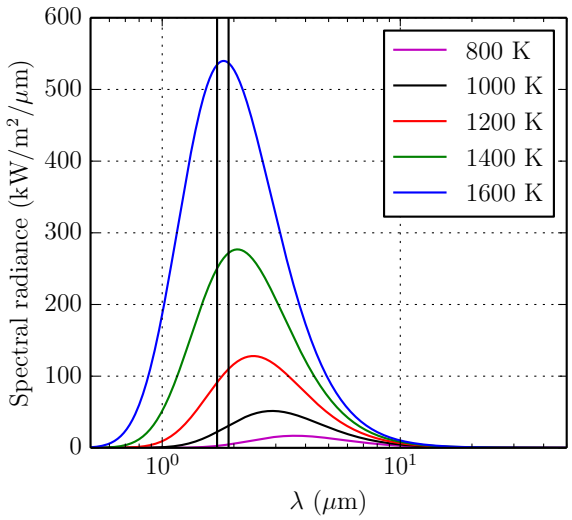

Figure 2.14: Blackbody spectral radiance at various temperatures, the black lines correspond to the wavelengths chosen for the two-color pyrometer.

In the infrared region of the spectrum, Eq. 2.4 is rewritten as the Wien approximation,

$$L_\lambda(T) \approx \epsilon_\lambda \frac{C_1}{\lambda^5} \exp\left(-C_2/\lambda T\right), \tag{2.5}$$

since $\lambda T \ll C_2$. To find the total intensity, I, Eq. 2.5 is integrated over a wavelength region, such that,

$$I(T) = \int_{\lambda-\Delta\lambda/2}^{\lambda+\Delta\lambda/2} \epsilon_\lambda \frac{C_1}{\lambda^5} \exp\left(-C_2/\lambda T\right) \, \mathrm{d}\lambda. \tag{2.6}$$

Since the region of integration, $\Delta\lambda$, is small (indicated in Section 2.3.1.2), Eq. 2.6 is approximated as,

$$I(T) = \epsilon_\lambda \frac{C_1}{\lambda^5} \exp\left(-C_2/\lambda T\right) \Delta\lambda. \tag{2.7}$$

The above relation is applied over two wavelength regions to obtain the ratio given by,

$$\frac{I_1}{I_2} = \frac{\epsilon_1}{\epsilon_2} \frac{\lambda_2^5}{\lambda_1^5} \frac{\Delta\lambda_1}{\Delta\lambda_2} \exp\left[\frac{C_2}{T\left(\frac{1}{\lambda_1} - \frac{1}{\lambda_2}\right)}\right]. \tag{2.8}$$

If the radiating body is assumed to be a graybody, i.e. the emissivity is independent

of wavelength, the ratio reduces to,

$$\frac{I_1}{I_2} = \frac{\lambda_2^5}{\lambda_1^5}\frac{\Delta\lambda_1}{\Delta\lambda_2}\exp\left[\frac{C_2}{T\left(\frac{1}{\lambda_1}-\frac{1}{\lambda_2}\right)}\right]. \tag{2.9}$$

Since the wavelengths, λ_1 and λ_2, and wavelength bandwidths, $\Delta\lambda_1$ and $\Delta\lambda_2$, are known (indicated in Section 2.3.1.2), the ratio is reduced to an expression that is a function of temperature only. Further manipulation of Eq. 2.9 yields,

$$\ln\left(\frac{I_1}{I_2}\right) = A/T + B, \tag{2.10}$$

where,

$$A = \frac{C_2}{\left(\frac{1}{\lambda_1}-\frac{1}{\lambda_2}\right)} \quad \text{and} \quad B = \ln\left(\frac{\lambda_2^5}{\lambda_1^5}\frac{\Delta\lambda_1}{\Delta\lambda_2}\right). \tag{2.11}$$

Equation 2.10 is the fundamental basis for building a two-color pyrometer that is shown in Fig. 2.15. The pyrometer measures a fraction of the intensity emitted by a radiating body over two wavelengths; Eq. 2.10 is used to calculate the temperature given the measured intensities.

2.3.1.2 Description of the Two-Color Pyrometer

The two-color pyrometer used in this study consists of a 1 mm diameter core multimode fiber optic cable that delivers light emitted by the radiating body into an optically isolated box containing optical components shown in Fig. 2.15. The fiber delivers a diverging beam of light into an achromatic lens that collimates the light. The collimated beam is incident on a dichroic mirror that transmits and reflects light with wavelengths longer than and shorter than 1.8 μm, respectively. The reflected and transmitted beams, shown in Fig. 2.15 by the blue and red paths, are focused by plano-convex lenses onto two InGaAs (Indium, Gallium, Arsenide) photodetectors. Before each beam is incident on a photodetector, it passes through a bandpass filter centered about a specific wavelength. The blue beam passes through a filter centered

at 1.705 μm with an admittance band of 105 nm and the red beam passes through a filter centered at 1.940 μm with an admittance band of 97 nm. A detailed description of each pyrometer component is given in Appendix B.

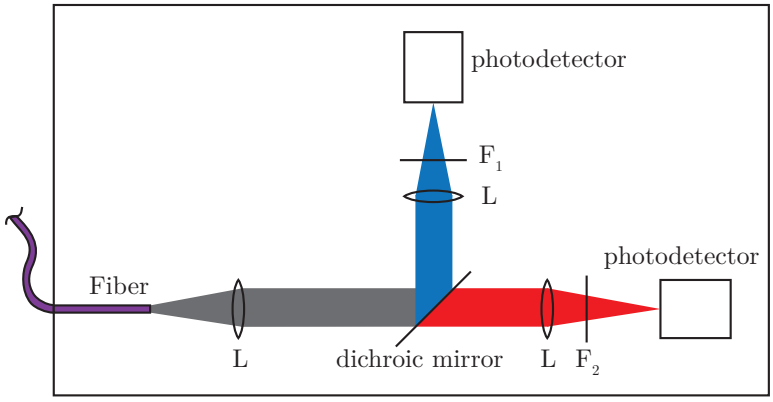

Figure 2.15: Schematic of two-color pyrometer with one input fiber (L: lens, F_1: filter, F_2: filter).[2]

After the optical elements are aligned to provide maximum incidence of radiation on the photodetectors, a calibration procedure is performed. The pyrometer is calibrated against a source with known temperatures to determine the relationship between temperature and the ratio of intensities (ratio of V_1/V_2), i.e. to determine the values of the constants A and B in Eq. 2.10. The blackbody calibration source has a temperature range of 20 to 1200°C (293 to 1473 K). Measurements are taken for temperatures between 800 K and 2500 K to provide the calibration curves shown in Fig. 2.16; V_1 and V_2 represent the voltages obtained from each photodetector. The lower limit of 800 K is determined by the sensitivity of the detectors and wavelengths selected for λ_1 and λ_2. The calibration curves are linear fits applied to the calibration measurements.

Figure 2.17 shows an additional fiber, fiber B, added to the pyrometer optical setup shown in Fig. 2.15. The pyrometer with two fibers allows for temperature measurements at two different locations. Fiber B is added to the optical setup by

[2]The author would like to acknowledge the work performed by Sebastian Rojas-Mata on developing the single fiber two-color pyrometer during his time as a SURF student in the summer of 2012.

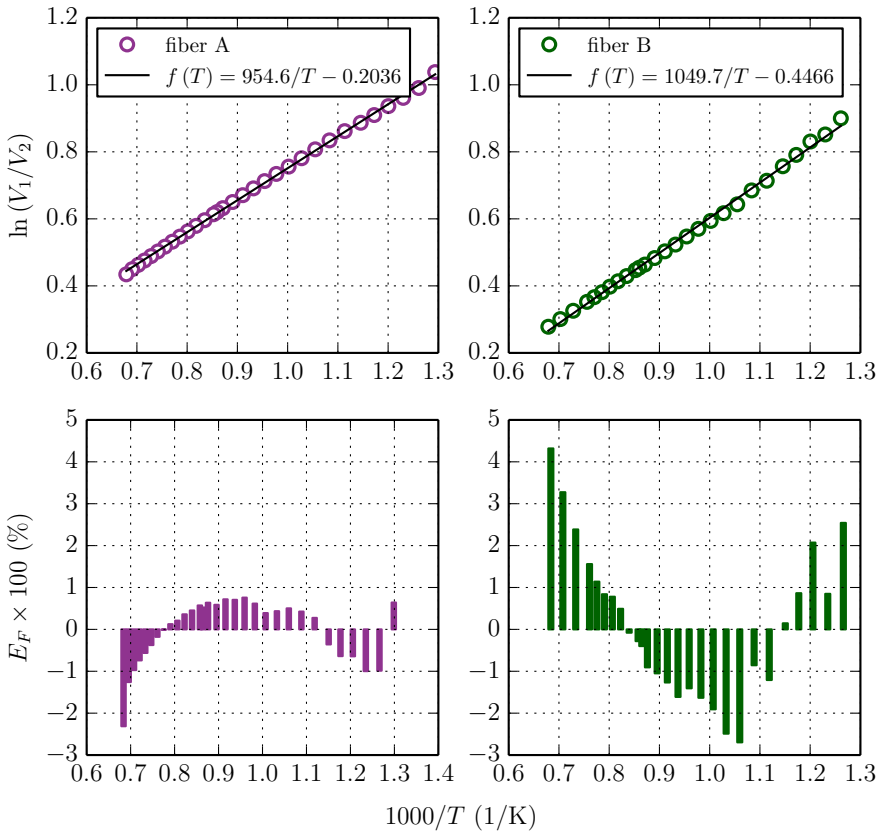

Figure 2.16: Calibration curves for fiber A and fiber B.

introducing a 50/50 beamsplitter that combines the beams coming from fiber A and fiber B. Additional details on the pyrometer calibrations are given in Appendix C.

Table 2.3 shows the constants A and B obtained from the fiber calibrations along with their respective standard deviations. The standard deviations are all less than 1% of their respective constants. The bottom images in Fig. 2.16 show the residuals calculated for each fiber; at each temperature measurement, the residual is less than 5% of the measured ratio of voltages. This translates to an error, E_T, of less than 2% in temperature, shown in Fig. 2.18.

	A (K)	B	σ_A^2 (K)	σ_B^2
fiber A	954.6	−0.2036	4.9	0.0045
fiber B	1049.7	−0.4466	11.2	0.011

Table 2.3: Calibration constants calculated for fiber A and fiber B.

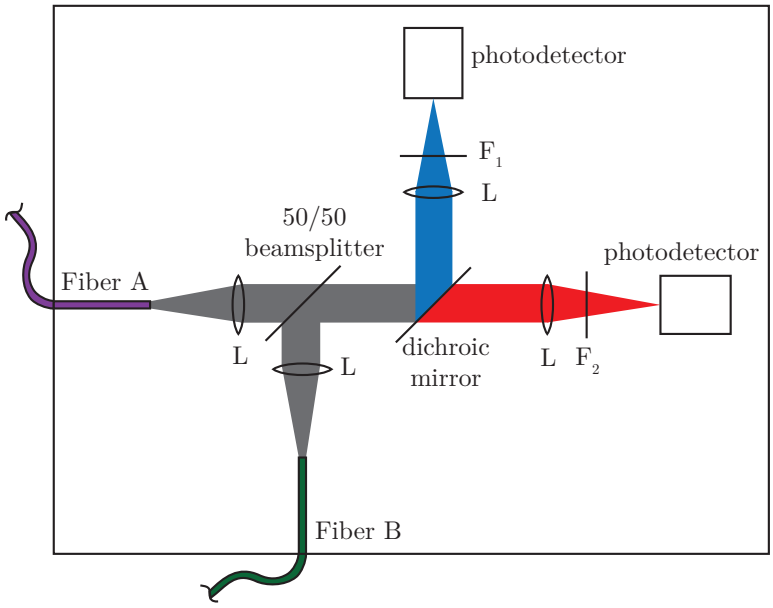

Figure 2.17: Schematic of two-color pyrometer with two input fibers (L: lens, F_1: filter, F_2: filter).

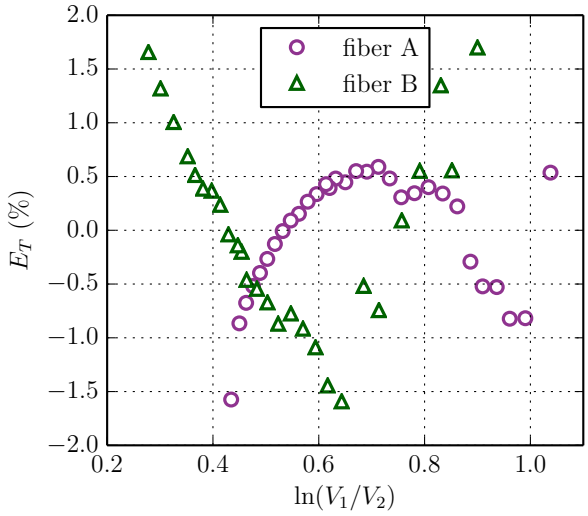

Figure 2.18: Error in temperature for fiber A and fiber B as a function of $\ln\left(V_1/V_2\right)$.

After the calibration is performed, the following equations are used to perform temperature measurements using fiber A and fiber B,

$$T_A = \frac{574.5}{\ln\left(V_1/V_2\right) + 0.1414} \tag{2.12}$$

$$T_B = \frac{599.2}{\ln\left(V_1/V_2\right) + 0.1712}. \tag{2.13}$$

The locations of fiber A and fiber B are shown in Fig. 2.4, fiber A is located above the 0.1 L aluminum chamber and fiber B is located on the lower part of the attached cylinder, above the optical shutter. Fiber A measures the sphere surface temperature during heating and Fiber B measures the surface temperature of the sphere prior to entering the reactive mixture.

2.3.2 Wollaston-Prism Shearing Interferometer

The shearing interferometer uses two Wollaston prisms with a prism angle of $\approx 19°$ and is capable of producing interferograms of either finite and infinite fringes. A simple schematic of the shearing interferometer setup is shown in Fig. 2.19 and the actual layout used is shown in Fig. 2.23.

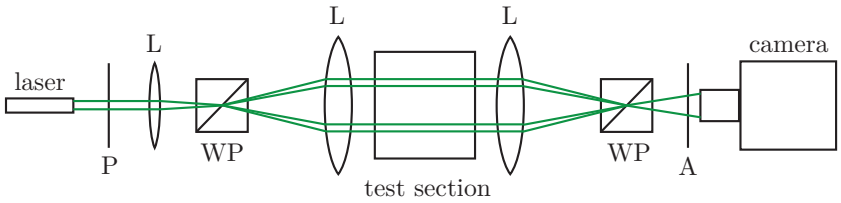

Figure 2.19: Shearing interferometer schematic (P: polarizer, L: lens, WP: Wollaston prism, A: analyzer).

Laser light passes through a linear polarizer whose plane of polarization is oriented 45° with respect to the $x - y$ plane shown in Fig. 2.20; the polarizer produces equal magnitude electric vector components, E_x and E_y, lying along the x and y axes (Black and Carr, 1971). The polarized light is incident on a lens that focuses the beam onto a Wollaston prism. The Wollaston prism consists of two quartz[3] prisms with optical axes that are perpendicular to each other. The Wollaston prism causes the rays associated with the two perpendicular electric field components (optical polarizations) to diverge as they leave the prism.

[3]Quartz has the property of birefringence: different indices of refraction along the crystallographic axes.

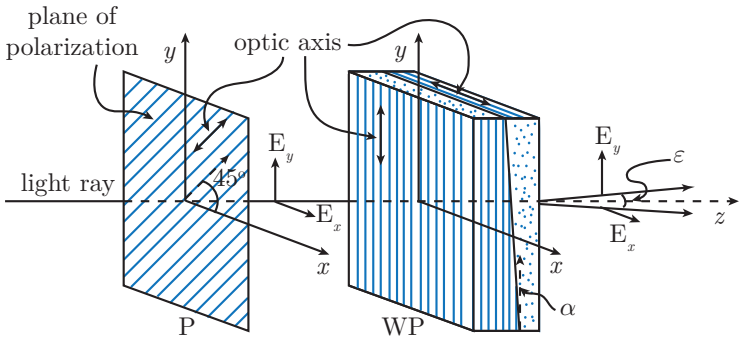

Figure 2.20: Orientation of polarizer (P) and first Wollaston prism (WP) for separation of E_x and E_y components of a single light ray, schematic adapted from Small et al. (1972) and Black and Carr (1971)

If the prism is placed at the focal point of the lens, the two rays are in phase with each other but separated and orthogonally polarized to each other; if the prism is placed away from the focal point, the two rays are out of phase (Merzkirch, 1987). The separation distance between the two rays is given by Snell's law of refraction and by assuming a small prism angle, α, (Merzkirch, 1987) giving,

$$\varepsilon = 2\alpha \left(n_e - n_o \right), \tag{2.14}$$

where n_e and n_o are the refractive indices of the extraordinary and ordinary rays, respectively, in the prism material. For light with a wavelength of 589 nm, $n_e = 1.5553$ and $n_o = 1.4864$ (Merzkirch, 1987); this results in $\varepsilon = 0.3 - 0.4°$ given $\alpha = 19°$.

The polarizer and first Wollaston prism shown in Fig. 2.19 can be freely rotated about the z axis so that the two beams leaving the Wollaston prism can intersect the test section at any arbitrary angle, β, measured from the positive $x-$axis in the $x - y$ plane. Examples of the two beams intersecting the test section are shown in Fig. 2.21. In the present experimental setup, $\beta = 90°$ was chosen so that the two beams are horizontally aligned along the $x-$axis.

After the two beams exit the test section, as shown in Fig. 2.19, they are incident on a focusing lens with a focal point that is coincident with the location of the second

Wollaston prism. The two beams incident on the second Wollaston prism recombine since the prism is identical to the first Wollaston prism and rotated 180° about the $z-$axis. The recombined light exits the second Wollaston prism and passes through an analyzer which allows for interference between E_x and E_y of a ray. The optical axis of the analyzer is parallel to that of the polarizer. The diverging beam is imaged onto the CCD of a high speed camera. A schematic of interference patterns obtained with different β orientations is shown in Fig. 2.22.

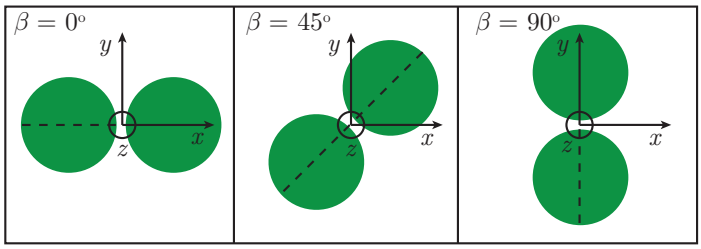

Figure 2.21: Orientation of beams separated by Wollaston prism.

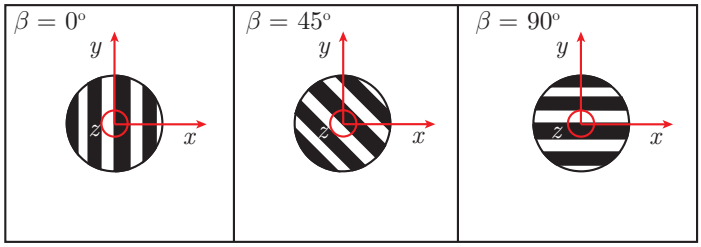

Figure 2.22: Interference patterns for different β values.

The experimental interferometer setup is shown in Fig. 2.23, and detailed specifications of each optical component are given in Appendix B; all the turning mirrors are $\lambda/20$ flat fused silica with enhanced aluminum coatings and the collimating parabolic mirrors are $\lambda/8$ BOROFLOAT with enhanced aluminum coatings. The beam from a 532 nm single mode Coherent solid state laser (Sapphire SF 532) is turned by a periscope to allow for precise directional control. The beam passes through a $5\times$ beam expander and turned using two mirrors (M). The beam is focused using a plano-convex lens (L) and linearly polarized (P) at 45°. The polarized beam is focused onto

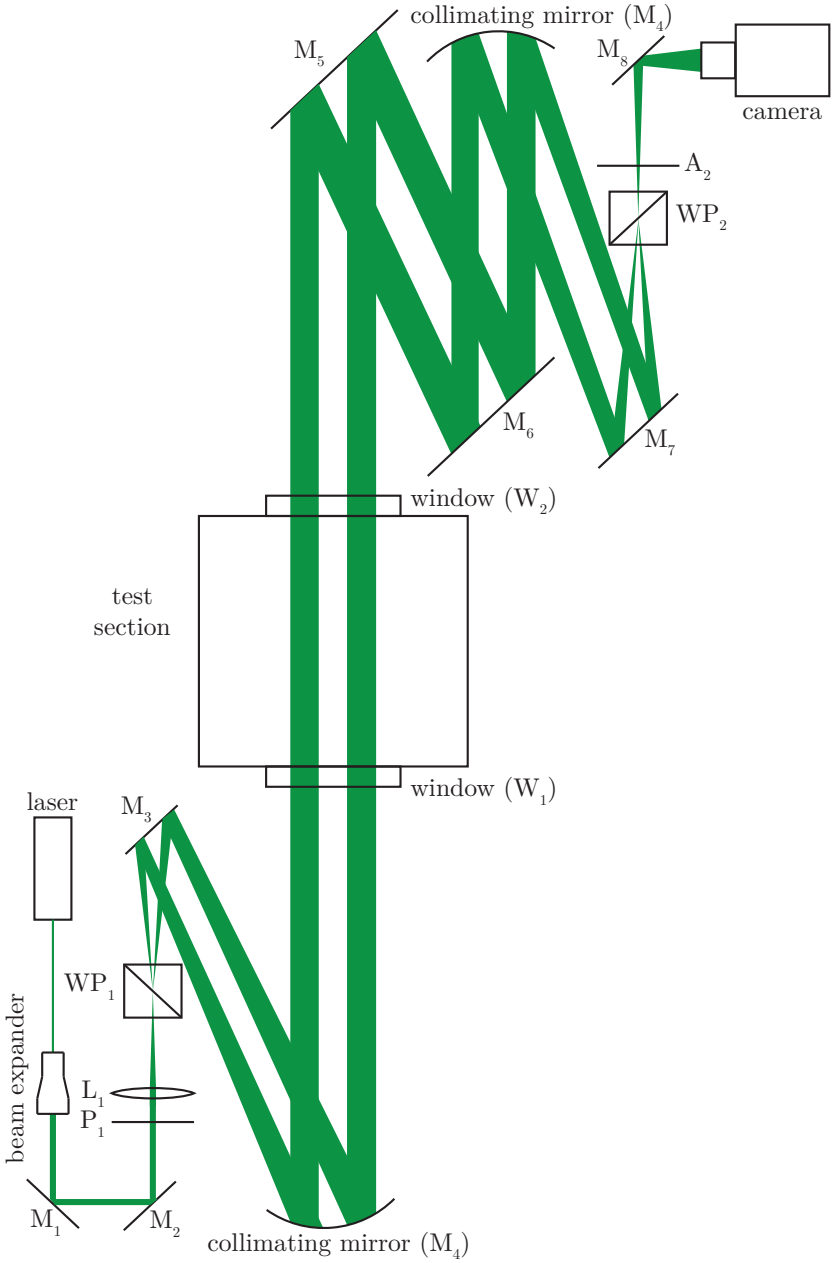

Figure 2.23: Shearing interferometer layout used in testing (P: polarizer, L: lens, WP: Wollaston prism, W: window, A: analyzer).

a Wollaston prism (WP) with a prism angle of $\approx 19°$. The two orthogonally polarized beams are turned by a mirror (M) onto a parabolic mirror with a focal length of 864 mm. The two collimated beams intersect the test section at $\beta = 90°$ as shown in Fig. 2.21. The parabolic mirror used results in a beam separation distance of ≈ 38 mm. Two turning mirrors (M) are used to direct the two beams onto a parabolic mirror with a focal length of 864 mm; the mirror focuses the two beams onto a second identical Wollaston prism rotated 180° about the z axis. The orthogonally polarized beams are recombined and passed through an analyzer (A) to create an interference pattern. The beam is then imaged onto a Phantom V711 high speed camera with a resolution of 800×600 px at $10,000$ fps.

2.4 Quantitative Analysis of Interferograms

The interferograms obtained with the shearing interferometer represent the optical path length difference between light traveling through a field of view with refractivity $n(z)$ and light traveling through a reference field with refractivity n_0. The difference in phase, $\Delta\varphi$, is related to the index of refraction by,

$$\Delta\varphi = \varphi - \varphi_0 = \frac{2\pi}{\lambda} \int_{\zeta_1}^{\zeta_2} [n(z) - n_0] \, \mathrm{d}z, \tag{2.15}$$

where ζ_1 and ζ_2 are the locations along the $z-$axis where a ray enters and leaves the test section, respectively, and λ is the wavelength of the light in a vacuum. In the current study, $\lambda = 5.32 \times 10^{-7}$ m. The intensity, I, of a two-dimensional fringe pattern is represented by an amplitude and frequency modulated function,

$$I\left(x, y\right) = a\left(x, y\right) + b\left(x, y\right) cos\left(\Delta\varphi\left(x, y\right)\right), \tag{2.16}$$

where a represents the background illumination and noise, b is the amplitude, and φ is the phase (Rastogi and Hack, 2015). The phase demodulation of the interferograms, i.e. obtaining $\Delta\varphi$, is accomplished by using the 2D Windowed Fourier Filtering method (WFF2) (Kemao, 2013).

2.4.1 Windowed Fourier Filtering (WFF2) Method

This section describes the method used to extract the phase from two dimensional images obtained with shearing interferometry. The two-dimensional Fourier transform, F, and inverse Fourier transform, f, are defined as,

$$F(\xi_x, \xi_y) = \int_{-\infty}^{\infty} f(x,y) e^{-i(\xi_x x + \xi_y y)} \, \mathrm{d}x\mathrm{d}y, \tag{2.17}$$

$$f(x,y) = \frac{1}{2\pi} \int_{-\infty}^{\infty} F(\xi_x, \xi_y) e^{i(\xi_x x + \xi_y y)} \, \mathrm{d}\xi_x \mathrm{d}\xi_y, \tag{2.18}$$

where ξ_x and ξ_y are frequency coordinates in the Fourier domain. Using the following windowed Fourier basis,

$$g_{\xi_x,\xi_y}(x,y) = g(x,y)\, e^{i(\xi_x x + \xi_y y)}, \tag{2.19}$$

where $g(x,y)$ is a Gaussian window,

$$g(x,y) = \frac{1}{2\pi\sqrt{\sigma_x \sigma_y}} e^{-x^2/2\sigma_x^2 - y^2/2\sigma_y^2}, \tag{2.20}$$

the 2D continuous windowed Fourier transform (WFT) and inverse WFT is written as,

$$F_W(u, v; \xi_x, \xi_y) = \int_{-\infty}^{\infty} \int_{-\infty}^{\infty} f(x,y) g_{\xi_x,\xi_y}(x-u, y-v) \, \mathrm{d}x\mathrm{d}y, \tag{2.21}$$

$$f(x,y) = \frac{1}{4\pi^2} \int_{-\infty}^{\infty} \int_{-\infty}^{\infty} \int_{-\infty}^{\infty} \int_{-\infty}^{\infty} F_W(u, v; \xi_x, \xi_y) g_{\xi_x,\xi_y}(x-u, y-v) \, \mathrm{d}\xi_x \mathrm{d}\xi_y \mathrm{d}u\mathrm{d}v, \tag{2.22}$$

where u and v are spatial coordinates. Equations 2.21 and 2.22 are expressed in terms of the convolution operator $\otimes$ and written as,

$$F_W(u, v; \xi_x, \xi_y) = f(u,v) \otimes g_{\xi_x,\xi_y}(x,y), \tag{2.23}$$

$$f(x,y) = \frac{1}{4\pi^2} \int_{-\infty}^{\infty} \int_{-\infty}^{\infty} F_W(u, v; \xi_x, \xi_y) \otimes g_{\xi_x,\xi_y}(x,y) \, \mathrm{d}\xi_x \mathrm{d}\xi_y. \tag{2.24}$$

The discrete form of Eq. 2.24 is written as,

$$f(x,y) = \frac{\xi_x^{(i)}\xi_y^{(i)}}{4\pi^2} \sum_{\xi_y=-\pi}^{\pi} \sum_{\xi_x=-\pi}^{\pi} F_W(u,v;\xi_x,\xi_y) \otimes g_{\xi_x,\xi_y}(x,y), \tag{2.25}$$

where $\xi_x^{(i)}$ and $\xi_y^{(i)}$ are the sampling intervals of ξ_x and ξ_y.

The windowed Fourier coefficient measures the similarity between a section of the signal and the windowed Fourier kernel given in Eq. 2.19. The coefficients are high if the signal is similar to the windowed Fourier kernel, and small if the section of the signal consists of noise. To accurately reconstruct Eq. 2.25, the coefficients that correspond to the signal noise need to be eliminated. This is done by setting a predetermined threshold, *thr*; coefficients lower than the threshold are discarded and not used in the reconstruction. Therefore,

$$\overline{f}(x,y) = \frac{\xi_x^{(i)}\xi_y^{(i)}}{4\pi^2} \sum_{\xi_y=-\pi}^{\pi} \sum_{\xi_x=-\pi}^{\pi} \overline{F_W}\left(u,v;\xi_x,\xi_y\right) \otimes g_{\xi_x,\xi_y}(x,y), \tag{2.26}$$

where $\overline{F_W}\left(u,v;\xi_x,\xi_y\right)$ denotes the thresholded spectrum,

$$\overline{F_W}\left(u,v;\xi_x,\xi_y\right) = \begin{cases} F_W\left(u,v;\xi_x,\xi_y\right), & \text{if } |F_W\left(u,v;\xi_x,\xi_y\right)| \geq thr \\ 0, & \text{if } |F_W\left(u,v;\xi_x,\xi_y\right)| < thr. \end{cases}$$

The thresholded phase is found by,

$$\overline{\Delta\varphi_W}(x,y) = \angle\overline{f}(x,y), \tag{2.27}$$

where $\angle\overline{f}(x,y)$ is the angle of the thresholded signal. The subscript W (wrapped) in Eq. 2.27 corresponds to a an optical phase difference that is bounded between $-\pi$ and π, modulo 2π. To construct a continuous optical phase difference, a quality guided phase map using a flood-filling algorithm was used to unwrap the phase (Ghiglia and Pritt, 1988). Several methods exist for performing phase unwrapping, one of them is the path following algorithm. Within the path following method there are fixed-path

and quality guided algorithms. The quality guided algorithm uses a quality map to determined the path along which the phase unwrapping is performed. The quality map, $Q(x,y)$, is given by,

$$Q(x,y) = 1 - \frac{\Delta\phi_r(x,y)}{2\pi}, \tag{2.28}$$

where ϕ_r is the wrapped thresholded phase $\overline{\Delta\varphi_W}$ and $\Delta\phi_r$ is the phase variance calculated from Eq. 2.29.

$$\begin{aligned}\Delta\phi_r(x,y) = \frac{1}{4}\Big(&\left|\phi_r(x,y) - \phi_r(x,y-\Delta y)\right| + \left|\phi_r(x,y) - \phi_r(x,y+\Delta y)\right| \\ &+ \left|\phi_r(x,y) - \phi_r(x-\Delta x,y)\right| + \left|\phi_r(x,y) - \phi_r(x+\Delta x,y)\right|\Big)\end{aligned} \tag{2.29}$$

To begin the quality guided algorithm, a pixel is chosen with the highest quality, which is where Q is highest; the phase is unwrapped, ϕ, at this location. Then, the quality of the 4 pixels surrounding this unwrapped location is checked, and the pixel with the highest quality is chosen next. At this chosen location the phase is unwrapped using Eq. 2.30.

$$\phi(n) = \begin{cases} \phi(n-1) + \Delta\phi_r(n) + 2\pi, & \text{if } \Delta\phi_r(n) \leq -\pi \\ \phi(n-1) + \Delta\phi_r(n), & \text{if } \pi < \Delta\phi_r(n) < \pi \\ \phi(n-1) + \Delta\phi_r(n) - 2\pi, & \text{if } \Delta\phi_r(n) \geq -\pi, \end{cases} \tag{2.30}$$

where n is the chosen pixel location and $\phi(n)$ is the unwrapped phase at that location. The unwrapped optical phase difference in the following sections is represented by $\Delta\varphi$.

2.4.2 From Optical Phase Difference to Gas Density

Since the index of refraction in the current study is assumed to be cylindrically symmetric (further details in Chapter 3), as illustrated in Fig. 2.24, the Abel transform, Eq. 2.31, is used to relate a line of sight integrated quantity to a radially distributed one (Poularikas, 2010).

$$F(x) = 2\int_x^\infty \frac{f(r)r}{(r^2 - x^2)^{1/2}}\,\mathrm{d}r. \tag{2.31}$$

The inverse Abel transform is given by (Poularikas, 2010),

$$f(r) = -\frac{1}{\pi}\int_r^\infty \frac{\mathrm{d}F}{\mathrm{d}x}\frac{\mathrm{d}x}{(x^2 - r^2)^{1/2}}, \tag{2.32}$$

where in the context of refractive index and optical phase difference,

$$f(r) = \frac{2\pi}{\lambda}[n(r) - n_o(r)] \quad \text{and} \quad F(x) = \Delta\varphi. \tag{2.33}$$

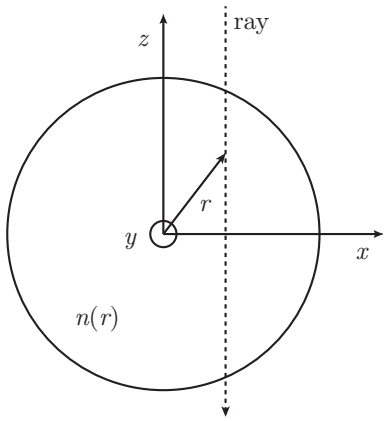

Figure 2.24: Light wave passing through a radially symmetric medium.

Errors in the refractive index due to the inversion of the Abel transform can arise from the assumption that the ray going through the disturbed medium, test ray, follows a straight path, shown in Fig. 2.24, similar to the ray traveling through the undisturbed medium, reference ray. However, a ray traveling through a flame will experience a large change in the refractive index which would result in refraction of the ray, i.e., a deviation from a straight path. Vest (1975) performed a study on the errors in the refractive index when performing the inversion of the optical phase difference of a ray passing through a strongly refracting medium. A schematic of a refracted ray and its corresponding reference ray is shown in Fig. 2.25. Path ABC corresponds to the path taken by the refracted ray as it passes through the disturbed

medium and path DEF corresponds to the path taken by the reference ray as it passes through an undisturbed medium. The two rays shown interfere and have the same optical phase at points A and D; beyond C and F, both rays will traverse the same optical path length if a lens is used to form an image of the center plane of the phase object. Vest (1975) determined that the interference patterns are due to the difference in optical phase of the disturbed ray as it travels through ABC and the reference ray as it travels through DEF. Taking only those paths into consideration, the assumption of the disturbed ray traveling a straight path accounts for an error in the refractive index of $0.6 - 5.1\%$ for a range of strongly refracting phase objects (Vest, 1975).

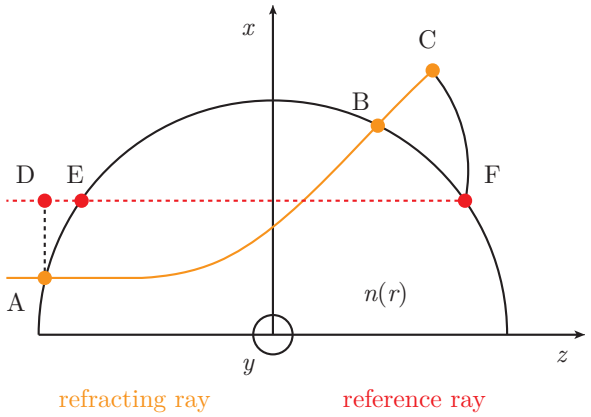

Figure 2.25: Strongly refracted ray (yellow) passing through disturbed medium and reference ray (red) passing through undisturbed medium, schematic adapted from Vest (1975).

Additionally, the refracted ray path can be approximated as straight since the angle at which it is refracted is very small. An example of a refracted ray passing through a flame is shown in Fig. 2.26 (a). The ray is incident on the flame a distance b from the centerline and exits the flame at an angle χ, defined as the scatter angle. For a stoichiometric hydrogen-air flame, the resulting scatter angle as a function of the normalized incident beam location b/R is shown in Fig. 2.26 (b). The largest scatter angle is observed for $b/R = 1$, that is close to the flame edge. A scatter angle of $0°$ is observed for $b/R = 0$ where the the ray is incident on the flame at $90°$. Regardless of

the differences in the refractive index observed by the ray, the scatter angle remains small, less than 1°. These small scatter angles indicate that the refracted rays barely deviate from a straight path.

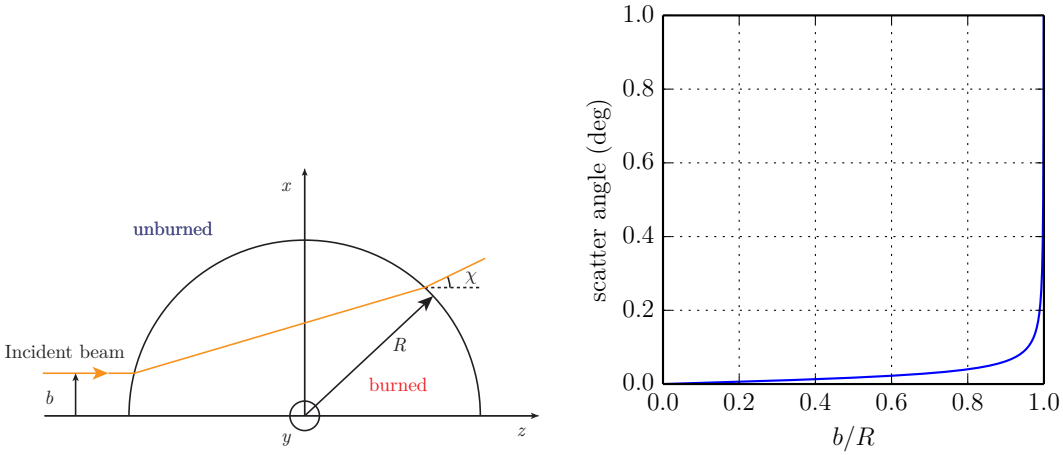

(a) Schematic of refracted ray (b) Scatter angle

Figure 2.26: (a) Schematic of ray passing through a spherical flame and its corresponding (b) scatter angle, χ, calculated for a stoichiometric hydrogen-air flame.

The inversion of the Abel transform is achieved by using the Nestor-Olsen numerical algorithm (Nestor and Olsen, 1960) that was implemented in the inversion of radially resolved intensity measurements by Álvarez et al. (2002). The Nestor-Olsen method approximates Eq. 2.32 by,

$$f(r) = \frac{-2}{\pi \Delta x} \sum_{i=j}^{N-1} F(x_i) B_{j,i}, \tag{2.34}$$

where,

$$B_{j,i} = \begin{cases} A_{j,i-1} - A_{j,i}, & \text{for } i \geq j+1 \\ -A_{j,i}, & \text{for } i = j \end{cases}$$

and,

$$A_{j,i} = \frac{\left[i^2 - (j-1)^2\right]^{1/2} - \left[(i-1)^2 - (j-1)^2\right]^{1/2}}{2i-1}. \tag{2.35}$$

The refractive index is found after obtaining $f(r)$, using Eqs. 2.34 and 2.35, and

manipulation of Eq. 2.33, which yields,

$$n(r) = n_0 + \frac{\lambda}{2\pi} f(r). \tag{2.36}$$

The density of the medium is calculated by using the Gladstone-Dale relation, Eq. 2.37, where $K = 2.274 \times 10^{-4}$ m^3/kg at for air at a temperature and pressure of 300 K and 100 kPa, respectively (Merzkirch, 1987).

$$n - 1 = K\rho \tag{2.37}$$

The refractive index is in general dependent on the composition, temperature, and pressure of the medium, as well as the wavelength of the light source used. For non-reacting ideal gases at constant pressure, Eq. 2.37 is approximated by,

$$n - 1 \propto 1/T, \tag{2.38}$$

and therefore,

$$\frac{n-1}{n_0-1} = \frac{T_0}{T}, \tag{2.39}$$

where T_0 is the reference field temperature. If δ is defined as $n - 1$, then,

$$\frac{\delta}{\delta_0} = \frac{T_0}{T}. \tag{2.40}$$

For air at room temperature and atmospheric pressure, the variation of δ with temperature is calculated using Eq. 2.40 and shown in Fig. 2.27.

At low temperatures, a change in temperature yields a large change in δ, e.g. a change of 1.5×10^{-4} for a temperature increase from 300 to 600 K; however at high temperatures, the changes in δ become smaller, e.g. 1×10^{-5} for a temperature increase from 1500 to 1800 K. For n-hexane-air mixtures, changes in the refractive index are clearly observed following an ignition and flame propagation in which the temperature of the gas ranges from 300 K (fresh reactants) to $\sim$ 2000 K (adiabatic flame temperature) (Law, 2006).

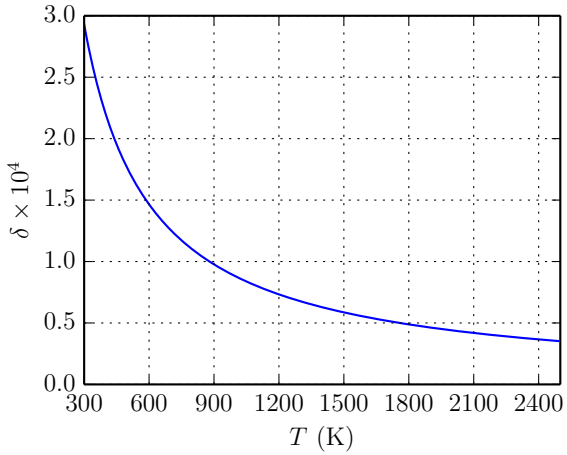

Figure 2.27: δ versus the gas temperature for air at room temperature and atmospheric pressure; $\delta_0 = 2.93 \times 10^{-4}$.

The refractive index of the medium is also affected by the change of composition due to combustion. Weinberg (1963) determined that in combustion processes, the change in refractive index due to composition changes is small compared to changes due to temperature. To demonstrate the smallness of the change in δ due to the change in number of moles, consider the stoichiometric oxidation in air of n-hexane (C_6H_{14}),

$$C_6H_{14} + 45.2(0.21O_2 + 0.79N_2) \longrightarrow 6CO_2 + 7H_2O + 35.7N_2$$

$$\delta_{\text{reactants}} = (\delta_{C_6H_{14}} + 9.5\delta_{O_2} + 35.7\delta_{N_2})/46.2 = 0.000329$$

$$\delta_{\text{products}} = (6\delta_{CO_2} + 7\delta_{H_2O} + 35.7\delta_{N_2})/48.7 = 0.000311.$$

The change in δ due to the change in number of moles is approximately 5%. The values for δ of each species used in the above calculations are given in Table 2.4.

$\delta_{C_6H_{14}}$	δ_{O_2}	δ_{N_2}	δ_{CO_2}	δ_{H_2O}
2.00	2.72	2.97	4.51	2.62

Table 2.4: $\delta \times 10^4$ values for various gases Weinberg (1963); Haynes (2014).

Finally, the refractive index has a wavelength dependence that is given by Cauchy's

dispersion formula shown in Fig. 2.41.

$$n - 1 = A_1 \left(1 + \frac{B_1}{\lambda^2}\right) \tag{2.41}$$

For air at room temperature and atmospheric pressure, $A_1 = 28.78 \times 10^{-5}$ and $B_1 = 5.67 \times 10^{10}$ nm^2 (Weinberg, 1963) . The resulting behavior of the refractive index is shown in Fig. 2.28 by the blue line. For $\lambda = 532$ nm, the refractive index appears to reach an horizontal asymptote. The change in the refractive index with wavelength is shown in the same figure by the red line; at 532 nm, $\mathrm{d}\delta/\mathrm{d}\lambda = -2.16 \times 10^{-8}$ nm^{-1}, an almost negligible value.

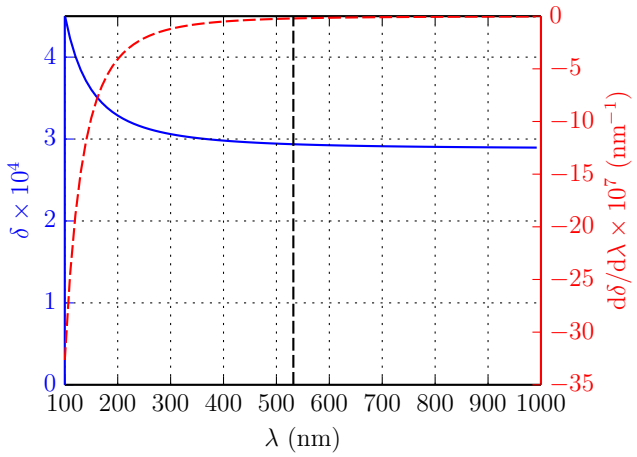

Figure 2.28: δ (blue) and $\mathrm{d}\delta/\mathrm{d}\lambda$ (red) versus wavelength for air at room temperature and atmospheric pressure; the vertical black dashed line corresponds to the laser wavelength of 532 nm.

Chapter 3

Analysis of Moving Hot Particle Interferograms Prior to Ignition[4]

3.1 Inteferograms of Hot Spheres

Two different types of interferograms are obtained using the shearing interferometer described in Section 2.3.2, finite fringe and infinite fringe interferograms. The former is used for extracting quantitative information and the latter is used for making qualitative assessments of the gas surrounding the hot sphere. Examples of finite fringe and infinite fringe interferograms are shown in Fig. 3.1. Figure 3.1 (a) shows a finite fringe interferogram, where the horizontal fringes (undisturbed medium) correspond to a finite value of initial optical phase difference between the reference beam and disturbed beam.

Figure 3.1 (b) shows an infinite fringe interferogram, where the undisturbed part of the image corresponds to a value of zero in the initial optical phase difference between the reference beam and disturbed beam. This chapter covers the image processing procedure of the finite fringe interferograms. Infinite fringe interferograms are presented in Chapter 4.

Figure 3.2 shows interferograms of spheres of 6.0, 3.5, and 1.8 mm in diameter, d, falling in n-hexane-air; however, no ignition takes place since the temperature of each sphere is below the ignition threshold. The raw images contain finite fringe

[4]The numerical simulations shown in this chapter were carried out by Josué Melguizo-Gavilanes.

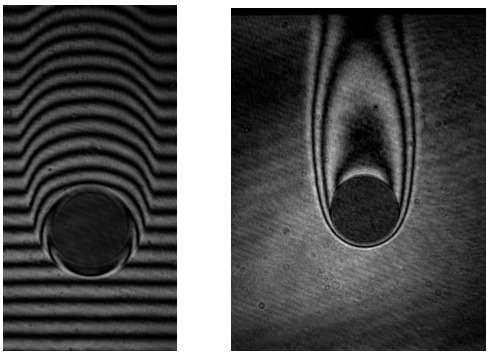

(a) Finite fringe (b) Infinite fringe

Figure 3.1: (a) Finite fringe (shot #89) and (b) infinite fringe (shot #17) interferograms of thermal boundary layer and wake surrounding falling hot spheres.

configurations with an undisturbed fringe spacing of 1.4 mm.

Figure 3.3 shows the temporal evolution of a vertical slice taken at each sphere centerline to determine the sphere velocity U. The angle ϕ shown in the figure is defined as,

$$\tan\phi = \frac{\mathrm{d}y}{\mathrm{d}t} = U, \tag{3.1}$$

Each pixel in t and y corresponds to 0.1 ms and 39 μm (nominal), respectively. Table 3.1 shows the measured sphere speeds for the three diameters tested; the average speed is 2.4 m/s, 2% less than the free falling calculation result of 2.45 m/s.

d (mm)	ϕ (deg)	U (m/s)
6.0	81.46	2.5 ± 0.1
3.5	80.79	2.4 ± 0.1
1.8	80.94	2.4 ± 0.2

Table 3.1: Sphere speed calculations based on angle ϕ shown in Fig. 3.3

The interferograms of Fig. 3.2 show a sharp shift in the fringes in the vicinity of the hot sphere; this shift corresponds to the edge of the thermal boundary layer. The fringe shift is more subtle in the wake of the sphere which corresponds to the region of flow recirculation. The flow field appears axisymmetric about the path of the sphere motion; the axisymmetry is required to use the inverse Abel transform to determine the radial distribution of the index of refraction.

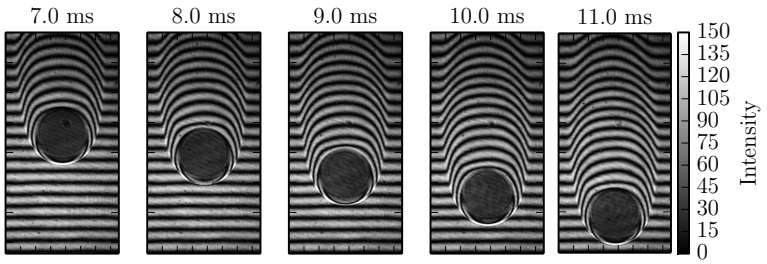

(a) $d = 6.0$ mm and $T_{\text{sphere}} = 1181 \pm 5$ K (shot #89)

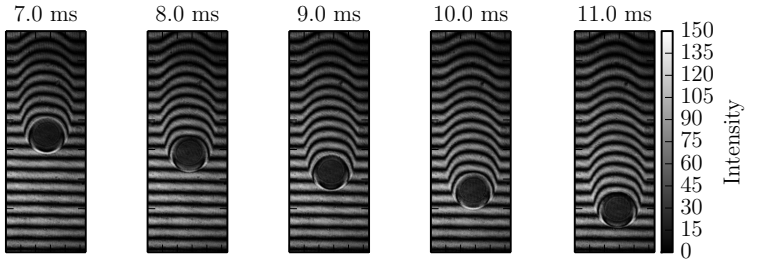

(b) $d = 3.5$ mm and $T_{\text{sphere}} = 1135 \pm 207$ K (shot #123)

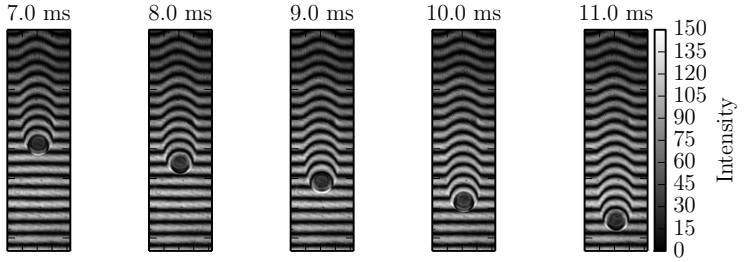

(c) $d = 1.8$ mm and $T_{\text{sphere}} = 1125 \pm 103$ K (shot #136)

Figure 3.2: Infinite fringe interferograms of wake around hot spheres falling in *n*-hexane-air.

The Reynolds number shown in Eq. 3.2 is not uniquely defined in the current study because of the large variation of fluid properties in the thermal boundary layer of the sphere; the corresponding range of values due to the temperature dependence of the fluid viscosity is shown in Fig. 3.4.

$$Re = \frac{Ud}{\nu\left(T\right)} \tag{3.2}$$

The gas in the thermal boundary layer of the sphere has temperatures ranging from the cold gas temperature, T_0, of 300 K to approximately the sphere surface temperature, T_{sphere}. Typical values of the kinematic viscosity as a function of temperature

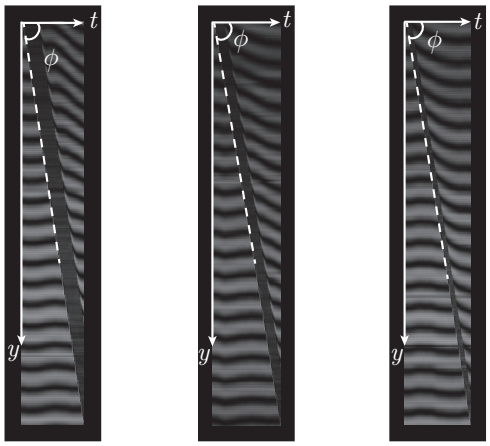

$d = 6.0$ mm $\quad d = 3.5$ mm $\quad d = 1.8$ mm

Figure 3.3: Temporal evolution of a vertical slice taken at the sphere centerline of the interferograms in Fig. 3.2

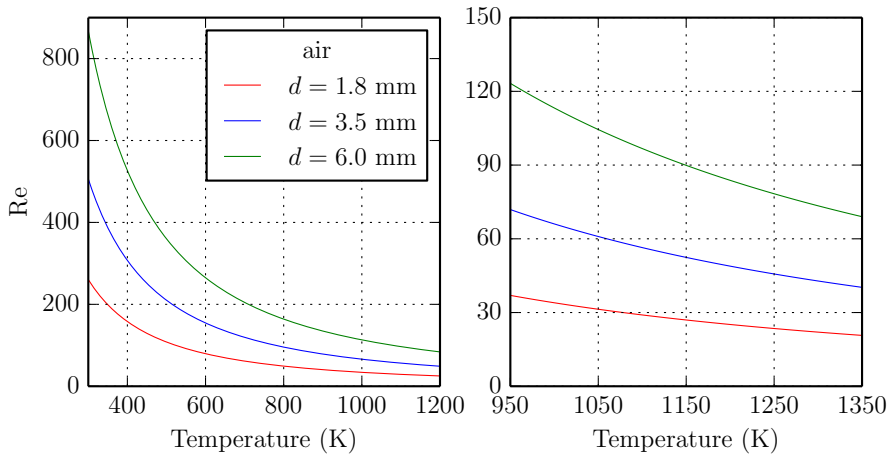

(a) $T = 300 - 1200$ K $\qquad$ (b) $T = 950 - 1350$ K

Figure 3.4: Reynolds number as a function of fluid temperature for three sphere diameters and a fixed velocity of 2.4 m/s: (a) Re for $T = 300 - 1200$ K and (b) Re for $T = T_{\text{sphere}} = 950 - 1350$ K; the gas is n-hexane-air.

for n-hexane air are shown in Fig. 3.5.

This large variation in the temperature within the thermal boundary layer results in a non-unique Reynolds number to describe the flow. Figure 3.4 (b) shows the Re calculated using the hot flow properties, e.g. the kinematic viscosity, ν in Eq. 3.2, is determined by assuming the fluid temperature is equal to the sphere surface temper-

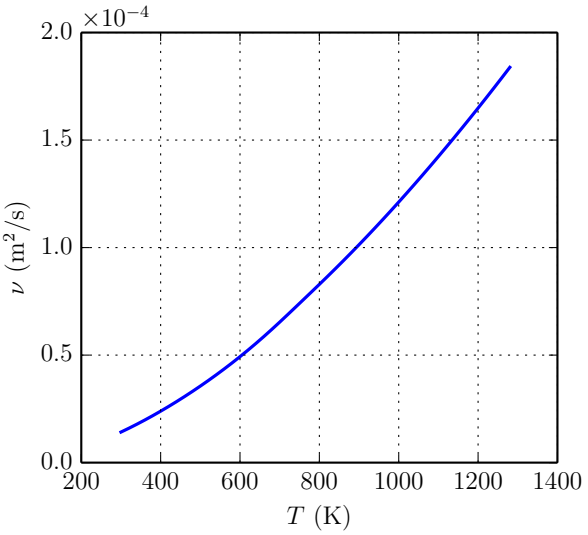

Figure 3.5: Kinematic viscosity as a function of gas temperature for n-hexane-air at $\Phi = 0.9$ and an initial temperature and pressure of 300 K and 100 kPa, respectively.

ature. The flow around the spheres of the interferograms of Fig. 3.2, has a film Re of 199, 123, 64 for d values of 6.0, 3.5 and 1.8 mm, respectively. Figure 3.6 shows the Re calculated using the cold ($T = T_0$), hot ($T = T_{\text{sphere}}$) and film ($T = \left[T_0 + T_{\text{sphere}}\right]/2$) flow properties.

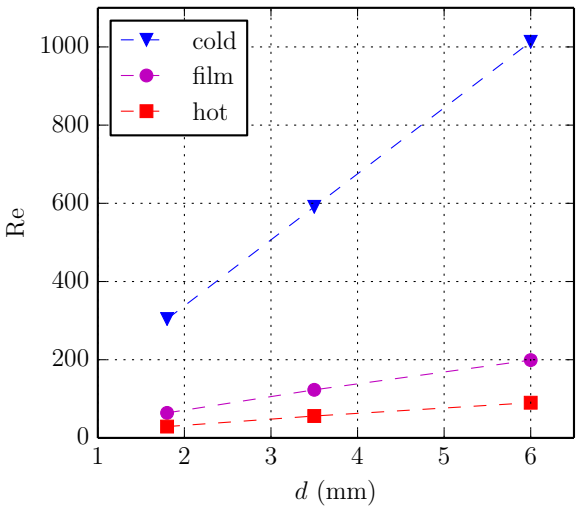

Figure 3.6: Cold, film, and hot flow Reynolds number for spheres traveling through n-hexane-air at 2.4 m/s.

Flows that are steady and axisymmetric have a wake that is composed of a steady toroidal vortex for $20 < \mathrm{Re} < 210$ in uniform temperature flows, as discussed by Johnson and Patel (1999). Clift et al. (2005) indicate that in the steady wake regime for $\mathrm{Re} > 20$, the recirculating wake widens and lengthens. Assuming the film properties to determine the Re, the values shown in Fig. 3.6 correspond to a wake that is steady and axisymmetric, with separation angles (calculated using Eq.1.5) at 117°, 123°, and 134° for 6 mm, 3.5 mm, and 1.8 mm diameter spheres, respectively. Figures 3.7, 3.8, and 3.9 show a comparison of experimental interferograms and numerical temperature fields (simulations performed by Melguizo-Gavilanes et al. (2016b) using OpenFOAM) of the wake of the three spheres; a dashed orange line is drawn on each interferogram to delineate an approximate location of the edge of the thermal boundary layer and wake. Additionally, the dashed black line on the simulation image indicates the location where the gas is 10 K above the freestream temperature. Qualitatively, the interferograms have a wake width that is comparable to the simulation widths.

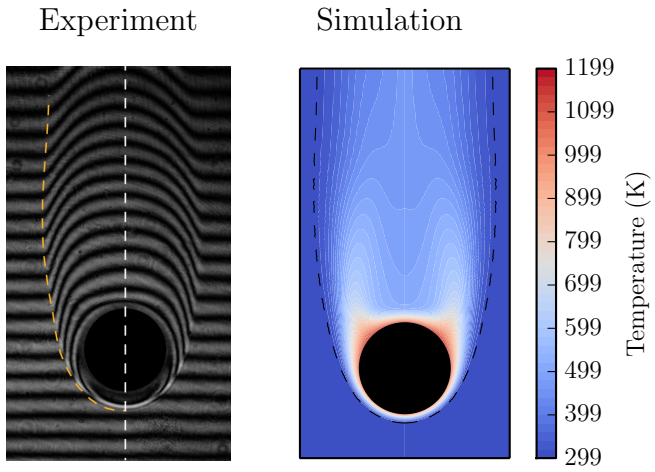

Figure 3.7: Experimental and simulation comparison of n-hexane-air wake at $\Phi = 0.9$ around hot sphere ($d = 6.0$ mm), on the left is a qualitative approximate description of the edge of the thermal boundary layer and wake shown by the orange dashed line for a sphere temperature of 1187 ± 18 K (shot #110) and on the right are temperature contours obtained from simulations for a sphere temperature of 1200 K.

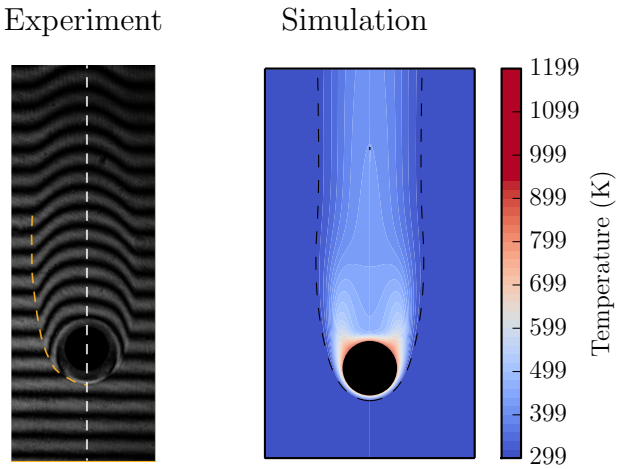

Figure 3.8: Experimental and simulation comparison of n-hexane-air wake at $\Phi = 0.9$ around hot sphere ($d = 3.5$ mm), on the left is a qualitative approximate description of the edge of the thermal boundary layer and wake shown by the orange dashed line for a sphere temperature of 1135±207 K (shot #123) and on the right are temperature contours obtained from simulations for a sphere temperature of 950 K.

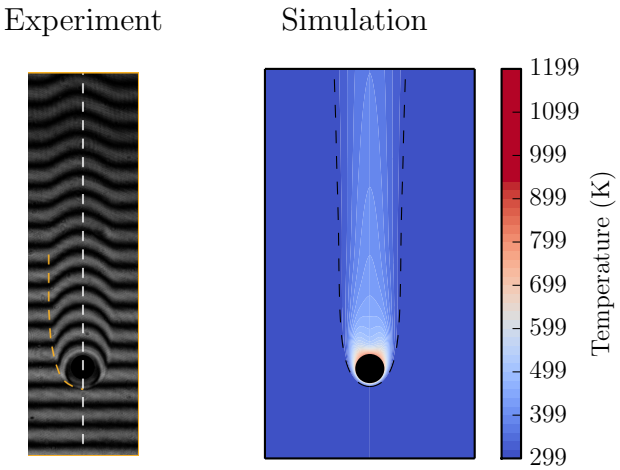

Figure 3.9: Experimental and simulation comparison of n-hexane-air wake at $\Phi = 0.9$ around hot sphere ($d = 1.8$ mm), on the left is a qualitative approximate description of the edge of the thermal boundary layer and wake shown by the orange dashed line for a sphere temperature of 1125±207 K (shot #103) and on the right are temperature contours obtained from simulations for a sphere temperature of 900 K.

3.2 Image Processing of Interferograms

Further image processing of the raw interferograms is needed to convert the experimental fringes to quantitative results, i.e. gas temperature. The process is as follows:

1. Crop images while still maintaining undisturbed regions, i.e. horizontal fringes, on the left and right side of each image.

2. Perform image smoothing to eliminate image imperfections.

3. Perform phase demodulation using the WFF2 method, i.e. obtain the wrapped optical phase difference, of each interferogram.

4. Perform phase unwrapping using quality guided method, and use time averaging over $\overline{\Delta\varphi_W}$

5. Symmetrize $\overline{\Delta\varphi_W}$ images if needed.

6. Obtain refractive indices by performing an Abel inversion of the optical phase difference using the Nestor-Olson method.

7. Apply Gladstone-Dale relation to obtain gas density.

8. Use ideal gas relation to convert gas density to temperature assuming constant pressure and no changes in the molecular weight.

The image processing steps are shown for shot #110 which corresponds to a 6 mm diameter sphere falling a 2.4 m/s with a surface temperature of 1187 ± 18 K. The interferograms (original) are convolved with a Gaussian filter to remove noise introduced by optical aberrations. An example of an interferogram before and after noise removal using a 15×15 px Gaussian kernel is shown in Fig. 3.10. Most of the small speckles observed in the constructive interference patterns of Fig. 3.10 (a) have been filtered, however the larger imperfections remain.

The noise removal is shown quantitatively in Fig. 3.11 in terms of the log of the absolute value of the Fourier spectrum for the original and Gaussian filtered images.

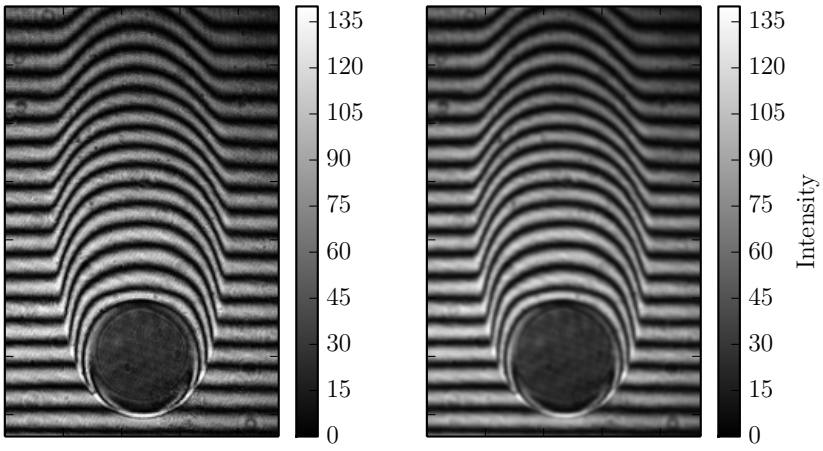

(a) Original (b) Gaussian filtered

Figure 3.10: Interferogram of hot 6.0 mm diameter sphere with a surface temperature of 1187 ± 18 K falling through air at 2.4 m/s (shot #110).

The histogram shows the filtered high frequency signals that are associated with noise; the frequency peak shifts from 7 px^{-1} (original) to 5 px^{-1} after the filter is applied. Figure 3.12 shows a 2D field of the Fourier spectrum; the regions away from the image centers correspond to high frequency signals, and it is evident that after filtering, those signals are suppressed.

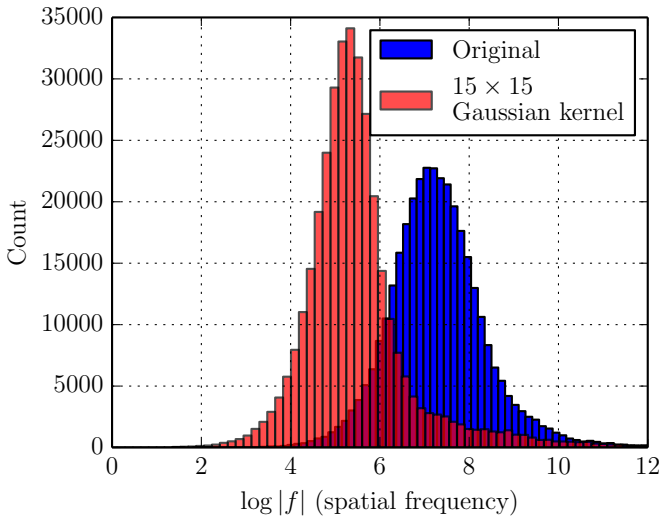

Figure 3.11: Histogram of $\log|f|$ taken from the images in Fig. 3.10, the blue and red histograms correspond to the original and Gaussian filtered images, respectively.

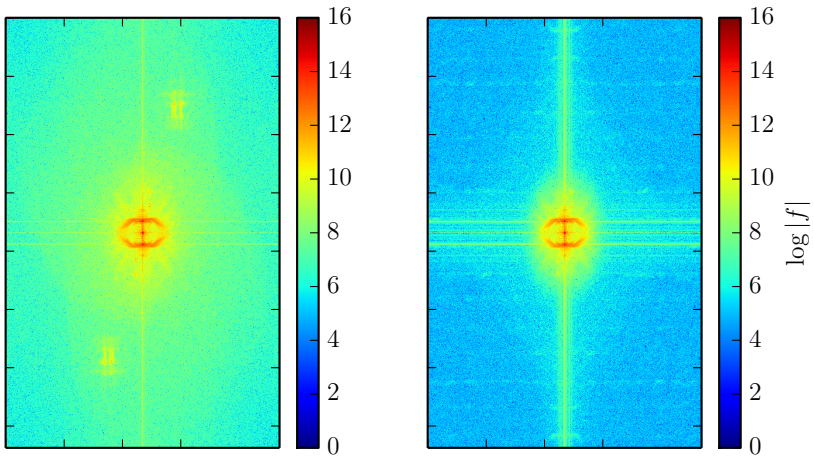

(a) Original (b) Gaussian filtered

Figure 3.12: 2D intensity plot of $\log|f|$ taken from the images in Fig. 3.10.

The original and Gaussian filtered interferograms, e.g. Fig. 3.14 (a) Fig. 3.15 (a), respectively, are analyzed using the WFF2 method described in Section 2.4.1. An initial guess for the threshold, $\text{thr} = 1.3b\sqrt{\sigma_x\sigma_y}$, is given by (Kemao, 2013), where,

$$b = \frac{||f(x,y)||_2}{\sqrt{2N_xN_y}}. \tag{3.3}$$

N_x and N_y correspond to the horizontal and vertical lengths (pixels) of the image, respectively, and $||f(x,y)||_2$ is the L^2 Euclidean norm of the image intensity. To ensure a tight window in the Fourier and space domain, a kernel size of $\sigma_x = \sigma_y = 20$ px is used, given that the image size is approximately 400×800 px along the x (horizontal) and y (vertical) axes, respectively. The wrapped optical phase difference, $\overline{\Delta\varphi_W}$, along a vertical slice of undisturbed fringes is shown in Fig. 3.13. The detected phase of the original and Gaussian filtered interferograms illustrates the benefits of noise removal before performing the phase demodulation. The $\overline{\Delta\varphi_W}$ of the original interferogram yields a few discrepancies near 350, 480, and 540 px.

Figure 3.14 (b) and Fig. 3.15 (b), and Fig. 3.14 (c) and Fig. 3.15 (c), show the thresholded phase and amplitude, respectively, for the original and Gaussian filtered interferograms. It is important to notice that in the vicinity of the sphere, near the

front stagnation point, the phase detection is irregular due to fringe shifts that go to infinity. Qualitatively, there are minor differences in the phase detection between the original and Gaussian filtered interferograms, as indicated by Fig. 3.14 (b) and Fig. 3.15 (b) and also shown in Fig. 3.13. The amplitude of the Gaussian filtered interferogram, shown in Fig. 3.15 (c), contains less noise than the amplitude of the original interferogram shown in Fig. 3.14 (c).

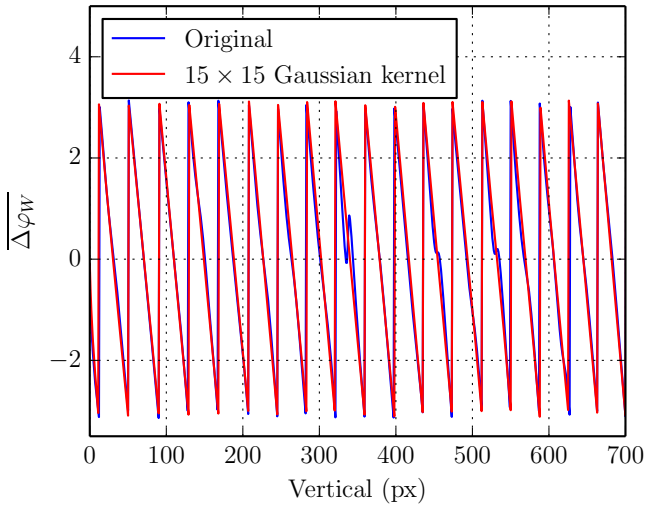

Figure 3.13: $\overline{\Delta\varphi_W}$ along a vertical slice of the interferogram shown in Fig. 3.10.

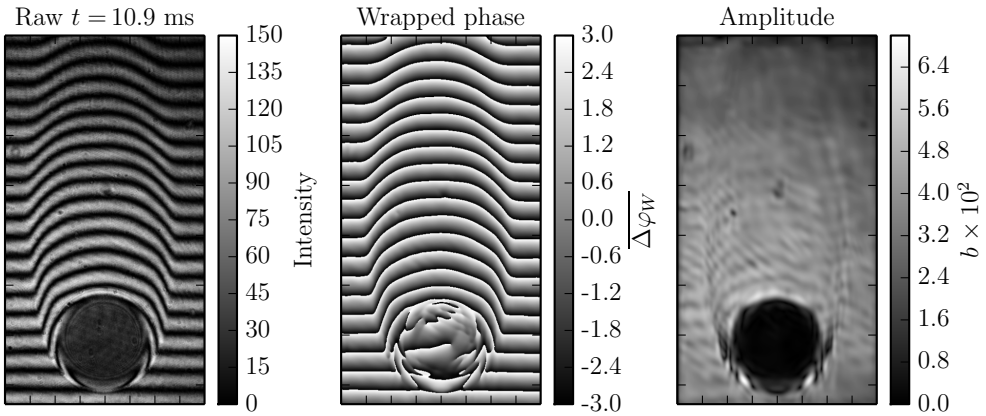

Figure 3.14: Phase demodulation of original interferogram using the WFF2 method, (a) interferogram, (b) wrapped optical phase difference, and (c) amplitude; shot #110.

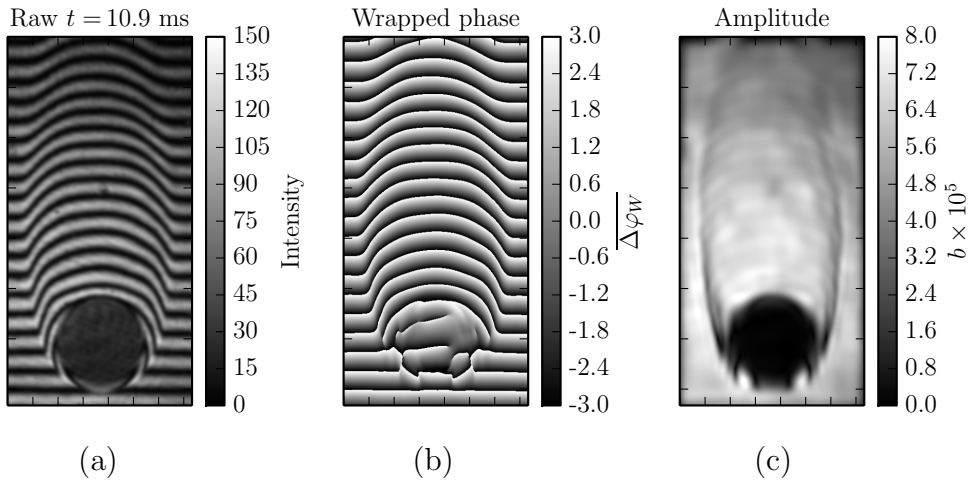

Figure 3.15: Phase demodulation of the Gaussian filtered interferogram using the WFF2 method, (a) interferogram, (b) wrapped optical phase difference, and (c) amplitude; shot #110.

3.2.1 Optical Phase Difference

Figures 3.16 and 3.17 show the time averaged unwrapped optical phase difference, $\overline{\Delta\varphi}$, obtained from the original and Gaussian filtered interferograms, respectively. Time averaging was possible for this example (6.0 mm diameter sphere with a temperature of 1187 ± 18 K falling in air at 2.4 m/s) since the wake is steady. The time averaging was performed by vertically and horizontally shifting the optical phase difference images so that each sphere center coincided with the sphere center of the last frame in the time averaging sequence. The time between each frame is 0.1 ms, e.g. averaging 10 frames corresponds to averaging over 1 ms.

Figure 3.16 (a) and Fig. 3.17 (a) show the noise that is present in an individual frame, mainly in the wake of the sphere. Figure 3.16 (b) and Fig. 3.17 (b) show $\overline{\Delta\varphi}$ averaged over 5 frames; the images are significantly smoother than the single frame fields. Figure 3.16 (c) and Fig. 3.17 (c) are averaged over 1 ms and show no significant changes when compared to $\overline{\Delta\varphi}$ averaged over 0.5 ms. Qualitatively, Figs. 3.16 and 3.17 indicate that time averaging (at least 5 frames) is necessary if no prior filtering is performed on the image before the phase demodulation; on the other hand, the Gaussian filtered images yield smooth $\overline{\Delta\varphi}$ fields regardless of time averaging. Unless

otherwise stated, the analysis proceeds using the Gaussian filtered interferograms.

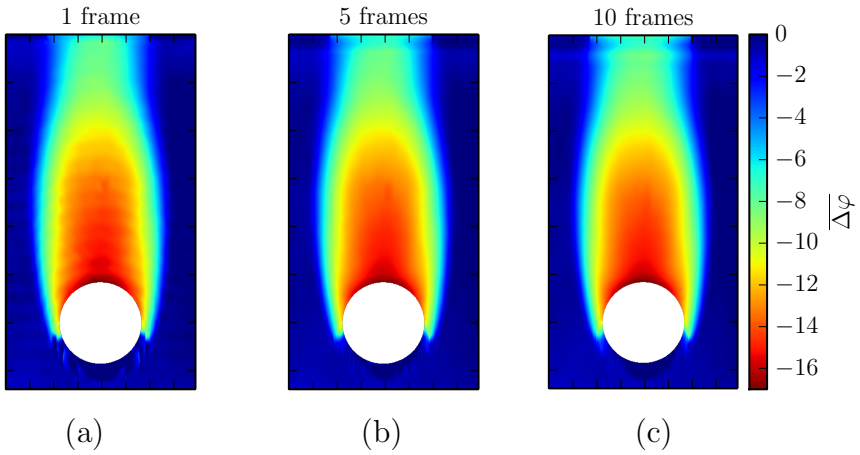

Figure 3.16: Time averaged unwrapped optical phase difference obtained from the phase demodulation of the original interferograms.

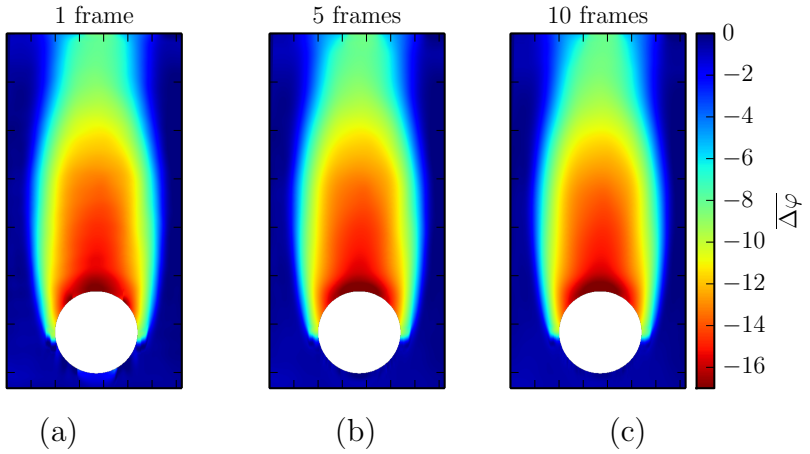

Figure 3.17: Time averaged unwrapped optical phase difference obtained from the phase demodulation of the Gaussian filtered interferograms.

Figure 3.18 shows y slices of $\overline{\Delta\varphi}$ as a function of x. The coordinate $(x, y) = (0, 0)$ corresponds to the center of the sphere. The plots do not show differences between the single frame and time averaged $\overline{\Delta\varphi}$.

However, Fig. 3.19 shows differences between the single frame and time averaged $\overline{\Delta\varphi}$ when plotted as a function of y for various x locations. Figure 3.18 shows that the width of the wake increases as y increases. In addition, for $y \geq 3$ mm, the maximum

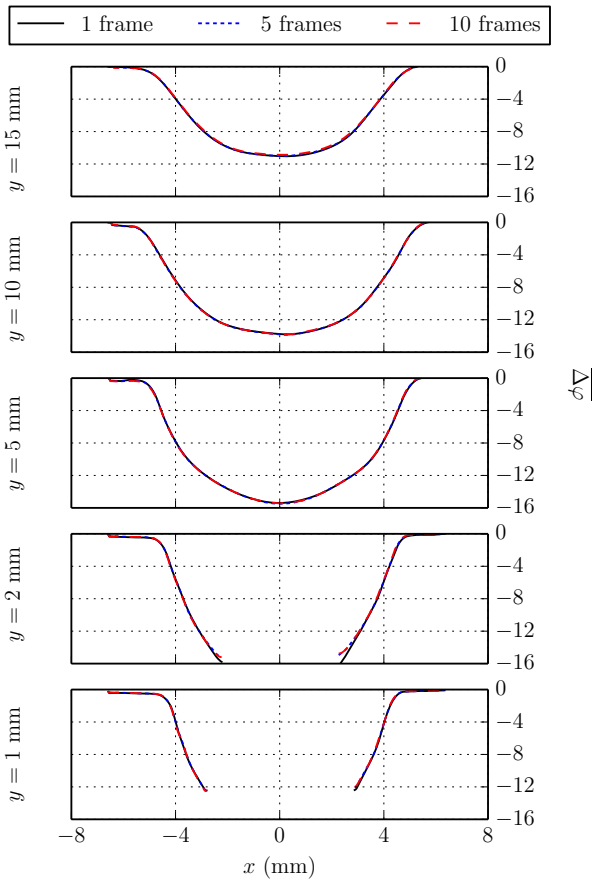

Figure 3.18: Slices of $\overline{\Delta\varphi}$ at $y = [1, 2, 5, 10, 15]$ mm as a function of x; the different line types correspond to the number of frames used in the time averaging.

$|\overline{\Delta\varphi}|$ occurs at $x = 0$ mm. The discontinuity in $\overline{\Delta\varphi}$ at $y = 1$ and 2 mm is a result of the presence of the sphere. Figure 3.19 shows that at the centerline of $x = 0$ mm, $|\overline{\Delta\varphi}|$ increases in magnitude as y approaches the sphere.

Figure 3.20 provides closer views of a single frame and time averaged $\overline{\Delta\varphi}$. Figure 3.20 (a) shows a single slice taken at $y = 1$ mm; the time averaged $\overline{\Delta\varphi}$ shows a negligible change in the absolute magnitude, except near the discontinuity. Figure 3.20 (b) shows a single slice taken at $x = 0$ mm (at the sphere centerline); the single frame $\overline{\Delta\varphi}$ noise fluctuations are prominent when compared to its time averaged counterparts. Further in the chapter, a discussion is provided on the effect of the noise fluctuations on the gas temperature.

Figure 3.21 shows the derivative of the optical phase difference, shown in Fig. 3.20

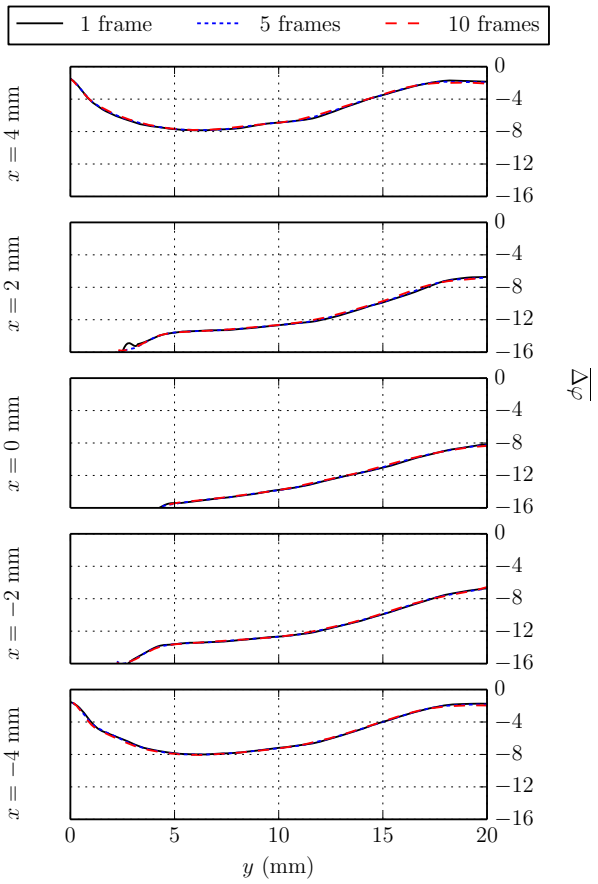

Figure 3.19: Slices of $\overline{\Delta\varphi}$ at $x = [-4, -1, 0, 2, 4]$ mm as a function of y.

(a), with respect to x; there are significant differences between the single frame and time averaging cases shown, in particular at the minimum and maximum derivatives. In addition, there are large differences between the left ($x = 0$ to $x = -6$ mm) and right parts ($x = 0$ to $x = 6$ mm) of the derivative, in particular in the shape of the peak, shown on the right side, and trough, shown on the left side of Fig. 3.21.

Figure 3.20 (b) has a maximum $|\overline{\Delta\varphi}|$ value of 16 rad occurring in the rear stagnation point; however, a smaller value of 12 rad is observed close the sphere surface at $y = 1$ mm, shown in Fig. 3.20 (a). Figure 3.22 (a) shows the numerical optical phase difference calculated from the simulated temperature field (Melguizo-Gavilanes et al., 2016b) shown in Fig. 3.22 (b). Similar to the experimental results, the numerical results show a maximum of $|\Delta\varphi|$ directly behind the sphere with a magnitude of 18

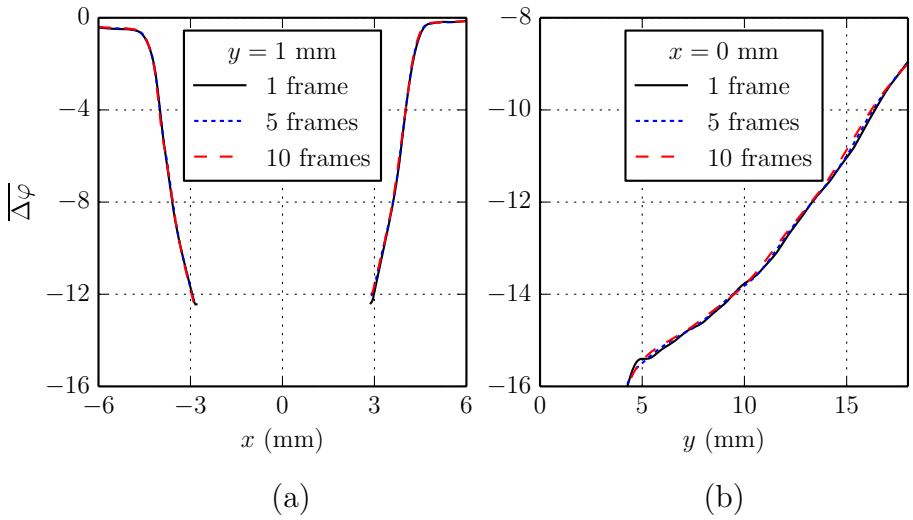

Figure 3.20: A slice of $\overline{\Delta\varphi}$ at (a) $y = 1$ mm and (b) $x = 0$ mm.

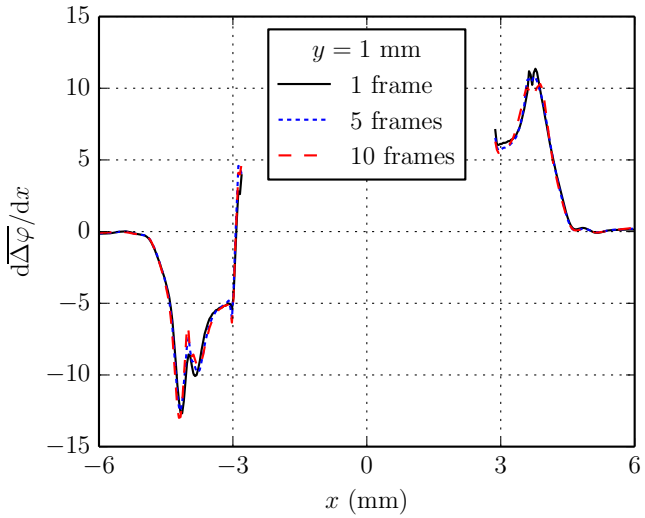

Figure 3.21: Derivative of a slice of $\overline{\Delta\varphi}$ at $y = 1$ mm.

rad, roughly 13% higher than the experimental result. A lower magnitude of 11.3 rad is observed at $y = 1$ mm close to the sphere wall, 6% lower than the experimental result. A maximum in the magnitude of $\Delta\varphi$ is to be expected in the rear stagnation point of the sphere as opposed to elsewhere close to the sphere since the width of the disturbed region is wider at the rear stagnation point than other locations between the front and rear stagnation points. Therefore an optical ray experiences a larger

shift in the optical phase difference through the wider disturbed region. Of course the wake becomes wider past the rear stagnation point; however, the gas is significantly cooler in the region of flow recirculation than in the boundary layer, and therefore lower magnitudes of the optical phase difference are observed.

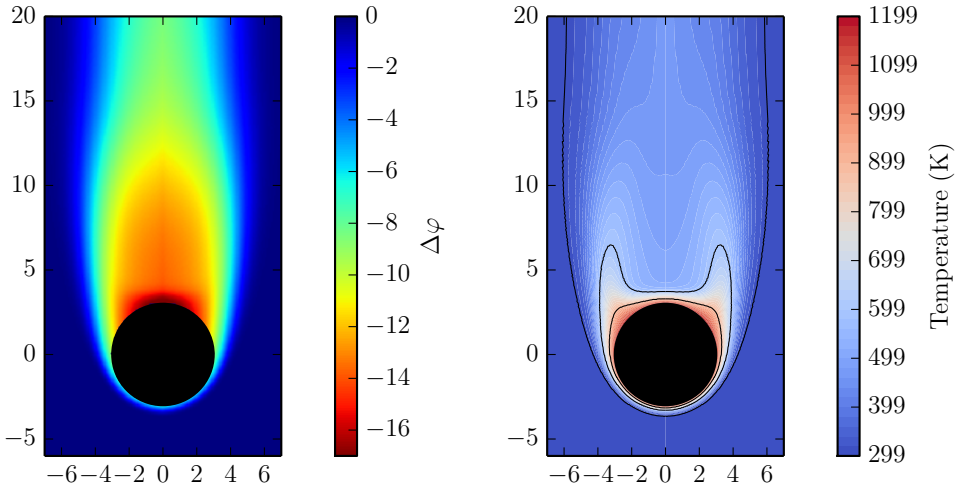

(a) Optical phase difference (b) Temperature

Figure 3.22: Numerical optical phase difference calculated from temperature field of simulated wake over a 6 mm diameter sphere with a surface temperature of 1200 K.

The conversion of $\overline{\Delta\varphi}$ to refractive index, as mentioned in Section 2.4.2, requires and axisymmetric density field; however, this is not always the case due to the alignment of the optical system and the trajectory of the sphere. Figure 3.23 shows the left ($x \leq 0$), $\overline{\Delta\varphi}_{\text{left}}$, and right ($x \geq 0$), $\overline{\Delta\varphi}_{\text{right}}$, side of a single frame $\overline{\Delta\varphi}$ at $y = 4$ mm. Figure 3.23 shows that there is symmetry near $x = 0$ mm. However the two lines deviate from one another while approaching the edge of the wake.

Figure 3.24 shows the difference between the two sides, $\overline{\Delta\varphi}_{\text{left}} - \overline{\Delta\varphi}_{\text{right}}$; the difference is approximately 0 near $x = 0$ mm and reaches a maximum of approximately -0.5 close to the edge of the wake.

The entire field of $\overline{\Delta\varphi}_{\text{left}} - \overline{\Delta\varphi}_{\text{right}}$ is shown in Fig. 3.25 (a); the largest difference

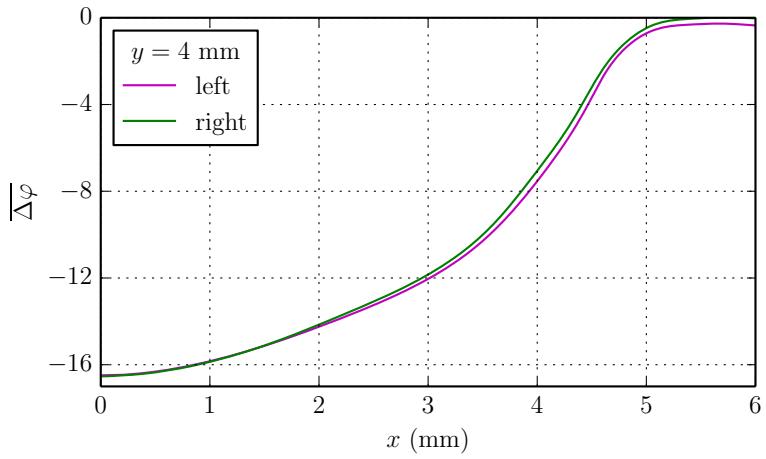

Figure 3.23: Left and right side of a single frame $\overline{\Delta\varphi}$ at $y = 4$ mm.

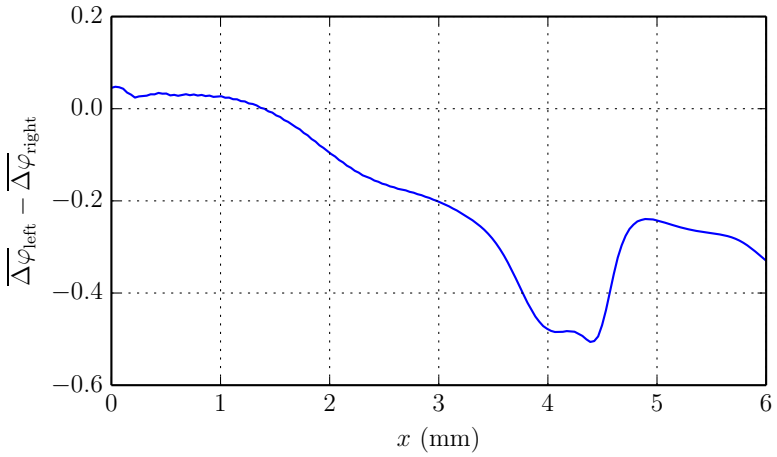

Figure 3.24: Difference between the left and right side of a single frame $\overline{\Delta\varphi}$ at $y = 4$ mm.

is observed at the edge of the wake. A rotation matrix given by

$$\begin{bmatrix} \alpha & \beta & (1-\alpha)\cdot c_x - \beta \cdot c_y \\ -\beta & \alpha & \beta \cdot c_x + (1-\alpha)\cdot c_y \end{bmatrix},$$

is applied to $\overline{\Delta\varphi}$ to improve the symmetry. $\alpha = \cos\theta_{\text{rot}}$, $\beta = \sin\theta_{\text{rot}}$, θ_{rot} is the rotation angle and (c_x, c_y) are the coordinates about which rotation is performed. In the present investigation, (c_x, c_y) represents the center of the sphere. The rotation matrix

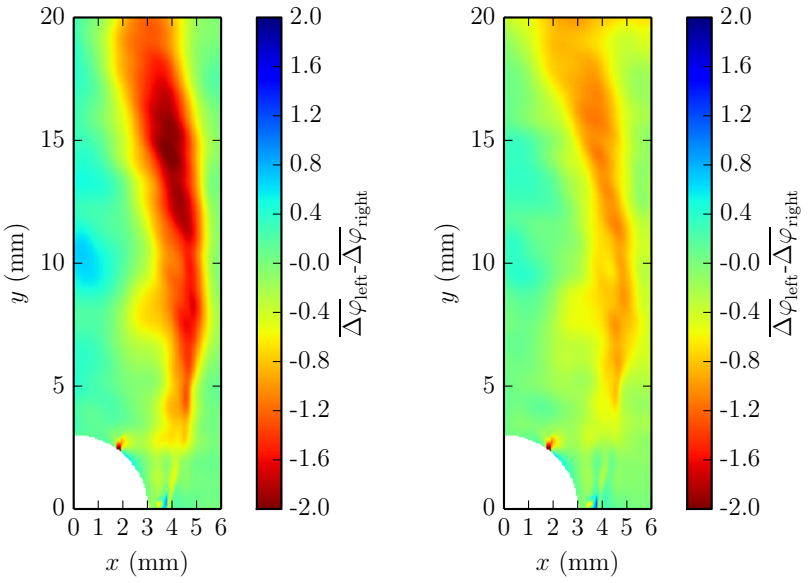

(a) $\theta_{\text{rot}} = 0°$ (b) $\theta_{\text{rot}} = -0.5°$

(c) $\theta_{\text{rot}} = -0.8°$ (d) $\theta_{\text{rot}} = -1.0°$

Figure 3.25: Difference in optical phase difference between left and right side of image when applying a rotation matrix such that (a) $\theta_{\text{rot}} = 0°$, (b) $\theta_{\text{rot}} = -0.5°$, (c) $\theta_{\text{rot}} = -0.8°$ and (d) $\theta_{\text{rot}} = -1.0°$.

is applied to Fig. 3.25 (a) using $\theta_{\text{rot}} = [-0.5°, -0.8°, -1.0°]$. Symmetry emerges when $\theta_{\text{rot}} = -0.8°$ and continues to improve for $\theta_{\text{rot}} = -1.0°$.

3.2.2 Gas Density Around Sphere

After time averaging and symmetrizing are performed on $\overline{\Delta\varphi}$, the inversion of the Abel transform is implemented using the Nestor-Olson method, discussed in Section 2.4.2, to obtain the refractive index. Next, the Gladstone-Dale relation given in Eq. 2.37 is used to calculate the gas density, shown in Fig. 3.26, around the sphere.

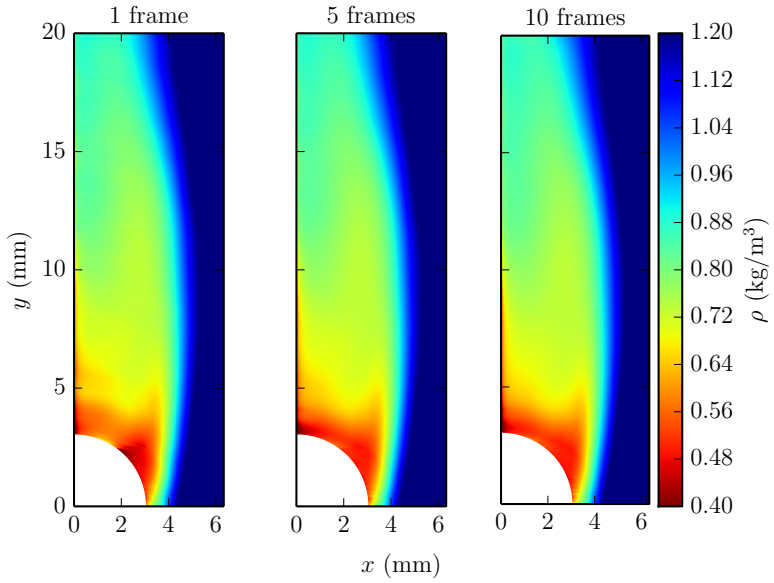

Figure 3.26: Gas density around 6.0 mm diameter sphere with a surface temperature of 1187 ± 18 K and velocity of 2.4 m/s (shot #110), the white region corresponds to the sphere location; each image corresponds to different number of frames used in the averaging of $\overline{\Delta\varphi}$.

Figure 3.27 shows y slices of the gas density as a function of x. The plot shows very minor differences between the single frame and time averaged density; however, Fig. 3.28 shows prominent differences when the density is plotted as a function of y for various x slices, in particular while approaching the sphere centerline of $x = 0$ mm. Figure 3.27 shows that the wake becomes wider as y increases from 1 to 10 mm and then decreases at 15 mm. In the recirculation region of the sphere, the density

is approximately 0.8 kg/m^3 and a minimum density of 0.4 kg/m^3 is reached close to the sphere surface.

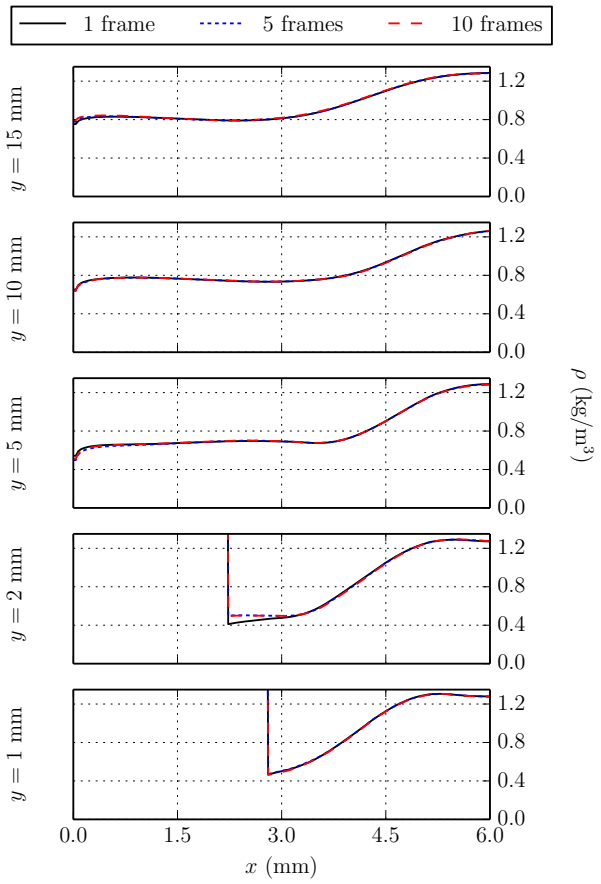

Figure 3.27: Slices of ρ at $y = [1, 2, 5, 10, 15]$ mm as a function of x taken from the density fields shown in Fig. 3.26; the different line types correspond to the number of frames used in the time averaging of $\overline{\Delta\varphi}$ prior to performing the inversion of the Abel transform.

The single frame result of Fig. 3.28 shows density fluctuations at the centerline of $x = 0$ mm. The fluctuations are attenuated away from the centerline. Table 3.2 shows the minimum density values for each y slice shown in Fig. 3.27. At $y = 1$ mm there is no change in the density from 1 to 5 frames; however, there is a 1% decrease from 1 to 10 frames. The largest difference in the table occurs at $y = 2$ mm.

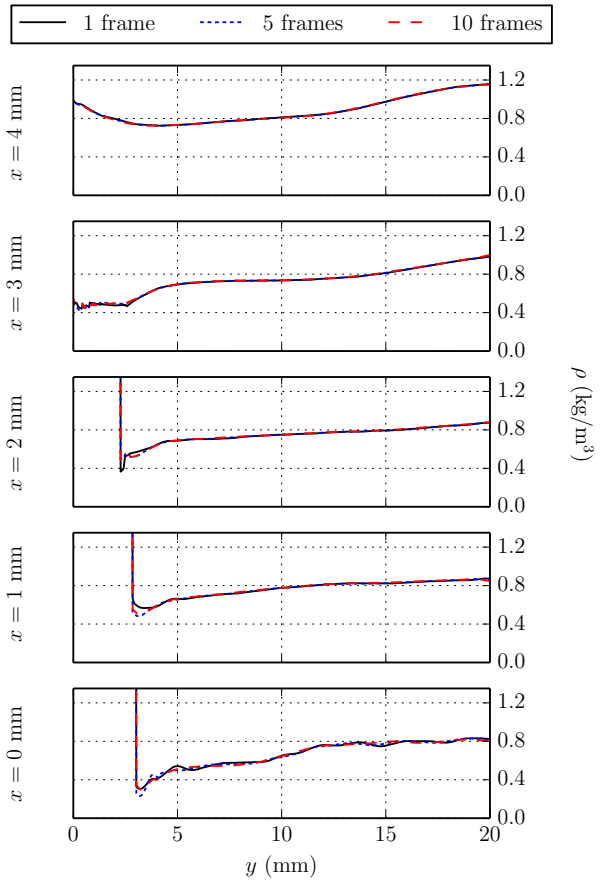

Figure 3.28: Slices of ρ at $x = [0, 1, 2, 3, 4]$ mm as a function of y taken from the density fields shown in Fig. 3.26; the different line types correspond to the number of frames used in the time averaging of $\overline{\Delta\varphi}$ prior to performing the inversion of the Abel transform.

y (mm)	1 frame (kg/m^3)	5 frames (kg/m^3)	10 frames (kg/m^3)
1.0	0.47	0.47	0.46
2.0	0.41	0.50	0.50
5.0	0.54	0.50	0.51
10.0	0.65	0.64	0.64
15.0	0.75	0.78	0.79

Table 3.2: Minimum density at various y slices taken from Fig. 3.27.

3.2.3 Gas Temperature Around Sphere

The final step in the data processing is to apply the ideal gas law, $T = P/\rho R$, to the density fields to obtain the temperature field. The resulting temperature fields are shown in Figs. 3.29 3.30 for both the original and Gaussian filtered interferograms, respectively. The temperature fields in Fig. 3.29 (a) contains artificial hot spots on the sphere surface near the sphere horizontal centerline. There is a significant amount of noise in the form of artifact fringes due to the lack of time averaging.

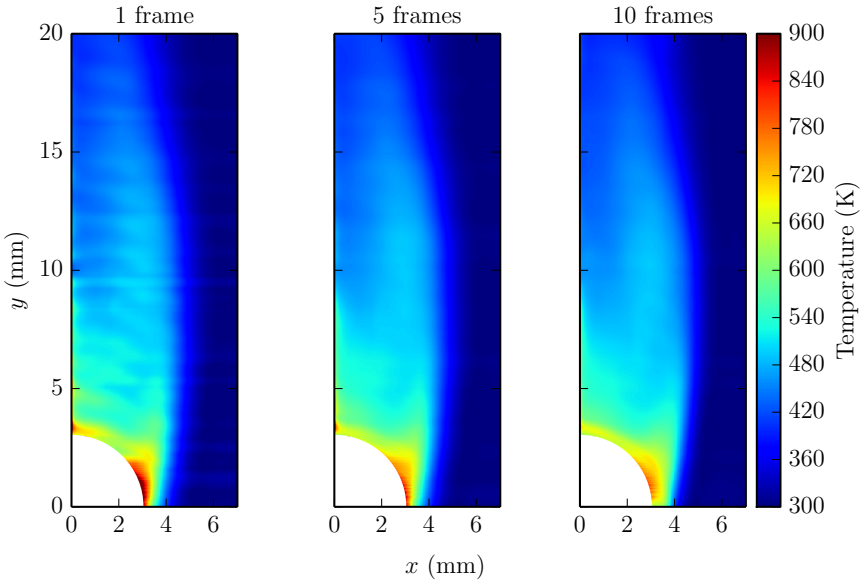

Figure 3.29: Gas temperature around 6.0 mm diameter sphere with a surface temperature of 1187 ± 18 K and velocity of 2.4 m/s (shot #110) in n-hexane-air extracted from "original interferograms", the white region corresponds to the sphere location; each image corresponds to different number of frames used in the averaging of $\overline{\Delta\varphi}$.

The Gaussian filtered interferogram results shown in Fig. 3.30 yield a temperature field that contains a hot spot near the region of flow separation, indicated by the black line, when 1 frame is used for $\overline{\Delta\varphi}$. This is in agreement with numerical results (Melguizo-Gavilanes et al., 2016b) that show that the smallest temperature gradient occurs near further downstream of the separation region, shown in Fig. 3.31. The time averaged results show a smoother distribution in the high temperature regions. These qualitative temperature observations suggest that time averaging is required

to further extract quantitative results from $\overline{\Delta\varphi}$.

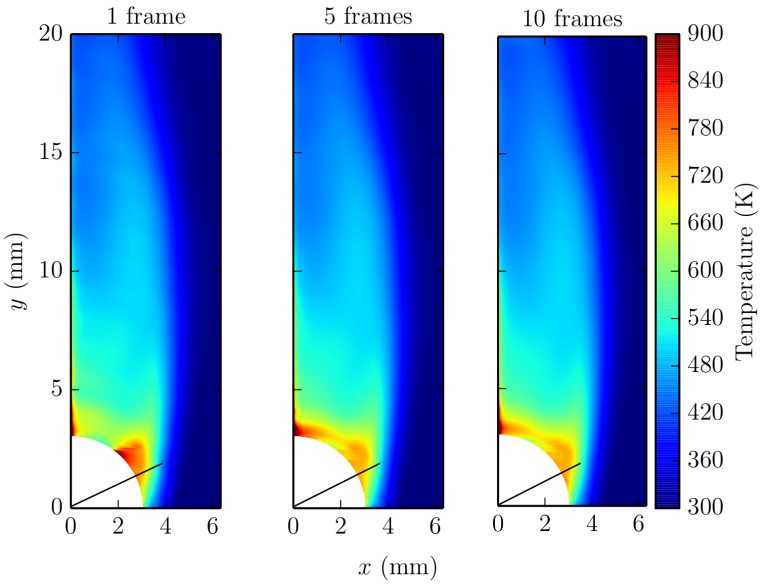

Figure 3.30: Gas temperature around 6.0 mm diameter sphere with a surface temperature of 1187 ± 18 K and velocity of 2.4 m/s (shot #110) in n-hexane-air extracted from "Gaussian filtered interferograms", the white region corresponds to the sphere location; each image corresponds to different number of frames used in the averaging of $\overline{\Delta\varphi}$.

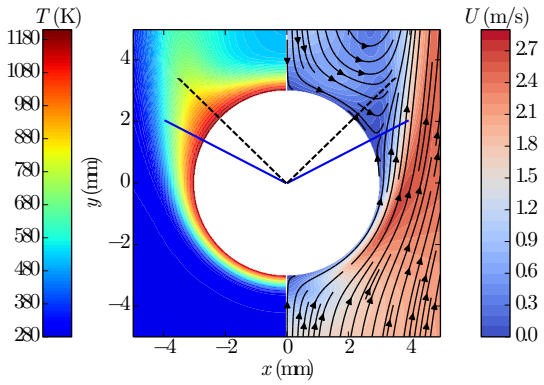

Figure 3.31: Numerical temperature field (left) and velocity field (right) with streamlines for a 6 mm diameter sphere with a surface temperature of 1200 K and freestream velocity of 2.4 m/; the blue solid line indicates the location of flow separation and the black dashed line corresponds to the location with the smallest temperature gradient normal to the sphere wall.

Figure 3.32 shows y slices of gas temperature as a function of x. The figure shows

that the wake becomes wider as y increases from 1 to 10 mm and decreases at 15 mm; this is in agreement with the numerical wake width results shown in Fig. 3.22 (b). There are very minor differences between the single frame and time averaged temperature; however, a maximum difference of approximately 200 K occurs at $y = 2$ mm. For all the slices, the gas temperature is approximately 300 K outside of the wake and then rises to over 700 K in the vicinity of the sphere, this is roughly 400 K lower than the sphere surface temperature. Clearly, the fringe shifts do not capture well the temperature close to the sphere. At $y = 5$, 10, and 15 mm, the temperature continues to rise while approaching $x = 0$ mm; however this is not physical and is purely an artifact of the accumulation of error during the inversion of the Abel transform. The calculation of the refractive index at the centerline is based on the integral of the derivative of the optical phase difference from 0 to 6 mm, and therefore any errors in the derivative in that x range are added to calculation of the refractive index at $x = 0$ mm. This is in contrast with the calculation of the refractive index close to 6 mm, say 5.9 mm, in which the errors added to the calculation come from that smaller x range.

Figure 3.33 shows the gas temperature of the single frame and time averaged curves when plotted as a function of y at various x locations. The plots show large fluctuations of the temperature at the centerline of $x = 0$ mm. The fluctuations become attenuated away from the centerline.

Table 3.3 shows the maximum temperature for each y slice shown in Fig. 3.32. At $y = 1$ mm there is a 1% decrease in the temperature from 1 frame to 5 frames, and less than a 1% increase from 1 frame to 10 frames. The largest difference in the table occurs at $y = 2$ and 5 mm; there is a decrease of 17% in the temperature from 1 frame to 5 and 10 frames at $y = 2$ mm and a $5 - 10\%$ increase from 1 frame to the time averaged results at $y = 5$ mm.

Figure 3.34 provides a closer view of the temperature obtained from a single and time averaged $\overline{\Delta\varphi}$. Figure 3.34 (a) shows a temperature slice at $y = 1$ mm; the temperature differences are negligible across the number of frames used for time averaging. Figure 3.34 (b) shows a temperature slice at $x = 0$ mm (at the sphere

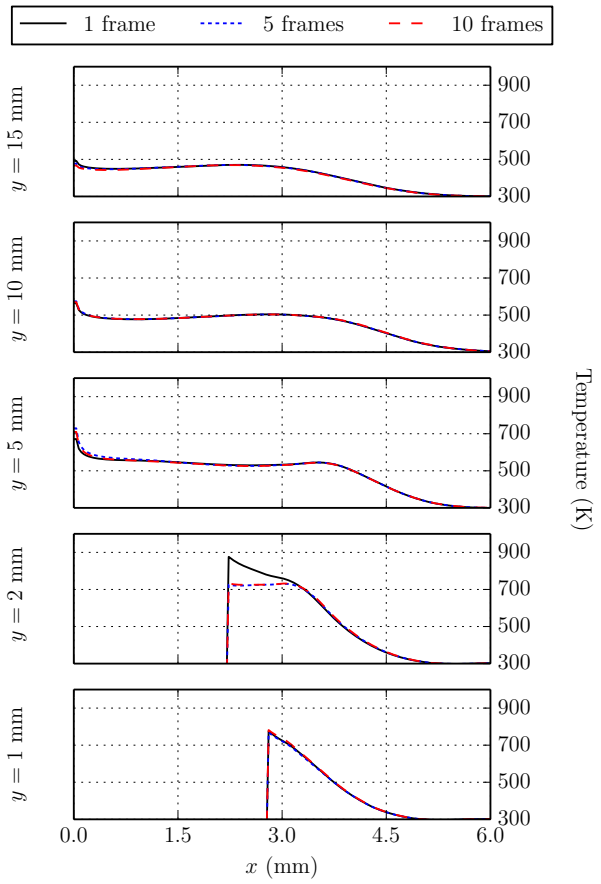

Figure 3.32: Slices of gas temperature at $y = [1, 2, 5, 10, 15]$ mm as a function of x taken from Fig. 3.30, the sphere surface temperature is 1187 ± 18 K; the different line types correspond to the number of frames used in the time averaging of $\overline{\Delta\varphi}$ prior to performing the inversion of the Abel transform.

y (mm)	1 frame (K)	5 frames (K)	10 frames (K)
1.0	777	769	782
2.0	876	731	733
5.0	671	729	710
10.0	564	574	570
15.0	492	477	469

Table 3.3: Maximum temperature for various y slices shown in Fig. 3.32.

centerline); the temperature fluctuations become attenuated as more frames are used. The figure indicates that the conversion to temperature is very sensitive to any sort of fluctuations in $\overline{\Delta\varphi}$, as evident by the large range ($1100 - 1500$ K) of maximum

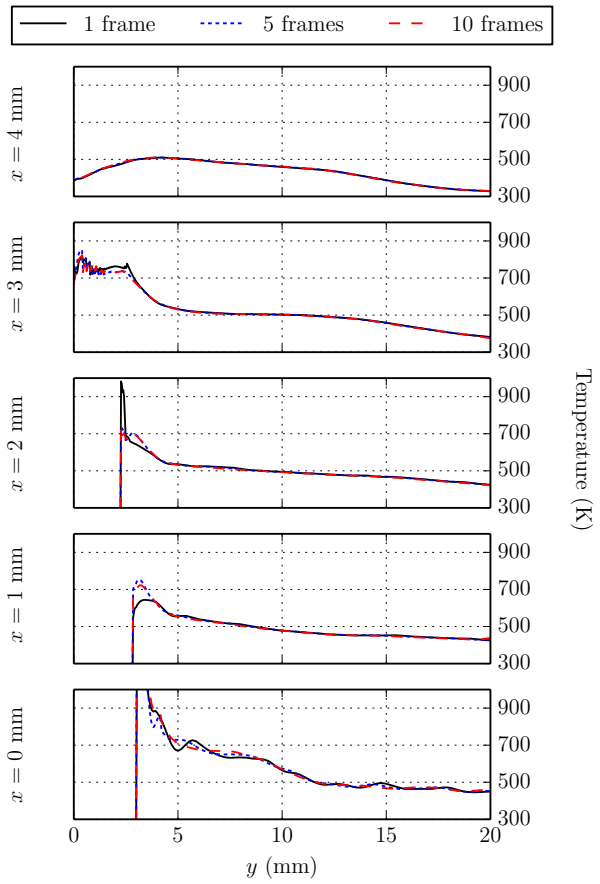

Figure 3.33: Slices of gas temperature at $x = [0, 1, 2, 3, 4]$ mm as a function of y taken from Fig. 3.30, the sphere surface temperature is 1187 ± 18 K; the different line types correspond to the number of frames used in the time averaging of $\overline{\Delta\varphi}$ prior to performing the inversion of the Abel transform.

temperatures reached at the sphere centerline. The sphere surface temperature lies within the temperature calculated at the rear stagnation point; however, very low temperatures, $700 - 900$ K, are observed in other regions close to the sphere, e.g. at $y = 1$ mm shown in Fig. 3.34 (a). Therefore, it can be concluded that the method of interferometry used in this study does not capture well the temperature gradients present in a thin thermal boundary layer. The centerline ($x = 0$ mm) temperature is particularly prone to incurring large uncertainties during the inversion of the Abel transform. The inverse Abel transform (Eq. 2.32) f at $r = 0$ mm requires an integration from $r = 0$ to ∞, in the current study, to R (field of view radius), it therefore

accumulates any error within those integration limits. The smallest accumulation of error therefore occurs for $r = R$. For this investigation, it is more appropriate to end the image processing after the unwrapped phase is obtained or risk introducing large uncertainties in the results by performing the inverse Abel transform.

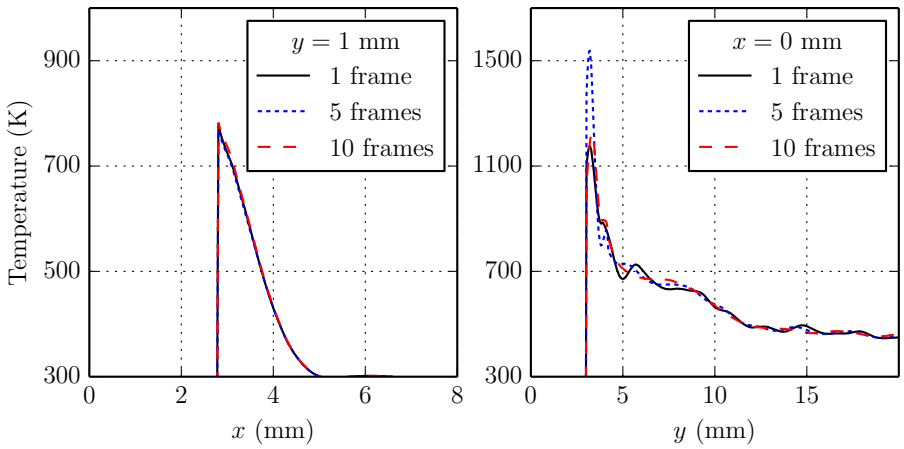

(a) (b)

Figure 3.34: A slice of temperature at (a) $y = 1$ mm and (b) $x = 0$ mm taken from Fig. 3.30.

3.3 Temperature Field Comparison with Simulations

The fluid mechanics and heat transfer are modeled by Melguizo-Gavilanes et al. (2016b) using the variable-density Navier-Stokes equations with temperature dependent transport properties. The governing equations are integrated in two dimensions using the Open source Field Operation And Manipulation (OpenFOAM) toolbox (Weller et al., 1998). The Sutherland Law, the Eucken Relation, and the JANAF polynomials are used to account for the functional dependence of mixture viscosity, thermal conductivity, and specific heat at constant pressure, respectively. The spatial discretization of the solution domain is done using finite volumes, and the pressure-velocity coupling is achieved using the PIMPLE (PISO+SIMPLE) algorithm. The

computational domain consists of a vertical rectangle with a 2D-axisymmetric sphere located at $(0, 0, 0)$ with diameter $d = 1.8, 3.5,$ and 6 mm. The top, bottom, and side boundaries are placed $15d$, $5d$, and $10d$ away from the center of the sphere, respectively. A resolution of approximately $300,000$ cells is used, with finer resolution near the sphere; a minimum cell size of 60 μm is used to ensure that the thermal/momentum boundary layers are properly resolved. The simulation is carried out with initial and boundary conditions that reproduce the experimental conditions. The simulation initial conditions are $P_0 = 101$ kPa, $T_0 = 300$ K, $\mathbf{U}_0 = (\, u_0 \,, v_0 \,, w_0 \,)$ m/s where $u_0 = v_0 = w_0 = 0$, and T_{sphere} =constant. The frame of reference is attached to the sphere, and hence a time dependent inflow boundary condition is prescribed at the bottom of the computational domain to properly simulate the fall of the heated particle, given by $\mathbf{U}(t) = (\, 0 \,, gt \,, 0 \,)$ m/s. At the top, a non-reflective/pressure transmissive boundary condition is used to simulate an outflow.

To test the heat transfer and fluid mechanics in the numerical model, an experimental temperature field of air heated by a 6 mm diameter sphere is compared with a simulated temperature field. Figure 3.35 shows the temperature field obtained numerically and experimentally. The simulation flow separation angle is shown by the gray dashed line. The maximum thermal boundary layer thickness is observed downstream of the region of flow separation. There is good qualitative comparison in the vicinity of the sphere; however, the temperatures do not match up, and lower temperatures are observed in the experimental thermal boundary layer. There are also large differences in the wake, the convection of heat in the recirculation region is not observed experimentally. The temperatures observed experimentally do not come close to the sphere surface temperature, indicating that interferometry is not sensitive in thin regions subjected to a temperature gradient such as in the thermal boundary layer around a sphere.

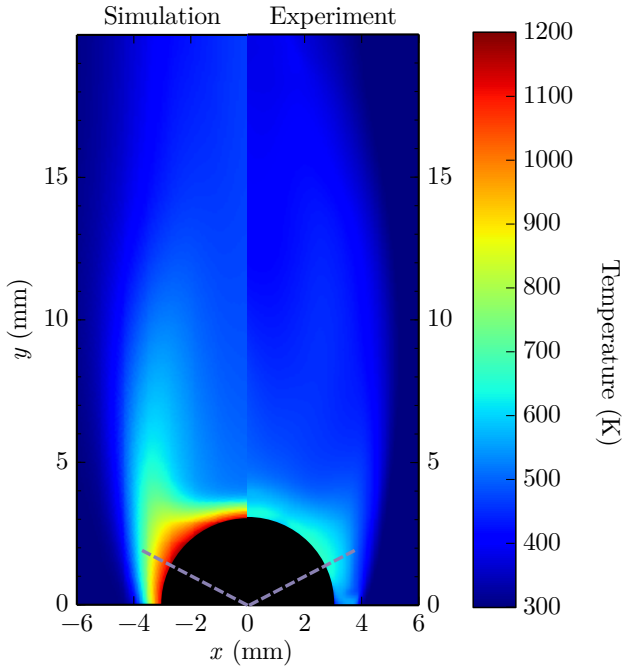

Figure 3.35: Simulation temperature field (left) generated by a freestream flow of 2.4 m/s over a 6 mm diameter sphere with a surface temperature of 1200 K and experimental temperature field (right) of 6 mm diameter sphere traveling at 2.4 m/s with a surface temperature of 1187 ± 18 .

Chapter 4

Ignition of *n*-Hexane-Air by Moving Hot Particles

4.1 Overview

Ignition tests were performed for n-hexane-air mixtures at an initial temperature and pressure of 298 K and 100 kPa, respectively. The mixture equivalence ratio was varied from 0.9 to 2.2 and alumina spheres of $d = 1.8$, 3.5 and 6.0 mm falling at 2.4 m/s were used as the ignition source. Figure 4.1 shows infinite fringe interferometer frames of a no-ignition (top) and an ignition (bottom) event taken at $0.0 - 12.5$ ms. The frame taken at 0.0 ms corresponds to the sphere exiting through the shutter at the bottom of the inert gas-filled tube. In the ignition case (bottom) of Fig. 4.1, the flow around the sphere is similar to the no-ignition case flow up to 2.5 ms, and afterwards the fringes begin to expand outwards away from the wake of the sphere, indicating that ignition has taken place; in addition, the appearance of thinner fringes at the boundary of the disturbed region indicates the presence of a large density gradient corresponding to a flame. In the ignition case, after 7.5 ms, the fringe contours in the recirculation region of the sphere show more structure than in the no-ignition case. The features in the wake suggests that there is no flame propagation directly behind the sphere, consistent with the numerical ignition simulations of Melguizo-Gavilanes et al. (2016b). This indicates that at the time of ignition, the recirculation region of the sphere is composed of N_2; therefore, a flame does not propagate in the wake of the

sphere. In the last ignition frame, at 12.5 ms, the axisymmetry of the wake is evident by the two approximately symmetric closed fringes behind the sphere, indicating that the flow has a toroidal feature consistent with recirculation. Further discussion of the flame propagation is presented in Fig. 4.2.3.

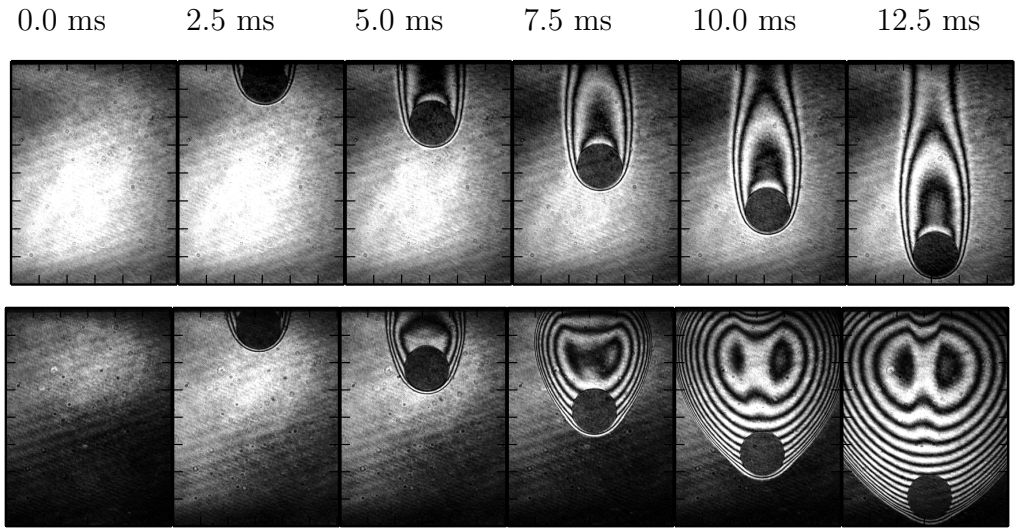

Figure 4.1: Infinite fringe interferometer images of no-ignition (top, shot #17) and ignition (bottom, shot #18) events using a 6.0 mm diameter sphere with surface temperatures of 1017 ± 57 K and 1185 ± 2 K, respectively, in n-hexane-air with an equivalence ratio of 0.9 and an initial temperature and pressure of 298 K and 100 kPa, respectively.

4.2 Effect of Mixture Composition

4.2.1 Pressure Measurements

The sphere surface temperature was varied in a series of tests from approximately 975 to 1349 K and at a fixed diameter of 6.0 mm in order to study the effect of mixture composition on ignition and flame propagation. The peak pressure measurements are shown in Fig. 4.2 and compared against constant volume adiabatic equilibrium calculations performed with Cantera (Goodwin, 2003). The peak pressure experimental results follow the same trend as the numerical results; however, the constant volume

equilibrium calculations are on average 150 kPa higher, and deviate significantly in the rich regime. This is a consequence of heat transfer during and following flame propagation.

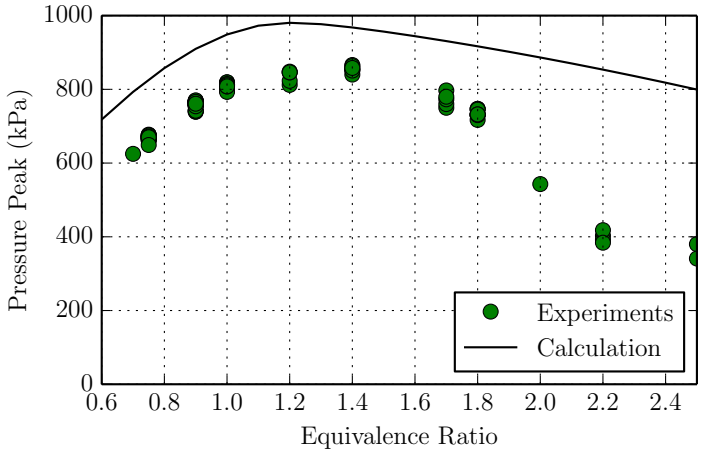

Figure 4.2: Experimental and calculated ideal maximum pressure (adiabatic constant volume explosion) during ignition event as a function of composition for n-hexane-air at an initial temperature and pressure of 298 K and 100 kPa, respectively.

Examples of Savitzky-Golay filtered[5] pressure traces for various equivalence ratios are shown in Fig. 4.3. A $\Phi = 1.4$ mixture yields a rapid pressure rise to above 800 kPa, 8 times the initial pressure and the largest peak pressure out of all the mixture compositions tested. The multiple peaks and plateaus in the pressure traces of $\Phi = 2.0$ and 2.2 are due to the effects of buoyancy which are characterized by lower peak pressures, a longer time to reach the peak pressures, and significant upward displacement of the flame due to buoyancy.

4.2.2 Ignition Threshold

The ignition and no-ignition events as a function of mixture composition are shown in Fig. 4.4. Previous work done by Boettcher (2012) using a glow plug to ignite n-hexane-air mixtures indicates that the ignition threshold is independent of the composition away from the flammability limits, and this is also observed in the current study.

[5]The window size used is 0.5 ms with a 9th order polynomial, the data is sampled at 300 kHz.

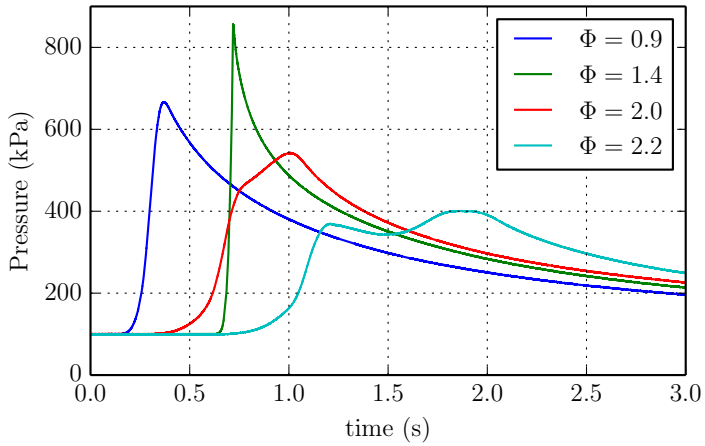

Figure 4.3: Pressure traces during ignition event for selected equivalence ratios of a few of the tests represented in Fig. 4.2.

Using the ignition result (0 or 1) as the outcome variable in a logistic regression model and the sphere surface temperature and composition as the independent variables yields the statistical significance of each parameter (Kabacoff, 2015). From the p-values for the regression coefficients, composition (p-value = 0.616) variations are not statistically significant.

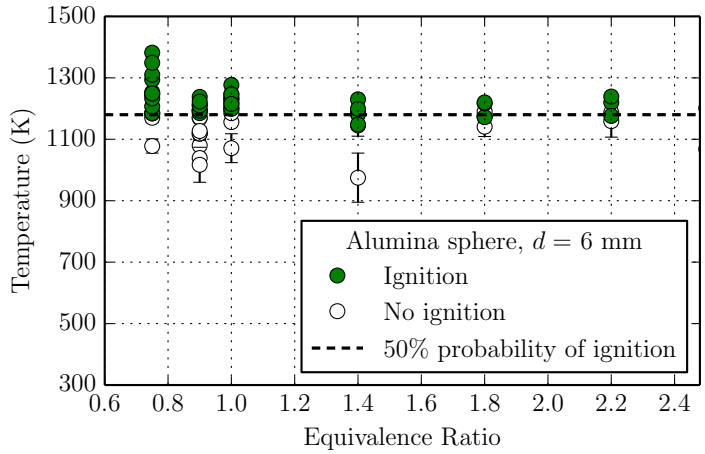

Figure 4.4: Hot particle ignition temperature as a function of composition in *n*-hexane-air at a nominal initial temperature and pressure of 298 K and 100 kPa, respectively; the closed and open markers correspond to ignition and no ignition events, respectively, and the black dashed line marks the 50% probability of ignition.

A Bayesian statistical analysis (Patil et al., 2010) of the ignition data yields a 90% probability of ignition at 1224 K. A comparison with previous experimental work on moving hot particle ignition is not possible since the fuels used by Paterson (1939, 1940) and Silver (1937) were hydrogen-air, pentane-air, and coal-gas-air, which we expect to be different in ignition behavior compared to n-hexane-air. However, for the 3%−vol pentane-air mixture tested by Silver (1937), the ignition threshold extrapolated to 6 mm is 1273 K, a 4% higher threshold compared to the current results for the same sphere diameter.

Figure 4.5 shows the probability distribution obtained from Bayesian analysis of the results in Fig. 4.4; the collapse of the data points is possible due to the lack of ignition dependence on the equivalence ratios tested. The probability of ignition distribution is indicated by the black line, and the corresponding 95% confidence envelope (Patil et al., 2010) is shown by the the red shaded region. The ignition results are shown by the filled circles. An ignition event has a probability of ignition value of 1 and a no ignition event has a probability of ignition value of 0. A narrow overlap region of $1103 - 1213$ K exists between the ignition and no ignition results; this overlap is attributed to uncertainty in the temperature measurements, variability in the incoming flow angle of the sphere, etc.

Bane (2010) used a measure of the relative width of the distribution to quantify the statistical variation of probability of ignition distributions obtained with spark ignition. The relative width used by Bane (2010) was in terms of the minimum ignition energy; in the context of the present study, the appropriate measure is in terms of the minimum ignition temperature,

$$\text{Relative width} = \frac{(T)_{p=0.9} - (T)_{p=0.1}}{(T)_{p=0.5}}, \tag{4.1}$$

where $(T)_{p=q}$ is the temperature corresponding to an ignition probability q; the relative width is illustrated graphically in Fig. 4.6. The relative width calculated from $(T)_{p=0.1} = 1132$ K, $(T)_{p=0.5} = 1176$ K, and $(T)_{p=0.9} = 1224$ K is 0.08. The width is 8% of the mean and is much smaller than the relative widths of $23 - 64$% obtained

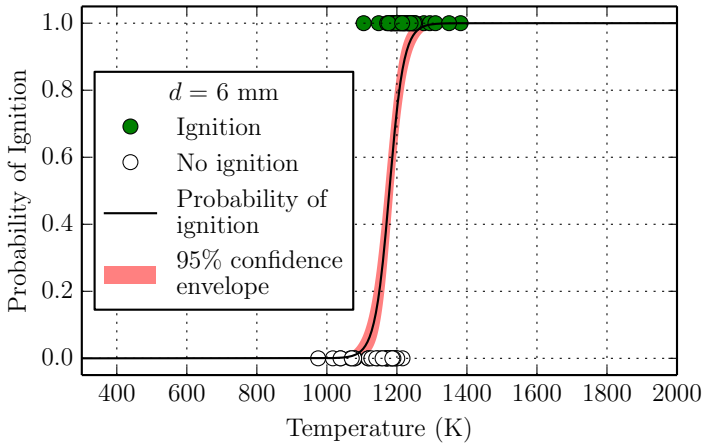

Figure 4.5: Probability of ignition distribution for n-hexane-air using a 6 mm diameter alumina sphere; the black line is the probability distribution, the filled and open markers are the ignition and no ignition results, and the red shaded region is the 95% confidence envelope.

by Bane (2010). The results demonstrate that ignition using a moving hot particle has sufficiently small statistical variation; a single value for an ignition threshold is appropriate for describing the test results.

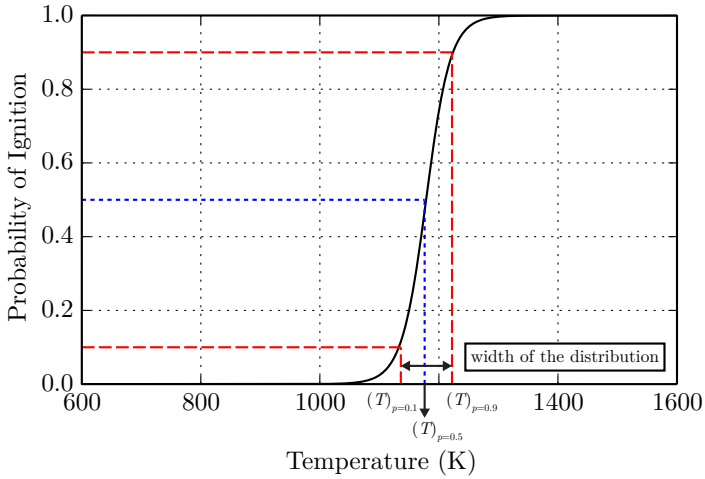

Figure 4.6: Illustration of the percentiles used to calculate the relative width.

Figure 4.7 shows the probability distribution in Fig. 4.5 plotted on a log scale, with probability values ranging from 10^{-11} to 1. The figure demonstrates that extrapolation of the logistic fit predicts a very low probability of ignition at temperatures

below 1100 K but with very large uncertainty. At 1100 K, the probability of ignition is 5% and drops two orders of magnitude to 0.05% at 1000 K. For temperatures in the range $300 - 1100$ K, the extrapolation predicts that the probability of ignition is $10^{-}3$.

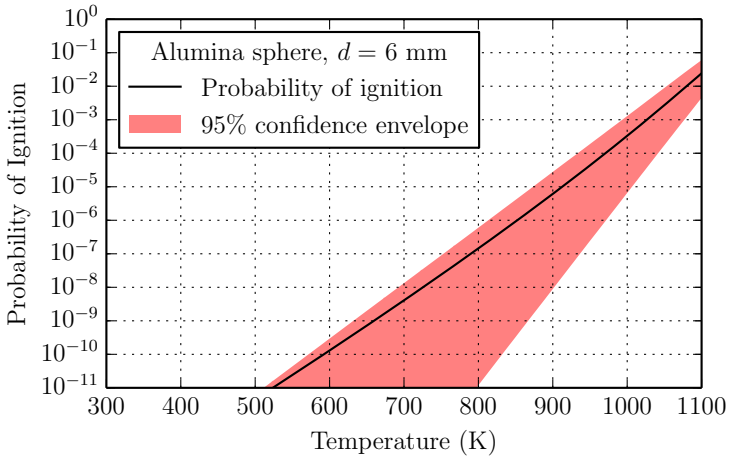

Figure 4.7: Probability of ignition distribution on log scale for n-hexane-air using a 6 mm diameter alumina sphere; the black line is the probability distribution; the red shaded region is the 95% confidence envelope, note that a log scale is used for the ordinate. Both probability and confidence intervals are extrapolated far from the actual temperature range of the data.

Previous studies on hot surface ignition in n-hexane-air mixtures yield comparable ignition thresholds. Melguizo-Gavilanes et al. (2016c) obtained an experimental threshold of 1275 ± 45 K using a stationary cylindrical hot surface measuring 9.1×5.1 mm in height and diameter; this is approximately 4% higher than the 90% probability of ignition threshold of 1224 K given in Fig. 4.5. Numerically, Melguizo-Gavilanes et al. (2016c) obtained an ignition threshold of 1282 K using an irreversible one-step model ($R \rightarrow P$) with kinetic parameters that are fitted to match the ignition delay times of the Mevél model (Mével et al., 2014); the numerical threshold is approximately 5% higher than the current threshold. Mével et al. (2016) used a simplified model to estimate the ignition threshold using a detailed chemistry and a one-step model. The simplified model used non-reactive two-dimensional simulations to estimate the temperature a fluid parcel experienced as it traveled within the thermal

boundary layer near the surface of a hot sphere ($d = 4$ mm) in a flow with a freestream velocity of 2.4 m/s. Reactive simulations using detailed reaction models and a one-step model were then used to investigate the chemical reaction dynamics in a constant pressure reactor with a variable heat transfer coefficient that reproduced the temperature history of a fluid parcel close to the sphere surface. With the simple model, Mével et al. (2016) obtained an ignition threshold of 1300 K, approximately 6% higher than the current threshold. It should be noted that the study of Mével et al. (2016) used a 4 mm diameter sphere; this may account for the higher predicted ignition threshold. A simplified model that uses a critical Damköhler number criterion to predict ignition is given in Appendix E. The model estimates an ignition threshold of 1211 K, this is 1% lower than the current threshold. It should be noted that the model neglects several features present in the momentum and thermal boundary layers around a sphere and was purely devised as a method for predicting the ignition trend as a function of the sphere diameter.

4.2.3 Flame Propagation

The observed variation of flame propagation with mixture composition is shown in Fig. 4.8 for $\Phi = 0.9 - 2.0$. The surface temperature in each case is higher than the ignition threshold, and therefore ignition occurs as soon as the thermal boundary layer has been flushed with the reactive mixture to replace the N_2 originally surrounding it. Laminar burning velocities and flame speeds have been measured in separate tests presented in Chapter 7.

At $\Phi = 0.9$, the flame has a spherical flame propagation speed of 2.6 m/s (Coronel et al., 2013c) which is comparable to the sphere speed of 2.4 m/s. Figure 4.8 (a) shows a flame that propagates outwards except near the front stagnation point where it remains attached to the sphere. The flame geometry and flame/sphere interaction at $\Phi = 0.9$ suggests that the sphere speed is comparable to the the flame propagation speed. Figure 4.8 (b) shows a flame that moves ahead of the sphere near the front stagnation point, indicating that the flame propagation speed is larger than the sphere

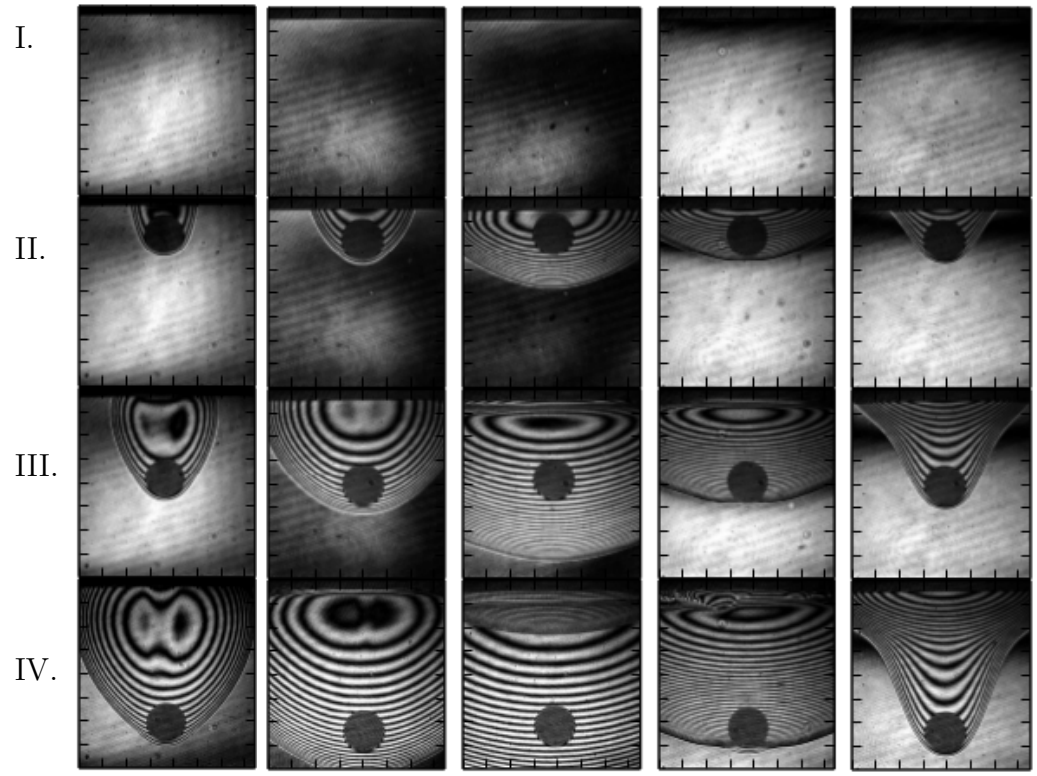

(a) $\Phi = 0.9$ (b) $\Phi = 1.0$ (c) $\Phi = 1.2$ (d) $\Phi = 1.7$ (e) $\Phi = 2.0$

Figure 4.8: Flame propagation in n-hexane-air at various equivalence ratios and an initial temperature and pressure of 298 K and 100 kPa, respectively; I. $t = 0.0$ ms, II. $t = 3.5$ ms, III. $t = 7.0$ ms, and IV. $t = 10.5$ ms; the corresponding shot numbers are (a) shot #25, (b) shot #44, (c) shot #51, (d) shot #54, and (e) shot #57.

speed.

Experimental values and 1D freely propagating propagating flame speed calculations are shown in Fig. 4.9 along with the sphere speed that is marked by the red dashed line. The calculations are performed with Cantera (Goodwin, 2003) using the JetSURF mechanism (Version 2.0) Wang et al. (2010) which has shown to agree well with experimental values of flame speeds of lean to stoichiometric n-hexane-air mixtures (for a detailed comparison of various mechanisms with experimental values, see Chapter 7).

Previous work by Coronel et al. (2013c) measured a spherical flame propagation speed of 2.9 m/s at $\Phi = 1.0$. Figure 4.8 (c) can be interpreted as a flame that

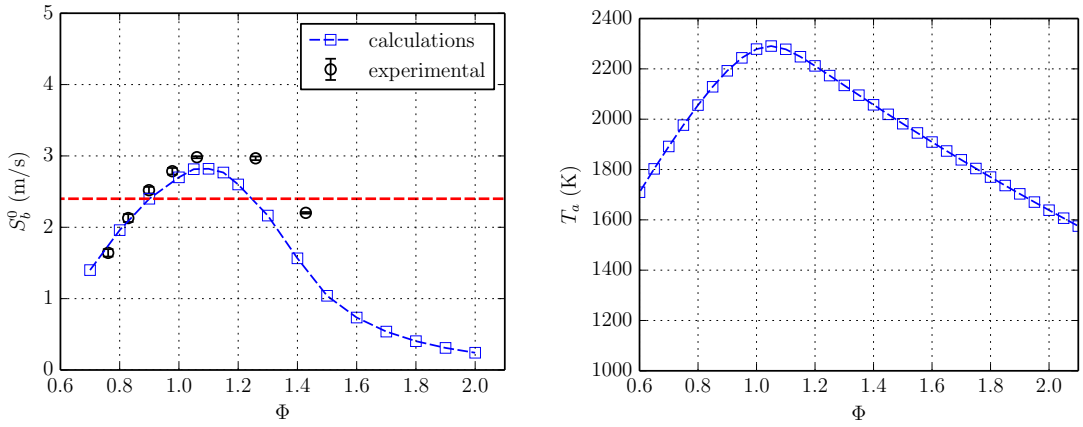

Figure 4.9: Unstretched flame speed calculations and experimental results for *n*-hexane-air at an initial temperature and pressure of 298 K and 100 kPa, respectively.

propagates away from the sphere in all directions and is not significantly affected by the presence of the sphere. The flame shape closely resembles that produced by a spark (Bane, 2010; Bane et al., 2011; Coronel et al., 2013a,c). Figure 4.8 (d) shows a flame with a propagation speed that is smaller than the sphere speed. The sphere appears to be "puncturing" through the flame front at 7.0 ms. Figure 4.8 (e) shows a flame at $\Phi = 2.0$ with the smallest propagation speed observed in this study. The sphere appears to be traveling ahead of the flame front at 3.5 ms. At later times, it is speculated that the burned products are entrained in the wake of the sphere, yielding the flame/burned products geometry observed in Fig. 4.8 (e). It is hypothesized that the fringe front seen is not a flame but a contact surface between hot products and cold gas; the flame speed at $\Phi = 2.0$ is approximately 0.3 m/s, based on 1D freely propagating laminar burning speed calculations, which is very slow compared to the propagation speed of the fringe front observed in Fig. 4.8 (e).

4.2.3.1 Flame Propagation: Analysis of $\Phi = 1.0$ and $\Phi = 2.0$ Cases

The approach presented in this section is an effort to determine the difference between a flame propagation front (Fig. 4.8 (a), (b), (c), and (d)) and what is speculated to be a contact surface between burned and unburned gas (Fig. 4.8 (e)). Processing the infinite fringe interferograms of Fig. 4.8 using the approach detailed in Section 2.4

to obtain the optical phase difference is not possible since there is difficulty in differentiating between the undisturbed region of the images and the leading fringe. The present approach focuses on analyzing the region near the front defined by the disturbance of the fringes.

Figure 4.10 shows the fringe fronts at 7 ms for all the compositions tested. The figure illustrates the variations in the fringe front propagation speed and shape. Of particular interest are the fringe fronts of the $\Phi = 1.0$ and $\Phi = 2.0$ cases, the former is a flame and the latter is speculated to be a contact surface separating burned products cold reactants. The red squares over each line at $\Phi = 1.0$ and $\Phi = 2.0$ are chosen as locations were the fringe front is further analyzed.

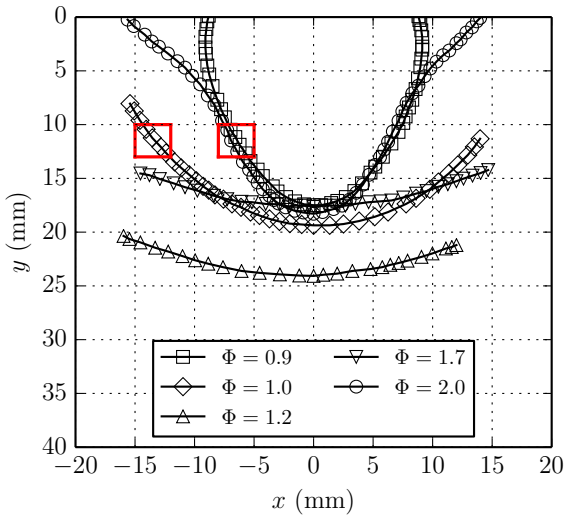

Figure 4.10: Fringe front for $\Phi = 0.9$ (shot 25), $\Phi = 1.0$ (shot 44), $\Phi = 1.2$ (shot 51), $\Phi = 1.7$ (shot 54) and $\Phi = 2.0$ (shot 57); $y = 0$ mm corresponds to the bottom edge of the shutter

The interferograms at the red square locations are shown in Fig. 4.11, and each image is 4×4 mm in width and height. Figure 4.11 (a) shows the flame front propagating into unburned reactants, the thin fringes delineating the flame are indicative of large temperature gradients. Thicker and less fringes are observed in Fig. 4.11 (b) indicating that at the fringe front, the temperature gradient is smaller than the gradient observed at the flame front of $\Phi = 1.0$.

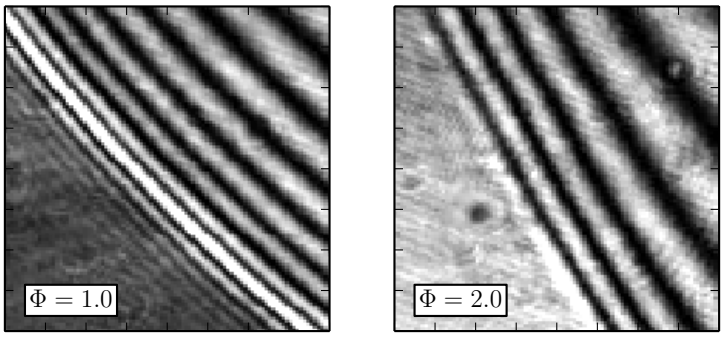

(a) (b)

Figure 4.11: Details of fringe front taken at 7.0 ms from Fig. 4.8 for (a) $\Phi = 1.0$ and (b) $\Phi = 2.0$; each image is 4×4 mm, the tick spacing is 0.5 mm.

The flame structure of a $\Phi = 1.0$ *n*-hexane-air mixture was obtained using a one dimensional freely propagating flame in Cantera (Goodwin, 2003). The flame structure was used to create a synthetic temperature field for a spherical flame, shown in Fig. 4.12, with a radius of 16 mm, comparable to the fringe front radius shown in Fig. 4.11 (a). Figure 4.12 shows a quarter section of the synthetic temperature field, where red corresponds to burned products that are at a temperature, T_b, of 2114 K, blue are the unburned reactants, at a temperature of 300 K, and the region in between is the flame.

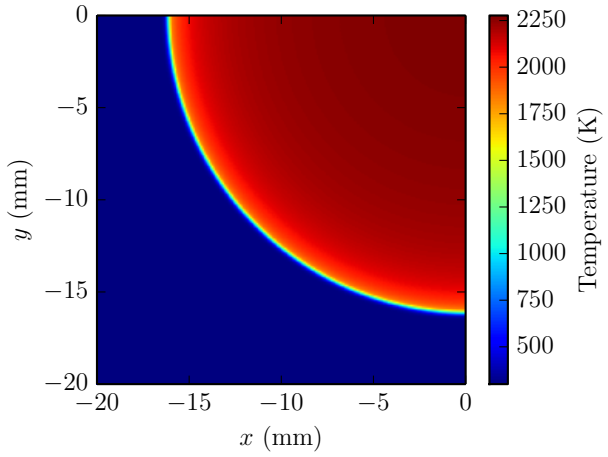

Figure 4.12: Synthetic spherical flame gas temperature for $\Phi = 1.0$.

The methods described in Section 2.4.2, mainly Eqs. 2.31 and 2.33, are used to obtain the synthetic unwrapped optical phase difference of Fig. 4.12. To do a direct comparison of the synthetic and experimental fringes of Fig. 4.11 (a), the synthetic optical phase difference is wrapped such that the phase values are bounded from $-\pi$ to π. The wrapped optical phase difference, $\Delta\varphi_W$, and corresponding temperature of the synthetic flame are shown in Fig. 4.13; only a section of the flame is shown to facilitate a direct comparison with the experimental image of Fig. 4.11 (a). A total of 9 fringes are visible in the synthetic image of Fig. 4.13 (a), and this is the same number of fringes observed in the experimental image. Additionally, the same variation of fringe thickness observed experimentally is also observed at the fringe front of the synthetic image.

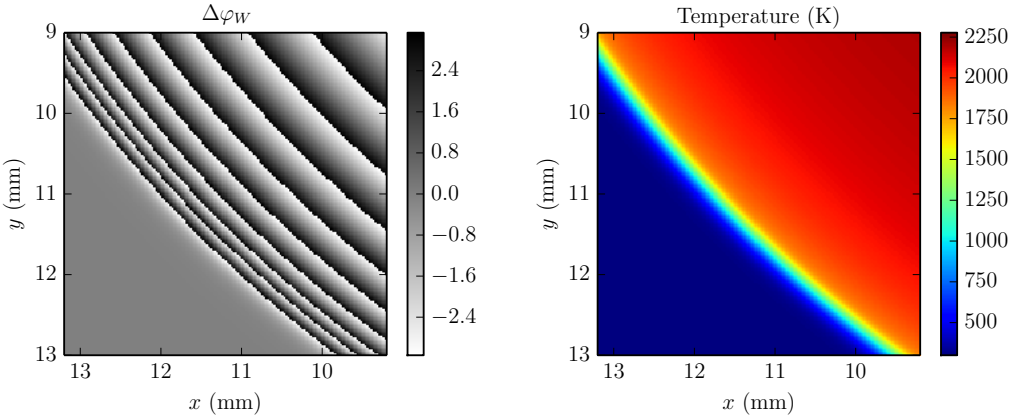

(a) Wrapped optical phase difference (b) Gas temperature

Figure 4.13: Synthetic flame (a) wrapped optical phase difference and (b) gas temperature; the tick spacing is 1.0 mm in each image.

Figure 4.14 shows the temperature and fringe count, $-\Delta\varphi_W/2\pi$, normal to the fringe contours taken from a radius of 13 to 17 mm, where $r = 0$ mm is the center of the flame. Figure 4.14 shows the first fringe ($\Delta\varphi_W/2\pi = 1$) at a temperature of 735 K, which is a temperature jump of 435 K from the 300 K unreacted mixture temperature, the second fringe ($\Delta\varphi_W/2\pi = 2$) appears as the temperature further increases to 1439 K, a temperature jump of 704 K from the previous fringe temperature, and the third fringe ($\Delta\varphi_W/2\pi = 3$) appears at a temperature of 1863 K, a temperature jump of 425

K from the second fringe temperature. The spacing of the remainder of the fringes begins to thicken as the temperature gradient becomes smaller, 101 K, 72 K, 53 K, 40 K, and 31 K for the fourth, fifth, sixth, seventh, and eight fringes, respectively. It can be concluded with confidence that due to the agreement in the fringe count and thickness between the synthetic fringe pattern in Fig. 4.13 (a) and the experimental image in Fig. 4.11 (a), the fringe front corresponds to a flame front.

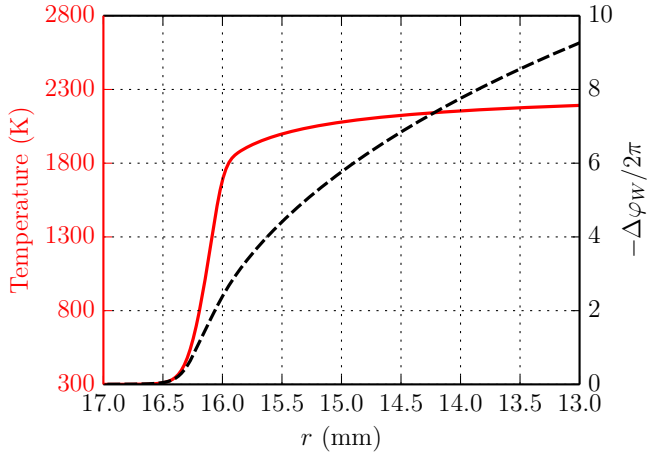

Figure 4.14: Gas temperature (red) and fringe count (black) taken normal to the fringes of a synthetic $\Phi = 1.0$ n-hexane-air spherical flame.

A synthetic fringe pattern corresponding to the experimental fringe pattern shown in Fig. 4.11 (b) is investigated to determine if the experimental pattern represents a flame or is simply composed of burned products that are cooling as they come into contact with the unburned mixture. The latter is possible since ignition occurred at the shutter exit and the subsequent flame propagation occurs so slowly that it is outrun by the sphere. A total of 5 distinct fringes are observed in Fig. 4.11 (b) and they are thicker at the fringe front when compared to the thin fringes observed in the flame propagation case of Fig. 4.11 (a).

The synthetic fringe pattern for a $\Phi = 2.0$ flame is shown in Fig. 4.15 (a), the thick fringes at the front correspond to flame thickness of approximately 6 mm. The thick synthetic fringes do not correspond to those observed experimentally in Fig. 4.11 (b). Figure 4.15 (b) shows a modified fringe pattern that corresponds to a higher

temperature gradient at the fringe front and a lower maximum temperature than Fig. 4.15 (a).

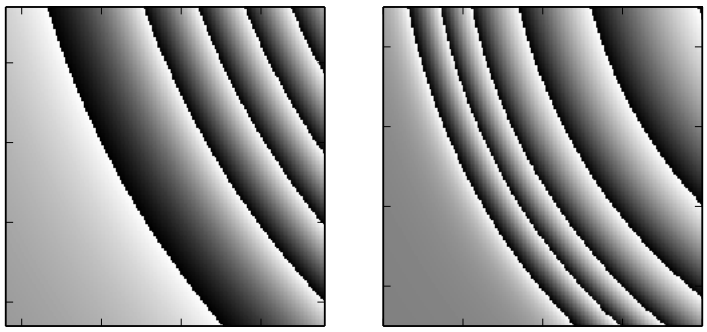

(a) $\Phi = 2.0$ (b) Modified

Figure 4.15: Synthetic interferograms created for a (a) $\Phi = 2.0$ flame and a (b) modified $\Phi = 2.0$ flame.

Figure 4.16 shows a comparison of the temperature and fringe count of the synthetic fringe patterns generated to match the experimental results of Fig. 4.11, the $\Phi = 1.0$ and $\Phi = 2.0$ cases are shown by the solid and dashed lines, respectively.

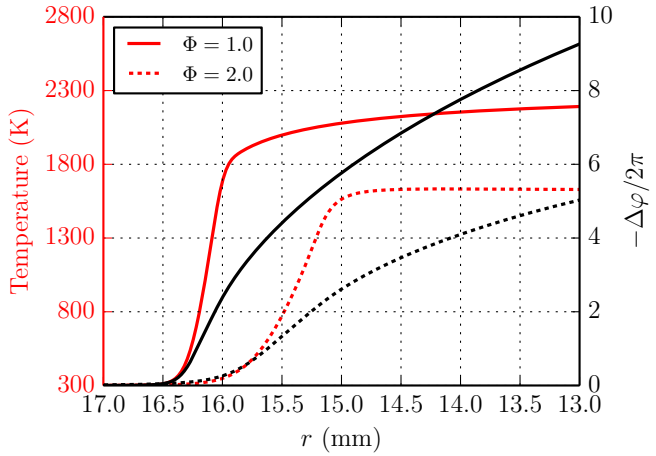

Figure 4.16: Gas temperature and fringe count taken normal to the synthetic fringes of the (a) $\Phi = 1.0$ and (b) $\Phi = 2.0$ cases.

Figure 4.17 shows a side-by-side comparison of the final experimental and synthetic fringe patterns. The synthetic replication of the experimental fringe pattern of the $\Phi = 1.0$ case using the flame structure of a $\Phi = 1.0$ flame obtained from

one-dimensional freely-propagating flame calculations was successful; no modifications were made to the flame structure to match the experimental fringe pattern. However, for the $\Phi = 2.0$ case, the synthetic flame structure of a $\Phi = 2.0$ flame had to be modified to better match the experimental fringe pattern. In particular, the flame thickness had to be decreased and the maximum temperature lowered to $0.95T_a$. Keep in mind that the flame structure of a $\Phi = 2.0$ flame was calculated using a one-dimensional freely-propagating flame; however, the chemical mechanism used has not been validated for that mixture composition. The results are not conclusive but strongly suggest that the $\Phi = 2.0$ case corresponds to an extinguished flame since the flame structure of the synthetic fringe pattern does not correspond to the structure of a $\Phi = 2.0$ flame.

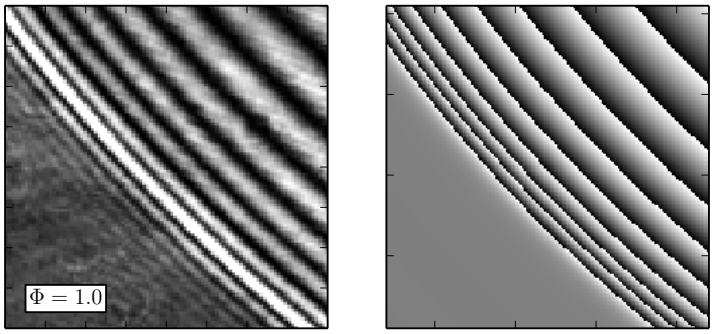

experiment synthetic

(a) $\Phi = 1.0$

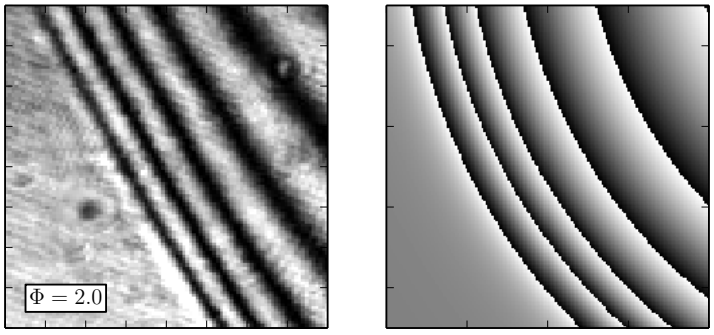

experiment synthetic

(b) $\Phi = 2.0$

Figure 4.17: Comparison of experimental and synthetic wrapped optical phase difference of the (a) $\Phi = 1.0$ and (b) $\Phi = 2.0$ cases; the corresponding synthetic temperature profiles are shown in Fig. 4.16.

4.3 Effect of Sphere Diameter

For this portion of the study, the mixture equivalence ratio, Φ, was fixed at 0.9 and alumina spheres 1.8 mm, 3.5 mm and 6.0 mm in diameter were used as the ignition source. A sphere reaches the field of view approximately 200 ms after being dropped, during that time, each accelerates to a speed of approximately 2.4 m/s. The sphere surface temperature was varied from 1000 to 1300 K; ignition and no-ignition events are shown in Fig. 4.18. Experimentally, the ignition threshold is 1180 ± 50 K, 1215 ± 10 K, and 1263 ± 234 K, for sphere diameters of 6.0 mm, 3.5 mm and 1.8 mm, respectively. The threshold is weakly dependent on the sphere size over the diameters tested, e.g. a difference of less than 100 K (7% of the ignition temperature thresholds) is observed between the smallest and largest sphere diameter ignition thresholds.

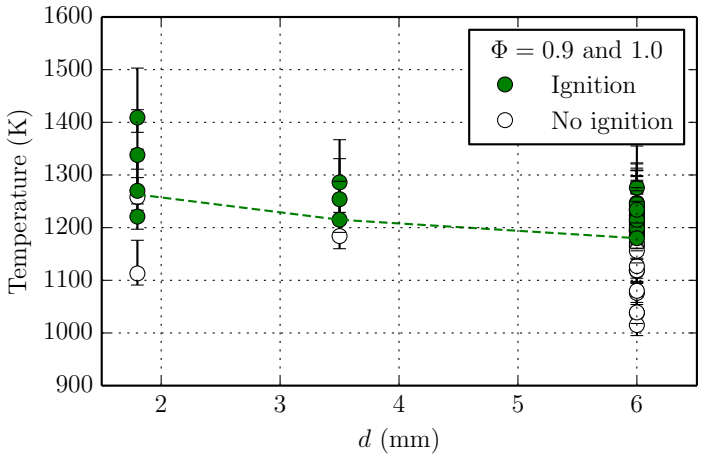

Figure 4.18: Hot particle ignition temperature as a function of sphere diameter in n-hexane air at $\Phi = 0.9$ and an initial temperature and pressure of 298 K and 100 kPa, respectively.

In the electrical heating configuration, a 4 mm titanium sphere was tested in n-hexane-air at $\phi = 0.9$. Schlieren images of an ignition event are shown in Fig. 4.19. The sphere enters the reactive mixture at 1 ms, and at 7.6 ms it appears that ignition has already take place. The flame propagation is observed at later times.

A series of experiments were performed to obtain a probability distribution. Figure 4.20 shows the ignition results and probability of ignition. The probability distri-

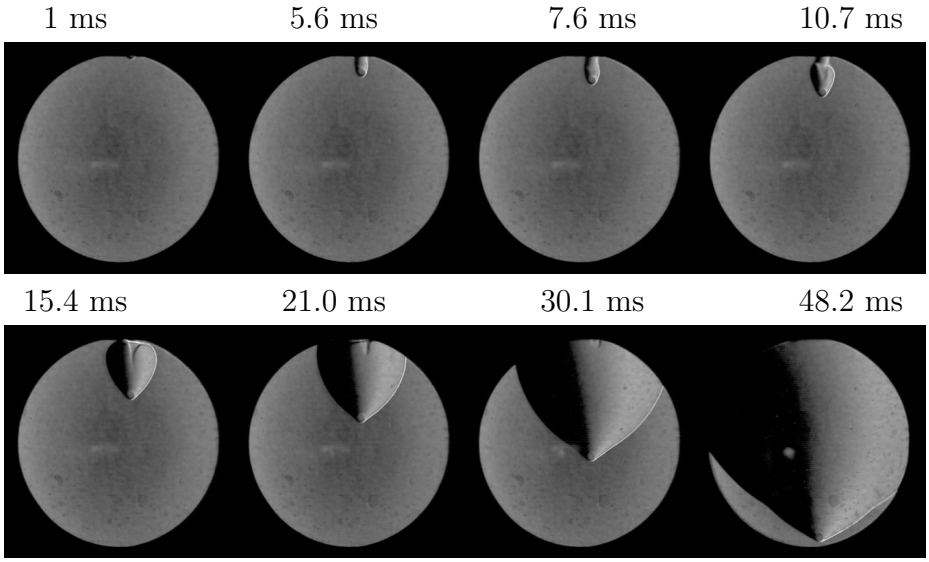

Figure 4.19: Schlieren images of ignition and flame propagation of n-hexane-air at $\Phi = 0.9$ using a 4 mm titanium sphere with $T_{\text{sphere}} = 1199\ +42/-10$ K (shot #22).

bution is indicated by the black line and the corresponding 95% confidence intervals are shown by the red shaded region. The ignition results are shown by the markers, where an ignition event has a probability of ignition value of 1 and a no ignition event has a probability of ignition value of 0. A narrow overlap region of $1150 - 1170$ K exists between the ignition and no ignition results.

The ignition threshold of the 4 mm titanium sphere is indistinguishable from the threshold of the 6 mm diameter alumina sphere. A comparison of the probability distributions is shown in Fig. 4.21; notice the overlap in the confidence envelopes of the two distributions.

4.3.1 Flame Propagation

Figure 4.22 shows flame propagation for the three diameter spheres tested at $\Phi = 0.9$. The time indicated below each set of images corresponds to the time elapsed from the sphere entering the field of view. According to the flame emission observed by the two-color pyrometer, Fig. 4.22 (a) and (b) ignited 4.2 ms and 2.6 ms, respectively, prior to entering the field of view and Fig. 4.22 (c) ignited 3.2 ms after entering

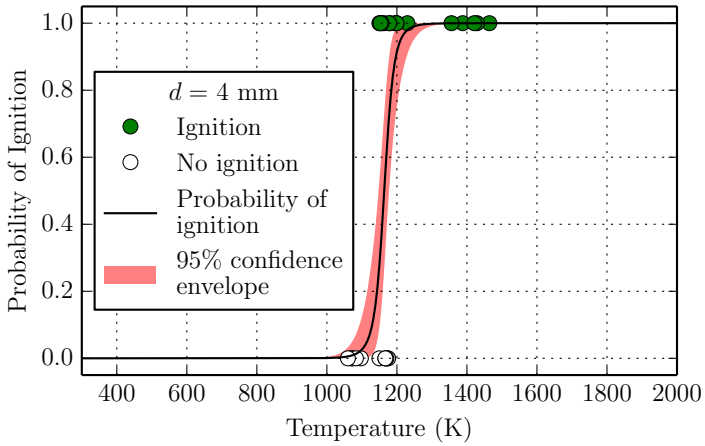

Figure 4.20: Probability of ignition distribution for n-hexane-air using a 4 mm diameter titanium alloy sphere; the black line is the probability distribution, the filled and open markers are the ignition and no ignition results, and the red shaded region is the 95% confidence envelope.

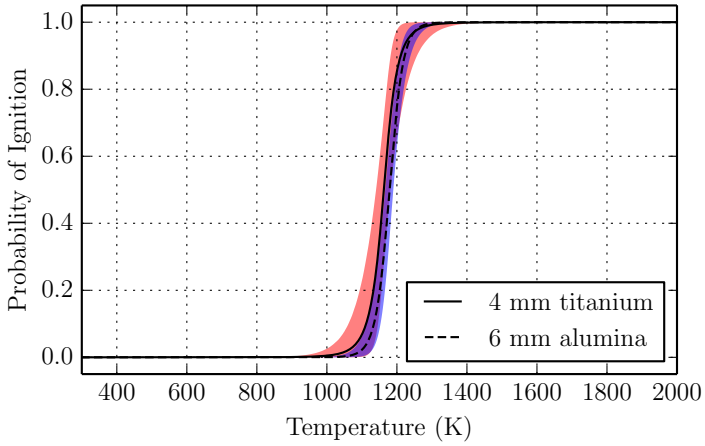

Figure 4.21: Comparison of probability of ignition distributions for n-hexane-air using a 4 mm diameter titanium alloy sphere and a 6 mm alumina sphere; the black lines are the probability distributions, and the red and blue shaded regions are the 95% confidence envelopes for the 4 mm and 6 mm diameter spheres, respectively.

the field of view. As mentioned earlier in Section 4.2.3, at $\Phi = 0.9$ the flame has a spherical propagation speed of approximately 2.6 m/s (Coronel et al., 2013c) which is comparable to the sphere speed of 2.4 m/s. Figure 4.22 shows flames that propagate outwards except near the front stagnation point where it remains close to the sphere

surface. It appears from the interferograms that the flame behavior at the front stagnation point is independent of the sphere diameters tested and only depends on the mixture composition. The flame propagation is expected to be independent of the sphere diameter since the flow outside of the momentum boundary layer is the same for the three diameters tested since the spheres are traveling at the same speed.

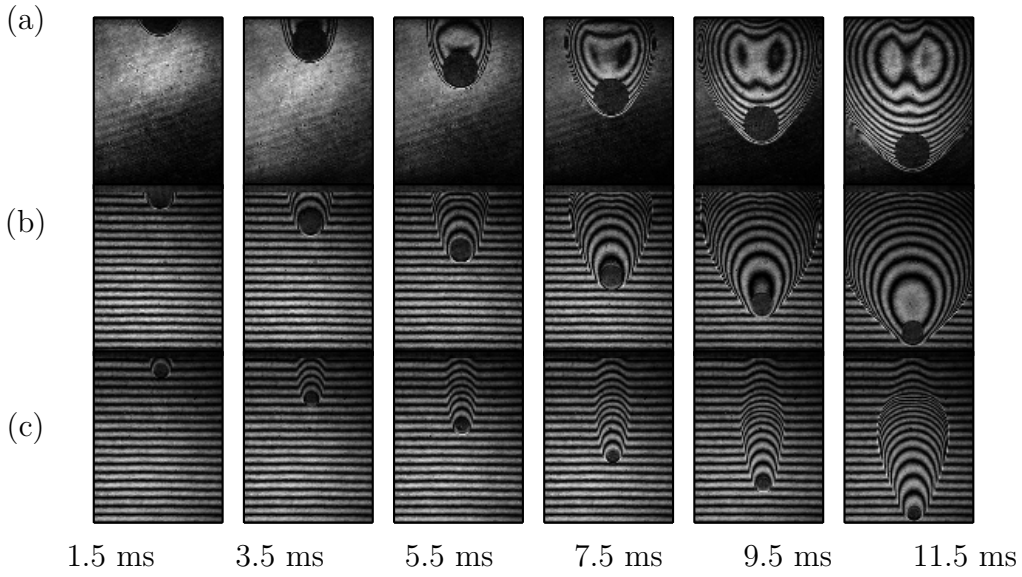

Figure 4.22: Finite fringe and infinite fringe interferograms of ignition and flame propagation in *n*-hexane-air at $\Phi = 0.9$ and an initial temperature and pressure of 298 K and 100 kPa, respectively, for (a) 6.0 mm (shot #18), (b) 3.5 mm (shot #131), and (c) 1.8 mm (shot #141) diameter spheres.

4.4 Ignition Location and Time

Determining the ignition location is possible due to extreme sensitivity of the interferometer setup when placed in the infinite fringe configuration. Figure 4.23 shows a sequence of interferograms for ignition of a $\Phi = 0.9$ mixture using a 6 mm diameter sphere with a surface temperature of 1277 ± 13 K at $t = 2.3 - 11.3$ ms. Due to the axisymmetry of the flow, only half of the image is shown. There are three distinct sets of fringe patterns. The fringes are thickest in the wake of the sphere due to the

toroidal vortex that produces a recirculating flow with small temperature gradients (see Fig. 3.22 (b)). The fringes appear unchanged up to 7.7 ms; at this time, the fringe that is attached to the sphere close to the rear stagnation point begins to expand outwards. The expansion and generation of new fringes continues at 9.5 and 11.3 ms, indicating the formation of a propagating flame front moving away from the sphere.

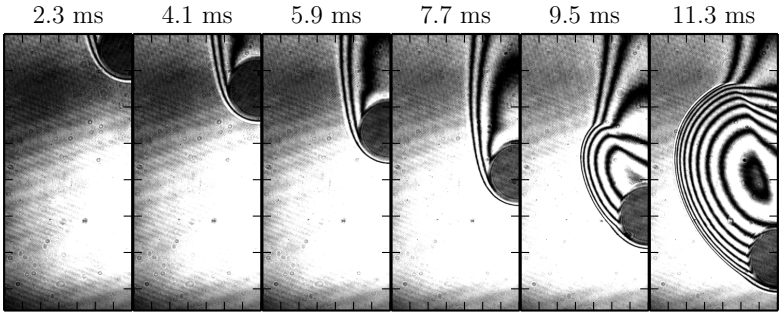

Figure 4.23: Infinite fringe interferograms of ignition and flame propagation of n-hexane-air at $\Phi = 0.9$ and an initial temperature and pressure of 298 K and 100 kPa, respectively, at $t = 2.3 - 11.3$ ms (shot #36).

Figure 4.24 shows the interferograms of the Fig. 4.23 ignition case at $t = 7.6 - 8.6$ ms at smaller time intervals bracketing the ignition time. The dark fringe attached to the sphere near the rear stagnation point begins to expand outwards between 7.6 and 7.8 ms. This initial expansion corresponds to an ignition event taking place; the fringes expand outwards as an ignition kernel is formed which corresponds to an increase in the optical phase difference as the temperature of the gas increases. The start of flame propagation is not visibly obvious until 8.6 ms. Visual inspection of the interferograms yields an ignition time of $7.6 - 7.8$ ms after the sphere enters the field of view or 0.6437 seconds after the sphere has fallen past the second temperature probe. It is also evident from the interferograms that the initial fringe expansion corresponding to an ignition event occurs near the region of flow separation. This is determined by superimposing the images shown in Fig. 4.24 and locating the region where the fringes deviate from the fringes in the previous frame.

Empirical relations for flow separation angles (Clift et al., 2005), discussed in Sec-

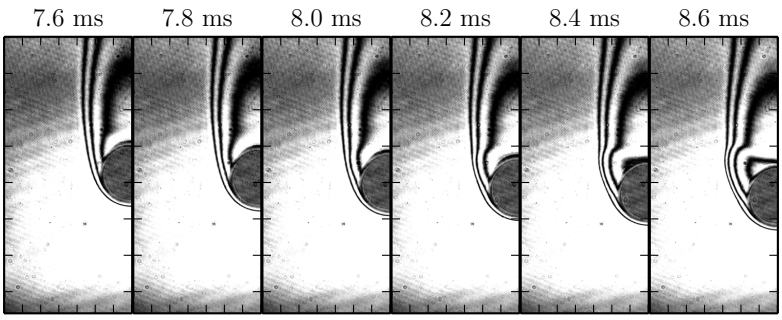

Figure 4.24: Infinite fringe interferograms of ignition and flame propagation of n-hexane-air at $\Phi = 0.9$ and an initial temperature and pressure of 298 K and 100 kPa, respectively, at $t = 7.6 - 8.6$ ms (shot #36).

tion 3.2, yield $\theta_s = 118°$ for $Re = 177$ (film conditions). The angle θ_s corresponds to the region where an adverse pressure gradient leads to flow reversal and eventually to flow separation (Johnson and Patel, 1999; Clift et al., 2005); the empirical separation angle obtained from Eq. 1.5 is illustrated in two images in Fig. 4.25, before and after ignition[6].

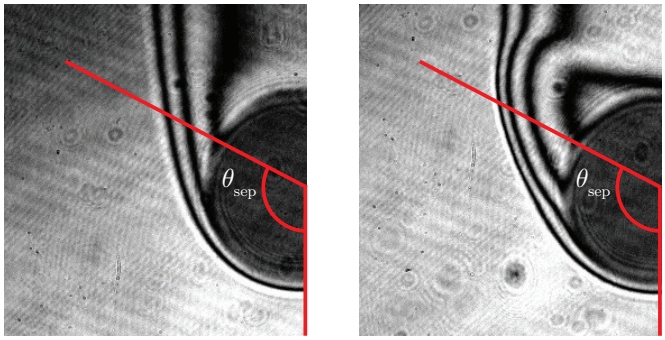

(a) Before ignition: $t = 7.0$ ms (b) After ignition: $t = 8.6$ ms

Figure 4.25: Empirical flow separation angle illustrated on (a) pre- and (b) post-ignition interferograms, (shot #36).

Although not observed directly in the experiments, it is hypothesized that a fluid parcel that enters the thermal boundary layer surrounding a hot sphere will continuously increase in temperature as it travels from the front stagnation point of the

[6]The separation angle is obtained from Eq. 1.5 using the Reynolds number based on the film temperature, i.e. $T = \left(T_0 + T_{\text{sphere}}\right)/2$

sphere to the region of flow separation; after or shortly after leaving this region, the fluid parcel will begin cooling down. Therefore, it is necessary for a fluid parcel to ignite in regions between the front stagnation and separation point of the sphere. At the ignition threshold, the last location along the fluid parcel trajectory that is plausible for ignition is the separation point.

Chapter 5

Thermal Boundary Layer Ignition Modeling[7]

5.1 Overview

The experimental investigation described in Chapter 4 led to the conclusion that at the ignition threshold, ignition occurs within the thermal boundary layer of the sphere near the region of flow separation. Given these experimental results, the goal of this chapter is to understand the ignition behavior within a thermal boundary layer adjacent to a hot surface. This chapter first covers the modeling efforts previously attempted on two-dimensional reactive flows over a hot sphere and then presents in Section 5.3 a simplified transient, one-dimensional analysis of ignition within thermal boundary layers using a model based on the Rayleigh or Stokes first problem. The modeling is not intended to be a representation of the experimental situation of hot sphere ignition but is an exploratory study of processes within a transient thermal boundary layer for a much simpler model problem.

[7]The author thanks Simon Lapointe for his extensive help in setting up the 1D problem and implementing the fluid parcel tracking in NGA.

5.2 Sphere Thermal Boundary Layer Ignition Modeling

Moving hot particle ignition is a complex problem to simulate since it incorporates chemistry, heat transfer, and fluid mechanics over a wide range of spatial and temporal scales. In addition, the problem is three-dimensional; however, it can occasionally be approximated as two-dimensional if the sphere flow is axisymmetric, that is, $\mathrm{Re} < 210$. Even with the reduction to two dimensions, there is still the high computational cost associated with the size of a realistic chemical reaction mechanism for a typical hydrocarbon fuel. The computational time is a strong function of the number of species transported and the computational complexity of evaluating the reaction source terms and transport properties such as viscosity and diffusivities.

Figure 5.1 shows the thermal boundary layer around a sphere at an instant in time. The flow around the spheres tested in Chapter 4 is steady and axisymmetric prior to ignition if the transient period of the sphere passing from inert to reactive gas is neglected. The thermal boundary layer around a sphere is thin at the front stagnation point and grows from the front to the separation region or rear stagnation point, depending on the Reynolds number. In the sphere fixed reference frame, the freestream has velocity and temperature of U_∞ and T_∞, respectively; the sphere surface is at a temperature of T_{wall}, where $T_{\mathrm{wall}} > T_\infty$.

Previous numerical studies on 2D axisymmetric hot particle ignition were performed by Coronel et al. (2013b) using the Flamelet Progress Variable (FPV) approach (Knudsen and Pitsch, 2009); the approach allows for multi-step reaction chemistry to be incorporated into a fluid dynamic simulation in a computationally efficient manner. That study did not include numerical ignition thresholds; however, it did enable a qualitative comparison of the numerical and experimental flame propagation geometry. That study clearly identified the importance of the role of the inert gas in the boundary layer and wake. That study was performed for a 40% N_2 diluted, n-hexane-oxygen-diluent mixture at $\Phi = 0.9$ and an initial temperature and pressure of 298 K and 50 kPa, respectively, using a particle diameter of approximately 1

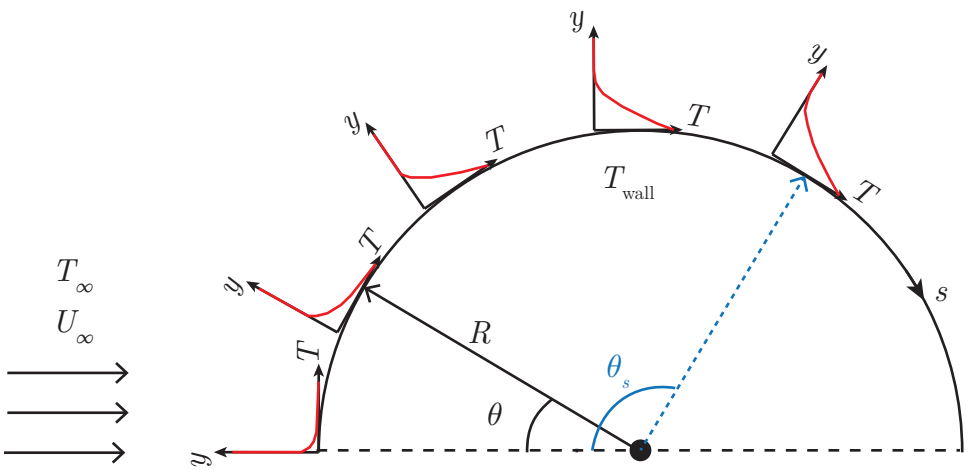

Figure 5.1: Illustration of the growth of the thermal boundary layer over a sphere, profiles are shown at different angles θ; the freestream gas temperature is T_∞ and the sphere surface temperature is T_{wall}, θ_s corresponds to the angle where flow separation occurs; there is also a corresponding momentum boundary layer which is not shown.

mm. Melguizo-Gavilanes et al. (2016b) performed an extensive study of moving hot particle ignition using a detailed reaction mechanism for hydrogen-air. That study indicated that at the ignition threshold, ignition occurs in the region of flow separation; spheres with surface temperatures greater than the threshold temperature result in ignition taking place between the front stagnation point and the separation region. A detailed analysis of species and energy transport in the vicinity of the ignition region is presented. Hot particle simulations for hydrocarbon-air mixtures with a reduced, realistic reaction mechanism are underway at Caltech by Melguizo-Gavilanes et al. (2016a).

5.3 Rayleigh Ignition Model Problem

The goal of this chapter is to gain insight into the processes leading to ignition in a thermal boundary layer. The thermal boundary layer surrounding a sphere was not analyzed in order to reduce the geometric complexity and computational cost. Instead a one-dimensional transient boundary layer is studied -this enables rapid

simulations even with relatively detailed chemical reaction mechanisms. Figure 5.2 illustrates that situation that is being considered. At time $t = 0$ a cold flow ($T = T_\infty$) is uniformly in motion in the $x-$direction with velocity $u = U_\infty$. The flow is transient but one-dimensional, all properties depend only on distance y and time t; for example $T(y,t)$, $u(y,t)$, $v(y,t)$. All properties are independent of the wall-parallel distance x, i.e., $\partial/\partial x = 0$. At $t \geq 0$ the temperature at the wall is set to T_{wall}, where $T_{\text{wall}} > T_\infty$, and the velocity u at the wall is set to zero. This model problem is an extension of the Rayleigh or Stokes first problem of elementary fluid mechanics and includes both a thermal as well as a momentum (vorticity) boundary layer.

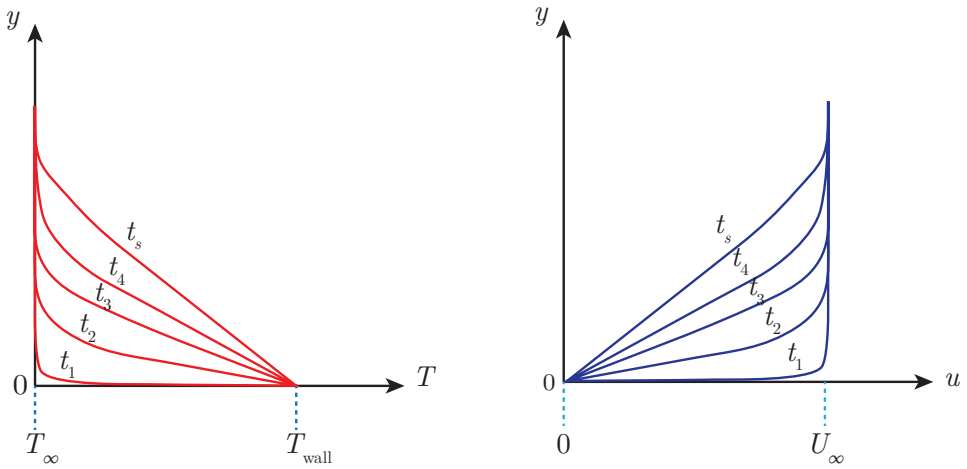

(a) Thermal boundary layer (b) Velocity boundary layer

Figure 5.2: Temporal growth of the (a) thermal and (b) velocity boundary layers due to an impulsively applied boundary condition at $y = 0$ and $t \geq 0$; the gas temperature is T_∞ as $y \to \infty$, and T_{wall} at $y = 0$; the flow velocity is U_∞ as $y \to \infty$ and $u = 0$ at $y = 0$.

A temporally growing thermal and momentum boundary layer omits a number of significant features that are present in the thermal/velocity boundary layer around a sphere such as:

- Variations in the edge velocity of the boundary layer due to the external flow over the sphere.
- Growth behavior of the boundary layer around a sphere. For example, at the

front stagnation point, the boundary layer has a finite thickness and as the boundary grows, the axisymmetric geometry creates additional flow divergence not found in planar geometries.

- Flow separation will ultimately limit the applicability of any boundary layer computation.

The goal of the present approach is to gain insights into ignition within a thermal boundary layer and due to the difference with the spherical case, quantitative results are not sought. Clearly, a full treatment of the spherical problem using a direct numerical simulation (Melguizo-Gavilanes et al., 2016b; Coronel et al., 2013b) is necessary to make quantitative predictions of the flow field and ignition thresholds.

5.3.1 Previous Numerical Work

Several numerical studies have been performed on ignition adjacent to a heated surface. Kumar (1989) performed a one-dimensional unsteady analysis of ignition of hydrogen-air adjacent to a vertical hot surface. The vertical motion of the gases due to buoyancy was neglected and only the motion normal to the heated surface was considered. The chemistry was modeled using multistep, chain-branching reactions of the modified Arrhenius type. The model consisted of 9 species and 48 elementary reactions. Kumar (1989) compared his calculations with experimental results of ignition by a vertical cylindrical igniter heated at 5 K/s and found them to be in excellent agreement for hydrogen-air mixtures even though the buoyancy induced flow was neglected. Chen and Faeth (1981) performed simulations of flow adjacent to a vertical hot surface; the problem was treated as two-dimensional and steady, and the chemistry was modeled using a one-step reaction of the Arrhenius type. Since the problem was steady, the velocity was obtained using a stream-function approach. Chen and Faeth (1981) assumed constant temperature as well as constant heat flux conditions on the heated wall In addition, Chen and Faeth (1981) determined that near the ignition threshold, a certain distance above the hot surface was needed for a deflagration wave to develop. Chen and Faeth (1981) did not compare with experimental results since

it was purely a study on understanding the effect of activation energy, wall boundary condition, and wall temperature on ignition. Sano and Yamashita (1994) performed thorough two-dimensional simulations of ignition in a methane-air laminar boundary layer over a horizontal hot plate. The reaction mechanism for methane-air consisted of 18 species and 61 elementary reactions. The plate consisted of a hot section placed between two cold sections. The study focused on the effects of wall temperature, flow velocity, hot plate length, and species boundary condition at the wall, i.e. (a) species concentration vanishing at the wall (reactive) and (b) zero species diffusion to the wall (inert), on ignition. Sano and Yamashita (1994) used an ignition criterion based on the peak of the methane consumption rate to determine an ignition delay time. Changing the flow velocity from 1 to 100 cm/s did not affect the ignition delay time since ignition occurred close to the wall. In addition, they found that decreasing the hot surface length led to an exponential increase in the delay time whereas increasing the length resulted in a constant delay time. Finally, to test the effect of a reactive wall, several species mass fractions were set to zero at the wall, e.g. H, O, OH, HO_2, H, CH_3, and CHO. Setting the mass fraction of CH_3 to zero at the wall resulted in a delay time 3.5 times larger than the ignition delay time calculated using an inert wall.

5.3.2 Governing equations

The problem illustrated in Fig. 5.2 is solved using the low Mach number Navier-Stokes equations. For completeness, the governing equations will be first written in the most general form then simplified for the model problem. Conservation of mass is,

$$\frac{\partial \rho}{\partial t} + \nabla \cdot (\rho \mathbf{u}) = 0, \tag{5.1}$$

where ρ is the mixture density and $\mathbf{u}$ is the velocity. The conservation of momentum,

$$\frac{\partial (\rho \mathbf{u})}{\partial t} + \nabla \cdot (\rho \mathbf{u} \otimes \mathbf{u}) = -\nabla p + \nabla \cdot \boldsymbol{\tau}, \tag{5.2}$$

where p is the hydrodynamic pressure and $\boldsymbol{\tau}$ is the deviatoric stress tensor which is defined as,

$$\boldsymbol{\tau} = \mu \left[\nabla \mathbf{u} + (\nabla \mathbf{u})^{\mathrm{T}} \right] - \frac{2}{3} \mu \left(\nabla \cdot \mathbf{u} \right) \mathrm{I}, \tag{5.3}$$

where μ is the mixture dynamic viscosity. The ideal gas thermal energy equation neglecting viscous dissipation is,

$$\begin{aligned} \frac{\partial \left(\rho T \right)}{\partial t} + \nabla \cdot \left(\rho \mathbf{u} T \right) = \nabla \cdot \left(\rho \alpha \nabla T \right) - \frac{1}{c_p} \sum_k c_{p,i} \mathbf{j}_i \cdot \nabla T + \frac{\rho \alpha}{c_p} \nabla c_p \cdot \nabla T - \\ \frac{1}{c_p} \sum_i h_i \left(T \right) \dot{\omega}_i + \frac{1}{c_p} \frac{\mathrm{D}p}{\mathrm{D}t}, \end{aligned} \tag{5.4}$$

where T is the temperature, $\alpha = \lambda / \left(\rho / c_p \right)$ is the mixture thermal diffusivity, c_p is the mixture specific heat capacity, $c_{p,i}$ is the species specific heat capacity, h_i is the species enthalpy at T, and $\dot{\omega}_i$ is the chemical source term of species i. $\mathbf{j}_i$ is the diffusive mass-flux vector given by,

$$\mathbf{j}_i = -\rho D_i \frac{Y_i}{X_i} \nabla X_i - \rho Y_i \mathbf{u}_c, \tag{5.5}$$

where D_i is the mixture averaged diffusion coefficient for species i, Y_i is the species mass fraction, X_i is the species mole fraction, and $\mathbf{u}_c = -\sum_i D_i \frac{Y_i}{X_i} \nabla X_i$ is a correction velocity that enforces zero net mass diffusion flux. The species mass conservation is written as,

$$\frac{\partial \left(\rho Y_i \right)}{\partial t} + \nabla \cdot \left(\rho \mathbf{u} Y_i \right) = -\nabla \cdot \mathbf{j}_i + \dot{\omega}_i. \tag{5.6}$$

Finally, the above equations are completed with the ideal gas law: $\rho = P_0 W / \tilde{R} T$, where P_0 is the thermodynamic pressure, W is the mixture molar weight, and $\tilde{R}$ is the universal gas constant and specification of species enthalpy as a function of temperature.

5.3.3 Simplified Equations

The Rayleigh ignition model only considers spatial variations of the scalars ρ, T, and Y_k and velocity (u, v) in the direction normal to the wall (y coordinate); therefore, all gradients in the x direction vanish. All variables are a function of time. This leads to the following simplified set of equations. Conservation of mass is written as,

$$\frac{\partial \rho}{\partial t} + \frac{\partial (\rho v)}{\partial y} = 0. \tag{5.7}$$

The simplified momentum equations in the $x-$direction (Eq. 5.8) and $y-$direction (Eq. 5.9) are,

$$\frac{\partial (\rho u)}{\partial t} + \frac{\partial (\rho u v)}{\partial y} = \frac{\partial}{\partial y}\left(\mu \frac{\partial u}{\partial y}\right) \tag{5.8}$$

$$\frac{\partial (\rho v)}{\partial t} + \frac{\partial \left(\rho v^2\right)}{\partial y} = -\frac{\partial p}{\partial y} + \frac{4}{3}\frac{\partial}{\partial y}\left(\mu \frac{\partial v}{\partial y}\right) \tag{5.9}$$

Combining the mass and momentum equations (Eqs. 5.7, 5.8, and 5.9) results in the following equations for conservation of momentum in the $x-$direction,

$$\rho\left(\frac{\partial u}{\partial t} + v\frac{\partial u}{\partial y}\right) = \frac{\partial}{\partial y}\left(\mu \frac{\partial u}{\partial y}\right) \tag{5.10}$$

and conservation of momentum in the $y-$direction,

$$\rho\left(\frac{\partial v}{\partial t} + v\frac{\partial v}{\partial y}\right) = -\frac{\partial p}{\partial y} + \frac{4}{3}\frac{\partial}{\partial y}\left(\mu \frac{\partial v}{\partial y}\right). \tag{5.11}$$

The ideal gas thermal energy equation is written as,

$$\begin{aligned}\frac{\partial (\rho T)}{\partial t} + \frac{\partial (\rho v T)}{\partial y} = \frac{\partial}{\partial y}\left(\rho\alpha \frac{\partial T}{\partial y}\right) - \frac{\rho}{c_p}\sum_k c_{p_i}\left(Y_i v_i - Y_i \sum_k Y_i v_i\right)\frac{\partial T}{\partial y} \\ + \frac{\rho\alpha}{c_p}\frac{\partial c_p}{\partial y}\frac{\partial T}{\partial y} - \frac{1}{c_p}\sum_i h_i(T)\,\dot{\omega}_i + \frac{1}{c_p}\frac{\mathrm{D}p}{\mathrm{D}t}\end{aligned} \tag{5.12}$$

where $v_i = -\frac{D_i}{X_i}\frac{\partial X_i}{\partial y}$ and $\frac{\mathrm{D}}{\mathrm{D}t} = \frac{\partial}{\partial t} + \mathbf{u}\cdot\nabla$ is the convective or substantial derivative. Combining Eq. 5.7 with Eq. 5.12 leads to,

$$\rho\left(\frac{\partial T}{\partial t} + v\frac{\partial T}{\partial y}\right) = \frac{\partial}{\partial y}\left(\rho\alpha\frac{\partial T}{\partial y}\right) - \frac{\rho}{c_p}\sum_i c_{p_i}\left(Y_i v_i - Y_i\sum_i Y_i v_i\right)\frac{\partial T}{\partial y} + \frac{\rho\alpha}{c_p}\frac{\partial c_p}{\partial y}\frac{\partial T}{\partial y} - \frac{1}{c_p}\sum_i h_i(T)\,\dot{\omega}_i + \frac{1}{c_p}\frac{\mathrm{D}p}{\mathrm{D}t} \tag{5.13}$$

Finally, species mass conservation is,

$$\frac{\partial(\rho Y_i)}{\partial t} + \frac{\partial(\rho v Y_i)}{\partial y} = \frac{\partial}{\partial y}\left(\rho Y_i v_i - \rho Y_i\sum_i Y_i v_i\right) + \dot{\omega}_i. \tag{5.14}$$

Combining Eq. 5.7 with Eq. 5.14 leads to,

$$\rho\left(\frac{\partial Y_i}{\partial t} + v\frac{\partial Y_i}{\partial y}\right) = \frac{\partial}{\partial y}\left(\rho Y_i v_i - \rho Y_i\sum_i Y_i v_i\right) + \dot{\omega}_i. \tag{5.15}$$

5.3.4 Initial and Boundary Conditions

The evolution of the thermal boundary layer is initiated by impulsively applied boundary conditions. The boundary conditions along y, normal to the wall, are as follows:

$$\begin{gathered} y = 0 \text{ and } t > 0 : u = 0, v = 0, T = T_{\text{wall}}, \frac{\partial Y_i}{\partial y} = 0 \\ y \to \infty \text{ and } t > 0 : u = U_\infty, \frac{\partial v}{\partial y} = 0, T = T_\infty, Y_i = Y_{i_\infty}, \\ p = p_\infty, \rho = \rho_\infty, \end{gathered} \tag{5.16}$$

and the initial conditions are:

$$t = 0 : u = U_\infty, v = 0, T = T_\infty, Y_i = Y_{i_\infty}, \text{ for } 0 \le y < \infty, \tag{5.17}$$

where T_{wall} is the wall temperature, T_∞, U_∞, and $Y_{i\infty}$ are the freestream temperature, velocity, and species k mass fractions, respectively. The wall temperature is varied

from 940 K to 1200 K for hydrogen-air mixtures and 1150 K to 1600 K for n-hexane-air mixtures. The $x-$direction momentum equation, Eq. 5.10, is decoupled from Eqs. 5.7, 5.11, 5.13, and 5.15; therefore the value of the freestream velocity U_∞ will not influence the solutions except for u itself. For the cases presented in this chapter, the freestream velocity is set to 0 m/s so that only the thermal boundary layer problem is considered. Sano and Yamashita (1994) accounted for spatial variations in the x and y directions and found that the solution was insensitive to the freestream velocity in the range of 0.1 to 10 m/s.

5.3.5 Numerical Solution

The structured, multi-physics and multi-scale finite difference code NGA (Desjardins et al., 2008) is used to solve the equations described in Section 5.3.2. NGA uses spatially staggered variables such that scalar quantities and velocity components are stored at the volume centers and volume faces, respectively. The time integration is performed using a second-order semi-implicit Crank-Nicolson scheme.

5.3.5.1 Convergence Test

Due to the stiffness of the equations, integrations steps on the order of the characteristic chemical time scale are used. To determine the appropriate time step, the ignition delay time was examined as a function of the time step. In the current context the ignition delay time is defined as the simulation time from $t = 0$ to the the time instant when the gas temperature reaches 150 K over the wall temperature. Figure 5.3 shows that the ignition delay time reached a constant value for integration time steps Δt less than 10^{-7} s. Based on this study, all solutions shown in the chapter were obtained using $\Delta t = 10^{-7}$ s. A stretched grid was used, with a higher density of points near the wall to resolve the boundary layer. The choice of grid parameters needed to obtain grid independence was verified through trial simulations. A domain of 40 mm yielded 720 points with spacing of 1 μm at the wall.

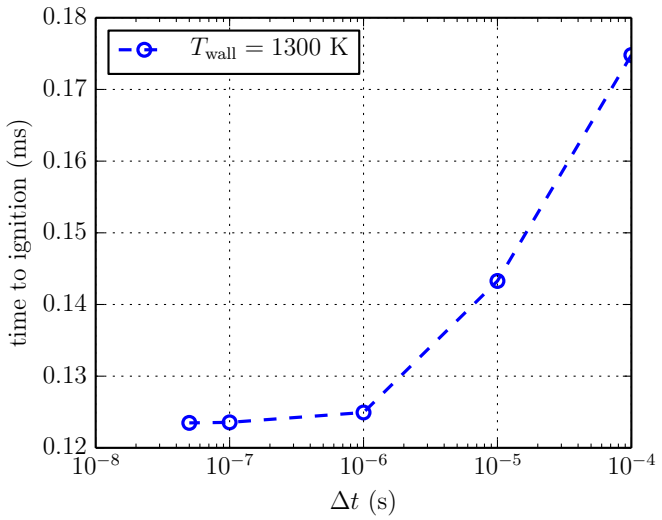

Figure 5.3: Effect of Δt on the ignition delay time of a stoichiometric hydrogen-air mixture at an initial temperature and pressure of 300 K and 100 kPa, respectively, $T_{\text{wall}} = 1300$ K.

5.3.5.2 Chemical Models

Two detailed chemical reaction models are used in the simulations, a hydrogen-air mechanism from Mével et al. (2009a) which consists of 9 species and 21 reactions and a n-hexane-air mechanism (62 species, 226 reactions) reduced from the mechanism described in Mével et al. (2014) using the methods of Davidenko et al. (2009). The species thermal conductivities λ_i are computed using Eucken's formula (Eucken, 1913), and the mixture-averaged thermal conductivity λ is obtained from the empirical formula (Mathur et al., 1967):

$$\lambda = 0.5 \left(\sum_{i=1}^{N} X_i \lambda_i + \frac{1}{\sum_{i=1}^{N} X_i / \lambda_i} \right) \tag{5.18}$$

The species viscosities, μ_i, are calculated using standard gas kinetic theory (Hirschfelder et al., 1954). The mixture-averaged viscosity, μ, is calculated using Wilke's mixture

rule (Wilke, 1950):

$$\mu = \sum_{i=1}^{N} \frac{X_i \mu_i}{\sum_{j=i}^{N} X_j \Phi_{ij}} \tag{5.19}$$

where

$$\Phi_{ij} = \frac{1}{\sqrt{8}} \left(1 + \frac{W_i}{W_j}\right)^{\frac{1}{2}} \left(1 + \left(\frac{\mu_i}{\mu_j}\right)^{\frac{1}{2}} \left(\frac{W_j}{W_i}\right)^{\frac{1}{4}}\right)^2 . \tag{5.20}$$

The individual species molecular diffusivities, D_i, are calculated using the following relation,

$$D_i = \alpha / Le_i, \tag{5.21}$$

where Le_i are the species Lewis numbers. In the simulations, the Lewis numbers are treated as constant but non-unity.

5.4 Hydrogen-Air Simulations

The hydrogen-air simulations are performed at an equivalence ratio of 1.0 and at an initial temperature and pressure of 300 K and 100 kPa, respectively. Figure 5.4 shows filled contours of temperature and a black contour line at 303 K to illustrate the evolution of the thermal boundary layer, the ignition, and the subsequent flame propagation; the wall temperatures are 940 K and 1200 K.

The flame location is indicated by the sudden temperature increase starting within the boundary layer and rapidly moving outside. The flame propagates quickly within the boundary layer due to the initial high gas temperatures that are present, and continues to propagate at a lower velocity once outside, shown in Fig. 5.4 (b). The flame speed (as indicated by the slope of the flame location) shown in Fig. 5.4 (a) appears drastically larger than the flame speed in Fig. 5.4 (b) due to the time scale difference of each figure, $\sim 10^2$ ms in Fig. 5.4 (a) and $\sim 10^{-1}$ ms in Fig. 5.4 (b). In this model problem, the flame can only propagate in the y direction; in the experiments or multidimensional models, the flame will propagate outward at different speeds and directions.

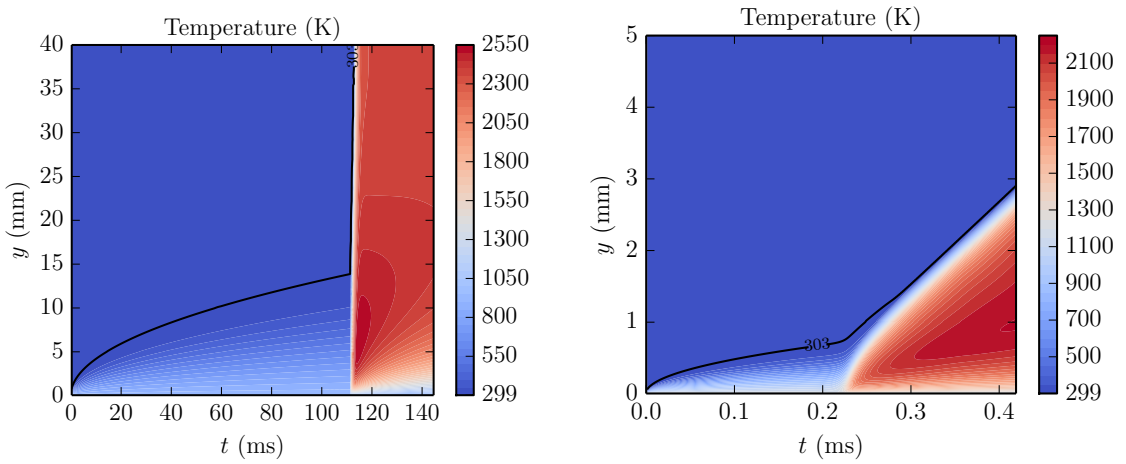

(a) $T_{\text{wall}} = 940$ K (b) $T_{\text{wall}} = 1200$ K

Figure 5.4: Temporal evolution of the thermal boundary layer and the subsequent ignition and flame propagation for (a) $T_{\text{wall}} = 940$ K and (b) $T_{\text{wall}} = 1200$ K.

In the present study, ignition is defined as the time and location when and where the gas temperature is 150 K higher than the wall temperature. This occurs at approximately 111.6 ms, 200 μm away from the wall for $T_{\text{wall}} = 940$ K and 0.2261 ms, 55 μm away from the wall for $T_{\text{wall}} = 1200$ K. A different ignition criterion will yield slightly different but very similar results given that the ignition event occurs over a short duration compared to the boundary layer development time up to that point. Figure 5.5 shows a close up of the onset of a flame within the thermal boundary layer, the ignition location is shown by the black filled circle. Note that ignition does not occur at the wall, where the gas temperature is highest prior to any significant heat release; this is because heat losses due to diffusion are highest near the wall, similar to the results of Melguizo-Gavilanes et al. (2016c). This is one of the important insights obtained from detailed models of processes within the boundary layer. At ignition, the thickness of the thermal boundary layer is approximately 15 mm in Fig. 5.4 (a) and less than 1 mm in Fig. 5.4 (b).

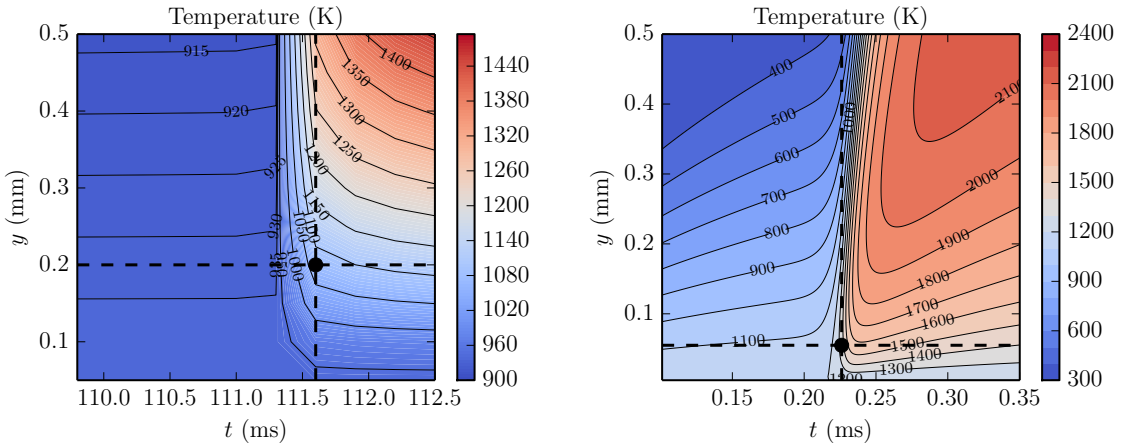

(a) $T_{\text{wall}} = 940$ K (b) $T_{\text{wall}} = 1200$ K

Figure 5.5: Enlarged view of graphs shown in Fig. 5.4 with the ignition location (black dot) as determined by the 150 K temperature rise.

5.4.1 Analysis of $T_{\text{wall}} = 1200$ K Case

This subsection contains analysis of the energy and species equations along several fluid parcel trajectories. The fluid parcel trajectory is based on the temporal displacement in y of a fluid parcel that is at y_0 at $t = 0$ seconds. The significant displacement of the fluid parcel is due to the positive v normal velocity component that is induced by expansion of the gas due to the increase in temperature in the boundary layer. The pressure is approximately constant so that density is inversely proportional to temperature ($\rho = P/RT$). Figure 5.6 (top) shows the ignition location (red filled circle) relative to two fluid parcel trajectories (black lines); the respective temperature profiles for these fluid parcels are shown in Fig. 5.6 (bottom). The fluid parcels originate at 15 and 20 μm and are displaced to 43 mm and 62 μm prior to ignition, which is a displacement of approximately 3 times the initial fluid parcel location. Based on these trajectories, the conclusion is that a fluid parcel that originates at $15 - 20$ μm away from the wall ignites and initiates the flame. The ignition event is marked by the sudden expansion of gases due to the temperature increase (shown in Fig. 5.6 (bottom)), which rapidly pushes the fluid parcels even further away from the wall; this can be observed in Fig. 5.6 (top) by the rapid displacement of the trajectories at

0.23 ms.

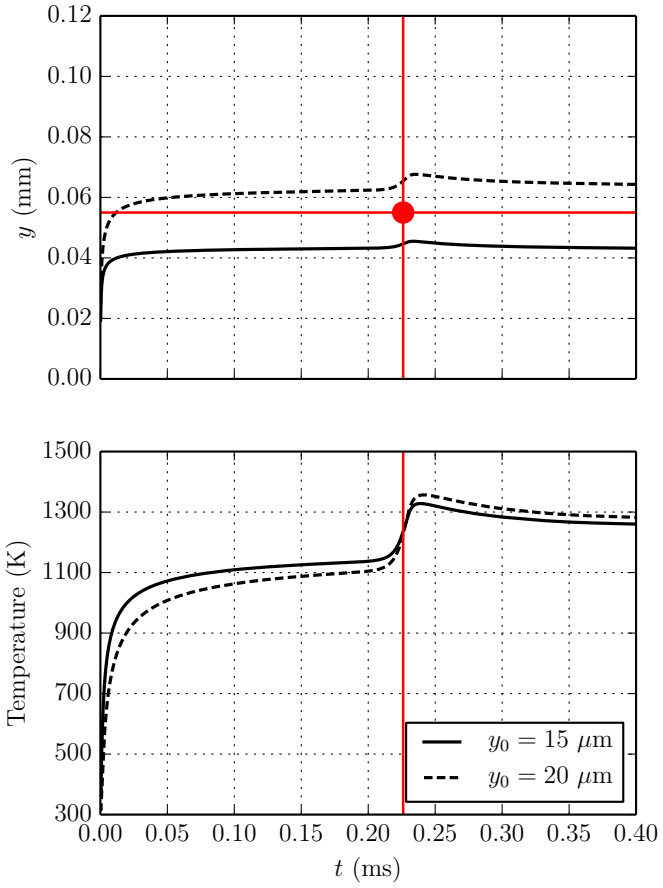

Figure 5.6: Trajectory (top) and temperature (bottom) of two fluid parcels originating at $y_0 = 15$ μm (——) and $y_0 = 20$ μm (-----); $T_{\text{wall}} = 1200$ K.

5.4.1.1 Thermal Energy Equation Analysis Along Fluid Parcel Paths

To obtain further insight into the processes leading to ignition, the major terms[8] in the thermal energy equation, Eq. 5.13, are computed along the fluid parcel path ($y_0 = 15$ μm) shown in Fig. 5.6 (top). The major terms, unsteady $= \partial_t (\rho T) + \nabla \cdot (\rho \mathbf{u} T)$, thermal diffusion $= \nabla \cdot (\rho \alpha \nabla T)$, and energy (heat) release $= -\frac{1}{c_p} \sum_i h_i (T) \dot{\omega}_i$ are shown in Fig. 5.7 (top); the fluid parcel path temperature profile is shown in Fig. 5.7 (bottom). The sum of the unsteady and convection terms is equivalent to

[8]The other terms in Eq. 5.13 were evaluated and found to be negligible in comparison to the terms shown.

the convective or Lagrangian derivative $\frac{\mathrm{D}(\rho T)}{\mathrm{D}t}$ representing the time rate of change following a given parcel of gas.

Initially, thermal diffusion balances the unsteady term. Following the initial unsteady period ($0 < t < 0.05$ ms), the temperature remains approximately constant until the ignition event begins at 0.20 ms. During this induction period, chain-branching chemical reactions are taking place leading to the ignition event marked by the rapid energy release between 0.2 and 0.25 ms. During the ignition event, the chemical energy release results in a further temperature increase due to the unsteadiness and after 0.23 ms the energy release is balanced by thermal diffusion.

The peak temperature following ignition is due to a combination of heating by thermal diffusion from the hot wall, the temperature rise due to combustion and thermal diffusion losses to the surrounding gas following the ignition transient. The temperature rise at the time of ignition is quite modest for trajectories near the wall; for the fluid parcel shown in Fig. 5.6, the rise is about 200 K. This can be compared to an adiabatic, constant-pressure temperature rise of 2325 K for a gas temperature of 940 K and 2427 for a gas temperature of 1200 K. The very low temperature rise during the ignition event demonstrates the significance of thermal and species diffusion and as discussed later, consumption of fuel prior to the ignition event. Outside the boundary layer, the peak temperature approaches the adiabatic value of 2302 K behind the flame propagating into cold gas (see Fig. 5.4).

5.4.1.2 Species Mass Fractions Along Fluid Parcel Path

Figures 5.8 and 5.9 show the evolution of major and minor species mass fractions along the trajectory of a fluid parcel originating at $y_0 = 15$ μm. The figures also show the species mass fractions obtained with Fig. 5.22 which neglects species diffusion and convection. The computed fluid parcel temperature profile $T(t)$ is used to calculate the chemical source term, $\dot{\omega}_i$, of each species at the fluid parcel temperature; the source term is then used in Eq. 5.22 to calculate the temporal evolution of each species mass fraction assuming a constant pressure reactor with no diffusive species

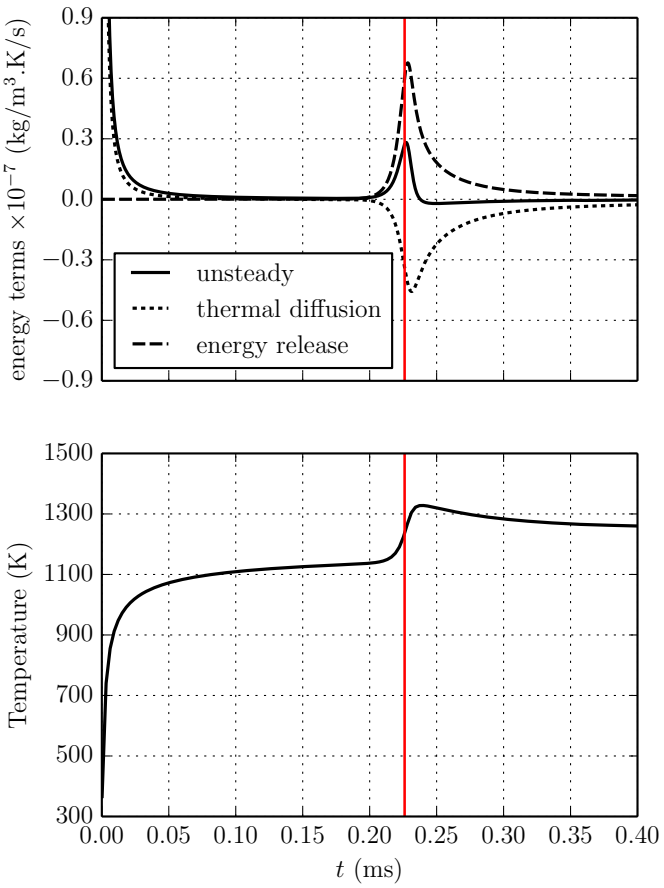

Figure 5.7: Contribution of each term in thermal energy equation along fluid parcel trajectory ($y_0 = 15$ μm) shown in Fig. 5.6 for hydrogen-air and $T_{\text{wall}} = 1200$ K (top) and temperature history along trajectory (bottom).

transport; the species equation is,

$$\frac{\mathrm{d}Y_i}{\mathrm{d}t} = \frac{\dot{\omega}_i \left(T\left(t\right), Y_1, Y_2, ...\right)}{\rho}. \tag{5.22}$$

A comparison of the one-dimensional (1D) and zero-dimensional (0D) species mass fractions show the effect of species diffusion and convection on ignition. Figures 5.8 and 5.9 show the major and minor species, respectively, as well as the temperature profile (red) along the fluid parcel path. Initially, both models show no significant chemical activity for temperatures below 1100 K. The 0D results in Fig. 5.9 (top) show an increase in the hydroperoxyl radical (HO_2) at 0.075 ms leading to a spike

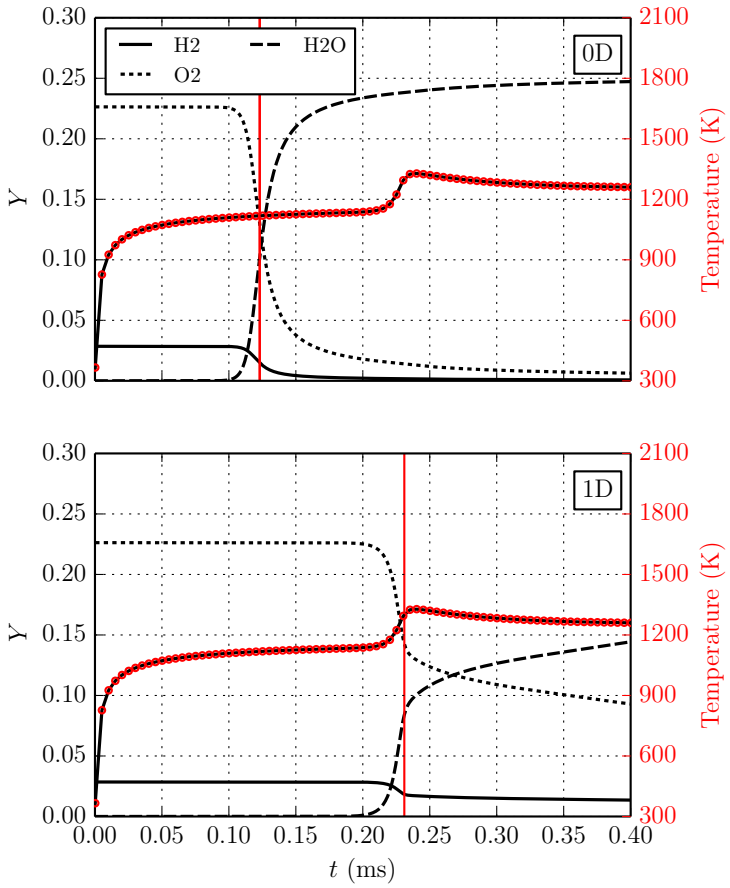

Figure 5.8: Major species mass fractions along fluid parcel trajectory using 0D (top) and 1D (bottom) models; the fluid parcel originates at a distance $y_0 = 0.015$ mm from the wall; the fluid parcel temperature (computed according to the 1D model) is given by the red markers and its corresponding ordinate is on the right of each figure.

in H, O, and OH at 0.124 ms (marked by the red vertical line). The 1D results (see Fig. 5.9 (bottom)) indicate no chemical activity for temperatures up to 1100 K, and at approximately 0.17 ms, significant accumulation of HO_2 commences and begins to decay prior to ignition (marked by the red vertical line).

The decay of HO_2 is due to its consumption to generate active species H, O, and OH, as well reactions with itself to generate hydrogen peroxide (H_2O_2). The two figures indicate that due to heat and species diffusion, there is a 47% increase in the time to OH peak (ignition criterion) in the 1D results when compared to the 0D calculations. The results show that species diffusion plays a significant role in

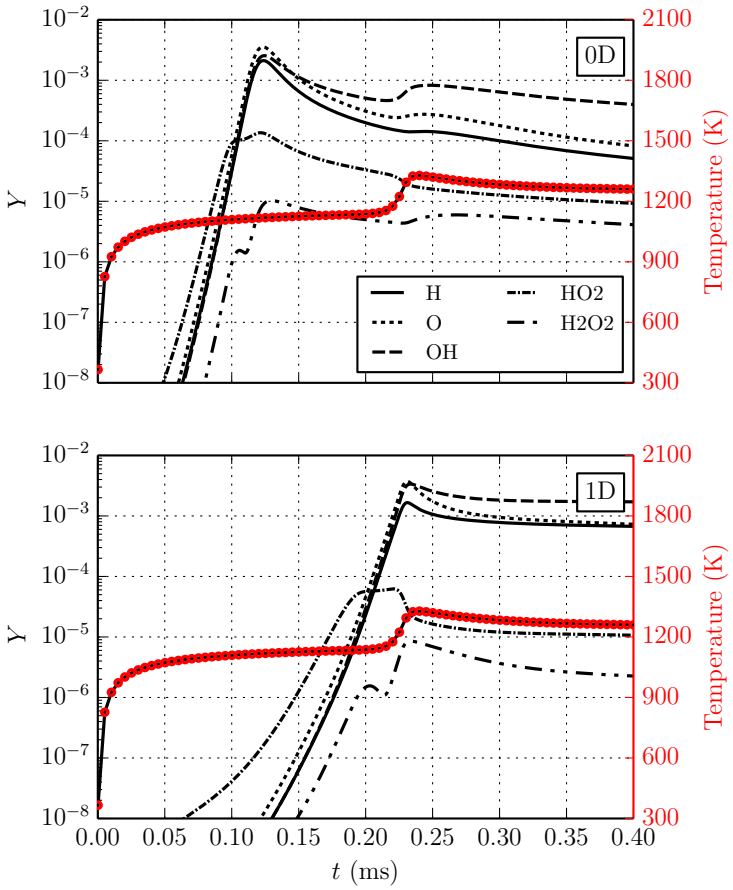

Figure 5.9: Minor species mass fractions along fluid parcel trajectory using 0D (top) and 1D (bottom) models; the fluid parcel originates at a distance $y_0 = 0.015$ mm from the wall; the fluid parcel temperature (computed according to the 1D model) is given by the red markers and its corresponding ordinate is on the right of each figure.

delaying the buildup of radicals and onset of recombinations that characterize the ignition event.

5.5 *n*-Hexane-Air Simulations

This section describes the simulations performed with n-hexane-air at $\Phi = 0.9$ and an initial temperature and pressure of 300 K and 100 kPa, respectively, similar to the experimental conditions described in Chapter 4. The main purpose of this section is to explore the differences between hydrogen and hexane fuels as well as examine

the ignition processes at low and high temperature cases. As done previously for the hydrogen case, the variations in temperature of various fluid parcels are analyzed as a function of time. Figure 5.10 shows filled contours of temperature and a contour line at 303 K to illustrate the evolution of the thermal boundary layer, the ignition, and the subsequent flame propagation; the wall temperatures are 1150 K and 1400 K.

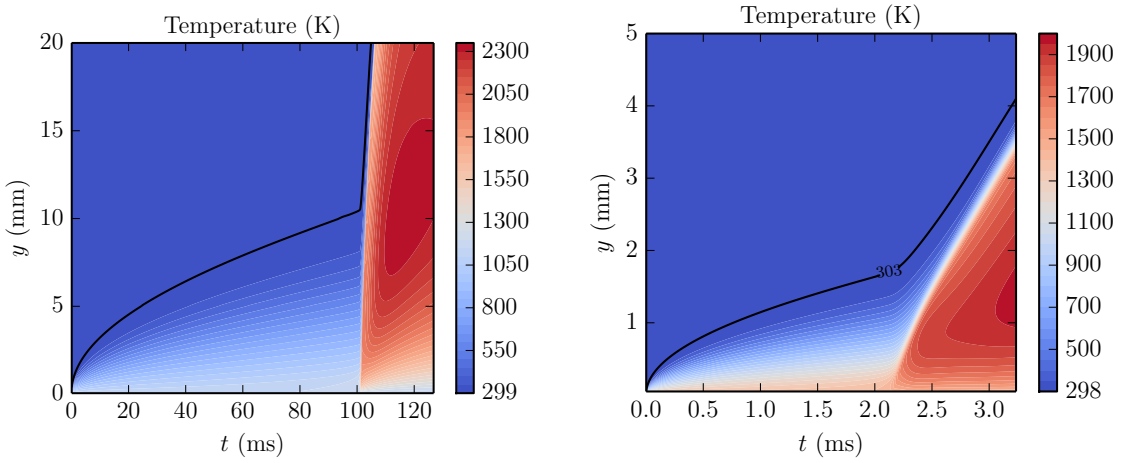

(a) $T_{\text{wall}} = 1150$ K (b) $T_{\text{wall}} = 1400$ K

Figure 5.10: Temporal and spatial evolution of the thermal boundary layer and the subsequent ignition and flame propagation in n-hexane-air at $\Phi = 0.9$ and an initial temperature and pressure of 300 K and 100 kPa, respectively, for (a) $T_{\text{wall}} = 1150$ K and (b) $T_{\text{wall}} = 1500$ K.

The results are very similar to what was found for the hydrogen cases. A flame originates deep within the boundary layer and propagates outward into the cold surrounding gas. The flame is indicated by the thin layer of sudden temperature increase. Ignition occurs at approximately 101 ms, 550 μm away from the wall for $T_{\text{wall}} = 1150$ K, and at 2 ms, 200 μm away from the wall for $T_{\text{wall}} = 1400$ K. At ignition, the thickness of the thermal boundary layer is approximately 10 mm in Fig. 5.10 (a) and over 1 mm in Fig. 5.10 (b).

Figure 5.11 shows the trajectory of the flame front for $T_{\text{wall}} = 1150$ K and its corresponding flame propagation speed, S_b. The approximate flame front trajectory is extracted from the temperature field shown in Fig. 5.10 (a) by locating the (t, y)

points where $T = 1300$ K. The flame front locations are shown in Fig. 5.11 (a) as well as a 5^{th} order polynomial fitted curve. Numerical differentiation is performed on the raw and smooth data to obtain the flame speed shown in Fig. 5.11 (b). Initially, the flame speed is over 5.5 m/s while the flame is still within the thermal boundary layer, and it drops to 4 m/s as it starts exiting the thermal boundary layer and continues to drop as the flame starts propagating into the cold reactants. The drop in flame speed from 5.5 to 2 m/s is caused by the temperature decrease in the gas from a temperature close to T_{wall} to 300 K outside of the thermal boundary layer. As mentioned in Chapter 4, the experimental flame speed for n-hexane-air at $\Phi = 0.9$ and an initial temperature and pressure of 298 K and 100 kPa, respectively, is 2.6 m/s.

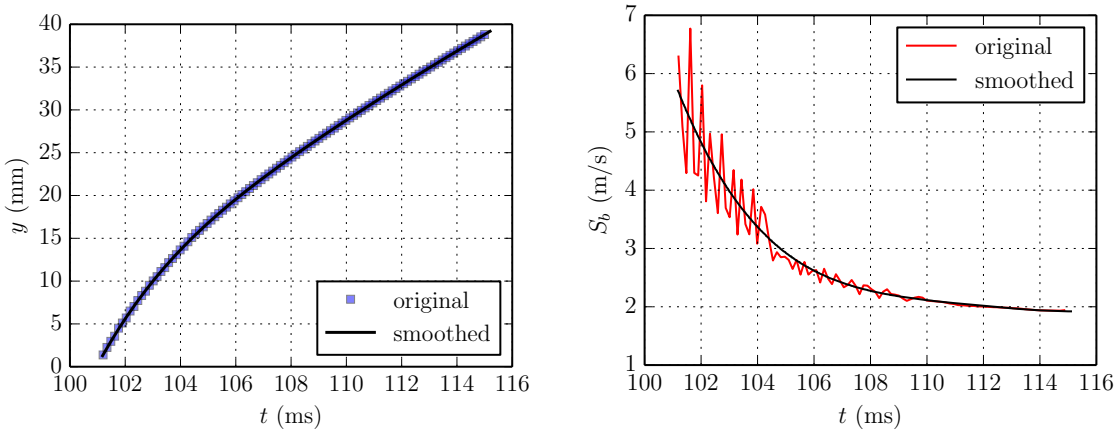

(a) Flame front (b) Flame speed

Figure 5.11: Flame front defined by an isocontour at $T = 1300$ K and the corresponding flame speed as the flame propagates within and outside the thermal boundary layer for $T_{\text{wall}} = 1150$ K.

5.5.1 Temperature and Species Mass Fractions along Fluid Parcel Paths

Figures 5.12, 5.13, and 5.14 show the evolution of species products and reactants, and intermediates along selected fluid parcel paths ($y_0 = 150$ μm) for the two temperature cases, $T_{\text{wall}} = 1150$ and 1400 K, respectively.

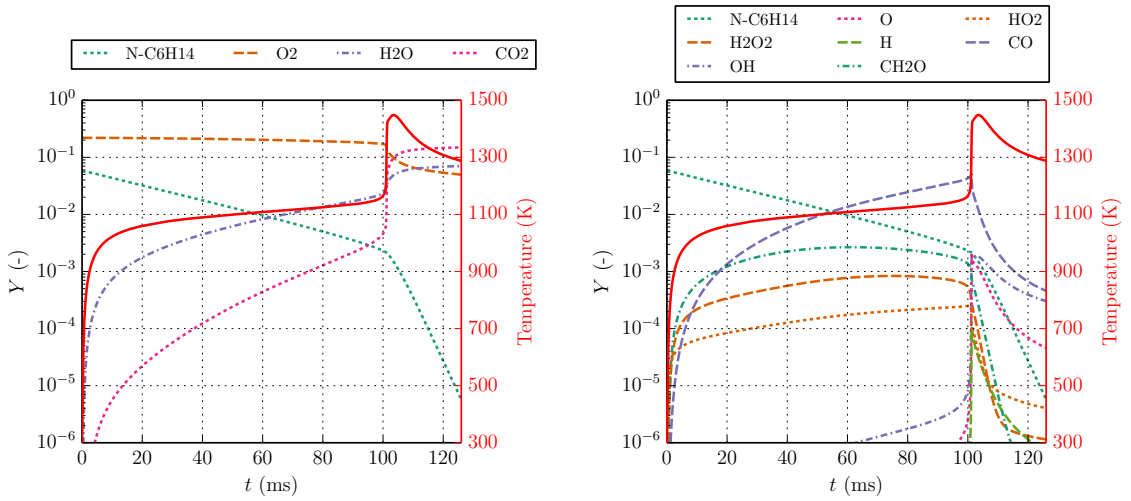

(a) Reactants and products (b) Intermediate species and radicals

Figure 5.12: Species mass fractions and temperature along fluid parcel path ($y_0 = 150$ μm) for $T_{\text{wall}} = 1150$ K case using n-hexane-air at $\Phi = 0.9$ and an initial temperature and pressure of 300 K and 100 kPa, respectively.

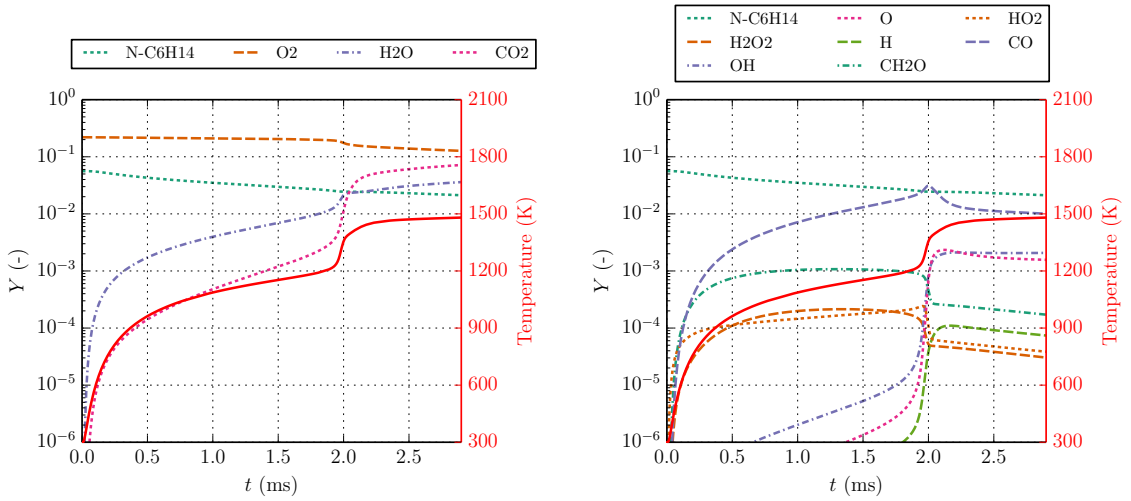

(a) Reactants and products (b) Intermediate species and radicals

Figure 5.13: Species mass fractions and temperature along fluid parcel path ($y_0 = 150$ μm) for $T_{\text{wall}} = 1400$ K case using n-hexane-air at $\Phi = 0.9$ and an initial temperature and pressure of 300 K and 100 kPa, respectively.

Figure 5.12 (a) shows that there is initially a linear depletion (log scale) of the fuel to 2.31×10^{-3} at 100 ms, after this time it is rapidly consumed. Prior to rapid consumption of the fuel, there is minimal decrease in O_2 indicating that the fuel is

being pyrolized to make smaller fuel components. A similar trend in the fuel and oxidizer is observed for the higher wall temperature case shown in Fig. 5.13 (a); however, the depletion of the fuel prior to rapid consumption stops at 2.0 ms; at 2.0 ms, the fuel mass fraction is 2.47×10^{-2}, and order of magnitude larger than the low temperature case fuel mass fraction prior to ignition. Small amounts of H_2O_2 and HO_2, shown in Fig. 5.13 (b) and Fig. 5.13 (b), are created until they are consumed to produce O, H, and OH in the ignition event.

The unimolecular decomposition of the three isomeric forms of the $\dot{\mu}$ radical (C_6H_{13}) which are produced by H abstraction, lead to the creation of several fuels: ethylene (C_2H_4), methane (CH_4), propene (C_3H_6), ethane (C_2H_6), 1-butene (C_4H_8-1), and 1-pentene (C_5H_{10}-1), as well as small amounts of H_2 (Malacarne et al., 1987). In Fig. 5.14 (a), a significant amount of C_2H_4 (1%) is produced at 30 ms until it peaks at 1.4% at approximately 65 ms.

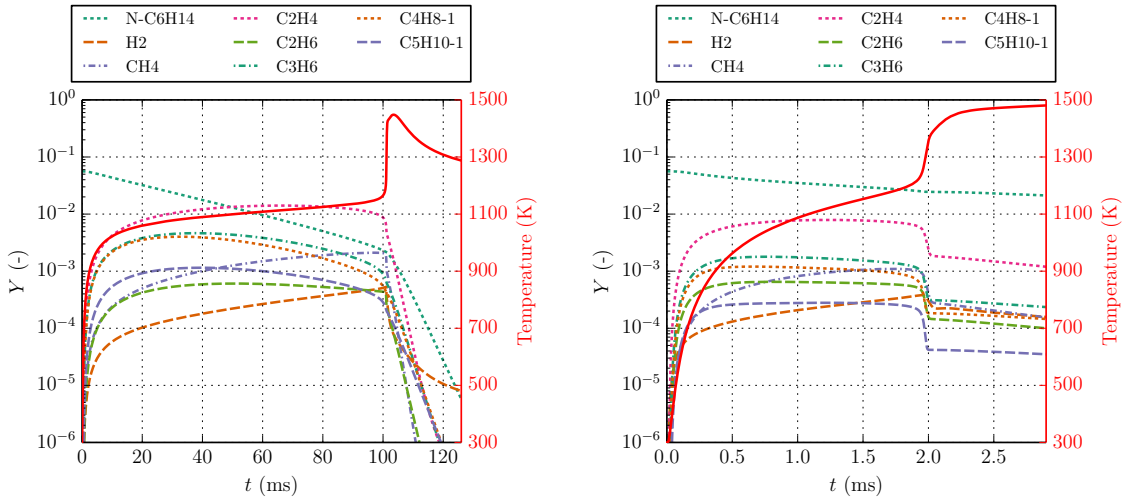

(a) $T_{\text{wall}} = 1150$ K (b) $T_{\text{wall}} = 1400$ K

Figure 5.14: Secondary fuels mass fractions and temperature along fluid parcel path ($y_0 = 150$ μm) prior to ignition for (a) $T_{\text{wall}} = 1150$ K and (b) $T_{\text{wall}} = 1400$, using n-hexane-air at $\Phi = 0.9$ and an initial temperature and pressure of 300 K and 100 kPa, respectively.

The C_6H_{14} mass fraction falls continuously, going below 1% at approximately 60 ms. The mass fraction of CH_4 continues to rise until it is consumed during the

ignition event at approximately 100 ms. A similar pattern is observed in Fig. 5.14 (b); however, lower amounts of the secondary fuel mass fractions are created since the decomposition of C_6H_{14} (approximately 2.5%) is not as extensive as shown in Fig. 5.14 (a). For example, prior to ignition, the C_2H_4 mass fraction is 8.75×10^{-3} and 5.44×10^{-3} for $T_{\text{wall}} = 1150$ and $T_{\text{wall}} = 1400$ K, respectively.

Table 5.1 shows the mass fractions of the fuel components prior to ignition for the two temperature cases. Substantial amounts ($\sim 10^{-3}$) of CH_4 and C_2H_4 are both created in the low temperature case while C_2H_4 is the largest fuel component created in the high temperature case. Smaller amounts ($\sim 10^{-4}$) of H_2, C_2H_6, C_3H_6, C_4H_8-1, and C_5H_{10}-1 are also created. For all the fuels except CH_4 the mass fractions are lower in the high temperature case since the fuel only has 2 ms to decompose as opposed to 100 ms in the low temperature case. The lower ignition delay time more than offsets the higher decomposition fuel rates associated with the high temperature case.

Species	$Y \times 10^2$	
	1150 K	1400 K
n-C_6H_{14}	0.231	2.47
H_2	0.0509	0.0380
CH_4	0.207	0.0912
C_2H_4	0.875	0.544
C_2H_6	0.0438	0.0438
C_3H_6	0.0899	0.0914
C_4H_8-1	0.0554	0.0163
C_5H_{10}-1	0.0288	0.0163

Table 5.1: Mass fractions of n-C_6H_{14} and secondary fuels for $T_{\text{wall}} = 1150$ K and $T_{\text{wall}} = 1400$ K cases just prior to the ignition event. Values are given for the fluid parcels shown in Fig. 5.14.

5.5.2 Temporal and Spatial Evolution of Temperature and Species Mass Fractions

This section analyzes the temporal and spatial evolution of OH, C_6H_{14}, and C_2H_4, as well as the ignition location relative to the wall for $T_{\text{wall}} = 1150$ and 1400 K.

Before giving results for boundary layers, the structure of laminar flames will be given as a point of reference. The computed steady, laminar flame structure of a n-hexane-air flame at $\Phi = 0.9$ and initial temperatures, T_0, of 300 K and 800 K, shown in Figs. 5.15 and 5.16. The values of T_0 were chosen to represent gas temperature values outside and within the boundary layer. The structures are obtained using a one-dimensional freely-propagating flame in Cantera (Goodwin, 2003) using the JetSurF chemical mechanism (Wang et al., 2010).

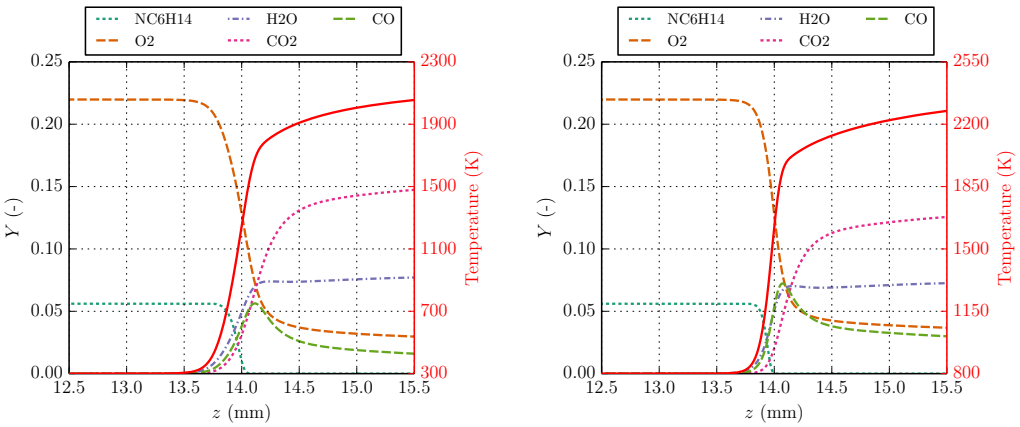

(a) $T_0 = 300$ K $\qquad$ $T_0 = 800$ K

Figure 5.15: Stucture of $\Phi = 0.9$ n-hexane-air flame propagating into reactants at an initial pressure of 100 kPa and initial temperatures of (a) $T_0 = 300$ K and (b) $T_0 = 800$ K; the reactants, products, and CO mass fractions are shown along with the flame temperature (red solid line); the $z-$coordinate is normal to the flame front.

A graphical representation of the flame thickness determined from the temperature profiles is shown in Fig, 5.17. A tangent, shown by the diagonal red dashed line, is placed at the location where $\mathrm{d}T/\mathrm{d}z$ is maximum, the locations where the tangent intersects with the horizontal lines, shown by the red dashed lines, at the unburned temperature, T_u, of 300 K and the burned temperature, T_b, mark the edges of the flame thickness, l_F, shown by the blue shaded region. Based on Fig. 5.17, the flame thickness is 0.37 mm and 0.34 mm for $T_0 = 300$ and 800 K, respectively. Note that these thicknesses are comparable to the location of the ignition region relative to the wall in the examples shown in Fig. 5.10

The reactants and major product species, including CO, are shown in Fig. 5.15,

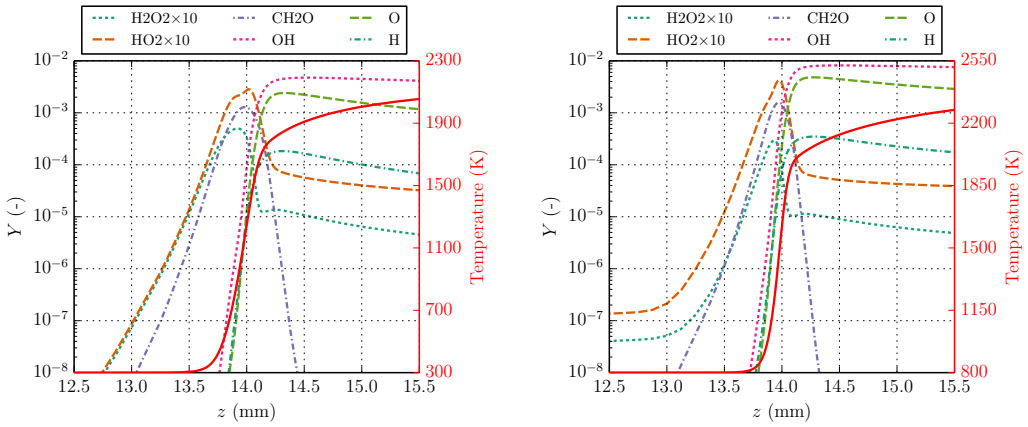

(a) $T_0 = 300$ K $T_0 = 800$ K

Figure 5.16: Stucture of $\Phi = 0.9$ n-hexane-air flame propagating into reactants at an initial pressure of 100 kPa and initial temperatures of (a) $T_0 = 300$ K and (b) $T_0 = 800$ K; the radicals and intermediates species mass fractions are shown along with the flame temperature (red solid line); the $z-$coordinate is normal to the flame front.

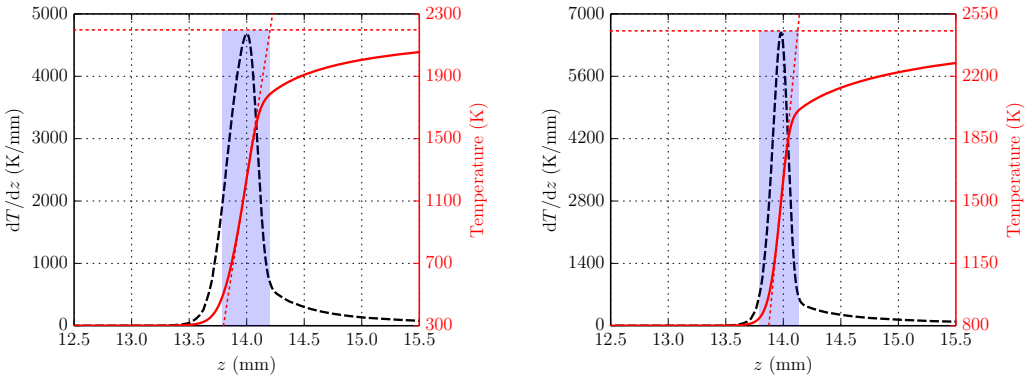

(a) $T_0 = 300$ K (b) $T_0 = 800$ K

Figure 5.17: Graphical representation of the flame thickness obtained for a $\Phi = 0.9$ n-hexane-air flame propagating into reactants at an initial pressure of 100 kPa, and initial temperatures of (a) 300 K and (b) 800 K; the $z-$coordinate is normal to the flame front.

the radicals and intermediate species are shown in Fig. 5.16, and the secondary fuels are shown in Fig. 5.18. A few key features are noted for this particular mixture and composition. First, Fig. 5.15 shows that, due to the lean condition of the mixture, not all of the O_2 is consumed after it has reacted with the fuel; the O_2 drops to a mass fraction of $3 - 4 \times 10^{-2}$ after going through the reaction zone. In addition,

Fig. 5.16 shows that the main radical created is OH, which peaks at a mass fraction of 4.8×10^{-3} and 8×10^{-3} for $T_0 = 300$ and 800 K, respectively. Finally, Fig. 5.18 shows that the main secondary fuel component created is C_2H_4, which peaks at a mass fraction of 8×10^{-3} and 1.3×10^{-2} for the lower and higher initial temperature cases, respectively. The half-maximum, full-width of the C_2H_4 distribution is 0.17 mm and 0.12 mm for $T_0 = 300$ K and 800 K, respectively, roughly 1/3 of the width of the flame as determined in Fig. 5.17.

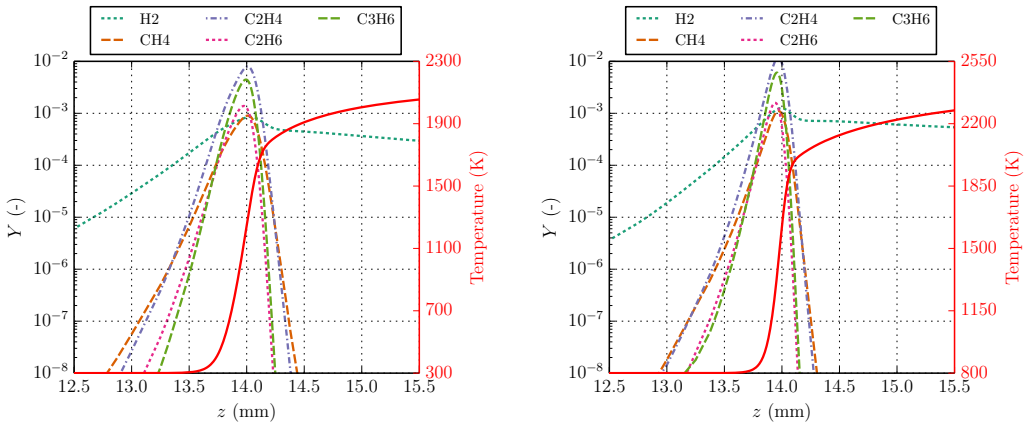

(a) $T_0 = 300$ K $\qquad$ $T_0 = 800$ K

Figure 5.18: Stucture of $\Phi = 0.9$ n-hexane-air flame propagating into reactants at an initial pressure of 100 kPa and initial temperatures of (a) $T_0 = 300$ K and (b) $T_0 = 800$ K; the secondary fuels species mass fractions are shown along with the flame temperature (red solid line); the $z-$coordinate is normal to the flame front.

5.5.2.1 Temperature and Species Profiles in the Boundary Layer with $T_{\mathbf{wall}} = 1150$ K

Figure 5.19 shows the temperature profiles at different times, leading up to ignition for a wall temperature of 1150 K. Figure 5.19 (a) shows thermal energy diffusing away from the hot wall; after 100 ms, the thermal boundary layer grows to a thickness of approximately 10 mm. At 100.1 ms there is a temperature increase a distance of 0.55 mm away from the wall, this location is where the ignition event originates. Over the next 2 ms, the flame propagates away from this location, as indicated by the rapid development of the gas temperature shown in Fig. 5.19 (b). Initially, the maximum

temperature reached is 1700 K at 101.3 ms and then increasing to 1900 K at 101.7 ms. The maximum temperature continues to increase rapidly in time as the flame moves away from the wall as the flame propagates into increasing concentrations of the fuel mass fraction, shown in Fig. 5.20 (b). The flame front is marked by the large temperature gradient observed at 2, 3, 4 ,and 5.5 mm at 101.3, 101.5, 101.7. and 101.2 ms, respectively. During the time instances shown in Fig. 5.19 (b), the flame is propagating at approximately 5 m/s, as indicated in Fig. 5.11.

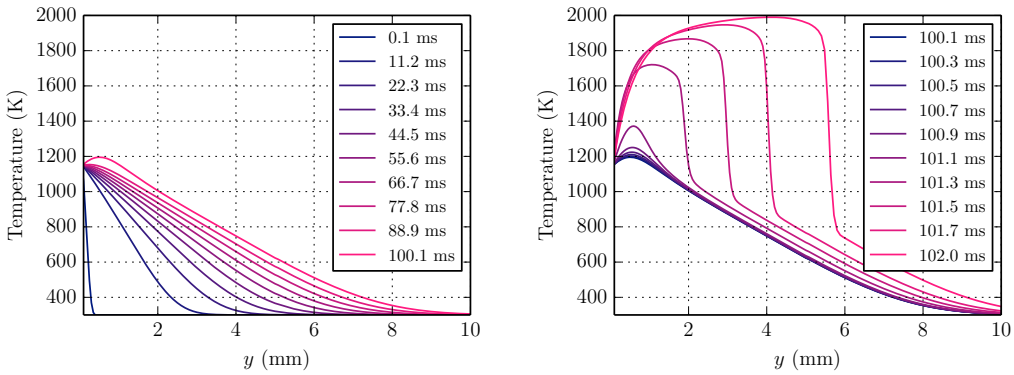

(a) $t = 0.1 - 101.1$ ms (b) $t = 101.0 - 101.8$ ms

Figure 5.19: Spatial profiles of temperature within the thermal boundary layer for n-hexane-air at $\Phi = 0.9$ and an initial temperature and pressure of 300 K and 100 kPa, respectively, and $T_{\text{wall}} = 1150$ K, at (a) $t = 0.1 - 100.1$ ms and (b) $t = 100.1 - 102.0$ ms.

Figure 5.20 (a) shows the depletion of C_6H_{14} as it is decomposed into smaller fuel molecules described in Section 5.5.1. At a given time, the fuel mass fraction decreases as y approaches 0, i.e. as the gas temperature increases from the freestream to the wall temperature. C_6H_{14} is fully depleted at 100.1 ms at y locations between 0 and 1 mm. At 100.1 ms, the depletion of C_6H_{14} extends up to 7 mm away from the wall. Although a temperature increase is already observed at 100.1 ms (see Fig. 5.19 (a)), rapid consumption of the fuel does not start until 101.3 ms, shown in Fig. 5.20 (b). This indicates that the formation of a self-sustained flame occurs approximately 1 ms after the initial heat release. At the ignition location, only a small amount of C_6H_{14} is consumed by the ignition since the majority of it has been converted to smaller fuel components such as C_2H_4, shown in Fig. 5.21 (a).

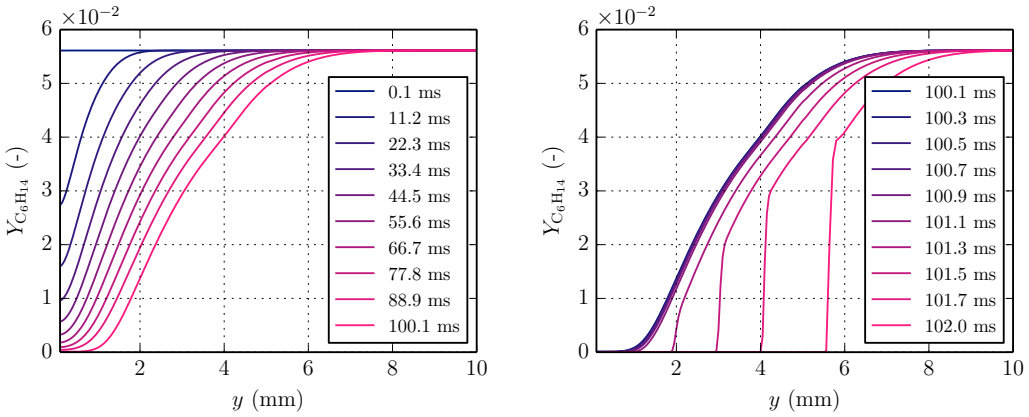

(a) $t = 0.1 - 101.1$ ms (b) $t = 101.0 - 101.8$ ms

Figure 5.20: Spatial profiles of C_6H_{14} mass fraction within the thermal boundary layer for n-hexane-air at $\Phi = 0.9$ and an initial temperature and pressure of 300 K and 100 kPa, respectively, and $T_{\text{wall}} = 1150$ K, at (a) $t = 0.1 - 100.1$ ms and (b) $t = 100.1 - 102.0$ ms.

Figure 5.21 (a) shows that the formation of C_2H_4 through decomposition of C_6H_{14} occurs throughout the thermal boundary layer with the lowest concentration near the thermal boundary layer edge. At the wall, the C_2H_4 mass fraction exceeds 1.5% at 55.6 ms; at this time and location, C_6H_{14} has been depleted to less than 0.5%. C_2H_4 begins to be depleted at $t > 55.6$ ms and rapid consumption starts at 101.3 ms, shown in Fig. 5.21 (b). The C_2H_4 mass fraction is depleted to 0.7% at 100.1 ms, which is when a temperature increase above 1150 K is first observed.

Figure 5.22 shows the mass fractions of the OH radical. Figure 5.22 (a) shows that the OH concentration is initially highest at the wall where the temperature is highest. At 88.9 ms, the maximum mass fraction of OH is close to 0.0004%, afterwards, at 100.1 ms, there is a rapid increase with the peak occurring approximately 0.3 mm away from the wall, marking the start of an ignition event. The flame is not observed until 101.3 ms, shown in Fig. 5.22 (b) by a two order of magnitude increase in the mass fraction of OH when compared to the maximum value observed at 100.1 ms. The figure also shows an increase in the maximum mass fraction of OH as the flame propagates into regions of increasing C_6H_{14} mass fraction.

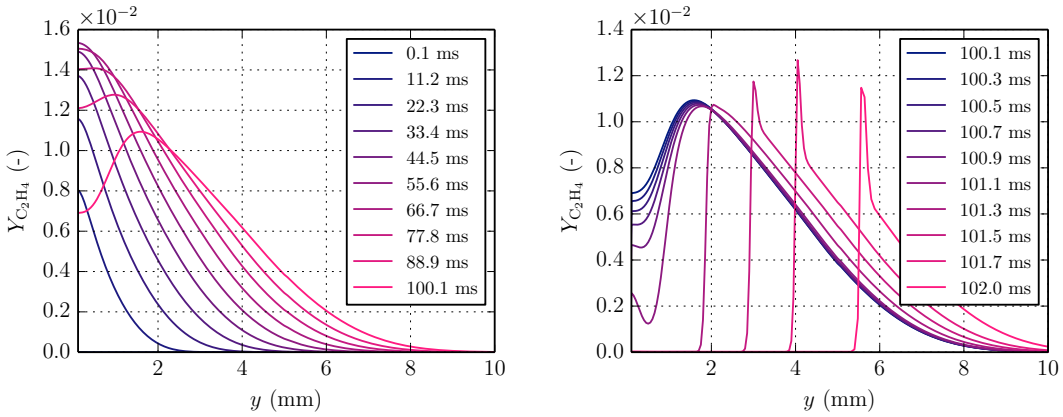

(a) $t = 0.1 - 101.1$ ms (b) $t = 101.0 - 101.8$ ms

Figure 5.21: Spatial profiles of C_2H_4 mass fraction within the thermal boundary layer for n-hexane-air at $\Phi = 0.9$ and an initial temperature and pressure of 300 K and 100 kPa, respectively, and $T_{\text{wall}} = 1150$ K, at (a) $t = 0.1 - 100.1$ ms and (b) $t = 100.1 - 102.0$ ms.

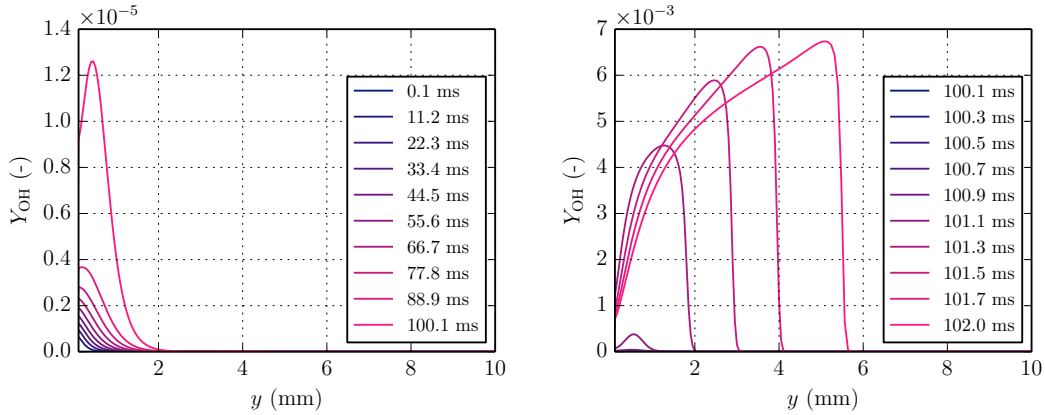

(a) $t = 0.1 - 101.1$ ms (b) $t = 101.0 - 101.8$ ms

Figure 5.22: Spatial profiles of OH mass fraction within the thermal boundary layer for n-hexane-air at $\Phi = 0.9$ and an initial temperature and pressure of 300 K and 100 kPa, respectively, and $T_{\text{wall}} = 1150$ K, at (a) $t = 0.1 - 100.1$ ms and (b) $t = 100.1 - 102.0$ ms.

5.5.2.2 Temperature and Species Profiles in the Boundary Layer with $T_{\text{wall}} = 1400$ K

Similar behavior, compared to Fig. 5.19, in terms of thermal diffusion to create the thermal boundary layer is observed in the temperature profiles of Fig. 5.23 (a) for a

wall temperature of 1400 K. An increase in temperature, above the wall temperature of 1400 K, is first observed at 2.101 ms. The rise in temperature first occurs at approximately 60 μm away from the wall, which marks the onset of the ignition event. The flame appears at 2.332 ms, shown in Fig. 5.23 (b) by the large temperature gradient.

Figure 5.24 (a) shows that the decomposition of C_6H_{14} occurs throughout the thermal boundary layer; the decrease in the fuel mass fraction is observed up to 1.25 mm at 2.101 ms. Due to the higher gas temperature, compared to the $T_{\text{wall}} = 1150$ K case, the decomposition of C_6H_{14} occurs rapidly, falling to 0.5% from 0.0001 to 0.234 ms. That same amount of decay occurs over 44.5 ms, shown in Fig. 5.20 (a), for $T_{\text{wall}} = 1150$ K. When the first increase in gas temperature above 1400 K is observed for $T_{\text{wall}} = 1400$ K, the C_6H_{14} mass fraction has dropped to zero at $y = 0 - 0.25$ mm.

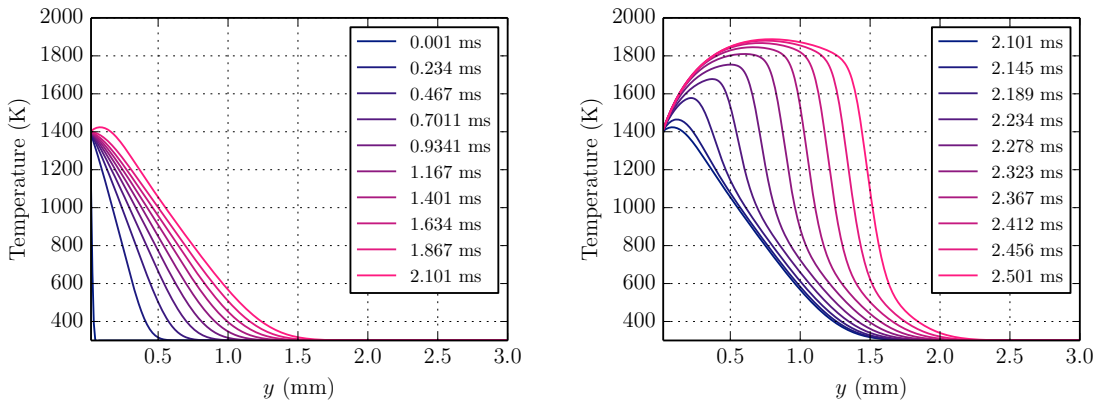

(a) $t = 0.001 - 2.101$ ms (b) $t = 2.101 - 2.501$ ms

Figure 5.23: Spatial profiles of temperature within the thermal boundary layer for n-hexane-air at $\Phi = 0.9$ and an initial temperature and pressure of 300 K and 100 kPa, respectively, and $T_{\text{wall}} = 1400$ K, at (a) $t = 0.001 - 2.101$ ms and (b) $t = 2.101 - 2.501$ ms.

As mentioned earlier, the C_6H_{14} decomposition to 0.5% occurs very rapidly, within 0.234 ms, at this time a large amount of C_2H_4 (1.9%) is created at the wall, shown in Fig. 5.25 (a). Later, at 0.7011 ms, the C_2H_4 begins to be depleted at the wall and to a lesser extent away from $y = 0$ mm. Figure 5.25 (b) shows the C_2H_4 distribution

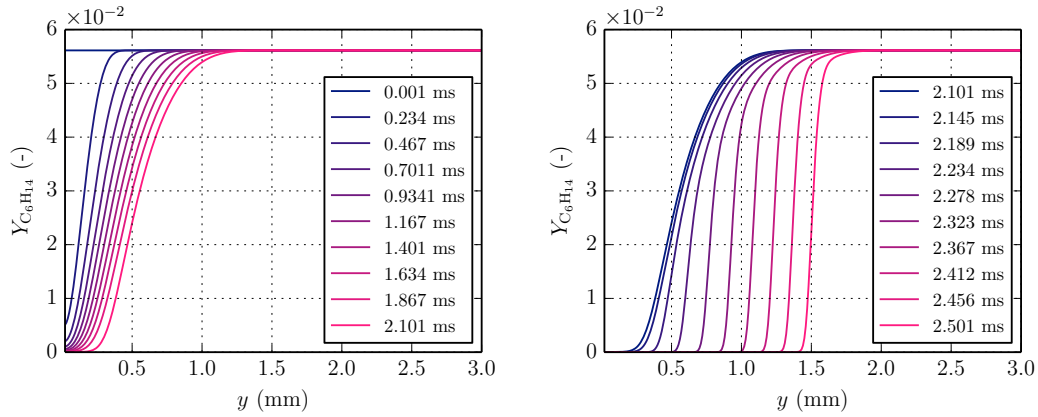

(a) $t = 0.001 - 2.101$ ms (b) $t = 2.101 - 2.501$ ms

Figure 5.24: Spatial profiles of C_6H_{14} mass fraction within the thermal boundary layer for n-hexane-air at $\Phi = 0.9$ and an initial temperature and pressure of 300 K and 100 kPa, respectively, and $T_{\text{wall}} = 1400$ K, at (a) $t = 0.001 - 2.101$ ms and (b) $t = 2.101 - 2.501$ ms.

becoming narrower in time, indicating the formation of a flame. Figure 5.16 shows a $\Phi = 0.9$ flame with a C_2H_4 width distribution of 0.5 mm, and a thickness of 0.8 mm is observed at 2.501 ms in Fig. 5.25 (b).

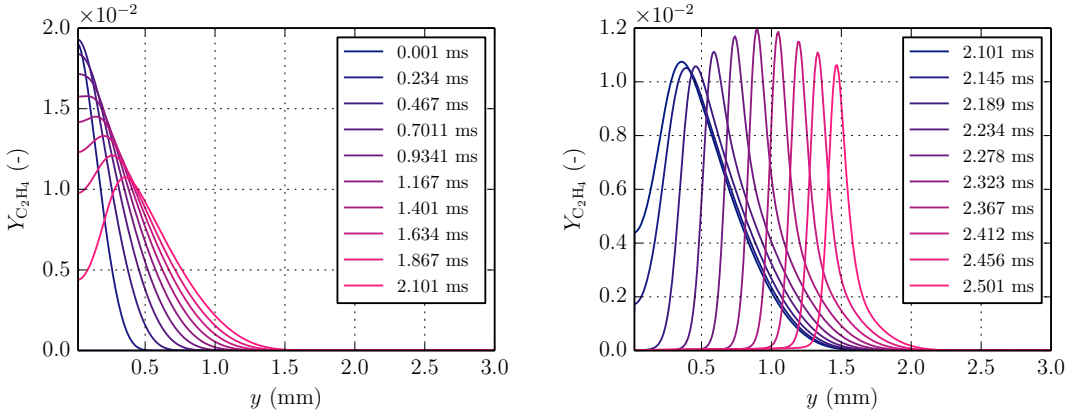

(a) $t = 0.1 - 101.1$ ms (b) $t = 101.0 - 101.8$ ms

Figure 5.25: Spatial profiles of C_2H_4 mass fraction within the thermal boundary layer for n-hexane-air at $\Phi = 0.9$ and an initial temperature and pressure of 300 K and 100 kPa, respectively, and $T_{\text{wall}} = 1400$ K, at (a) $t = 0.001 - 2.101$ ms and (b) $t = 2.101 - 2.501$ ms.

5.5.3 Temperature Profile along Fluid Parcel Paths

This section focuses on the temporal evolution of temperature and displacement of various fluid parcels within the thermal boundary layer. Figure 5.26 shows the fluid parcel path as a function of time for various fluid parcels from the time the wall is impulsively heated until ignition takes place. Each line corresponds to the trajectory of a fluid parcel originating at y_0 (shown in the legend in mm) at $t = 0$. All the fluid parcels, except for the one next to the wall, are immediately displaced due to the normal velocity component that is induced by the density changes due to thermal diffusion from the hot wall. A fluid parcel that is initially at 0.02 mm is displaced to approximately 0.08 mm before ignition. Figure 5.27 shows the fluid parcel displacement at $t = 2$ ms as a function of the initial fluid parcel location. The figure indicates that prior to ignition, the fluid parcel displacement is linear with respect to the initial fluid parcel location, with a slope of approximately 4.5. This can be understood analytically by using the formulation for the mass weighted variable, ζ, shown in Eq. 5.28. Assuming no ignition events taking place, the fluid parcel displacement can be obtained by integrating Eq. 5.28 and obtaining,

$$y_p = \frac{\rho_\infty}{\rho_{\text{wall}}} y_0, \tag{5.23}$$

by ignoring the brief transient at the start of the boundary layer and assuming a constant gas temperature equal to the wall temperature thereafter. This approximation is valid for parcels sufficiently close to the wall.

Subtle bumps along the paths corresponding to $y_0 = 0.026 - 0.064$ mm, shown in Fig. 5.26, are a result of the temperature increase due to heat release into the gas by chemical reactions causing an increase in the normal component of velocity.

Figure 5.28 shows two additional fluid parcel paths that correspond to $y_0 = 0.235$ and 0.49 mm. The fluid parcels are displaced to 0.83 and 1.25 mm prior to ignition, the path taken by the fluid parcel corresponding to $y_0 = 0.49$ goes through regions along the edge of the thermal boundary, as indicated in Fig. 5.19 (a), therefore maintaining a temperature slightly over 300 K during the travel time of 2.5 ms.

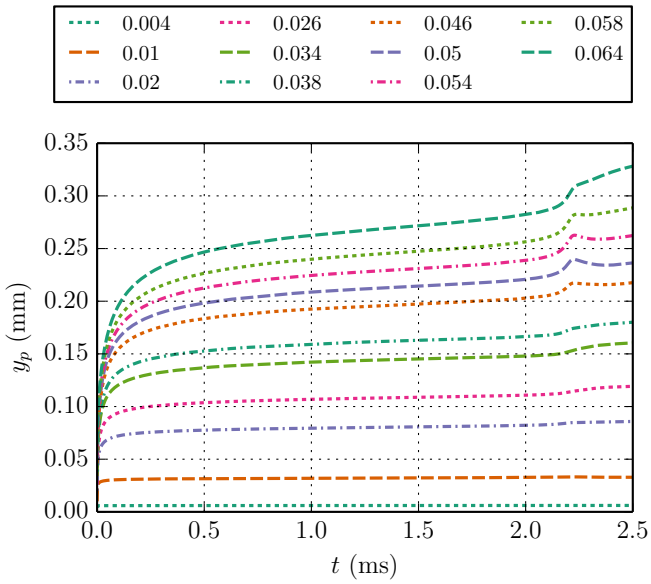

Figure 5.26: Temporal displacement of fluid parcels for $T_{\text{wall}} = 1400$ K case; the mixture is n-hexane-air at $\Phi = 0.9$ and an initial temperature and pressure of 300 K and 100 kPa, the units of the initial fluid parcel location, y_0, shown in the legend are given in mm.

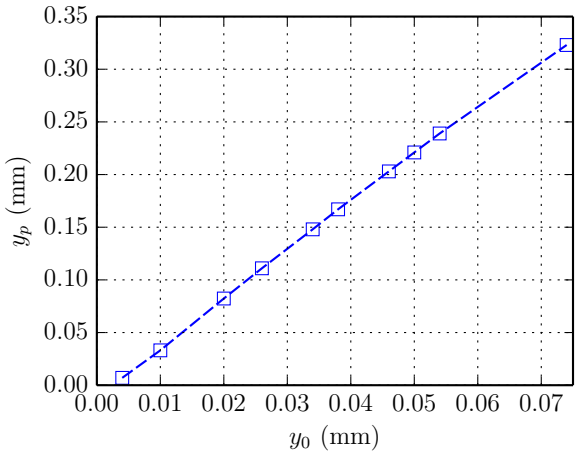

Figure 5.27: Fluid parcel location normal to the wall at $t = 2.0$ ms as a function of the initial fluid parcel location, y_0; the mixture is n-hexane-air at $\Phi = 0.9$ and an initial temperature and pressure of 300 K and 100 kPa, and $T_{\text{wall}} = 1400$ K.

Figure 5.29 shows the temperature profiles of the fluid parcel paths shown in Figs. 5.26 and 5.28. The fluid parcels closest to the wall are rapidly heated, e.g. the fluid parcel next to the wall, $y_0 = 0.004$ mm, reaches 99% of the wall temperature

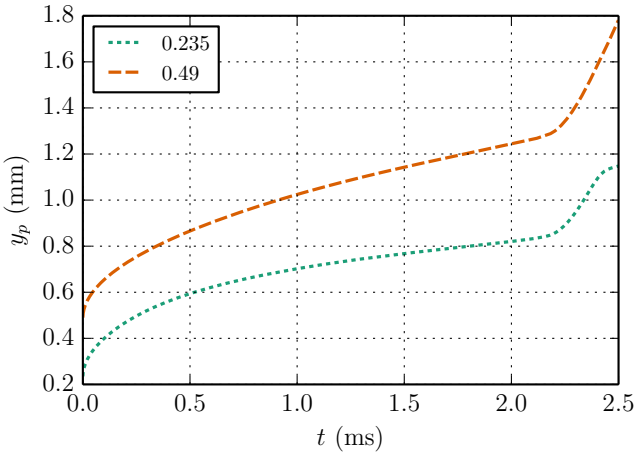

Figure 5.28: Temporal displacement of additional fluid parcels for $T_{\text{wall}} = 1400$ K case; the mixture is n-hexane-air at $\Phi = 0.9$ and an initial temperature and pressure of 300 K and 100 kPa, the units of the initial fluid parcel location, y_0, shown in the legend are given in mm.

within 0.05 ms. Although that is the fluid parcel with the highest temperature, it does not ignite since any thermal energy released through chemical reactions is lost by conduction to the wall. The fluid parcels that see a rapid temperature increase after the initial heating by the wall through thermal diffusion are $0.034 < y_0 < 0.234$ mm. The fluid parcel corresponding to $y_0 = 0.234$ mm is consumed by the propagating flame as indicated by the rapid temperature increase from 700 K to close $\sim$ 1800 K. Fluid parcels corresponding to $y_0 = 0.034 - 0.038$ mm see a slow temperature increase of $220 - 290$ K in 0.5 ms after the initial heating of the fluid through heat diffusion from the wall. Fluid parcels corresponding to $0.05 < y_0 < 0.064$ mm see a temperature jump over a shorter period of time, e.g. for $y_0 = 0.05$ mm, there is a temperature increase of 325 K over 0.24 ms ($t = 2.0 - 2.24$ ms) after the initial heating of the fluid through thermal diffusion from the wall. The fluid parcel at $y_0 = 0.49$ mm, has a temperature increase to 400 K during the first 2.5 ms; the fluid parcel is outside of the thermal boundary layer until 1.0 ms and then it experiences a modest temperature increase due to thermal diffusion from the wall.

Figure 5.30 shows temperature histories for selected fluid parcels from Fig. 5.29. A continuous range of temperature increase is observed with increasing distance from

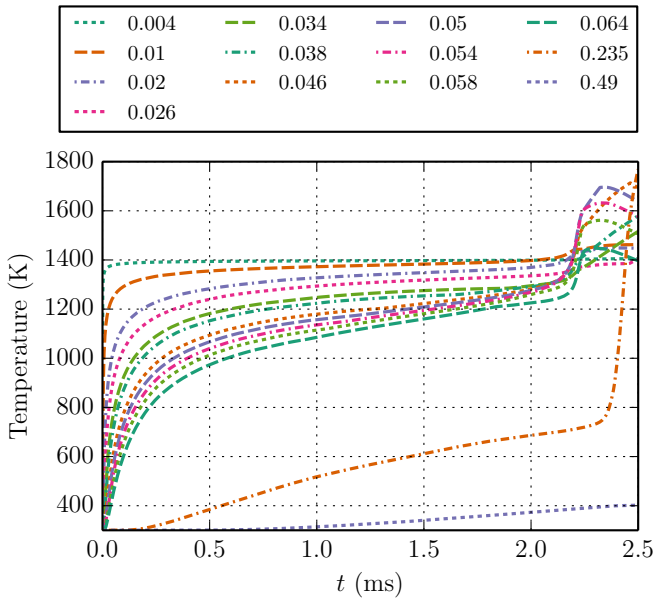

Figure 5.29: Temporal evolution of temperature of fluid parcels for $T_{\text{wall}} = 1400$ K case; the mixture is n-hexane-air at $\Phi = 0.9$ and an initial temperature and pressure of 300 K and 100 kPa, the units of the initial fluid parcel location, y_0, shown in the legend are given in mm.

the wall. It is clear that parcels with $0.02 < y_0 < 0.026$ do not ignite but parcels with $0.05 < y_0 < 0.058$ mm experience a higher temperature increase, suggesting that these parcels are igniting.

5.5.4 Ignition Criteria

Earlier in Section 5.4, ignition was defined by the time and location when a temperature increase of $\Delta T = 150$ K over the wall temperature (reference temperature) is first observed. In Fig. 5.30, this ΔT criterion corresponds to igniting fluid parcels of $y_0 = 0.05$ and 0.054 mm at 2.22 ms; however, the choice of defining a ΔT to mark ignition is rather arbitrary. Using a reference temperature equivalent to the wall temperature is suitable if the entire domain is initially at this temperature, but this is not the case in thermal boundary layer flows adjacent to a hot wall. In the thermal boundary layer, the gas has a range of temperatures, e.g. Fig. 5.30 shows fluid parcel path temperatures ranging from 1200 K to over 1350 K at 1.8 ms.

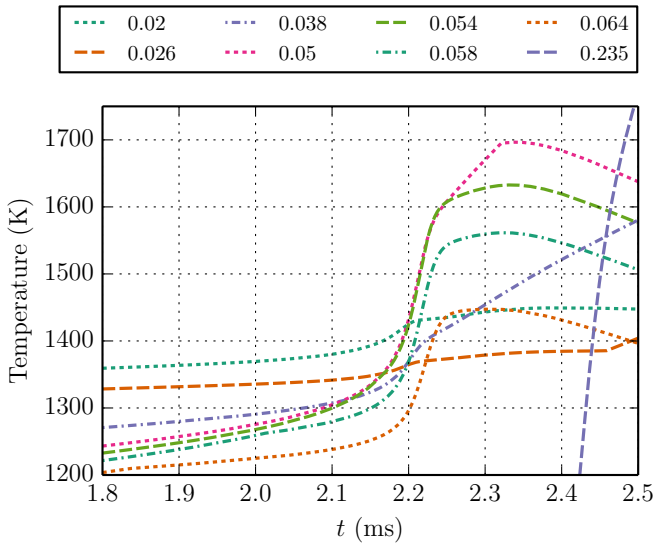

Figure 5.30: Temporal evolution of temperature of select fluid parcels shown in Fig. 5.29 for $T_{\text{wall}} = 1400$ K case; the mixture is n-hexane-air at $\Phi = 0.9$ and an initial temperature and pressure of 300 K and 100 kPa, the units of the initial fluid parcel location, y_0, shown in the legend are given in mm.

A different criterion is needed to pinpoint the ignition location and time that does not rely on picking an arbitrary value such as ΔT. One option is to look at the evolution of a specific species mass fraction along the fluid parcel paths. Figure 5.31 shows the CO species mass fraction along several fluid parcel trajectories, and the fluid parcels that have the highest peak in CO correspond to $y_0 = 0.05$ and 0.054 mm, reaching a value of approximately 5.8×10^{-2}. The second highest peak is given by $y_0 = 0.235$ mm; however, as discussed earlier, this particular fluid parcel is encountering a propagating flame. An ignition criterion based on the maximum concentration in CO is still somewhat arbitrary since other species can be used that would yield slightly different results; however, a peak is a well defined feature when compared to an arbitrary value of ΔT. Using the peak in CO mass fraction as the ignition criterion, the ignition location corresponds to the $y_0 = 0.058$ mm fluid parcel. At the ignition time of 2.23 ms, the fluid parcel is approximately 0.26 mm away from the wall. The igniting fluid parcel (based on the CO criterion) is slightly further away at $t = 0$ from the igniting fluid parcel of $y_0 = 0.05 - 0.054$ based on the $\Delta T = 150$ K

criterion.

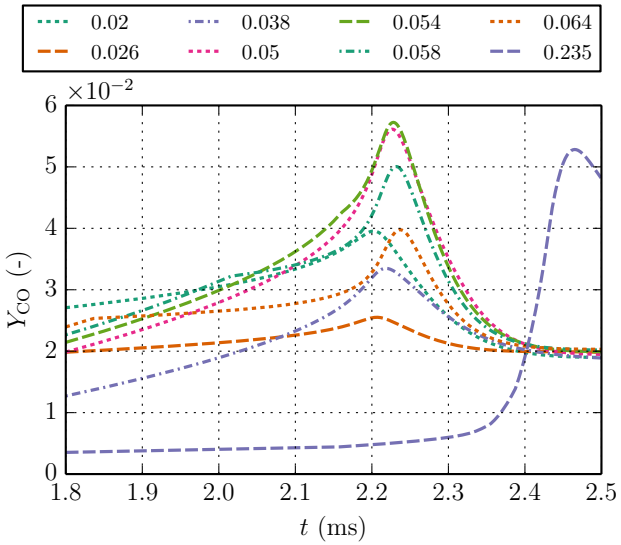

Figure 5.31: Temporal evolution of CO mass fraction of select fluid parcels shown in Fig. 5.29 for $T_{\text{wall}} = 1400$ K case; the mixture is n-hexane-air at $\Phi = 0.9$ and an initial temperature and pressure of 300 K and 100 kPa, the units of the initial fluid parcel location, y_0, shown in the legend are given in mm.

5.6 Ignition Delay Time

The differences observed in the ignition delay times, τ_{ign}, from 0D and 1D simulations for H_2-air and n-hexane-air mixtures are shown in Fig. 5.32. The 0D calculations are obtained using a constant-pressure-zero dimensional reactor in Cantera (Goodwin, 2003) and the 1D calculations are obtained from the Rayleigh ignition model problem.

Similar trends are observed between the 0D and 1D calculations, mainly that there is an increase in delay time with decreasing temperature. However, the delay times are larger in the 1D calculations. The 0D calculations do not account for heat losses due to diffusion and convection, or species transport. Longer delay times compared to the H_2-air mixture are observed for the n-hexane-air mixture. For a temperature of 1200 K, the delay time for n-hexane-air is over 2 orders of magnitude larger than the H_2-air delay time; this is consistent with previous experimental data and detailed

investigations of chemical kinetics that these simulations are based upon.

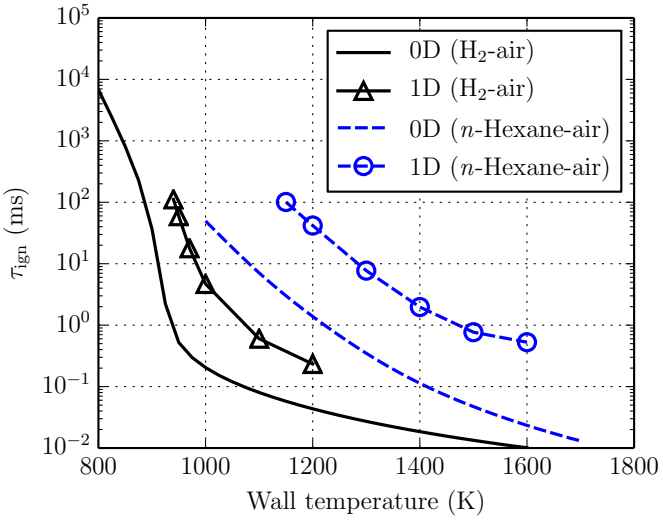

Figure 5.32: 0D and 1D ignition delay time calculations for n-hexane-air ($\Phi = 0.9$) and hydrogen-air ($\Phi = 1.0$) at an initial temperature and pressure of 300 K and 100 kPa, respectively.

5.7 Analytic Model of the Model Boundary Layer Problem

The current section presents an analytic formulation of one-dimensional, non-reactive, temporally evolving momentum and thermal boundary layer that was investigated numerically in earlier sections of this chapter.

The model assumptions and initial and boundary conditions are the same as in Sections 5.3 and 5.3.4; $\partial/\partial x = 0$ and only gradients in the $y-$direction are considered. Assuming a zero pressure gradient in both the x and y directions and neglecting the viscous effects on the $y-$component of velocity, the equations of unsteady, non-reactive flow reduce to:

$$\frac{\partial \rho}{\partial t} + \frac{\partial (\rho v)}{\partial y} = 0 \tag{5.24}$$

$$\rho \left(\frac{\partial u}{\partial t} + v \frac{\partial u}{\partial y} \right) = \frac{\partial}{\partial y} \left(\mu \frac{\partial u}{\partial y} \right) \tag{5.25}$$

$$\rho c_p \left(\frac{\partial T}{\partial t} + v \frac{\partial T}{\partial y} \right) = \frac{\partial}{\partial y} \left(\lambda \frac{\partial T}{\partial y} \right), \tag{5.26}$$

which are functions of y and t only. The $y-$component of momentum does not need to be considered given the approximations that are made for this analytic model. The density gradient imposed by the impulsively heated wall results in an induced velocity v. By assuming that $\partial p/\partial y \approx 0$, the $y-$momentum equation is eliminated and the $y-$velocity v can be computed by using the continuity relation shown in Eq. 5.24 which is rearranged so that,

$$v = -\int_0^y \frac{1}{\rho} \frac{\mathrm{d}\rho}{\mathrm{d}t} \, \mathrm{d}y', \tag{5.27}$$

where $\mathrm{d}\rho/\mathrm{d}t$ is the convective derivative $\partial\rho/\partial t + v\partial\rho/\partial y$. Using the mass weighted variable of

$$\zeta = \int_0^y \frac{\rho}{\rho_\infty} \, \mathrm{d}y', \tag{5.28}$$

Eq. 5.27 becomes,

$$v = -\int_0^\zeta \frac{\rho_\infty}{\rho^2} \frac{\mathrm{d}\rho}{\mathrm{d}t} \, \mathrm{d}\zeta', \tag{5.29}$$

and is rearranged to give,

$$v = \int_0^\zeta \frac{\mathrm{d}}{\mathrm{d}t} \left(\frac{\rho_\infty}{\rho} \right) \, \mathrm{d}\zeta'. \tag{5.30}$$

The displacement in time of a fluid parcel normal to the wall is:

$$y = \int_0^t v \, \mathrm{d}t'. \tag{5.31}$$

Using Eq. 5.30, Eq. 5.32 becomes,

$$y = \int_0^\zeta \frac{\rho_\infty}{\rho} \, \mathrm{d}\zeta'. \tag{5.32}$$

Applying the mass weighted variable ζ to Eqs. 5.25 and 5.26 and using the assumptions that $\rho\mu =$ constant and $\rho k =$ constant results in two independent equations,

$$\frac{\partial u}{\partial t} = \nu_\infty \frac{\partial^2 u}{\partial \zeta^2}, \tag{5.33}$$

$$\frac{\partial T}{\partial t} = \alpha_\infty \frac{\partial^2 T}{\partial \zeta^2}, \tag{5.34}$$

where ν_∞ and α_∞ are the kinematic viscosity and thermal diffusivity at the freestream temperature, respectively. The boundary and initial conditions for Eqs. 5.33 and 5.34 are,

$$\begin{aligned} t \leq 0: &\quad u = U_\infty \text{ and } T = T_\infty \quad \text{for all } \zeta \\ t > 0: &\quad u = 0 \text{ and } T = T_{\text{wall}} \quad \text{for } \zeta = 0 \\ : &\quad u = 0 \text{ and } T = T_\infty \quad \text{for } \zeta = \infty. \end{aligned} \tag{5.35}$$

The partial differential equation shown in Eq. 5.33 reduces to an ordinary differential equation through the use of a non-dimensional variable η, where,

$$\eta = \frac{\zeta}{2\sqrt{\nu_\infty t}}. \tag{5.36}$$

and assuming a similarity solution of the form,

$$u = U_\infty f(\eta). \tag{5.37}$$

Equation 5.33 is rewritten as,

$$f'' + 2\eta f' = 0, \tag{5.38}$$

where the new boundary conditions are $f = 0$ at $\eta = 0$ and $f = 1$ at $\eta = \infty$. Equation 5.38 has the well known solution in terms of the error function, i.e.,

$$f = \text{erf}(\eta) \qquad \text{and} \qquad \text{erf}(\eta) = \frac{2}{\sqrt{\pi}} \int_0^\eta \exp\left(-\xi^2\right) \mathrm{d}\xi. \tag{5.39}$$

The solution to Eq. 5.33 is,

$$u = U_\infty \,\text{erf}(\eta). \tag{5.40}$$

5.7.1 Residence Time

The residence time of fluid parcels in a momentum boundary layer is presented in the current section. A flow with freestream velocity $U_\infty \neq 0$ is considered with a

stationary boundary condition at $y = 0$ and $t = 0$; the growth of the temporally evolving momentum boundary layer is illustrated in 5.33 for initial times t_0 and t_1 and for the residence time t_s. The displacement in time of a fluid parcel y_p is also illustrated.

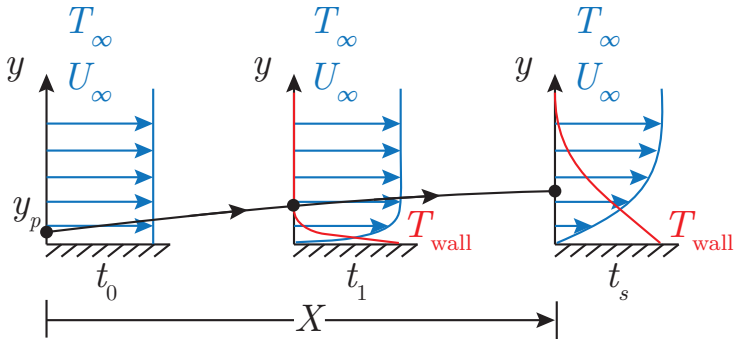

Figure 5.33: Velocity and temperature profiles adjacent to wall for the transient boundary layer model. A fluid parcel trajectory is shown from location y_p at the initial time $t_0 = 0$.

Given the velocity profile of Eq. 5.40, the residence time, t_s, for a fluid parcel that travels a distance X beginning at $t_0 = 0$ (illustrated in Fig. 5.33) is calculated using,

$$X = \int_0^{t_s} u\left(\zeta_p, t\right)\, \mathrm{d}t, \tag{5.41}$$

where ζ_p is the mass weighted fluid parcel location normal to the wall and is defined as,

$$\zeta_p = \int_0^{y_p} \frac{\rho\left(y', t\right)}{\rho_\infty}\, \mathrm{d}y'. \tag{5.42}$$

A change of variables is applied to Eq. 5.41 to give a non-dimensional formulation. Rearranging Eq. 5.36 yields,

$$t = \frac{\zeta_p^2}{4\nu_\infty \eta^2} \qquad \text{and} \qquad \mathrm{d}t = -\frac{\zeta_p^2}{2\nu_\infty \eta^3}\, d\eta. \tag{5.43}$$

The new integration limits are as follows:

$$\begin{aligned} t = 0: &\quad \eta = \infty \\ t = t_s: &\quad \eta = \eta_s \quad \text{where} \quad \eta_s = \frac{\zeta_p}{2\sqrt{\nu_\infty t_s}}. \end{aligned} \tag{5.44}$$

The non-dimensional travel distance, $\tilde{X}$, is written as,

$$\tilde{X} = \int_{\eta_s}^{\infty} \frac{\operatorname{erf}(\eta)}{\eta^3}\, \mathrm{d}\eta, \tag{5.45}$$

where,

$$\tilde{X} = \frac{2\nu_\infty X}{\zeta_p^2 U_\infty}. \tag{5.46}$$

Figure 5.34 shows the dependence of the similarity variable, η_s, on the non-dimensional distance traveled $\tilde{X}$. For a fixed distance X, values of $\tilde{X} \to 0$ correspond to fluid parcel locations far from the wall, and the corresponding value of η_s approaches infinity. Values of $\tilde{X} \to \infty$ correspond to fluid parcel locations approaching the wall, and the corresponding value of η_s approaches zero.

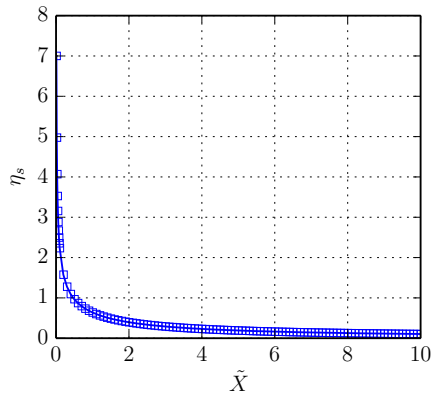

Figure 5.34: Similarity variable η_s as a function of the non-dimensional distance traveled.

Figure 5.35 shows the residence time, t_s as a function of mass weighted fluid parcel location normal to the wall, ζ_p, for different values of X and U_0. The behavior shown is as expected: as X increases so does the residence time for a fluid parcel, and as U_0

increases it takes less time for a fluid parcel to travel a fixed distance X.

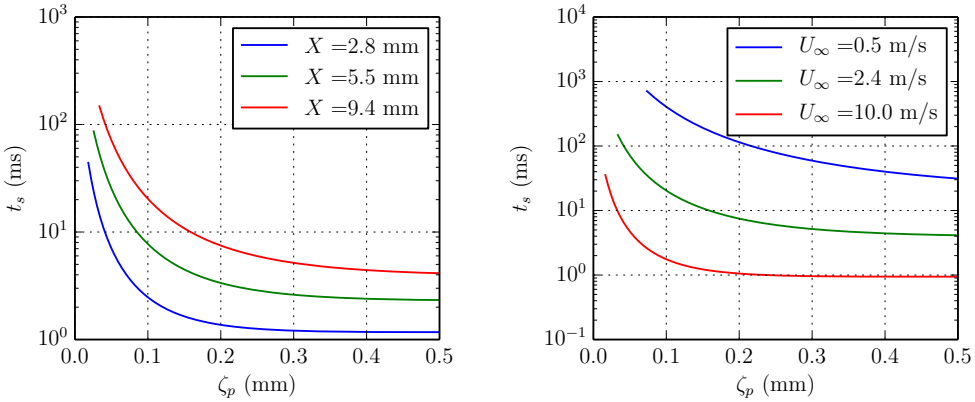

(a) Effect of travel distance X (b) Effect of freestream velocity

Figure 5.35: Residence time as a function of mass weighted fluid parcel location ζ_p normal to the wall for different values of (a) distance traveled X and (b) freestream velocity.

Two limiting cases are obtained from Eq. 5.45:

1. $\eta_s > 2$: corresponds to $\text{erf}(\eta_s) = 1$, reducing Eq. 5.45 to,

$$\tilde{X} = \int_{\eta_s}^{\infty} \frac{1}{\eta^3}\, \mathrm{d}\eta. \tag{5.47}$$

The integration results in $\tilde{X} = -1/\eta_s^2$, which converted back to dimensional variables yields $t_s = X/U_\infty$. This applies to fluid parcels that are in the freestream outside of the boundary layer, i.e. $\zeta_p \geq \delta$ (momentum boundary layer thickness) where $\delta = \sqrt{4\nu_\infty X/U_\infty}$.

2. $\eta << 1$: in this case, a Taylor expansion of the $\text{erf}(\eta)$ is performed, where,

$$\begin{aligned} \text{erf}\,(\eta) &= \frac{2}{\sqrt{\pi}} \int_{\eta}^{\infty} \left(1 - \xi^2 + \frac{\xi^4}{4} - \frac{\xi^6}{6} + ...\right) \mathrm{d}\xi \\ &= \frac{2}{\sqrt{\pi}} \left(\eta - \frac{\eta^3}{3} + \frac{\eta^5}{10} + \frac{\eta^7}{42} + ...\right). \end{aligned} \tag{5.48}$$

Substituting Eq. 5.48 into Eq. 5.45, then performing a term by term integration and eliminating higher order terms results in $\tilde{X} = 2/\eta_s\sqrt{\pi}$. The dimensional

residence time is,

$$t_s = \frac{\pi \nu_\infty}{4\zeta_p^2} \left(\frac{X}{U_\infty} \right)^2. \tag{5.49}$$

Using the residence time and boundary layer thickness at $\eta_s > 2$, scaled variables are constructed for the residence time and fluid parcel distance normal to the wall, i.e.,

$$\begin{aligned} t_r &= \frac{t_s}{X/U_\infty} = \frac{1}{2\eta_s^2 \tilde{X}} \\ \zeta_r &= \frac{\zeta_p}{\sqrt{4\nu_\infty X/U_\infty}} = \frac{1}{\sqrt{2\tilde{X}}}. \end{aligned} \tag{5.50}$$

An analysis of the limiting cases of $\eta_s \geq 2$ and $\eta_s << 1$ results in the following scaled limits of t_r and y_r:

$$\begin{aligned} \eta_s \geq 2: \quad & t_s = \frac{X}{U_\infty} \quad \rightarrow \quad t_r = 1 \\ \eta_s << 1: \quad & t_s = \frac{\pi \nu_\infty}{4\zeta_p^2} \left(\frac{X}{U_\infty} \right)^2 \quad \rightarrow \quad t_r = \frac{\pi}{16\zeta_r^2} \end{aligned} \tag{5.51}$$

Figure 5.36 shows the scaled residence time and location based on the numerical integration of Eq. 5.45 as well as the limiting case curve (black dashed line) corresponding to $\eta_s << 1$. The dashed line agrees with the numerical result for $\zeta_r < 0.2$, corresponding to fluid parcels located below 0.2δ, and the limit of $t_r = 1$ occurs for $\zeta_r > 1$, fluid parcels above and at δ. For example, in the analysis presented in Section 5.5.3, it is a fluid parcel that is located at $0.15\delta_T$ that eventually ignites. If a $\mathrm{Pr} = 1$ assumption is made, then the scaled residence time approximation for $\eta_s << 1$ is applicable to fluid parcels that could potentially ignite in a reactive mixture.

Following the same approach used to determine the velocity profile of an impulsively stopped flow, the temperature profile for an impulsively heated plate is determined by solving Eq. 5.34. Using a nondimensional temperature, Θ, and the similarity variable χ, where,

$$\Theta = \frac{T_{\text{wall}} - T}{T_{\text{wall}} - T_\infty} \quad \text{and} \quad \chi = \frac{\zeta}{2\sqrt{\alpha_\infty t}}, \tag{5.52}$$

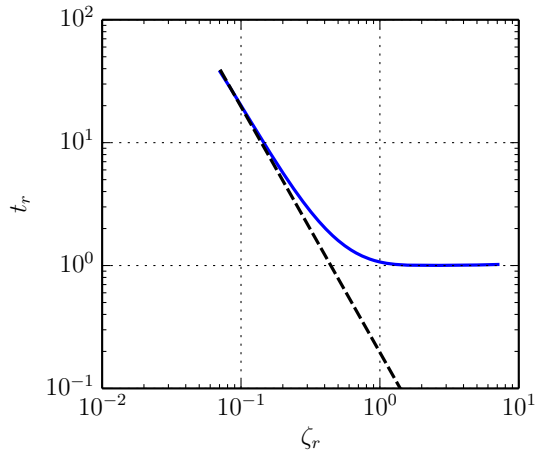

Figure 5.36: Scaled residence time, t_r, as a function of the scaled mass weighted fluid parcel location normal to the wall, ζ_r; the numerical result is shown by the blue line and the limiting case of $\eta_s << 1$ is shown by the black dashed line.

the solution to Eq. 5.34 is,

$$\Theta = \mathrm{erf}\,(\chi) \quad \text{where} \quad \frac{T}{T_{\text{wall}}} = 1 + \left(\frac{T_\infty}{T_{\text{wall}}} - 1\right) \mathrm{erf}\,(\chi)\,. \tag{5.53}$$

Assuming Pr= 1, Eq. 5.53 rewritten in terms of ζ_r and scaled time $U_0 t/X$ is,

$$\frac{T}{T_{\text{wall}}} = 1 + \left(\frac{T_\infty}{T_{\text{wall}}} - 1\right) \mathrm{erf}\left(\frac{\zeta_r}{\sqrt{U_0 t/X}}\right). \tag{5.54}$$

Figure 5.37 shows the scaled temporal evolution of scaled temperature (T/T_{wall}) for various values of ζ_r using $T_{\text{wall}} = 1400$ K. In addition, the black markers indicate the scaled residence time of each fluid parcel as they travel a distance X. The figure shows that an increase in the values of ζ_r corresponds to a decrease in the scaled residence time. Also, the fluid parcels with the longest scaled residence times have temperature profiles with values close to the wall temperature.

Figure 5.38 shows the scaled temporal evolution of scaled temperature (T/T_{wall}) for various values of scaled wall normal distance y_r where,

$$y_r = \frac{y_p}{\sqrt{4\nu_\infty X/U_\infty}}, \tag{5.55}$$

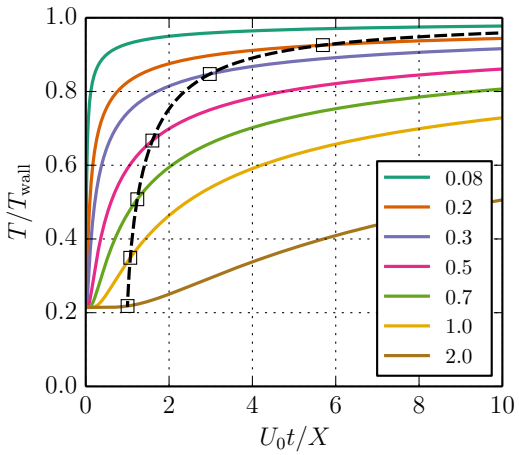

Figure 5.37: Temperature as a function of scaled time for various values of ζ_r; the black markers indicate the final temperature for the scaled residence time of fluid parcel y_r.

and y_p, the fluid parcel location, is determined from Eq. 5.32 for given ζ_p values. The black markers in the figure indicate the scaled residence time of each fluid parcel as they travel a distance X. A fluid parcel originating at 0.05δ, where $\delta = \sqrt{4\nu_\infty X/U_\infty}$, will take 65× longer to reach distance X than a fluid parcel that originates at a distance δ from the wall.

Finally the fluid parcel trajectory for the temperature profiles shown in Fig. 5.37 are given in Fig. 5.39. For the fluid parcels that reach a steady value within the scaled time shown, the fluid parcel displacement is roughly 4 times the initial fluid parcel location. This is in agreement with the numerical solution shown in Fig. 5.27.

5.8 Closing Remarks

A numerical study was performed on ignition within a temporally evolving thermal boundary layers of hydrogen-air and n-hexane-air using detailed chemistry. We determined that heat and species diffusion play a very important role in determining the ignition delay time. For example, in a hydrogen-air mixture with a wall temperature of 1200 K, neglecting diffusion resulted in a 50% decrease in the ignition

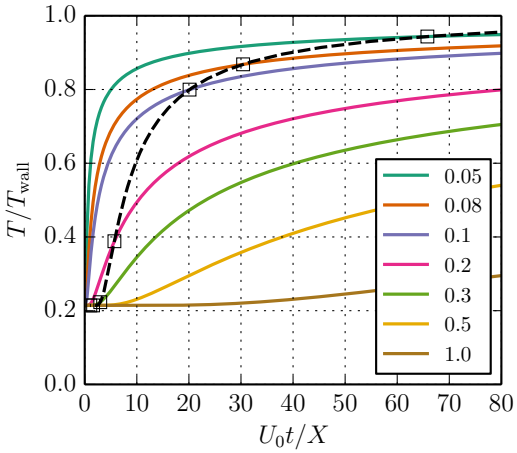

Figure 5.38: Temperature as a function of scaled time for various values of y_r; the black markers indicate the final temperature for the scaled residence time of fluid parcel y_r.

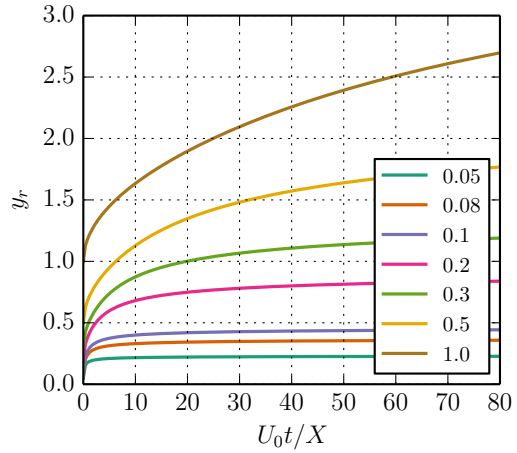

Figure 5.39: Fluid parcel trajectory as a function of scaled time for various initial values of y_r.

delay time. Additionally for a n-hexane-air mixture, the temperature history of a fluid parcel had an significant effect on the gas composition prior to ignition. The long delay times corresponding to a wall temperature of 1150 K resulted in n-hexane decomposing into smaller fuel molecules before ignition. Just prior to ignition, the main fuel species present was ethylene. At a higher wall temperature of 1400 K, the n-hexane did not undergo significant decomposition and prior to ignition the main

fuel species was still n-hexane. It was also evident from spatial plots of the fuel and temperature, that ignition always occurred some distance away from the wall. In the case of a n-hexane-air mixture with $T_{\text{wall}} = 1400$ K, ignition took place at $0.15\delta_T$ normal to the wall, where δ_T is the thickness of the thermal boundary layer at the time of ignition. The fuel profiles indicated that prior to any temperature increase resulting from chemical reactions, a thin region normal to the wall had already been decomposed to produce secondary fuels. The width of this depleted region was 1 mm for $T_{\text{wall}} = 1150$ and and 0.25 mm for $T_{\text{wall}} = 1400$ K, corresponding to $7 - 10\%$ of their respective thermal boundary layer thicknesses. The use of fluid parcel tracking allowed us to analyze the behavior of several fluid parcels close to the hot wall and two parcels close to the edge of the thermal boundary layer. The temperature and species mass fraction of CO allowed us to pinpoint the igniting fluid parcel based on the ignition criterion that uses the peak in CO to mark ignition. Finally, a simple analysis of the residence time of a fluid parcel in the model boundary layer problem (Rayleigh problem) was presented. The residence time determined the time needed for a fluid parcel y_p to traverse a distance X given a freestream velocity U_∞. A fluid parcel originating at 0.05δ, where $\delta = \sqrt{4\nu_\infty X/U_\infty}$, takes $65\times$ longer to reach distance X than a fluid parcel that originates at a distance δ from the wall.

Chapter 6

Spherically Propagating Flame Properties

Laminar flame properties such as the laminar burning speed and the Markstein length are important fundamental parameters for a wide number of combustion applications including spark ignition engines (Huang et al., 2006) and gas turbines (Bougrine et al., 2011). Knowledge of the laminar burning speed is important in modeling turbulent combustion since the turbulent burning speed is often modeled as a function of the laminar burning speed (Glassman, 1987; Chomiak, 1990). The laminar burning speed is defined as the normal propagation velocity of fresh gas relative to a fixed, planar flame front; it is frequently measured experimentally using spherically expanding flames (Tahtouh et al., 2009; Kwon and Faeth, 2001; Jerzembeck et al., 2009). An example of a spherically expanding n-hexane-air flame is shown in Fig. 6.1. The presence of flame stretch in such experiments precludes direct measurement of the laminar flame speed (Dowdy et al., 1990). Instead, the measured flame speed has to be extrapolated to conditions of zero stretch. Markstein (1951) first proposed this correction to the burning speed by introducing a parameter known as the Markstein length which characterizes the response of the flame to stretch. Asymptotic theoretical analysis (Ronney and Sivashinsky, 1989; Matalon and Matkowsky, 1982; Clavin, 1985) performed in the limit of high activation energy and low stretch rate have related the stretched and unstretched burning speeds through a linear relationship. This approach has been applied extensively during the past 20 years to extract

the laminar burning speed from experimental data (Aung et al., 1997, 1995; Bane et al., 2011; Mével et al., 2009b; Lamoureux et al., 2003). Further theoretical work by Ronney and Sivashinsky (1989) has led to a nonlinear relationship between the stretched and the unstretched burning speed which has been used by a number of groups in the past few years to account for nonlinear effects of stretch on the flame propagation (Kelley and Law, 2009; Halter et al., 2010; Kelley et al., 2011; Bouvet et al., 2011; Varea et al., 2012). Comparison of the results obtained through linear and nonlinear extrapolations demonstrated that both the burning speed and Markstein length can be poorly estimated by the linear method for mixtures that are away from stoichiometric (Kelley and Law, 2009; Halter et al., 2010). To account for the nonlinear effects of stretch without performing numerical differentiation of the experimental data, Kelley and Law (2009) analytically integrated the expression of Ronney and Sivashinsky (1989). Halter et al. (2010) also evaluated this latter methodology for methane-air burning speed measurements and reported a strong sensitivity to the initial guesses required to obtain the flame parameters.

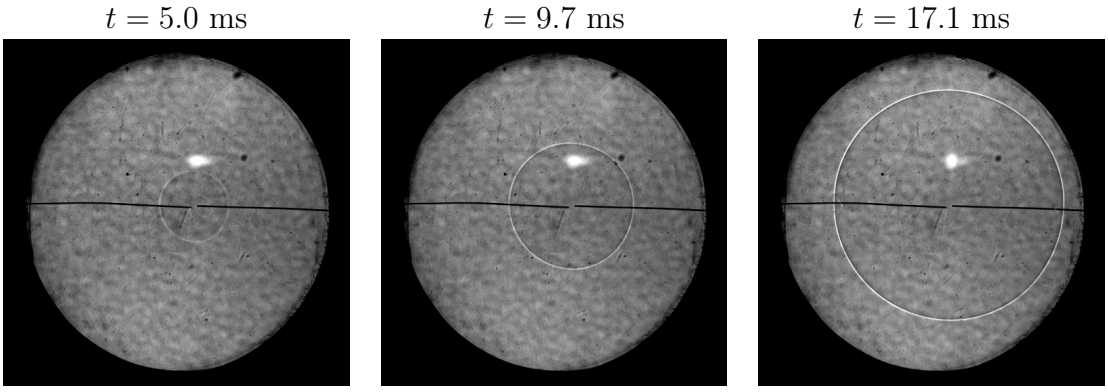

Figure 6.1: Spherical expanding flame propagation in a n-hexane-air mixture at $\Phi = 0.9$ and initial temperature and initial pressure of 393 K and 50 kPa, respectively.

This chapter discusses the performance of nonlinear fitting methods by extracting the laminar flame properties from synthetic data sets. The sensitivity of the results to experimental parameters like initial and final flame radius, the number of points in the data set, and measurement noise, as well as numerical parameters like the initial guess that is used to start the nonlinear fit, are investigated. First, the linear and

non-linear approaches are reviewed and the limits of applicability of the relationship between flame speed and stretch rate are discussed. Then the present nonlinear fitting procedure is described and the performance of the method is evaluated.

6.1 Methodologies to Extract Properties from Spherically Expanding Flames

6.1.1 Linear Methodology

Asymptotic theoretical analysis by Sivashinsky (1976), Matalon and Matkowsky (1982), and Clavin (1985), performed in the limit of high activation energy, reveals a linear relation between the stretched and unstretched propagation speed with respect to the unburned gas in the low stretch rate regime,

$$S_u = S_u^0 - L_B' \kappa. \tag{6.1}$$

S_u and S_u^0 are the stretched and unstretched propagation speeds with respect to the unburnt gas, respectively, $L_B^{'}$ is the unburnt gas Markstein length and κ is the stretch rate. S_u is commonly referred to as the burning speed and S_u^0 as the laminar burning speed. Karlovitz et al. (1953) expressed the stretch rate in terms of the normalized rate of change of an elementary flame front area as,

$$\kappa = \frac{1}{A}\frac{\mathrm{d}A}{\mathrm{d}t}, \tag{6.2}$$

where A is the flame front area. In the case of a spherical flame, the flame surface is given by $A = 4\pi R_f^2$, leading to the following expression for the stretch rate (Lamoureux et al., 2003; Aung et al., 1997; Dowdy et al., 1990; Jerzembeck et al., 2009):

$$\kappa = 2\frac{S_b}{R_f}, \tag{6.3}$$

and given that the stretched propagation speed relative to the burned gas, S_b, corresponds to the flame radius increase rate,

$$S_b = \frac{\mathrm{d}R_f}{\mathrm{d}t}. \tag{6.4}$$

S_b is commonly referred to as the stretched flame speed or spatial velocity and S_b^0 as the unstretched flame speed. For the remainder of the chapter, S_u and S_u^0 will be referred to as burning speed and laminar burning speed, respectively, and S_b and S_b^0 as stretched and unstretched flame speed, respectively. The measured rate of increase of the flame radius, $\mathrm{d}R_f/\mathrm{d}t$, is assumed to be the flame speed since the combustion product is stationary in the laboratory frame. In the case of a large volume vessel and for measurements limited to the initial period of propagation when the flame radius is small compared to the experimental set-up dimensions, the pressure increase can be neglected (Bradley et al., 1996) so that the stretched flame speed and burning speed are linked only through the expansion ratio across the flame front, i.e. $S_u = S_b/\sigma$, where σ is the expansion ratio defined as $\sigma = \rho_u/\rho_b$, where ρ_u and ρ_b are the unburnt and burnt gas densities, respectively. Equation 6.1 can then be rewritten in terms of the stretched and unstretched flame speed as,

$$S_b = S_b^0 - L_B\kappa, \tag{6.5}$$

where $L_B = \sigma L_B'$ is the burnt gas Markstein length or Markstein length. Since the flame radius is a function of time, the stretched flame speed and stretch rate can be linearly extrapolated to zero stretch to obtain the unstretched flame speed.

Substituting Eq. 6.3 into Eq. 6.5, and integrating with respect to time produces an expression for the unstretched flame speed as a function of time and flame radius,

$$S_b^0 \cdot (t_i - t_N) = R_{f,i} - R_{f,N} + 2L_B \ln\left(\frac{R_{f,i}}{R_{f,N}}\right) + C, \tag{6.6}$$

where $i = 0, 1, 2, ..., N$ and C is an integration constant. Equation 6.6 can be used

as part of a least squares fitting procedure and applied to an experimental set of $R_f = f(t)$ data, provided that $R_f \ll D_{\text{exp}}$; D_{exp} is the characteristic dimension of the experimental set-up, i.e. the radius of optical access. The unstretched flame speed, S_b^0, and Markstein length, L_B, are determined from this procedure as the coefficients of the linear fit.

6.1.2 Nonlinear Methodology

Using asymptotic methods based on large activation energy, Ronney and Sivashinsky (1989) obtained a nonlinear model for spherical flame speed as a function of curvature (Eq. 6.7).

$$\left(\frac{S_b}{S_b^0}\right)^2 \ln\left(\frac{S_b}{S_b^0}\right)^2 = -2\frac{L_B\kappa}{S_b^0}. \tag{6.7}$$

This expression can be used directly to derive the unstretched flame speed and the Markstein length, however, $R_f = f(t)$ data must be fitted to polynomials and differentiated to determine $S_b = \mathrm{d}R_f/\mathrm{d}t$ (Halter et al., 2010; Bouvet et al., 2011). Numerical differentiation of the experimental data leads to amplification of existing noise. To avoid differentiating the experimental data, Kelley and Law (2009) proposed an integrated form of Eq. 6.7. In the present study, numerical integration rather than analytic integration, as examined by Kelley and Law (2009), is proposed for extracting the flame properties from the nonlinear result of Ronney and Sivashinsky (1989); the proposed approach is described in Section 6.1.3.

6.1.3 Present Approach for Extracting Flame Properties

Equation 6.7 has unknowns S_b^0 and L_B for a given R_f and $S_b = \mathrm{d}R_f/\mathrm{d}t$. The data, $R_f = f\,(t)$, can be synthetically generated or obtained from an experiment. To avoid numerical differentiation of R_f to obtain S_b, Eq. 6.7 is numerically integrated using the Matlab implicit ode solver ode15i using an initial set of guesses for S_b^0 and L_B.

The integration yields a solution, R_f^{trial}, that is used to compute an objective function,

$$\text{Error} = \sum_{i=0}^{N} \left[R_{f,i} - R_{f,i}^{\text{trial}}\left(\vec{a}, t_i\right) \right]^2, \tag{6.8}$$

where $\vec{a} = \left\{ L_B, S_b^0 \right\}$. The values of L_B and S_b^0 are iteratively refined by minimizing the objective function, Eq. 6.8, using the Levenberg-Maarquardt algorithm implemented in the Matlab nonlinear least squares solver, lsqnonlin.

Previous studies (Kelley and Law, 2009; Halter et al., 2010) investigated the accuracy of the linear and nonlinear methods by using experimental data to extract flame properties. However, the exact unstretched flame speed and Markstein length were not known a priori and the two methods (linear vs. nonlinear) yielded different results. The approach of Chen (2011) used synthetic data generated through detailed numerical simulations; however, the high computational cost yielded a limited sample size. In the performance section of the present nonlinear approach, synthetic data is generated by numerically integrating the flame radius as a function of time, i.e. integrating Eq. 6.9 (Eq. 6.7 rewritten in terms of R_f) for a set of L_B and S_b^0 values.

$$\frac{\mathrm{d}R_f/\mathrm{d}t}{S_b^0} \cdot \ln\left(\frac{\mathrm{d}R_f/\mathrm{d}t}{S_b^0} \right) = -2\frac{L_B}{R_f} \tag{6.9}$$

Different levels of Gaussian noise are added to the solution R_f to simulate the noise present in experimental data. Consequently, the present study assumes that the dynamics of the spherically expanding flame can be perfectly described by Eq. 6.9. As discussed in previous studies (Wu et al., 2015; Jayachandran et al., 2015; Varea et al., 2015), Eq. 6.9 does not always exactly describe the propagation of realistic flames (experimental or from DNS simulations) and other nonlinear equations could be employed (Jayachandran et al., 2015).

6.2 Performance of the Nonlinear Methodology using Numerical Integration

The proposed nonlinear fitting method minimizes the objective function given by Eq. 6.8. The rate of convergence, sensitivity to noise, and robustness of this procedure depends on the minimization method and the behavior of the objective function. An example of the objective function is shown in Fig. 6.2 (a); the contour plot is created by generating synthetic data points of flame radius vs. time for a test case ($L_B = -1$ mm and $S_b^0 = 2.5$ m/s) and then evaluating Eq. 6.8 at different values of the Markstein length and unstretched flame speed. The minimum error occurs over the correct solution point; however, the objective function is rather elongated, indicating that the solution point is much less sensitive to the Markstein length than to the unstretched flame speed. The elongated shape of the minimum in the objective function is also a property of the linear method described in Section 6.1.1. Contours of the objective function obtained through the linear method are shown in Fig. 6.2 (b). The qualitative behavior of the two methods is similar; however, the minimum for the linear method deviates from the actual solution of $L_B = -1$ mm and $S_b^0 = 2.5$ m/s since the flame lies slightly outside of the linear stretch regime.

The minimum error at each Markstein length is shown in Fig. 6.3 for different levels of Gaussian noise added to the test case. The objective function exhibits a global minimum at the correct solution, but the depth of the minimum and the slope in its vicinity decrease when noise is added. For noise levels 1% and higher, the minimum is shallow is shifted to more negative Markstein lengths. Other noise models have been employed, including uniform noise and noise that decreases with increasing flame radius; the results from those models are nearly indistinguishable from those shown in Fig. 6.3.

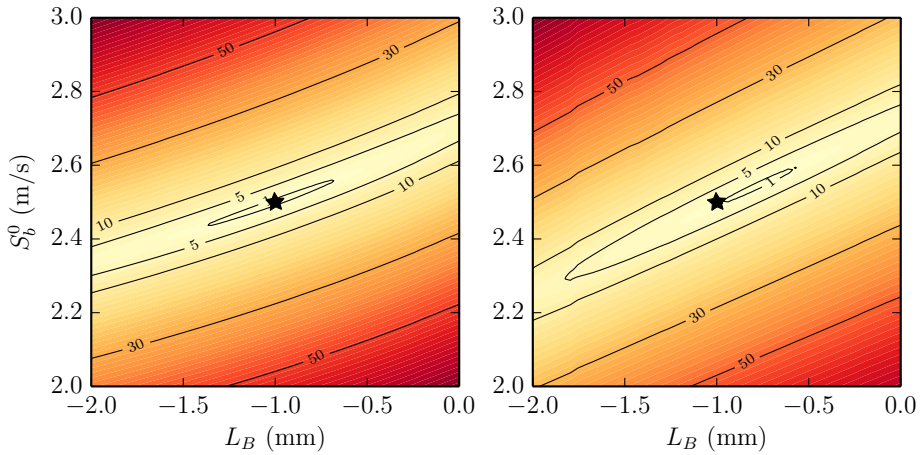

(a) Nonlinear (b) Linear

Figure 6.2: Contour plots of the objective function; the actual solution (indicated by the filled black star) is $L_B = -1$ mm, $S_b^0 = 2.5$ m/s.

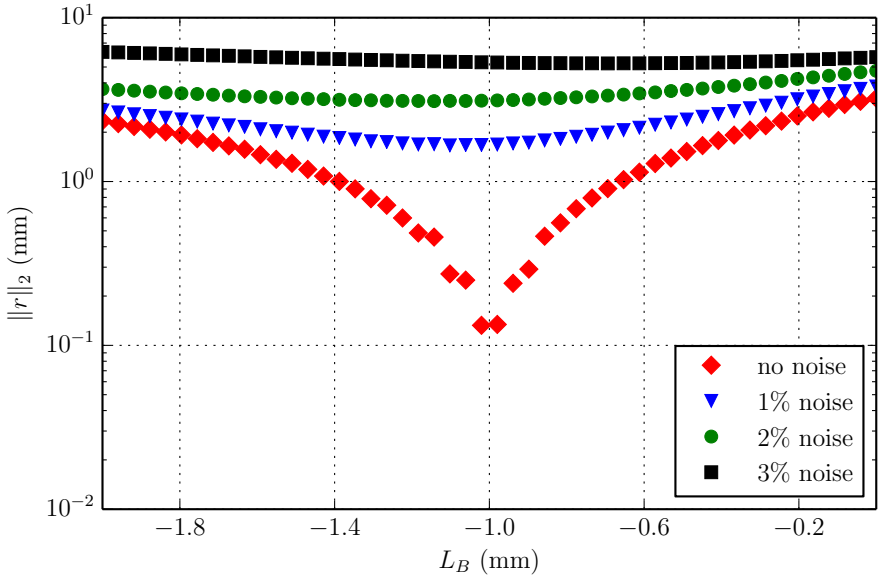

Figure 6.3: Minimum error values for range of S_b^0 as a function of L_B; the actual solution is $L_B = -1$ mm and $S_b^0 = 2.5$ m/s; random Gaussian noise has been included by adding 1%, 2%, and 3% relative error to each flame radius point.

6.2.1 Performance Parameters

To evaluate the performance of the minimization method, synthetic $R_{f,i}$ vs. t_i data with added Gaussian noise are generated using Eq. 6.9 for $L_B \in [-5.0,\ L_{B,\max}]$

mm where $L_{B,\max} = R_{f,0}/2e$ and $S_b^0 \in [0.3, 35]$ m/s; the range of L_B and S_b^0 values are representative of flame properties for typical hydrocarbon-air and hydrogen-air mixtures. The choice of $L_{B,\max}$ is based on a limit obtained from Eq. 6.7. After generating the data, an attempt is made to recover the laminar flame parameters from the synthetic data using a set of initial guesses for L_B and S_b^0. The performance of the present method is evaluated by varying the range of R_f, the size of the data set, i.e. $|R_f|$, and the added Gaussian noise. The performance of the method is quantified in terms of the uncertainty and variance of the fitted values of L_B and S_b^0. The uncertainty for $\vec{a}$ is found by extracting the Jacobian, J_{ik}, using the Matlab function lsqnonlin where

$$J_{ik}^2 = \left.\frac{\partial^2 r_i}{\partial a_k^2}\right|_{\vec{a}^*} \tag{6.10}$$

$$r_i = R_{f,i} - R_{f,i}^{\text{trial}}\left(\vec{a}^*, t_i\right) \tag{6.11}$$

and $\vec{a}^*$ is the vector of parameters giving the best fit. The uncertainty is then given by,

$$\Delta\vec{a}_k = \left[3\sum_i \Delta {R_{f,i}}^2 / \sum_i J_{ik}^2\right]^{1/2}, \tag{6.12}$$

where $\Delta R_{f,i}$ is the uncertainty in the i^{th} data point and $\Delta\vec{a} = \left\{\Delta L_B, \Delta S_b^0\right\}$. The variance, σ^2, of the Markstein length and the unstretched flame speed is found by sampling each combination of L_B and S_b^0 100 times. The samples for an individual combination are then fitted to a Gaussian distribution,

$$\phi\left(\vec{a}^*, \vec{\sigma}, \vec{\mu}\right) = \frac{1}{\vec{\sigma}\sqrt{2\pi}}\exp\left(\frac{\left(\vec{a}^* - \vec{\mu}\right)^2}{2\vec{\sigma}^2}\right), \tag{6.13}$$

to find $\vec{\sigma}$ and the mean, μ.

Figure 6.4 shows examples of synthetic data sets characterized by positive and negative Markstein lengths. The sets are generated using 100 points and added Gaussian noise of 1%. In each case, both the correct values of the unstretched flame

speed and Markstein length are obtained by applying the nonlinear least-squares fitting procedure. The quality of the fitting is evident in the plot presenting the evolution of S_b as a function of the stretch rate κ.

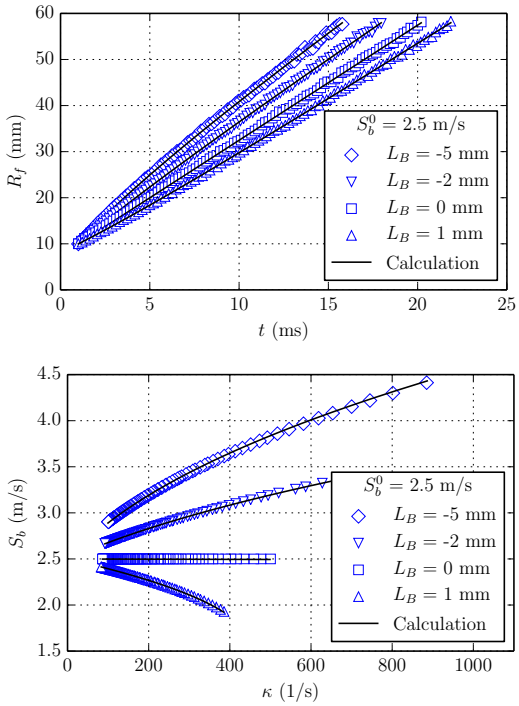

Figure 6.4: Examples of synthetic data and nonlinear least-square regression curves obtained using the present numerical method; flame radius as a function of time (top) and flame speed as a function of stretch (bottom).

6.2.2 Effect of Data Set Size: $|R_f|$

To study the effect of data set size on convergence, sets of R_f vs. t are generated based on the following parameters: $R_{f,0} = 10$ mm, $R_{f,N} = 58$ mm, $|R_f| = \{10, 20, 50, 100\}$ and 1% added Gaussian noise. The $|R_f|$ values represent typical data set sizes obtained from experiments. The size of the data set depends on the framing rate of the camera that is used to acquire the flame images, the initial energy deposition used to ignite the mixture, and the mixture: faster flames lead to less images and vice-versa. The nonlinear least-squares solver uses the linear method solution as an initial guess for L_B and S_b^0.

The results shown in Fig. 6.5 indicate that the variance of L_B increases as the size of the data set decreases. There is a decrease of 60% in the variance of L_B as $|R_f|$ increases from 10 to 100 points for $L_B = -5.0$ mm, this is shown in Fig. 6.5. Qualitatively, the change in variance of L_B from 100 to 50 points is not significant. The variance of L_B does not change over the range of unstretched flame speeds tested; this is shown in the top ($S_b^0 = 0.3$ m/s) and bottom ($S_b^0 = 35.0$ m/s) plots of Fig. 6.5. The variance of L_B decreases as L_B increases from negative to positive values; however, it should be noted that the variance has not been normalized with the Markstein length. Overall, Fig. 6.5 indicates that for the $|R_f|$ values tested, 100 points yields the lowest variance in L_b; however, the use of 50 points yields comparable results, suggesting that at least 50 points should be used when extracting flame properties.

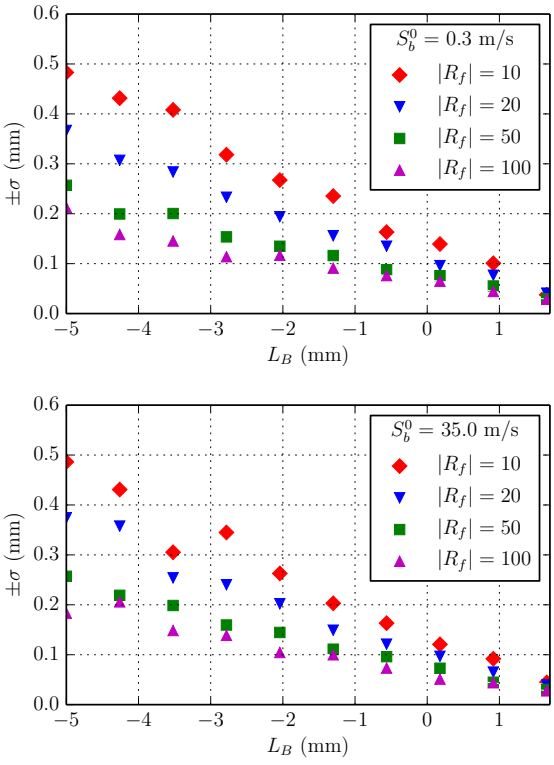

Figure 6.5: Effect of $|R_f|$ on variance of L_B for $R_f = [10, 58]$ mm, 1% Gaussian noise, $S_b^0 = 0.3$ m/s (top) and $S_b^0 = 35.0$ m/s (bottom).

There is a decrease in the variance of S_b^0 from 2% to 1% as $|R_f|$ increases from

10 to 100 points for $L_B = -5.0$ mm; this is shown in the top plot of Fig. 6.6. The bottom plot of Fig. 6.6 shows a decrease in the variance of S_b^0 from 0.9% to 0.3% as $|R_f|$ increases from 10 to 100 points for $L_B = 1.7$ mm. The variance of S_b^0 changes over the range of Markstein lengths tested; this is shown in the top ($L_B = -5$) and bottom ($L_B = 1.7$ mm) plots of Fig. 6.6. The variance of S_b^0 is constant over all the unstretched flame speeds tested. The variance of S_b^0 is 2% and 0.9% for $L_B = -5$ mm and $L_B = 1.7$ mm, respectively, and $|R_f| = 10$.

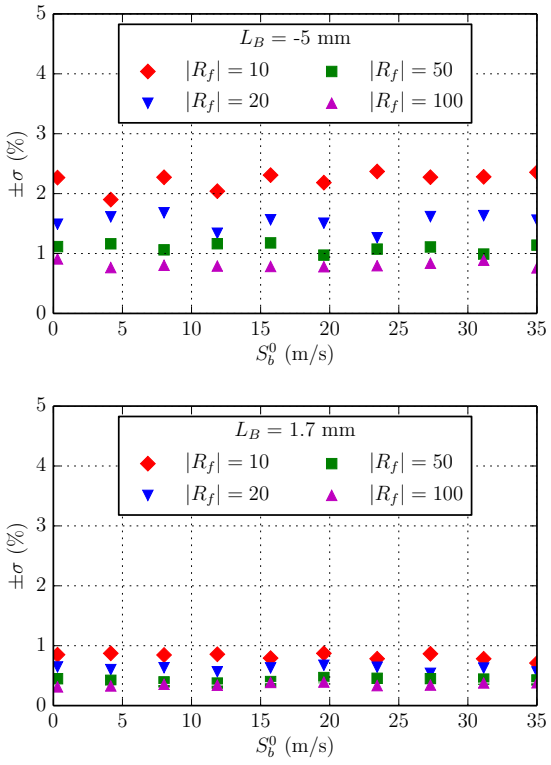

Figure 6.6: Effect of $|R_f|$ on variance of S_b^0 for $R_f = [10, 58]$ mm, 1% Gaussian noise, $L_B = -5$ mm (top) and $L_B = 1.7$ mm (bottom).

The uncertainty for a combination of $L_B \in \left[-5.0, L_{B,\max}\right]$ mm and $S_b^0 = 0.3$ m/s is shown in Fig. 6.7 for $|R_f| = 10$ (top) and 100 (bottom). The black solid line indicates the actual result, and the markers show the calculated result using the nonlinear methodology, and in addition, the uncertainty in the calculated result is illustrated by the shaded region. The top plot in Fig. 6.7 indicates that 10 points is not sufficient to obtain an accurate calculation of the Markstein length for $L_B \in [-5, -1]$

mm. This is shown by the shaded regions lying outside of the black line. When the number of points increases to 100 (bottom plot of Fig. 6.7) the correct calculation of the Markstein length (within the uncertainty) is obtained for the entire L_B range tested.

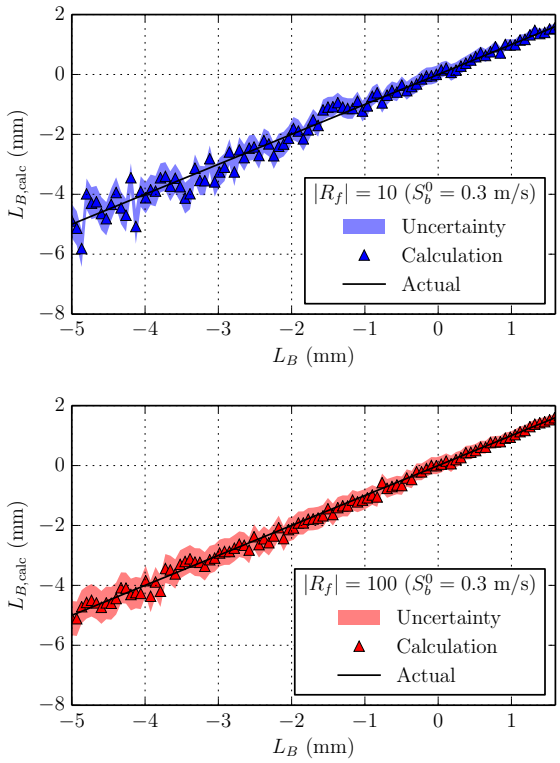

Figure 6.7: Effect of $|R_f|$ on uncertainty of L_B for $R_f = [10, 58]$ mm, 1% Gaussian noise, $S_b^0 = 0.3$ m/s.

The uncertainty for a combination of $S_b^0 \in [0.3, 35]$ m/s and $L_B = -5.0$ mm is shown in Fig. 6.8 for $|R_f| = 10$ (top) and 100 (bottom). The top plot in Fig. 6.8 indicates that 10 points is not sufficient to obtain an accurate calculation of the unstretched flame speed for $S_b^0 \in [18, 35]$ m/s. When the number of points increases to 100, the correct calculation of the unstretched flame speed (within the uncertainty) is obtained for the entire S_b^0 range tested.

Analysis of the figures presented in this subsection and in Appendix F suggests that for the range of L_B and S_b^0 tested, there needs to be at least 50 points in the data set, i.e. flame radius vs. time, to obtain accurate results of the flame properties.

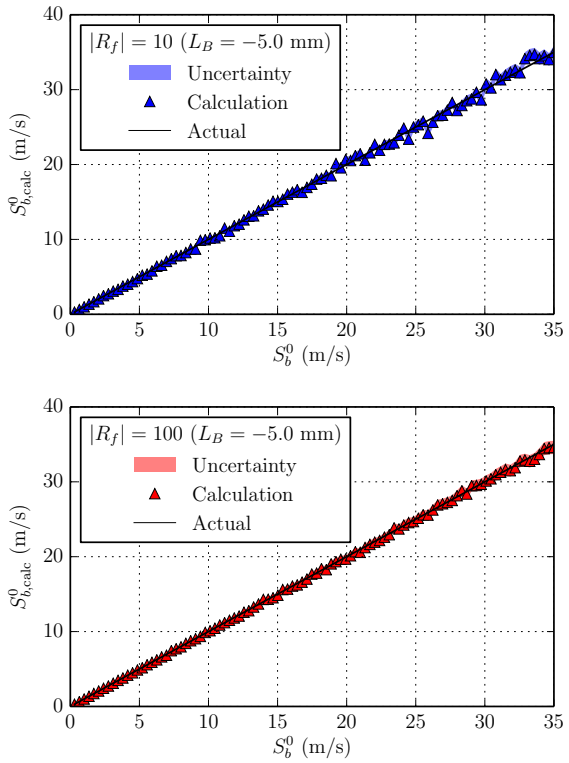

Figure 6.8: Effect of $|R_f|$ on uncertainty of S_b^0 for $R_f = [10, 58]$ mm, 1% Gaussian noise, $L_B = -5.0$ mm.

However, there does exist a range of L_B and S_b^0 values over which a lower number of values in the data, i.e. $|R_f| = 10$ would be sufficient to extract accurate flame properties.

6.2.3 Effect of Data Set Range: $R_f = \left[R_{f,0}, R_{f,N}\right]$

To study the effect of data set range on convergence, sets of R_f vs. t are generated based on the following parameters: $R_f = \left[R_{f,0}, R_{f,N}\right]$, where $R_{f,0} = 10$ mm and $R_{f,N} = \{25, 38, 58, 70\}$ mm, $|R_f| = N = 100$ and 1% added Gaussian noise. The $R_{f,N}$ values represent typical data set sizes obtained from experiments. The range of the flame radius depends on the size of the combustion vessel windows, the initial energy deposition used to ignite the mixture, and the mixture; instabilities in the flame lead to a maximum usable flame radius below which the flame is still laminar.

The results shown in Fig. 6.9 indicate that the variance of L_B increases as $R_{f,N}$ decreases. There is a decrease of 80% in the variance of L_B as $R_{f,N}$ increases from 25 to 70 mm for $L_B = -5.0$ mm. Qualitatively, the change in variance of L_B from a 58 to 70 mm final flame radius is not significant. The variance of L_B does not change over the range of unstretched flame speeds tested. Similar to Fig. 6.5, the variance of L_B decreases as L_B increases from negative to positive values. Overall, Fig. 6.9 indicates that for the $R_{f,N}$ values tested and a fixed $R_{f,0}$ of 10 mm, a final flame radius of 70 mm yields the lowest variance in L_B; however, $R_{f,N} = 58$ mm yields comparable results.

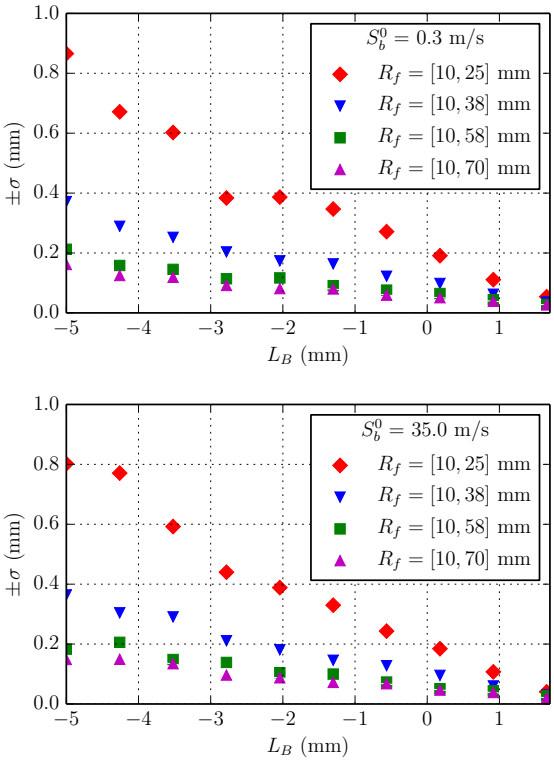

Figure 6.9: Effect of $R_f = \left[R_{f,0}, R_{f,N}\right]$ on variance of L_B for 1% Gaussian noise, $|R_f| = 100$, $S_b^0 = 0.3$ m/s.

There is an increase in the variance of S_b^0 from 0.5% to 4.5% as $R_{f,N}$ increases from 25 to 70 mm for $L_B = -5.0$ mm; this is shown in the top plot of Fig. 6.10. The bottom plot of Fig. 6.10 shows a decrease in the variance of S_b^0 from 1.2% to 0.2% as $R_{f,N}$ increases from 25 to 70 mm for $L_B = 1.7$ mm. The variance of S_b^0 changes

over the range of Markstein lengths tested; this is shown in the top ($L_B = -5$) and bottom ($L_B = 1.7$ mm) plots of Fig. 6.10. The variance of S_b^0 is constant over all the unstretched flame speeds tested.

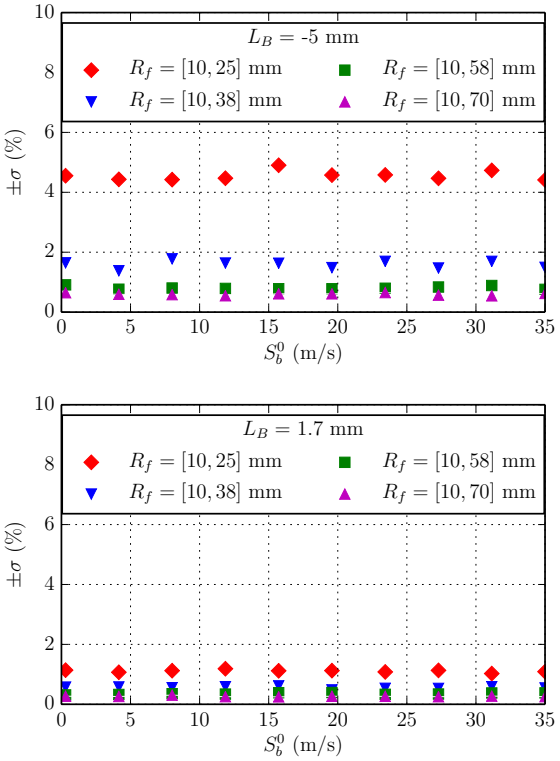

Figure 6.10: Effect of $R_f = \left[R_{f,0}, R_{f,N}\right]$ on variance of S_b^0 for 1% Gaussian noise, $|R_f| = 100$, $L_B = -5$ mm (top) and $L_B = 1.7$ mm (bottom).

The uncertainty for a combination of $L_B \in \left[-5.0, L_{B,\max}\right]$ mm and $S_b^0 = 0.3$ m/s is shown in Fig. 6.11 for $R_{f,N} = 25$ mm (top) and $R_{f,N} = 70$ mm (bottom). The top plot indicates that a final flame radius of 25 mm is not sufficient to obtain an accurate calculation of the Markstein length for $L_B \in [-5, 0]$ mm. This is shown by the shaded regions lying outside of the black line. When the final flame radius increases to 70 mm, bottom plot of Fig. 6.11, the correct calculation of the Markstein length (within the uncertainty) is obtained for the entire L_B range tested.

The uncertainty for a combination of $S_b^0 \in [0.3, 35]$ m/s and $L_B = -5.0$ mm is shown in Fig. 6.12 for $R_{f,N} = 25$ mm (top) and $R_{f,N} = 70$ mm (bottom). The top plot in Fig. 6.12 indicates that $R_{f,N} = 25$ mm is not sufficient to obtain an accurate

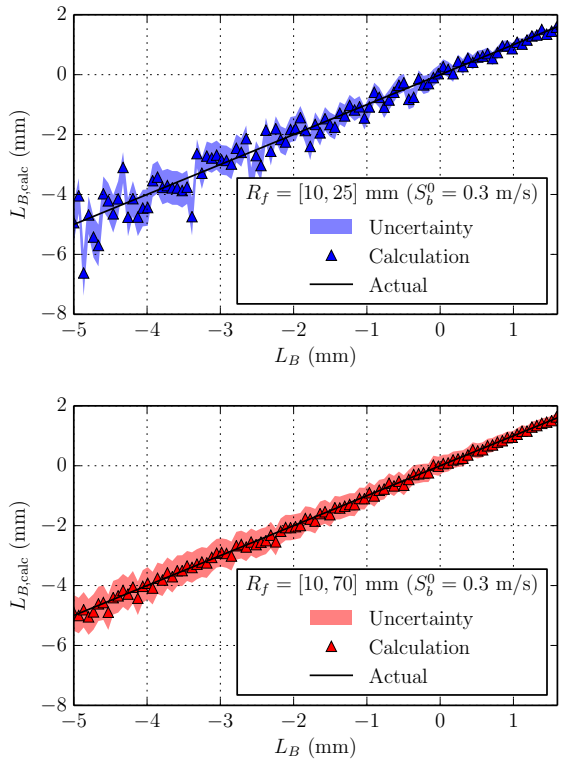

Figure 6.11: Effect of $R_f = \left[R_{f,0}, R_{f,N}\right]$ on uncertainty of L_B for 1% Gaussian noise, $|R_f| = 100$, $S_b^0 = 0.3$ m/s.

calculation of the unstretched flame speed for $S_b^0 \in [8, 35]$ m/s. When $R_{f,N} = 70$ mm, the correct calculation of the unstretched flame speed (within the uncertainty) is obtained for the entire S_b^0 range tested.

Analysis of the figures presented in this subsection and in Appendix F suggests that for the range of L_B and S_b^0 tested, there needs to a minimum final flame radius of 58 mm in the data for a fixed initial flame radius of 10 mm to obtain accurate results of the flame properties; this corresponds to a range of 48 mm. However, if only an accurate representation of the unstretched flame speed is needed, then a minimum final flame radius of 38 mm is sufficient; this corresponds to a range of 28 mm.

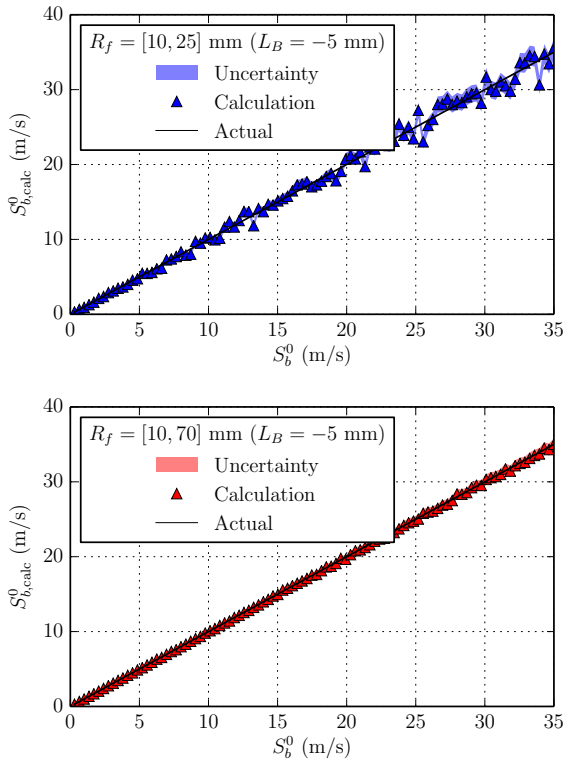

Figure 6.12: Effect of $R_f = \left[R_{f,0}, R_{f,N}\right]$ on uncertainty of S_b^0 for 1% Gaussian noise, $|R_f| = 100$, $L_B = -5.0$ mm.

6.2.4 Effect of Gaussian Noise Addition

The addition of noise to R_f is more representative of what is obtained experimentally when extracting flame radii from spherically propagating flame images. To study the effect of noise on convergence, sets of $R_{f,i}$ vs. t_i were generated based on the following parameters: $R_f = \left[R_{f,0}, R_{f,N}\right]$, where $R_{f,0} = 10$ mm and $R_{f,N} = 58$ mm, $|R_f| = 100$ and $1\%, 3\%, 5\%$, and 10% added Gaussian noise. Gaussian noise is introduced to the instantaneous flame radius with no noise, $R_f^{0\%\text{ noise}}$, via a noise vector, $\hat{e}$. The resulting noisy data sets are described by

$$R_{f,i} = R_{f,i}^{0\%\text{ noise}} \cdot (1 + j \cdot \hat{e}), \tag{6.14}$$

where j is the fractional noise. The amount of noise in an experimental data set depends on the number of pixels on the camera CCD, the sphericity of the flame which

is affected by the initial energy deposition as well as the method of energy deposition (spark versus laser ignition), the geometry of the electrodes (Bane, 2010; Bane et al., 2015), the robustness of the flame detection software, and flame instabilities.

The results shown in Fig. 6.13 indicate that the variance of L_B increases as the Gaussian noise increases. There is a decrease of 90% in the variance of L_B as the Gaussian noise decreases from 10% to 1% for $L_B = -5.0$ mm. The variance of L_B does not change over the range of unstretched flame speeds tested. Similar to Figs. 6.5 and 6.9, the variance of L_B decreases as L_B increases from negative to positive values.

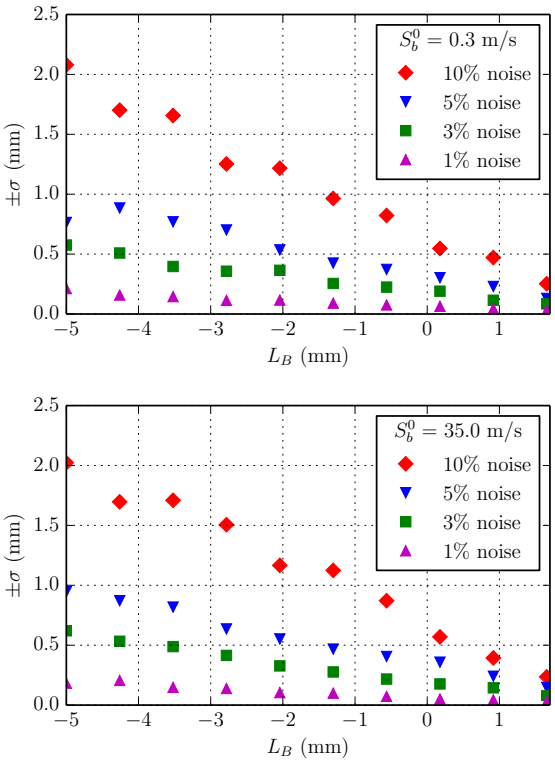

Figure 6.13: Effect of Gaussian noise on variance of L_B for $R_f = [10, 58]$ mm, $|R_f| = 100$, $S_b^0 = 0.3$ m/s (top) and $S_b^0 = 35.0$ m/s (bottom).

There is a decrease in the variance of S_b^0 from 8% to 0.5% as the Gaussian noise decreases from 10% to 1% for $L_B = -5.0$ mm; this is shown in the top plot of Fig. 6.14. The bottom plot of Fig. 6.14 shows a decrease in the variance of S_b^0 from 3% to 0.1% as the Gaussian noise decreases from 10% to 1% for $L_B = 1.7$ mm. The

variance of S_b^0 changes over the range of Markstein lengths tested; this is shown in the top ($L_B = -5$) and bottom ($L_B = 1.7$ mm) plots of Fig. 6.14. The variance of S_b^0 is constant over all the unstretched flame speeds tested.

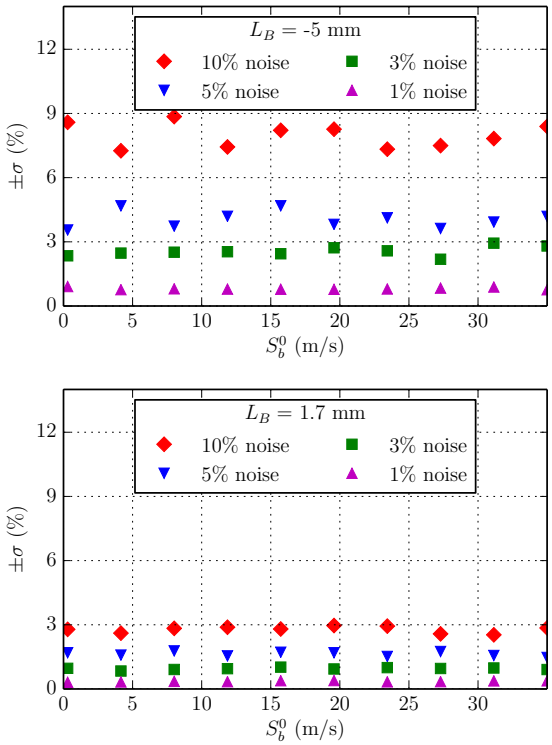

Figure 6.14: Effect of Gaussian noise on variance of S_b^0 for $R_f = [10, 58]$ mm, $|R_f| = 100$, $L_B = -5$ mm (top) and $L_B = 1.7$ mm (bottom).

The uncertainty for a combination of $L_B \in \left[-5.0, L_{B,\max}\right]$ mm and $S_b^0 = 0.3$ m/s is shown in Fig. 6.15 for 10% (top) and 1% (bottom) Gaussian noise. The top plot indicates that data with 10% Gaussian noise will not yield an accurate calculation of the Markstein length; however, the results will have the appropriate uncertainty bounds. This is shown by the black line lying within the shaded regions. The same can be said for added Gaussian noise of 1% (shown in Fig. 6.15), although the results will be a more accurate representation of the Markstein length. In addition, the calculated Markstein lengths are more closely clustered to the actual result for positive values.

The uncertainty for a combination of $S_b^0 \in [0.3, 35]$ m/s and $L_B = -5.0$ mm is shown in Fig. 6.16 for 10% (top) and 1% (bottom) Gaussian noise. The top plot

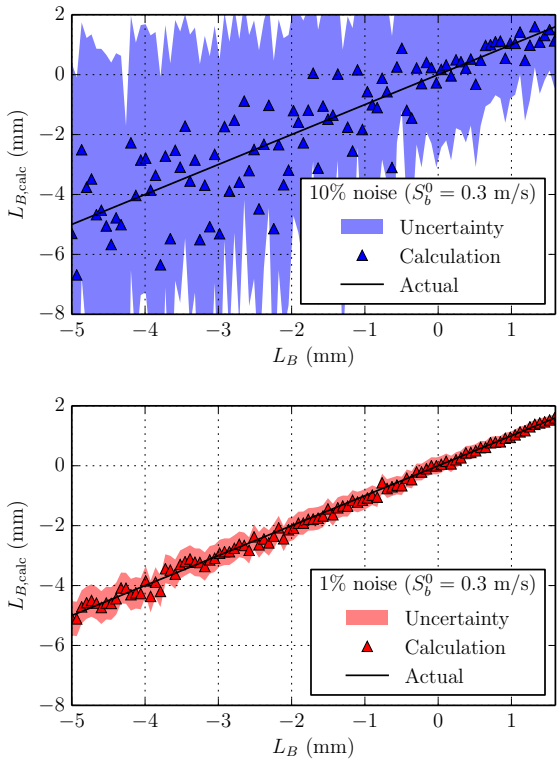

Figure 6.15: Effect of Gaussian noise on uncertainty of L_B for $R_f = [10, 58]$ mm, $|R_f| = 100$, $S_b^0 = 0.3$ m/s.

in Fig. 6.16 shows similar behavior to that observed in the uncertainty of L_B; 10% Gaussian noise will not yield an accurate calculation of the unstretched flame speed; however, the results will have the appropriate uncertainty bounds. Added Gaussian noise of 1% (shown in Fig. 6.16) will yield a more accurate representation of the unstretched flame speed.

Analysis of the figures presented in this subsection and in Appendix F suggests that there is no minimum uncertainty in the flame radius needed to extract flame properties. The accuracy of the results does depend on the amount of noise in the data set; however, the method used to calculate the uncertainty of flame properties yields the appropriate uncertainty bounds.

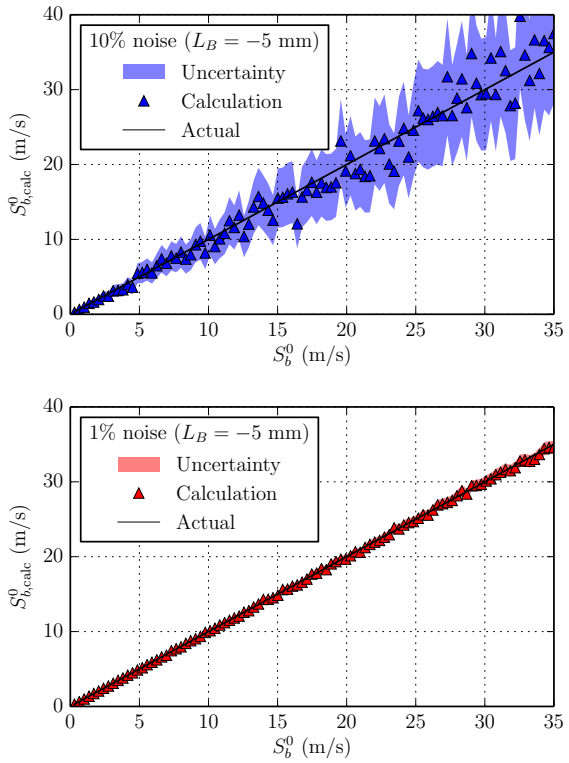

Figure 6.16: Effect of Gaussian noise on uncertainty of S_b^0 for $R_f = [10, 58]$ mm, $|R_f| = 100$, $L_B = -5.0$ mm.

6.2.5 Implementation in Experimental Results

Two experimental cases are tested with the nonlinear methodology using numerical integration discussed in Section 6.1.3. The cases correspond to premixed spherically propagating n-hexane-air flames. The characteristics of each test are shown in Table 6.1.

case	Φ $(-)$	R_f^0 (mm)	R_f^{final} (mm)	$\lvert R_f \rvert$ $(-)$	$L_{B,\max}$ (mm)	L_B (mm)	S_b^0 (m/s)
1	0.76	22.4	44.8	151	4.12	1.02 ± 0.09	16.01 ± 0.12
2	0.86	25.3	34.0	37	4.65	0.24 ± 0.05	24.62 ± 0.09

Table 6.1: Parameters describing premixed n-hexane-air flames and flame properties extracted with the nonlinear methodology of Section 6.1.3.

Case 1 ($T_0 = 300$ K, $P_0 = 100$ kPa), shown in Fig. 6.17, is a lean flame that has an

initial and final flame radius of 22.4 mm and 44.8 mm, respectively; this corresponds to a flame radius range of 22.4 mm. In general, 22.4 mm is a rather small range, however this particular flame has a Markstein length of 1.02 mm; according to Fig. F.54 and F.55 in Appendix F, at the aforementioned Markstein length, a minimum range of 15 mm is sufficient to extract accurate flame properties if $|R_f| = 100$. Case 1 is described by $|R_f| = 151$.

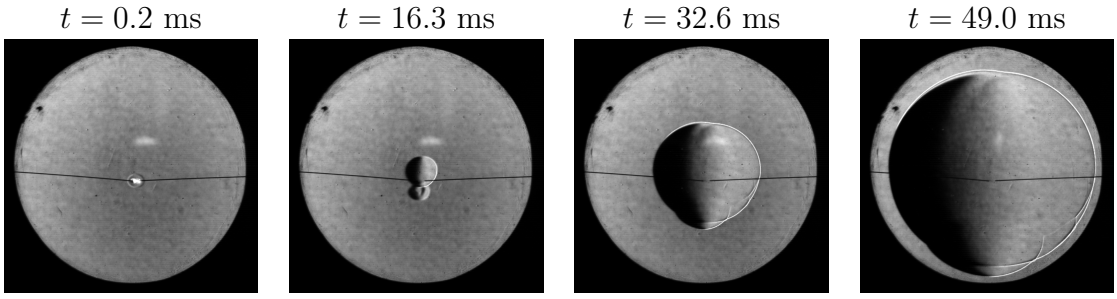

Figure 6.17: Spherical expanding flame propagation in a n-hexane-air mixture at $\Phi = 0.76$ and initial temperature and initial pressure of 300 K and 100 kPa, respectively.

Case 2 ($T = 300$ K, $P_0 = 50$ kPa), shown in Fig. 6.18, has an initial and final flame radius of 25.3 mm and 34.0 mm, respectively; this corresponds to a flame radius range of 8.7 mm. This flame has a Markstein length of 0.24 mm; according to the range tested in Fig. F.54 in Appendix F, at the aforementioned Markstein length, a range less than 15 mm was not tested; however, the results are expected to become noisier with a decrease in range. Given such a low flame radius range and number of points ($|R_f| = 37$), the accuracy of case 2 is questionable.

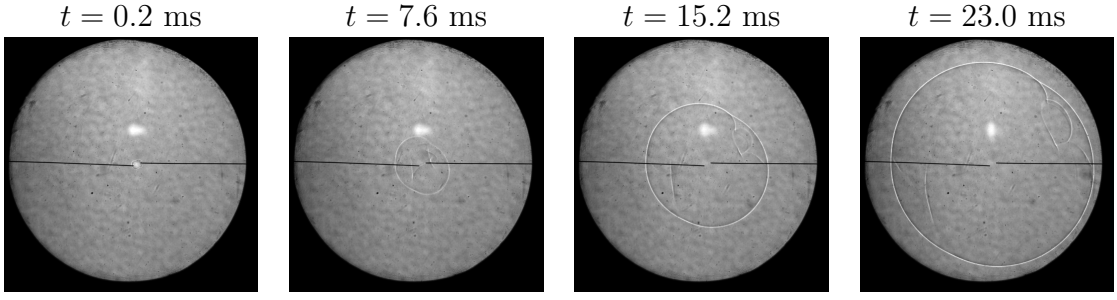

Figure 6.18: Spherical expanding flame propagation in a n-hexane-air mixture at $\Phi = 0.86$ and initial temperature and initial pressure of 300 K and 50 kPa, respectively.

Figure 6.19 shows the radius and calculated flame speed for the cases described in Table 6.1. The uncertainty in the flame radius, ΔR_f, is approximated by assuming a linear dependence over time. The flame radius uncertainty can then be applied to Eq. 6.13 to estimate the uncertainty in the Markstein length and unstretched flame speed.

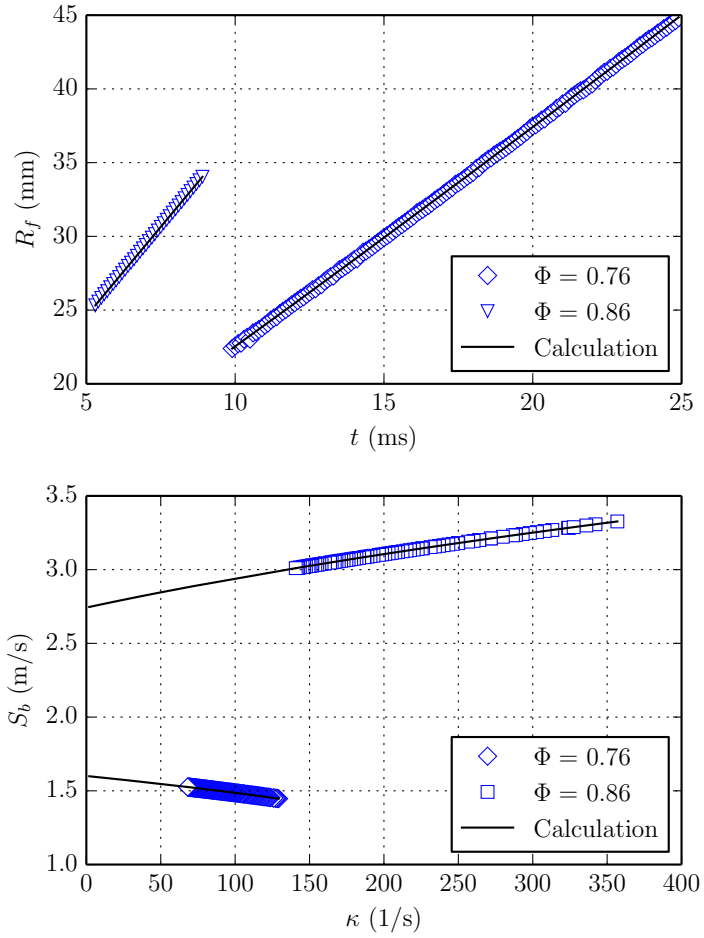

Figure 6.19: Radius and calculated flame speed for the cases described in Table 6.1.

6.3 Closing Remarks

The performance and sensitivity of a nonlinear flame speed extraction method is analyzed in this chapter. The objective function, Eq. 6.8, exhibits a shallow minimum

that depends only weakly on the Markstein length. When noise is added to the synthetic data, the local minimum becomes shallower and its depth is decreased. This can produce substantial errors in the calculated Markstein length. The uncertainty of L_B and S_b^0 is affected by the size of the flame radius data; there needs to be at least 50 points in the data, i.e. flame radius vs. time, to obtain accurate results of the flame properties. However, there does exist a range of L_B and S_b^0 values over which a lower number of values in the data, i.e. $|R_f| = 10$ would be sufficient to extract accurate flame properties. The uncertainty of L_B and S_b^0 is also affected by the data range; there needs to a minimum final flame radius of 58 mm in the data for a fixed initial flame radius of 10 mm to obtain accurate results of the flame properties; this corresponds to a range of 48 mm. However, if only an accurate representation of the unstretched flame speed is needed, then a minimum final flame radius of 38 mm is sufficient; this corresponds to a range of 28 mm. In addition, a small range can be used for certain flames that have a positive Markstein length, as long as a sufficient number of data points are used.

Chapter 7

Spherical *n*-Hexane-Air Flame Characterization[9]

The present chapter implements the methods described in Chapter 6 to characterize spherically expanding n-hexane-air flames.

During the flight phases of an aircraft, the pressure within the fuel tank varies between 0.2 atm to 1 atm. To assess the risk of an accidental combustion event during the flight phases of an aircraft, it is necessary to characterize properties such as the burning speed of fuel-air mixtures over a wide range of initial pressures. n-Hexane has been extensively used at the Explosion Dynamics Laboratory as a single component surrogate of kerosene (Boettcher et al., 2012; Bane, 2010; Boettcher, 2012), n-hexane exhibits a relatively high vapor pressure which facilitates experimenting at ambient temperature. Although more representative surrogates can be used for kerosene (Dagaut and Cathonnet, 2006; Dagaut et al., 2006; Dooley et al., 2010), n-hexane exhibits a relatively high vapor pressure which facilitates experimenting at ambient temperature. In contrast to n-heptane, which has been widely studied, n-hexane oxidation has received much less interest (Simmie, 2003). Curran et al. (1995) studied hexane isomer chemistry through the measurement and modeling of exhaust gases from an engine. Ignition delay-time behind a shock wave has been measured by Burcat et al. (1996) and Zhukov et al. (2004). Boettcher et al. (2012) studied the effect of the heating rate on the low temperature oxidation of n-hexane by air, and

[9]The author thanks Dr. Nabiha Chaumeix for sharing with the EDL her flame detection program and Simon Lapointe for performing the FlameMaster calculations.

the minimum temperature of a heated surface to ignite n-hexane-air mixtures. Bane (2010) measured the minimum ignition energy of several n-hexane-air mixtures. A limited number of studies have been found on the laminar burning speed. Davis and Law (1998) measured the laminar burning speed of n-hexane-air mixtures at ambient conditions using the counterflow twin flame technique. Farrell et al. (2004) used pressure traces from spherically expanding flames to determine the burning speed of n-hexane-air mixtures at an initial temperature and pressure of 450 K and 304 kPa, respectively. Kelley et al. (2011) reported experimental measurements using spherically expanding flames, at an initial temperature of 353 K and a pressure range of $100 - 1000$ kPa. Ji et al. (2010) used the counterflow burner technique to measure the burning speed of n-hexane-air mixtures at an initial temperature and pressure of 353 K and 100 kPa, respectively. In contrast to previous work, the present chapter focuses on initial conditions below atmospheric pressure in order to simulate aircraft fuel tank conditions.

7.1 Experimental Setup and Extraction of Flame Properties

The experiments are performed in the 22 L combustion vessel described in Section 2.1, the set of experiments is tabulated in Appendix D.2. Two parallel flanges are used to mount electrodes for the ignition system. The flames are ignited using a capacitive discharge through a transformer to create a spark between two electrodes. The circuit is described in detail by Kwon et al. (2007). The ignition system generates a spark with energy on the order of 300 mJ across $2 - 4$ mm spark gaps. The electrodes are made out of tungsten wire and are 0.38 mm in diameter. A high-speed camera is used to record the flame propagation observed using Schlieren visualization and shadowgraphy at a rate of $10,000$ frames per second with a resolution of 512×512. The spherically propagating flames are processed by first applying a mask over each image to remove the background (electrodes). Edge detection is then used to identify

the expanding flame edge. A binary value of 0 indicates the background and a binary value of 1 indicates the flame edge. An ellipse is fitted to the detected flame edge; the ellipse parameters are then used to obtain an equivalent radius. Finally, the nonlinear methodology described in Section 6.1.3 is applied to the radius data to obtain the unstretched flame speed, S_b^0, and the Markstein length, L_B. The laminar burning speed, S_u^0, is related to the unstretched flame speed through the expansion so that,

$$S_u^0 = \frac{S_b^0}{\sigma} \quad \text{where} \quad \sigma = \frac{\rho_u}{\rho_b}. \tag{7.1}$$

7.2 Unstretched Burning Speed Experimental Results

A set of experiments at an initial temperature of 296 K and pressure of 100 kPa were performed and compared with previous studies and with 1D freely propagating flame calculations obtained using FlameMaster (Pitsch.). The results are shown in Fig. 7.1 along with results previously obtained by Davis and Law (1998). The uncertainty in the burning speeds is on average 6%, the value is based on previous estimates made by Mével et al. (2009a) who used the same flame detection software implemented in the present study. A Mann-Whitney-Wilcoxon (MWW) RankSum test is used to test if two distributions are significantly different or not. The test provides a p-value, p, to indicate whether the differences between two data sets are statistically significant. If $p \leq 0.05$, the two distributions are significantly different, and if $p > 0.05$, the distributions do not significantly differ. A comparison of the data at 100 kPa obtained in the present study with the data of Davis and Law (1998) results in $p = 0.59$; on this basis, the differences between the two data sets are not statistically significant.

The evolution of the unstretched burning speed as a function of equivalence ratio is studied at an initial pressure of 50 kPa. Figure 7.2 shows the results obtained at initial pressures of 100 kPa and 50 kPa. The uncertainty associated with the burning speed measurements, on the order of 6%, makes it difficult to differentiate between

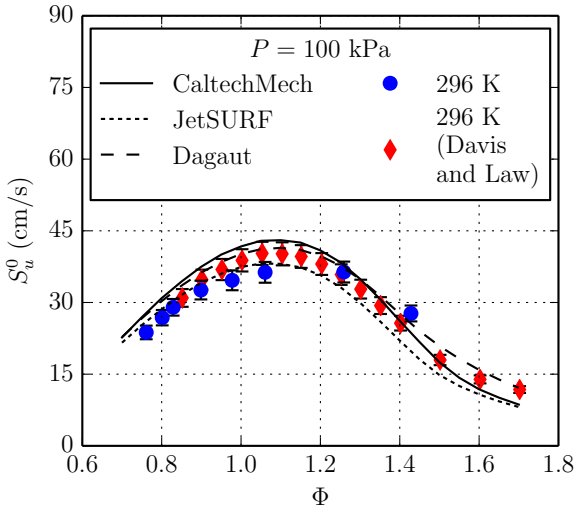

Figure 7.1: Experimental laminar burning speed of n-hexane-air mixtures as a function of equivalence ratio at an initial pressure of 100 kPa along numerical calculations.

the results obtained at an initial pressure of 50 kPa and those obtained at an initial pressure of 100 kPa. Using the MWW Ranksum test to compare the unstretched burning speeds at 100 kPa and 50 kPa results in a p-value of 0.52, therefore the differences between the two data sets are not statistically significant.

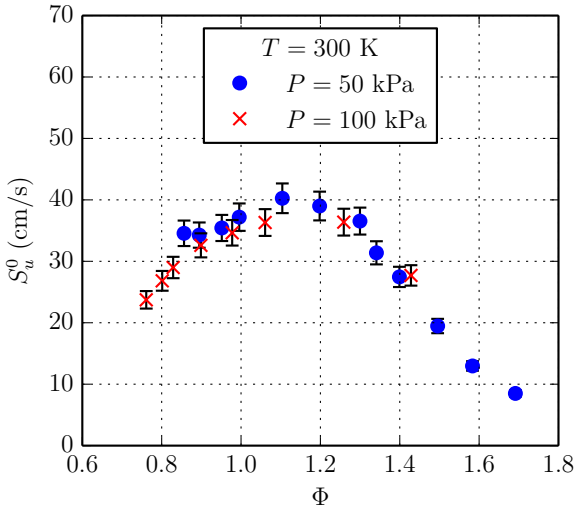

Figure 7.2: Experimental laminar burning speed of n-hexane-air mixtures as a function of equivalence ratio at an initial temperature of 296 K and initial pressures of 50 kPa and 100 kPa.

The effect of initial pressure on the S_u^0 is investigated at $\Phi = 0.90$ and an initial temperature of 353 K. The results are shown in Fig 7.3 along with the results of Kelley et al. (2011) obtained at initial pressures of $100 - 1000$ kPa.

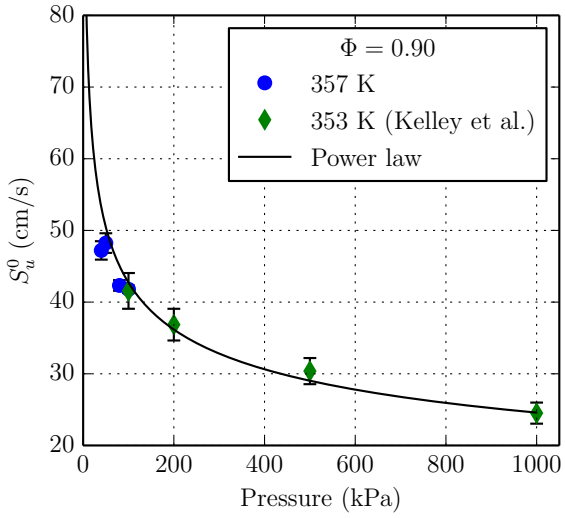

Figure 7.3: Experimental laminar burning speed of n-hexane-air mixtures as a function of initial temperature and pressure.

The unstretched burning speed decreases significantly with increasing initial pressure, 20% between 50 and 100 kPa and 53% between 50 and 1000 kPa. This dependence can be modeled by a power law: $S_u^0(P) = 129 \times P^{-0.24}$.

The effect of initial temperature is studied at an initial pressure of 50 kPa and three equivalence ratios, $\Phi = \{0.90, 1.10, 1.40\}$. The results are shown in Fig. 7.4.

At initial temperatures of 296 K to 380 K, the unstretched burning speed increases 47% at $\Phi = 1.00$ and 64% at $\Phi = 0.90$. The lean mixtures exhibit the highest rate of unstretched burning speed increase (0.27 cm.s^{-1}.K^{-1}) with initial temperature increase, whereas the rich mixtures exhibit the lowest rate of unstretched burning speed increase (0.18 cm/s.K) with initial temperature increase.

Figure 7.5 shows the variation of the Marsktein length with equivalence ratio at an initial temperature and pressure of 296 K and 50 kPa, respectively. Lean and rich mixtures exhibit large positive (0.2 mm) and negative (-1.1 mm) Markstein lengths, respectively. The transition from positive to negative Markstein length values occurs

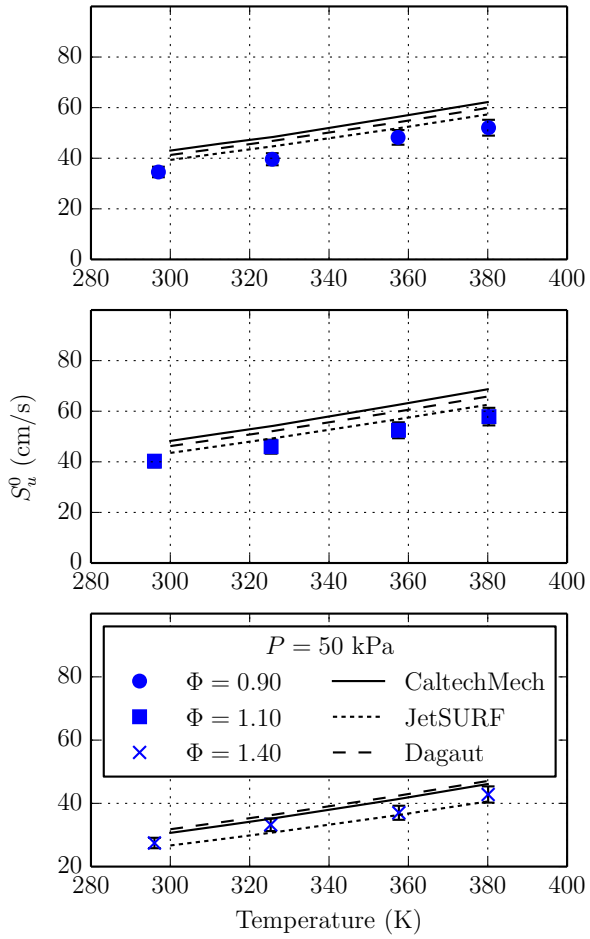

Figure 7.4: Experimental and numerical laminar burning speed of n-hexane-air mixtures as a function of equivalence ratio at an initial temperature of 296 K and initial pressures of 50 kPa and 100 kPa.

at $\Phi \approx 1.30$. This trend is consistent with previous Markstein length data obtained for C_5 to C_8 n-alkane-air mixtures (Kelley et al., 2011).

Figure 7.6 shows examples of a stable lean mixture and an unstable rich mixture flame propagation. For the lean mixture shown in Fig. 7.6 (a), the flame front remains smooth and undisturbed during the propagation within the field of view ($R_f \leq R_{\text{window}}$), where R_{window} is the window radius. For the rich mixture shown in Fig. 7.6 (b), the flame front becomes progressively more disturbed as it grows, and exhibits significant cellular structures before the flame exits the field of view. The development of the cellular pattern is apparently due to thermo-diffusive instabilities

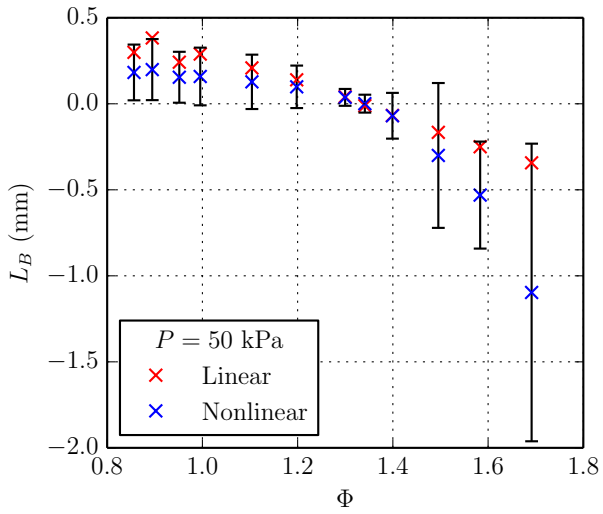

Figure 7.5: Evolution of the Marsktein length for n-hexane-air mixtures as a function of equivalence ratio at an initial temperature and pressure of 296 K and 50 kPa, respectively

that are characteristic of rich hydrocarbon-air mixtures (Jomaas et al., 2007).

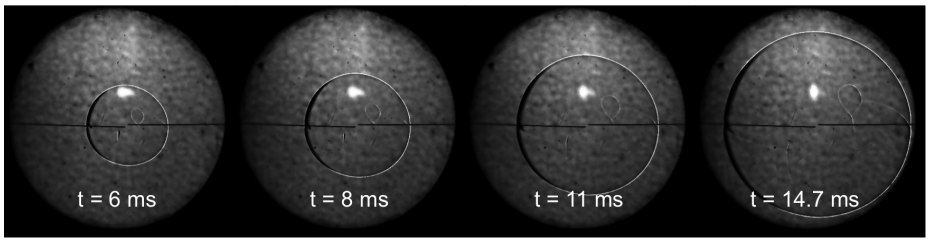

(a) $\Phi = 0.91$

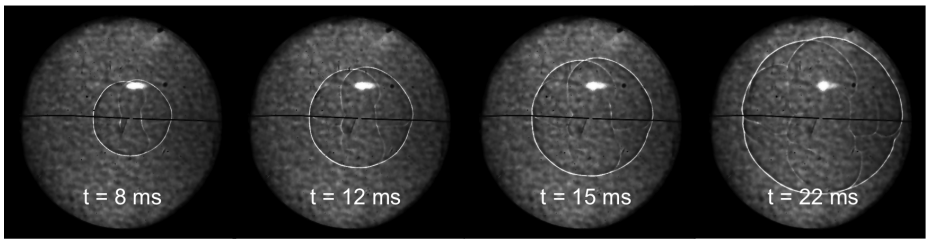

(b) $\Phi = 1.65$

Figure 7.6: Example of stable and unstable flame propagations of n-hexane-air mixtures at an initial temperature and initial pressure of 296 K and 50 kPa, respectively.

The pressure rise coefficient, K_g, shown in Eq. 7.2 is,

$$K_g = V^{1/3} \cdot \left(\frac{\mathrm{d}p}{\mathrm{d}t}\right)_{\max} \tag{7.2}$$

The parameter is used by safety engineers to characterize the explosions. To estimate the derivative shown in Eq. 7.2, the numerically differentiated combustion pressure trace is filtered using a Savitzky-Golay filter with a fifth-order polynomial and 11 data points. The results of K_g are shown in Fig. 7.7 as a function of the equivalence ratio along with the uncertainty ranges for n-hexane-air mixtures at an initial temperature and pressure of 296 K and 50 kPa, respectively; K_g values obtained by Kunz (1998) are also shown for hydrogen-air, methane-air, ethane-air, and propane-air. The K_g values for n-hexane-air mixtures at an initial temperature and pressure of 296 K and 50 kPa, respectively, are comparable to the K_g values of methane-air and propane-air mixtures obtained by Kunz (1998) using a 11.25 L vessel with initial temperature and pressure of 295 K and 100 kPa, respectively. The K_g values of ethane-air mixtures are slightly larger than the current values, approximately 2 times larger at $\Phi = 1.0$. The K_g values of hydrogen-air mixtures are significantly larger than the current values, over 3 times larger at $\Phi = 0.93$ than the average K_g value (3 MPa.m/s) obtained in the present study.

7.3 Summary

In the current chapter, n-hexane-air mixtures are characterized through experimental measurements and calculations of the unstretched burning speed and explosion pressure. The effect of equivalence ratio, temperature, and pressure on the unstretched burning speed is investigated experimentally by varying the equivalence ratio $\Phi = 0.62 - 1.60$, the initial temperature from 296 K to 380 K, and the initial pressure from 50 kPa to 100 kPa.

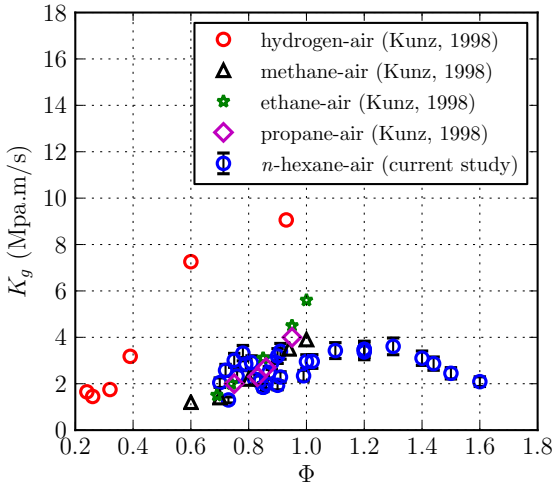

Figure 7.7: Pressure rise coefficient, K_g, for n-hexane-air mixtures as a function of equivalence ratio; initial temperature and pressure of 296 K and 50 kPa, respectively.

Chapter 8

Summary and Conclusions

The goal of the present study was to examine the ignition behavior of a flammable mixture surrounding a moving hot particle, supplementing the existing work on stationary hot particle ignition and limited work on moving hot particle ignition. Additionally, a second goal was to characterize the flame propagation behavior of n-hexane-air mixtures. This required the development of a methodology for extracting the Markstein length and unstretched flame speed by fitting a nonlinear relationship to experimental data from spherically expanding flames.

8.1 Experiment Development

An experiment was developed that is capable of heating small spheres inside of an inert environment and subsequently introducing them into a reactive mixture with a velocity of 2.4 m/s. The experiment was designed such that different sphere diameters could be used and contained optical access to implement pyrometry and high speed shearing interferometry. Using interferometry, we were able to observe qualitatively and quantitatively the gas behavior surrounding the sphere in no-ignition and ignition cases. To extract quantitative information from the inteferograms, software tools were implemented for performing phase demodulation, i.e. obtaining the optical phase difference from each raw image, phase unwrapping, and an inversion of the Abel transform to obtain the refractive index. Once the refractive index was obtained, the Gladstone-Dale relation and ideal gas law were applied to obtain the

gas temperature. For three-dimensional phase objects such as the thermal boundary layer and wake surrounding the sphere, several issues were encountered. The main one was the lack of spatial resolution within the thin thermal boundary layer. This prevented us from observing the temperature variations in the gas due to the presence of the hot sphere. However, the interferograms still allowed us to make qualitative assessments of the ignition and flame propagation. In particular, producing synthetic fringe patterns enabled us to make a qualitative comparison with the experimental fringe patterns to have an approximation of the gas temperature after a mixture had been ignited. Furthermore, the sensitivity of the shearing interferometer provided us with images that clearly showed the ignition location and time. Based on the experimental interferograms and numerical simulations, ignition occurred in the region of flow separation. Finally, over the conditions tested, the ignition threshold was insensitive to the reactive mixture concentration and showed little variation with changes in the sphere diameter. The range of parameters tested were limited, however, for smaller spheres and/or higher velocities, we expect that ignition will still occur in the region of flow separation at the ignition threshold.

8.2 Thermal Boundary Layer Ignition Modeling

A numerical study was performed on ignition within temporally evolving thermal boundary layers of hydrogen-air and n-hexane-air using detailed chemistry. We determined the important role that heat and species diffusion plays in determining the ignition delay time. For example, in a hydrogen-air mixture with a wall temperature of 1200 K, neglecting diffusion resulted in a 50% decrease in the ignition delay time. Additionally for a n-hexane-air mixture, the temperature along a fluid parcel path had an effect on the gas composition prior to ignition. The long delay times corresponding to a wall temperature of 1150 K resulted in n-hexane decomposing into smaller fuel molecules. Just prior to ignition, the main fuel species present was ethylene. At a higher wall temperature of 1400 K, the n-hexane did not undergo much decomposition and prior to ignition the main fuel species was still n-hexane.

It was also evident from spatial plots of the fuel and temperature, that ignition occurred some distance away from the wall. In the case of a n-hexane-air mixture with $T_{\text{wall}} = 1400$ K, ignition took place at $0.15\delta_T$ normal to the wall, where δ_T is the thickness of the thermal boundary layer at the time of ignition. The fuel profiles indicated that prior to any temperature increase resulting from chemical reactions, a thin region normal to the wall had already been decomposed to produce secondary fuels. The width of this depleted region was 1 mm for $T_{\text{wall}} = 1150$ and 0.25 mm for $T_{\text{wall}} = 1400$, corresponding to $7 - 10\%$ of their respective thermal boundary layer thicknesses. Fluid parcel tracking was used to analyze the behavior of several fluid parcels close to the hot wall and two fluid parcels close to the edge of the thermal boundary layer. A critical gas temperature rise and the location of peak species mass fraction of CO were investigated as criteria to determine the onset of ignition. Finally, a simple analysis of the residence time of a fluid parcel was presented for the model problem of a temporal boundary layer propagating into a moving gas. Fluid parcels close to the wall have longer residence times than fluid parcels further away from the wall due to the no-slip condition at the wall and the resulting velocity variation within the boundary layer. A fluid parcel originating at $0.05\delta_T$ (ignition location normal to the wall for $T_{\text{wall}} = 1400$ K) has a residence time $65\times$ longer than the residence time of a fluid parcel traveling along the edge of the momentum boundary layer. This is an important finding since conventional ignition estimates using a critical Damköhler number approach are based on a flow time scale corresponding to the edge of the momentum boundary layer. However, based on the ignition modeling, the fluid parcel that ignites is close to the wall. Therefore, to use a critical Damköhler criterion as a predictive method requires a physically representative flow time scale based on a detailed analysis of the boundary layer.

8.3 Spherically Propagating Flame Properties

A fitting technique was used to extract laminar flame properties from experimental data on spherical flames. The nonlinear technique was tested on synthetically gen-

erated flame propagation data. The performance and sensitivity to noise of flame speed extraction techniques were analyzed. The objective function used in the fitting procedure, Eq. 6.8, exhibited a shallow minimum that depended only weakly on the Markstein length L_B. When noise was added to the synthetic data, the local minimum became shallower and its depth was decreased. This resulted in substantial errors in the calculated Markstein length. The uncertainty of L_B and S_b^0 was affected by the size of the flame radius data; at least 50 points are required in the data set, i.e. flame radius vs. time, to obtain accurate results of the flame properties. However, there does exist a range of L_B and S_b^0 values over which a lower number of values in the data, i.e. $|R_f| = 10$ was sufficient to extract accurate flame properties. The uncertainty of L_B and S_b^0 was also affected by the data range.

8.4 Spherically *n*-Hexane-Air Flame Characterization

n-Hexane-air mixtures were characterized through experimental measurements and calculations of the unstretched burning speed and explosion pressure. The methods presented in Chapter 6 were used to analyze the experimental flame propagation results. The effect of equivalence ratio, temperature, and pressure on the unstretched burning speed was investigated experimentally by varying the equivalence ratio $\Phi = 0.62 - 1.60$, the initial temperature from 296 K to 380 K and the initial pressure from 50 kPa to 100 kPa. One-dimensional freely propagating flame calculations using the JetSurF model (Wang et al., 2010), CaltechMech model (Blanquart et al., 2009), and the model of Ramirez et al. (2011) were used to predict the behavior of the unstretched burning speed as a function of composition. The JetSurF (Wang et al., 2010) model compared well with the experimental results for lean conditions, however, it slightly under-predicted the unstretched burning speed for rich conditions. The opposite was observed with the CaltechMech model, it compared well with unstretched burning speed in the rich regime and a slightly over-predicted in the lean regime.

8.5 Future Work

To facilitate testing using the moving hot particle ignition experiment that was developed, I would suggest that the reactive mixture and inert volume containing the sphere during heating be separated using a pressure-tight shutter. If a hot sphere is dropped into the reactive mixture and does not lead to an ignition, the shutter can be closed again to separate the reactive mixture from the inert gas, subsequently the inert gas can be evacuated and replaced with the room air and the smaller chamber can be opened to place a new sphere within it. This would allow for reuse of the reactive mixture that is contained in the larger combustion vessel and therefore save time since a new mixture does not need to be prepared.

The experiment needs further modifications so that different sphere velocities can be obtained. One example is the use of an actuator that impacts the hot sphere to give it an initial velocity. However, contact of the hot sphere with a cold actuator could lead to significant heat loss from the sphere. A more sophisticated method is to charge the sphere surface and then use a potential to electrostatically accelerate the sphere. This would be a non-contact way of accelerating spheres; however, a method would need to be developed to charge each sphere.

The use of interferometry gave us insight into the gas behavior surrounding a moving hot sphere. It proved to be a very useful tool; however, there were a few drawbacks, in particular the lack of spatial resolution within the thermal boundary layer. For our particular application, we were limited to a large field of view since the sphere was moving and therefore we could not exactly pinpoint the vertical location were it would ignite. This large field of view led to poor spatial resolution within the thermal boundary layer. Therefore accurate extraction of the gas temperature from the images was not possible. To make improvements to this project, I would suggest that a smaller field of view be used, and this would require previous knowledge of the ignition behavior since a specific vertical location of the sphere trajectory would be imaged. The ignition location along the sphere trajectory would vary depending on the mixture and sphere temperature. I suggest that the interferometer optics be

arranged in a manner that allows for flexible vertical translation of the laser beam through the test section. In this manner the field of view can be easily moved vertically to accommodate for the given test conditions.

Although vast improvements can be made by having better spatial resolution of the thermal boundary layer, the use of interferometry is not a direct measurement of the gas temperature and significant errors are introduced throughout the image post-processing. Several methods exist that perform direct measurements of the gas temperature such as Two-Line Atomic Fluorescence (TLAF). Similar to pyrometry, TLAF relates the ratio of the fluorescence signal of a molecule at two different wavelengths to a gas temperature. TLAF can be used to excite seeded molecules or molecules native to the gas mixture. In some instances, TLAF has been used with indium atoms since a good characterization of the fluorescence of the atoms to the gas temperature is possible, it is also found to be sensitive at high temperatures. To implement TLAF requires the use of two diode lasers that emit at the necessary wavelengths to excite indium, 410 and 451 nm, and two high speed ccd cameras with filters to capture the fluorescence signal at 451 and 410 nm, respectively. Additionally, if the fluorescence signal is not strong enough, image intensifiers need to be used for each camera. Since a laser sheet is used, two-dimensional measurements of the thermal boundary layer and wake around the sphere can be made.

Finally, a wider range of parameters still needs to be examined for moving hot particle ignition, for example performing tests at different velocities and smaller diameters (< 1 mm) and using different reactive mixtures such as hydrogen-air and ethylene-air. The use of simpler fuel-air mixtures is important to validate numerical simulations of moving hot particle ignition such as those performed by Melguizo-Gavilanes et al. (2016b).

Bibliography

S. I. Abu-Eishah. Correlations for the thermal conductivity of metals as a function of temperature. *International Journal of Thermophysics*, 22(6):1855–1868, 2001.

R. Álvarez, A. Rodero, and M. C. Quintero. An Abel inversion method for radially resolved measurements in the axial injection torch. *Spectrochimica Acta Part B: Atomic Spectroscopy*, 57(11):1665–680, 2002.

K. Aung, L. Tseng, M. Ismail, and G. Faeth. Laminar burning velocities and Markstein numbers of hydrocarbon/air flames. *Combustion and Flame*, 102:526–530, 1995.

K. Aung, M. Hassan, and G. Faeth. Flame stretch interactions of laminar premixed hydrogen/air flames at normal temperature and pressure. *Combustion and Flame*, 109:1–24, 1997.

H. D. Baehr and K. Stephan. *Heat and Mass Transfer*. Springer-Verlag Berlin Heidelberg, 2011.

S. P. Bane, J. L. Ziegler, and J. E. Shepherd. Investigation of the effect of electrode geometry on spark ignition. *Combustion and Flame*, 162(2):462 – 469, 2015.

S. P. M. Bane. *Spark Ignition: Experimental and Numerical Investigation With Application to Aviation Safety*. PhD thesis, California Institute of Technology, 2010.

S. P. M. Bane, R. Mével, S. A. Coronel, and J. E. Shepherd. Flame burning speeds of undiluted and nitrogen diluted hydrogen-nitrous oxide mixtures. *International Journal of Hydrogen Energy*, 36:10107–10116, 2011.

M. Beyer and D. Markus. Ignition of explosive atmospheres by small hot particles: Comparison of experiments and simulations. *Science and Technology of Energetic Materials*, 73(1), 2012.

F. Beyrau, M. A. Hadjipanayis, and R. P. Lindstedt. Ignition of fuel/air mixtures by radiatively heated particles. *Proceedings of the Combustion Institute*, 34:2065–2072, 2013.

S. Bhattacharyya and A. Singh. Mixed convection from an isolated spherical particle. *International Journal of Heat and Mass Transfer*, 51(56):1034–1048, 2008.

J. R. Birch and F. J. J. Clarke. Fifty categories of ordinate error in Fourier transform spectroscopy. *Spectroscopy Europe*, 7(4):16–22, 1995.

W. Z. Black and W. W. Carr. Application of a differential interferometer to the measurement of heat transfer coefficients. *Review of Scientific Instruments*, 42(3): 337–340, 1971.

G. Blanquart, P. Pepiot-Desjardins, and H. Pitsch. Chemical mechanism for high temperature combustion of engine relevant fuels with emphasis on soot precursors. *Combustion and Flame*, 156(3):588–607, 2009.

P. A. Boettcher. *Thermal Ignition*. PhD thesis, California Institute of Technology, 2012.

P. A. Boettcher, R. Mével, V. Thomas, and J. E. Shepherd. The effect of heating rates on low temperature hexane air combustion. *Fuel*, 96:392–403, 2012.

H. Bothe, S. Schenk, S. Hawksworth, F. Carleton, and F. Weinberg. The safe use of optics in potentially explosive atmospheres. In *Explosion Safety in Hazardous Areas, 1999. International Conference on (Conf. Publ. No. 469)*, pages 44–49, 1999.

S. Bougrine, S. Richard, A. Nicolle, and D. Veynante. Numerical study of laminar flame properties of diluted methane-hydrogen-air flames at high pressure and tem-

perature using detailed chemistry. *International Journal of Hydrogen Energy*, 36: 12035–12047, 2011.

N. Bouvet, C. Chauveau, I. Gökalp, and F. Halter. Experimental studies of the fundamental flame speeds of syngas (H_2/CO)/air mixtures. *Proceedings of the Combustion Institute*, 33:913–920, 2011.

D. Bradley, P. Gaskell, and X. Gu. Burning velocities, Markstein length and flame quenching for spherical methane-air flames: a computational study. *Combustion and Flame*, 104:176–198, 1996.

A. Burcat, E. Olchanski, and C. Sokolinski. Kinetics of hexane combustion in a shock tube. *Israel Journal of Chemistry*, 36:313–320, 1996.

L.-D. Chen and G. Faeth. Ignition of a combustible gas near heated vertical surfaces. *Combustion and Flame*, 42:77–92, 1981.

T. Chen and A. Mucoglu. Analysis of mixed forced and free convection about a sphere. *International Journal of Heat and Mass Transfer*, 20(8):867 – 875, 1977.

Z. Chen. On the extraction of laminar flame speed and Markstein length from outwardly propagating spherical flames. *Combustion and Flame*, 158:291–300, 2011.

J. Chomiak. *Combustion : a study in theory, fact and application.* Gordon and Breach Science Publishers, Switzerland, 1990.

P. Clavin. Dynamic behavior of premixed flame fronts in laminar and turbulent flows. *Progress in Energy and Combustion Science*, 11:1–59, 1985.

R. Clift, J. R. Grace, and M. E. Weber. *Bubbles, Drops, and Particles.* Dover Publications, Inc., 2005.

S. Coronel, R. Mével, S. Bane, and J. Shepherd. Experimental study of minimum ignition energy of lean H_2-N_2O mixtures. *Proceedings of the Combustion Institute*, 34(1):895 – 902, 2013a.

S. A. Coronel and J. E. Shepherd. Effect of equivalence ratio on ignition and flame propagation of *n*-hexane-air mixtures using moving hot particles. In *25th International Colloquium on the Dynamics of Explosions and Reactive Systems (ICDERS 2015)*, Leeks, UK, August 2-7 2015.

S. A. Coronel, S. Menon, R. Mével, G. Blanquart, and J. E. Shepherd. Ignition of nitrogen diluted hexane-oxygen mixtures by moving heated particles. In *24th International Colloquium on the Dynamics of Explosions and Reactive Systems (ICDERS 2013)*, Taipei, Taiwan, 28 July-2 August 2013b.

S. A. Coronel, R. Mével, P. Vervish, P. A. Boettcher, V. Thomas, N. Chaumeix, N. Darabiha, and J. E. Shepherd. Laminar burning speed of *n*-hexane-air mixtures. In *8th US National Combustion Meeting*, University of Utah, May 19-22 2013c. Paper 070LT-0383.

S. A. Coronel, V. Bitter, N. Thomas, R. Mével, and J. E. Shepherd. Non-linear extrapolation of laminar flame properties from spherically expanding flames. In *Spring Meeting, Western States Section of the Combustion Institute*, California Institute of Technology, March 24-25 2014. Paper 087LF-0020.

S. A. Coronel, J. Melguizo-Gavilanes, and J. E. Shepherd. Ignition of *n*-hexane-air by moving hot particles: effect of particle diameter. In *9th US National Combustion Meeeting*, Cincinnati OH, May 17-20 2015. Paper 0114RK-0452.

H. F. Coward and P. G. Guest. Ignition of natural gas-air mixtures by heated metal bars. *Journal of the American Chemical Society*, 49(10):2479–2486, 1927.

H. Curran, P. Gaffuri, W. Pitz, C. Westbrook, and W. Leppard. Autoignition chemistry of the hexane isomers: an experimental and kinetic modelling study. In *SAE International Fuels and Lubricants Meeting and Exposition*, 1995.

P. Dagaut and M. Cathonnet. The ignition, oxidation, and combustion of kerosene: A review of experimental and kinetic modeling. *Progress in Energy and Combustion Science*, 32:48–92, 2006.

P. Dagaut, A. El Bakali, and A. Ristori. The combustion of kerosene: experimental results and kinetic modelling using 1- to 3-component surrogate model fuels. *Fuel*, 85:944–956, 2006.

D. Davidenko, R. Mével, and G. Dupré. Reduced kinetic scheme for the simulation of detonation in H_2-N_2O-Ar mixtures. *Proceedings of the European Combustion Meeting*, 4:6, 2009.

D. Davidson, W. Ren, and R. Hanson. Experimental database for development of a HiFiRE JP-7 surrogate fuel mechanism. In *Aerospace Sciences Meetings*. American Institute of Aeronautics and Astronautics, Jan. 2012.

D. F. Davidson, S. C. Ranganath, K.-Y. Lam, M. Liaw, Z. Hong, and R. K. H. Ignition delay time measurements of normal alkanes and simple oxygenates. *Journal of Propulsion and Power*, 26(2):280–287, Mar. 2010.

S. Davis and C. Law. Determination of and fuel structure effects on laminar flame speeds of C_1 to C_8 hydrocarbons. *Combustion Science and Technology*, 140:427–449, 1998.

C. de Izarra and J.-M. Gitton. Calibration and temperature profile of a tungsten filament lamp. *European Journal of Physics*, 31(4):933, 2010.

O. Desjardins, G. Blanquart, G. Balarac, and H. Pitsch. High order conservative finite difference scheme for variable density low Mach number turbulent flows. *Journal of Computational Physics*, 227(15):7125 – 7159, 2008.

S. Dooley, S. Wona, M. Chaos, J. Heyne, Y. Ju, F. Dryer, K. Kumar, C.-J. Sung, H. Wang, M. Oehlschlaeger, R. Santoro, and T. Litzinger. A jet fuel surrogate formulated by real fuel properties. *Combustion and Flame*, 157:2333–2339, 2010.

D. Dowdy, D. Smith, T. S.C., and A. Williams. The use of expanding spherical flames to determine burning velocities and stretch effects in hydrogen/air mixtures. *Proceedings of the Combustion Institute*, 23:325–332, 1990.

T. H. Dubaniewicz. Threshold powers and delays for igniting propane and butane-air mixtures by cw laser-heated small particles. *Journal of Laser Applications*, 18(4): 312–319, 2006.

T. H. Dubaniewicz, K. L. Cashdollar, G. M. Green, and R. F. Chaiken. Ignition of methaneair mixtures by laser heated small particles. *Journal of Loss Prevention in the Process Industries*, 13(35):349 – 359, 2000.

T. H. Dubaniewicz, K. L. Cashdollar, and G. M. Green. Continuous wave laser ignition thresholds of coal dust clouds. *Journal of Laser Applications*, 15(3):184–191, 2003.

A. Eucken. The heat-carrying capabilities, the specific heat and the internal friction of gas. *Physikalische Zeitschrift*, 14:324–332, 1913.

J. Farrell, R. Johnston, and I. Androulakis. Molecular structure effects on laminar burning velocities at elevated temperature and pressure. In *SAE Technical Paper*, number 2004-01-2936, 2004.

P. Feraboli and M. Miller. Damage resistance and tolerance of carbon/epoxy composite coupons subjected to simulated lightning strike. *Composites Part A: Applied Science and Manufacturing*, 40(67):954 – 967, 2009.

D. Ghiglia and M. D. Pritt. *Two-Dimensional Phase Unwrapping: Theory, Algorithms, and Software*. John Wiley and Sons, Inc., 1988.

I. Glassman. *Combustion*. Academic Press, Inc, London, 1987.

D. G. Goodwin. An open-source, extensible software suite for CVD process simulation. In M. Allendorf, F. Maury, and F. Teyssandier, editors, *Proceedings of CVD XVI and EuroCVD Fourteen*, pages 155–162, 2003.

T. A. Griffin and L. D. Pfefferle. Gas phase and catalytic ignition of methane and ethane in air over platinum. *AIChE Journal*, 36(6):861–870, 1990.

F. Halter, T. Tahtouh, and C. Mounaïm-Rousselle. Nonlinear effects of stretch on the flame front propagation. *Combustion and Flame*, 157:1825–1832, 2010.

S. Hawksworth, R. Rogers, C. Proust, M. Beyer, S. Schenk, J. Gummer, and D. Raveau. Ignition of explosive atmospheres by mechanical equipment. *Symposium Series No. 150*, 2004.

W. M. Haynes, editor. *CRC Handbook of Chemistry and Physics*. CRC Press, 95th edition, 2014.

J. Hirschfelder, C. Curtiss, and R. Bird. *Molecular theory of gases and liquids*. Wiley, 1954.

C. Y. Ho and T. K. Chu. Electrical resistivity and thermal conductivity of nine selected AISI stainless steels. Technical Report CINDAS Report 45, Thermophysical Properties Research Center, 1977.

H. S. Homan. Minimum mass of burning aluminum particles for ignition of methane/air and propane/air mixtures. *Proceedings of Eighteenth Symposium (International) on Combustion*, pages 1709–1717, 1981.

Z. Huang, Y. Zhang, K. Zeng, B. Liu, Q. Wang, and D. Jiang. Measurements of laminar velocities for natural gas-hydrogen-air mixtures. *Combustion and Flame*, 146:302–311, 2006.

IAE. Thermophysical properties of materials for water cooled reactors. Technical report, International Atomic Energy Agency, June 1997.

B. V. Ioffe and A. G. Vitenberg. *Head-Space Analysis and Related methods in Gas Chromatography*. John Wiley & Sons, New York, 1984. Traslated from russian by I. A. Mamantov.

J. Ishii and A. Ono. Uncertainty estimation for emissivity measurements near room temperature with a Fourier transform spectrometer. *Measurement Science and Technology*, 12(12):2103, 2001.

J. Jayachandran, A. Lefebvre, R. Zhao, F. Halter, E. Varea, B. Renou, and F. N. Egolfopoulos. A study of propagation of spherically expanding and counterflow

laminar flames using direct measurements and numerical simulations. *Proceedings of the Combustion Institute*, 35(1):695 – 702, 2015.

S. Jerzembeck, M. Matalon, and N. Peters. Experimental investigation of very rich laminar spherical flames under microgravity conditions. *Proceedings of the Combustion Institute*, 32:1125–1132, 2009.

C. Ji, E. Dames, Y. Wang, H. Wang, and F. Egolfopoulos. Propagation and extinction of premixed c−5-c−12 n-alkane flames. *Combustion and Flame*, 157:277–287, 2010.

T. A. Johnson and V. C. Patel. Flow past a sphere up to a Reynolds number of 300. *Journal of Fluid Mechanics*, 378:19–70, 1 1999.

G. Jomaas, C. Law, and J. Bechtold. On transition to cellularity in expanding spherical flames. *Journal of Fluid Mechanics*, 583:1–26, 2007.

R. Kabacoff. *R in Action: Data Analysis and Graphics with R*. Manning Publications Co., Greenwich, CT, USA, 2015.

B. Karlovitz, J. Denission, D. Knapschaffer, and F. Wells. Studies on turbulent flames. *Proceedings of the Combustion Institute*, 4:613–620, 1953.

A. Kelley and C. Law. Nonlinear effects in the extraction of laminar flame speeds from expanding spherical flames. *Combustion and Flame*, 156:1844–1851, 2009.

A. P. Kelley, A. J. Smallbone, D. L. Zhu, and C. K. Law. Laminar flame speeds of C_5 to C_8 *n*-alkanes at elevated pressures: Experimental determination, fuel similarity, and stretch sensitivity. *Proceedings of the Combustion Institute*, 33:963–970, 2011.

Q. Kemao. *Windowed Fringe Pattern Analysis*. SPIE, 2013.

H. M. Kim, H. Enomoto, H. Kato, M. Tsue, and M. Kono. A study of the ignition mechanism of methane-air mixtures by inert and catalytic hot surfaces. *Combustion Science and Technology*, 128(1-6):197–213, 1997.

E. Knudsen and H. Pitsch. Capabilities and limitations of multi-regime flamelet combustion models. *Combustion and Flame*, 159(1):242–264, 2009.

R. Kumar. Ignition of hydrogen-oxygen-diluent mixtures adjacent to a hot, nonreactive surface. *Combustion and Flame*, 75(2):197 – 215, 1989.

O. Kunz. Combustion characteristics of hydrogen- and hydrocarbon-air mixtures in closed vessels. Master's thesis, California Institute of Technology, 1998.

E. Kwon, S. P. Moffett, J. E. Shepherd, and A. C. Day. Combustion characteristics of hydrogen as used in a flammable test mixture. In *Proceedings of the International Conference of Lightning and Static Electricity*, 2007. Paper PPR-48.

O. Kwon and G. Faeth. Flame/stretch interactions of premixed hydrogen-fueled flames: measurements and predictions. *Combustion and Flame*, 124:590–610, 2001.

K.-Y. Lam. *Shock Tube Measurements of Oxygenated Fuel Combustion using Laser Absorption Spectroscopy*. PhD thesis, Stanford University, June 2013.

N. Lamoureux, N. Djebaïli-Chaumeix, and C. Paillard. Laminar flame velocity for H_2-air-He-CO_2 mixtures using the spherical bomb method. *Experimental Thermal and Fluid Science*, 27:385–393, 2003.

C. K. Law. *Combustion Physics*. Cambridge University Press, 2006.

B. Lewis and G. von Elbe. *Combustion, Flames and Explosions of Gases*. Academic Press, 1961.

R. D. Lide, editor. *CRC Handbook of Chemistry and Physics*. CRC Press, 72nd edition, 1991.

K. Maglic and D. Pavicic. Thermal and electrical properties of titanium between 300 and 1900 K. *International Journal of Thermophysics*, 22(6):1833–1841, 2001.

P. Malacarne, F. Billaud, and F. Baronnet. Thermal decomposition of 3-methylpentane and *n*-hexane: Reaction mechanism and correlations between structure and formation of light olefins. *Journal of Analytical and Applied Pyrolysis*, 12 (3):243 – 256, 1987.

G. Markstein. Experimental and theoretical studies of flame front instability. *Journal of the Aeronautical Sciences*, 18:199–209, 1951.

M. Matalon and B. Matkowsky. Flames as gasdynamic discontinuities. *Journal of Fluid Mechanics*, 124:239–259, 1982.

S. Mathur, P. K. Tondon, and S. C. Saxena. Thermal conductivity of binary ternary and quaternary mixtures of rare gases. *Molecular Physics*, 12(6):569–579, 1967.

R. A. Matula. Electrical-resistivity of copper, gold, palladium, and silver. *Journal of Physical and Chemical Reference Data*, 8(4):1147–1298, 1979.

J. Melguizo-Gavilanes, S. Coronel, R. Mével, and J. E. Shepherd. Numerical and experimental investigations of ignition by moving heated spheres. *Combustion and Flame*, 2016a. In preparation.

J. Melguizo-Gavilanes, S. Coronel, R. Mével, and J. E. Shepherd. Dynamics of ignition of stoichiometric hydrogen-air mixtures by moving heated particles. *International Journal of Hydrogen Energy*, 2016b. Accepted for publication.

J. Melguizo-Gavilanes, A. Nové-Josserand, S. Coronel, R. Mével, and J. E. Shepherd. Hot surface ignition of *n*-hexane mixtures using simplified kinetics. *Combustion Science and Technology*, 2016c. Accepted for publication.

W. Merzkirch. *Flow Visualization*. Academic Press, 1987.

R. Mével, S. Javoy, F. Lafosse, N. Chaumeix, G. Dupré, and C.-E. Paillard. Hydrogen-nitrous oxide delay times: Shock tube experimental study and kinetic modelling. *Proceedings of the Combustion Institute*, 32(1):359–366, 2009a.

R. Mével, F. Lafosse, N. Chaumeix, G. Dupré, and C.-E. Paillard. Spherical expanding flames in H_2-N_2O-Ar mixtures: Flame speed measurement and kinetic modeling. *International Journal of Hydrogen Energy*, 34(21):9007–9018, 2009b.

R. Mével, K. Chatelain, P. A. Boettcher, and J. E. Shepherd. Low temperature oxidation of *n*-hexane in a flow reactor. *Fuel*, 126:282–293, 2014.

R. Mével, J. Melguizo-Gavilanes, S. A. Coronel, and J. E. Shepherd. Chemical kinetics of ignition of *n*-hexane by a moving hot sphere. In *25th International Colloquium on the Dynamics of Explosions and Reactive Systems (ICDERS 2015)*, Leeds, UK, August 2-7 2015.

R. Mével, J. Melguizo-Gavilanes, U. Niedzielska, S. Coronel, and J. E. Shepherd. Chemical kinetics of *n*-hexane-air atmospheres in the boundary layer of a moving hot sphere. *Combustion Science and Technology*, 2016. Accepted for publication.

K. Mikkelsen. An experimental investigation of ignition propensity of hot work processes in the nuclear industry. Master's thesis, University of Waterloo, 2014.

O. H. Nestor and H. N. Olsen. Numerical methods for reducing line and surface probe data. *SIAM Review*, 2(3):200–207, 1960.

S. Paterson. I. The ignition of inflammable gases by hot moving particles. *The London, Edinburgh, and Dublin Philosophical Magazine and Journal of Science*, 28 (186):1–23, 1939.

S. Paterson. XLII. The ignition of inflammable gases by hot moving particles. *The London, Edinburgh, and Dublin Philosophical Magazine and Journal of Science*, 30 (203):437–457, 1940.

A. Patil, D. Huard, and C. J. Fonnesbeck. PyMC: Bayesian stochastic modeling in Python. *Journal of Statistical Software*, 35(4):1–81, July 2010.

H. Pitsch. Flamemaster, a C++ computer program for 0D combustion and 1D

laminar flame calculations. URL http://web.stanford.edu/group/pitsch/FlameMaster.htm.

A. D. Poularikas, editor. *Tranforms and Applications Handbook*. CRC, 2010.

H. P. Ramirez, K. Hadj-Ali, P. Dievart, G. Dayma, C. Togbe, G. Moreac, and P. Dagaut. Oxidation of commercial and surrogate bio-Diesel fuels (B30) in a jet-stirred reactor at elevated pressure: Experimental and modeling kinetic study. *Proceedings of the Combustion Institute*, 33(1):375–382, 2011.

P. Rastogi and E. Hack, editors. *Phase Estimation in Optical Interferometry*. CRC Press, 2015.

R. C. Reid, J. M. Prausnitz, and B. E. Poling. *The Properties of Gases and Liquids*. McGraw-Hill, New York, 1987.

P. D. Ronney and G. I. Sivashinsky. A theoretical-study of propagation and extinction of nonsteady spherical flame fronts. *SIAM Journal on Applied Mathematics*, 49(4): 1029–1046, 1989.

D. Roth, P. Sharma, T. Haeber, R. Schiessl, H. Bockhorn, and U. Maas. Ignition by mechanical sparks: Ignition of hydrogen/air mixtures by submillimeter-sized hot particles. *Combustion Science and Technology*, 186(10-11):1606–1617, 2014.

O. Rozenbaum, D. D. Meneses, Y. Auger, S. Chermanne, and P. Echegut. A spectroscopic method to measure the spectral emissivity of semi-transparent materials up to high temperature. *Review of Scientific Instruments*, 70(10):4020–4025, 1999.

M. Z. Salleh, R. Nazar, and I. Pop. Mixed convection boundary layer flow from a solid sphere with Newtonian heating in a micropolar fluid. *SRX Physics*, 2010, 2010.

T. Sano and A. Yamashita. Flame ignition of premixed methane air mixtures on a high-temperature plate. *JSME International Journal Series B*, 37(1):180–186, 1994.

R. S. Silver. The ignition of gaseous mixtures by hot particles. *The London, Edinburgh, and Dublin Philosophical Magazine and Journal of Science*, 23(156):633–657, 1937.

J. Simmie. Detailed chemical kinetic models for the combustion of hydrocarbon fuels. *Progress in Energy and Combustion Science*, 29:599–634, 2003.

G. Sivashinsky. On a distorted flame front as a hydrodynamic discontinuity. *Acta Astronautica 3 (1976)*, 3:889–918, 1976.

R. D. Small, V. A. Sernas, and R. H. Page. Single beam schlieren interferometer using a Wollaston prism. *Applied Optics*, 11(4):858–862, 1972.

I. Sochet, J. M. Pascaud, and P. Gillard. Experimental and numerical investigation of kerosene flammability. *Journal de Physique IV*, 12:429–435, 2002.

M. Suh, P. S. Bagus, S. Pak, M. P. Rosynek, and J. H. Lunsford. Reactions of hydroxyl radicals on titania, silica, alumina, and gold surfaces. *Journal of Physical Chemistry B*, 104(12):2736–2742, 2000.

T. Tahtouh, F. Halter, and C. Mounaïm-Rousselle. Measurement of laminar burning speeds and Markstein lengths using a novel methodology. *Combustion and Flame*, 156:1735–1743, 2009.

G. Teodorescu and P. D. Jones. Spectral and directional emittance of alumina at 823 K. *Journal of Materials Science*, 43(22):7225–7229, 2008.

I. Thomas. Fuel air ratio calculator, October 2001. http://www.fire.tc.faa.gov/systems/fueltank/. Online; accessed: 12-August-2011.

E. Varea, V. Modica, A. Vandel, and B. Renou. Measurement of laminar burning velocity and Markstein length relative to fresh gases using a new postprocessing procedure: Application to laminar spherical flames for methane, ethanol and isooctane/air mixtures. *Combustion and Flame*, 159:577–590, 2012.

E. Varea, J. Beeckmann, H. Pitsch, Z. Chen, and B. Renou. Determination of burning velocities from spherically expanding H_2/air flames. *Proceedings of the Combustion Institute*, 35(1):711 – 719, 2015.

S. S. Vasu, D. F. Davidson, and R. K. Hanson. Shock tube study of syngas ignition in rich CO_2 mixtures and determination of the rate of H + O2 + CO2 HO2 + CO2. *Energy & Fuels*, 25(3):990–997, 2011.

C. M. Vest. Interferometry of strongly refracting axisymmetric phase objects. *Applied Optics*, 14(7):1601–1606, 1975.

H. Wang, E. Dames, B. Sirjean, D. A. Sheen, R. Tango, A. Violi, J. Y. W. Lai, F. N. Egolfopoulos, D. F. Davidson, R. K. Hanson, C. T. Bowman, C. K. Law, W. Tsang, N. P. Cernansky, D. L. Miller, and R. P. Lindstedt. A high-temperature chemical kinetic model of *n*-alkane (up to *n*-dodecane), cyclohexane, and methyl-, ethyl-, *n*-propyl and *n*-butyl-cyclohexane oxidation at high temperatures, JetSurF version 2.0, September 19 2010. URL http://web.stanford.edu/group/haiwanglab/JetSurF/JetSurF2.0/index.html.

J. Warnatz, U. Maas, and R. W. Dibble. *Combustion: Physical and Chemical Fundamentals, Modeling and Simulation, Experiments, Pollutant Formation*. Springer Science & Business Media, 2013.

F. J. Weinberg. *Optics of Flames*. Butterworth and Co. (Publishers) Ltd., 1963.

H. G. Weller, G. Tabor, H. Jasak, and C. Fureby. A tensorial approach to computational continuum mechanics using object-oriented techniques. *Computational Physics*, 12(6):620–631, Nov. 1998.

F. M. White. *Viscous Fluid Flow*. McGraw Hill, Inc., 1991.

G. K. White and S. J. Collocott. Heat capacity of reference materials: Cu and W. *Journal of Physical and Chemical Reference Data*, 13(4):1251–1257, 1984.

C. R. Wilke. A viscosity equation for gas mixtures. *The Journal of Chemical Physics*, 18(4):517–519, 1950.

J. E. Woodrow. The laboratory characterization of ARCO jet fuel vapor and liquid. Final report for NTSB, Center for Environmental Sciences and Engineering, University of Nevada, Reno, NV, 2000.

F. Wu, W. Liang, Z. Chen, Y. Ju, and C. K. Law. Uncertainty in stretch extrapolation of laminar flame speed from expanding spherical flames. *Proceedings of the Combustion Institute*, 35(1):663 – 670, 2015.

V. P. Zhukov, V. A. Sechenov, and A. Y. Starikovskii. Ignition delay times in lean *n*-hexane-air mixture at high pressures. *Combustion and Flame*, 136:257–259, 2004.

Appendix A

Analytic Model for Vapor Pressure Prediction

A kerosene-based fuel consists of hundreds of hydrocarbons, and therefore the first step is to model its liquid composition. Two different approaches were found for modeling the liquid composition: the first by Woodrow (2000), who obtained the liquid composition of twelve different kerosene based fuels with varying flash points using a gas chromatograph, and the second by Thomas (2001), who obtained distillation curves for Jet A, Jet B, JP-5 and TS-1. Woodrow's analysis was performed by injecting the fuel into a gas chromatograph and using a flame ionization detector to determine the retention times for compounds grouped by the number of carbon atoms. The composition of each fuel was modeled by using sixteen alkane reference standards (C_nH_{2n+2} where $n = 5, 6, ..., 20$). In Thomas' analysis, the alkane boiling points were used as a guide to cut the fuel into a number of "buckets"; all species of the same carbon number were placed in the same bucket. Thomas' analysis simplified the approach to focus on nineteen buckets rather that several hundred buckets. The ASTM D2887 distillation curve was used to determine the weight of each bucket. Two adjustments were introduced by Thomas to account for the fact that the compounds in any one bucket were not all alkanes. The first was to decrease the hydrogen content as the carbon number increases, i.e. C_nH_{2n+c}, where

$$c = 2 - 0.25 \cdot (n - 1) \quad \text{for} \quad n = 1, 2, ..., 19. \tag{A.1}$$

The second adjustment was made to the "cut temperature" (i.e., the boiling temperature separating each bucket in the distillation curve) to better match the predicted vapor pressure to the actual vapor pressure of the fuels analyzed in Thomas' study.

Once the liquid composition is known, Woodrow's method for modeling the fuel vapor composition is applied. Woodrow provides the liquid composition, shown in Fig. A.1, for kerosene based fuels formulated to have a range of flash points, shown in Table A.1.

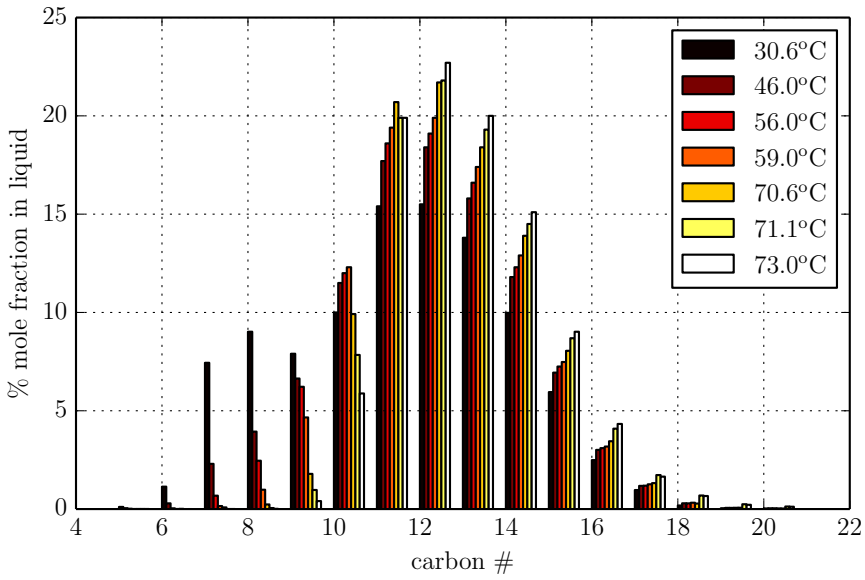

Figure A.1: Percent mole fraction of liquid fuel samples for kerosene based fuels with different flash points (Woodrow, 2000).

Sample	Flash Point (°C)
2.5 wt% OH	30.6
Base Jet A	45.6
97.5 wt% Btm	55.6
95 wt% Btm	59.4
92.5 wt% Btm	64.4
90 wt% Btm	70.6
87.5 wt% Btm	71.1
85 wt% Btm	73.9

Table A.1: Flash point of kerosene based fuel samples (Woodrow, 2000).

The flash point is the minimum temperature that yields sufficient fuel vapor to form a flammable vapor-air mixture (Sochet et al., 2002). As the flash point increases, the percent mole fraction of the lighter hydrocarbons decreases, therefore higher temperatures are required to vaporize the heavier hydrocarbons and yield a flammable mixture.

Given the database of liquid fuel composition for a range of flash points (Woodrow, 2000), linear interpolation is performed for flash points between 30.6°C and 73.9°C to obtain a liquid composition. A flash point temperature of 42°C is chosen to provide an example of the typical vapor composition of a kerosene based fuel. A prediction of the liquid composition for the 42°C flash point fuel is shown in Fig. A.2. The liquid fuel composition is nearly symmetric across C_{12}.

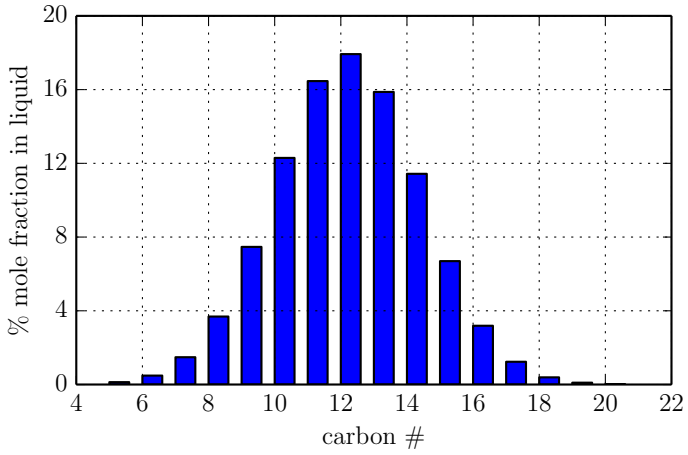

Figure A.2: Prediction of percent mole fraction of kerosene based fuel with a flash point of 42°C.

With the knowledge of the predicted liquid composition of the fuel, the saturation vapor pressures, P_{vp}, of each subsection hydrocarbon are calculated using the following equations (Reid et al., 1987):

$$\ln\left(P_{\text{vp}}/P_{\text{C}}\right) = (1-x)^{-1}\left[Ax + Bx^{1.5} + Cx^3 + Dx^6\right] \tag{A.2}$$

$$x = 1 - T/T_{\text{C}} \tag{A.3}$$

$$\ln\left(P_{\mathrm{vp}}\right) = A - B/T + C\ln T + DP_{\mathrm{vp}}/T^2 \tag{A.4}$$

$$\ln\left(P_{\mathrm{vp}}\right) = A - B/\left[T + C\right], \tag{A.5}$$

where A, B, C, D, are constants, T_{C} is the critical temperature, and P_{C} is the critical pressure (values can be taken from Appendix A of Reid et al. (1987)). The saturation pressures of n-alkanes with a carbon number of 5, 6, 7, 8, 9, and 10 are calculated using Eqs. A.2 and A.3; those with carbon numbers of 11, 12, 14, 15, and 16 are calculated using Eq. A.4 and those with carbon numbers of 13, 17, 18, 19, and 20 are calculated using Eq. A.5. The subsection partial pressure of the vapor, P_i, is obtained using Raoult's Law

$$P_i = X_i P_{\mathrm{vp},i} \quad \text{for} \quad i = 5, 6, ..., 20, \tag{A.6}$$

where X_i is the subsection mole fraction of the liquid. The number of moles, n_i, in each subsection of the fuel vapor was found by applying the ideal gas law,

$$P_i = \frac{n_i \tilde{R} T}{V_{\mathrm{V}}}, \tag{A.7}$$

where V_{V} is the volume of the fuel vapor and $\tilde{R}$ is the universal gas constant. The volume of the fuel vapor is rewritten as the difference between the volume of the vessel, V, and the volume of the liquid, V_{L}, where,

$$V_{\mathrm{V}} = V - V_{\mathrm{L}} = V - \frac{\sum W_i N_i - \sum W_i n_i}{\rho}. \tag{A.8}$$

In Eq. A.8, W_i is the molecular weight of each hydrocarbon in the fuel, N_i is the number of moles of each hydrocarbon and ρ is the liquid fuel density. Raoult's law does not take into consideration the mass loading, i.e. the ratio of the fuel liquid mass to the volume of the vessel, when calculating the partial pressure of each subsection; therefore, the expression known as the "headspace equation" (Ioffe and Vitenberg, 1984), shown in Eq. A.9, is applied,

$$C_{\mathrm{G}} = \frac{C_{\mathrm{L}}^{o}}{K + V_{\mathrm{V}}/V_{\mathrm{L}}}. \tag{A.9}$$

C_{G} is the concentration in the vapor, $\mathrm{C}_{\mathrm{L}}^{\circ}$ is the initial concentration in the liquid, and K is the hydrocarbon liquid-vapor distribution coefficient. The headspace equation is a manipulation of the conservation of moles for each subsection hydrocarbon as shown below,

$$n_i = n_{\mathrm{L},i} + n_{\mathrm{V},i}. \tag{A.10}$$

where n_i is the total number of moles, $n_{\mathrm{L},i}$ is the number of moles in the liquid fuel, and $n_{\mathrm{V},i}$ is the number of moles in the fuel vapor of each subsection hydrocarbon. Dividing the above equation by V_{V} and further manipulation yields Eq. A.9. Equation A.9 shows that for a given value of K, as $V_{\mathrm{V}}/V_{\mathrm{L}}$ increases, C_{G} decreases since the number of moles of each hydrocarbon in the liquid fuel that can be vaporized decreases. A comparison of Eq. A.9 with the ideal gas law leads to,

$$K_i = \frac{N}{W_{\mathrm{L}}} \frac{\tilde{R} T_{\mathrm{L}}}{P_{\mathrm{vp},i}}, \tag{A.11}$$

N, W_{L}, and T_{L} are the total number of moles, molecular weight, and temperature of the liquid fuel, respectively, and $P_{\mathrm{vp},i}$ is the subsection vapor pressure. Equation A.11 is independent of mass loading.

Applying Eqs. A.2 to A.11 provides a prediction of the composition of the flammable vapor as a function of the mass loading, flash point, and temperature of the liquid fuel. As the mass loading increases, the vapor pressure of the lighter hydrocarbons increases significantly as shown in Fig. A.3; as temperature increases, the vapor pressure of each hydrocarbon increases noticeably as shown in Fig. A.4.

For low mass loadings, the lighter hydrocarbons become depleted from the liquid fuel due to evaporation. As the mass loading increases the depletion decreases, until finally for a vessel nearly full of liquid fuel the fuel vapor concentrations reach the values given by Raoult's law. The partial pressure of all components is an increasing function of mass loading with the largest effect observed at the smallest mass loadings. For example, the vapor pressure of the C_7 (heptanes) component increases by approximately 0.6 mbar with an increase in mass loading from 3 to 50 kg/m^3 and only 0.03 mbar from 50 to 100 kg/m^3.

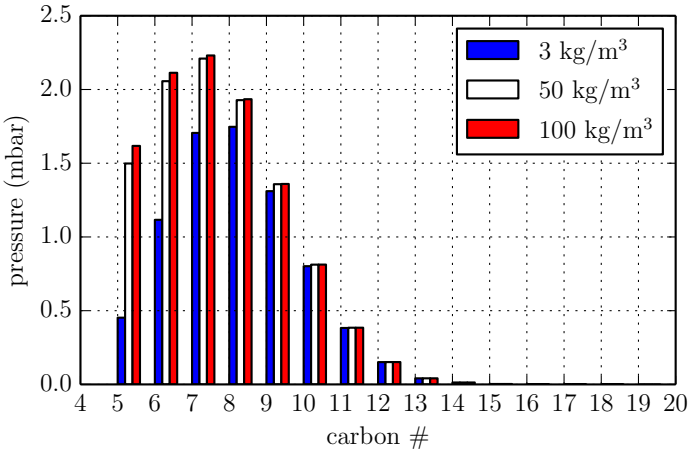

Figure A.3: Effect of mass loading on vapor pressure of each n-alkane for a flash point of 42°C at a fuel temperature of 45°C.

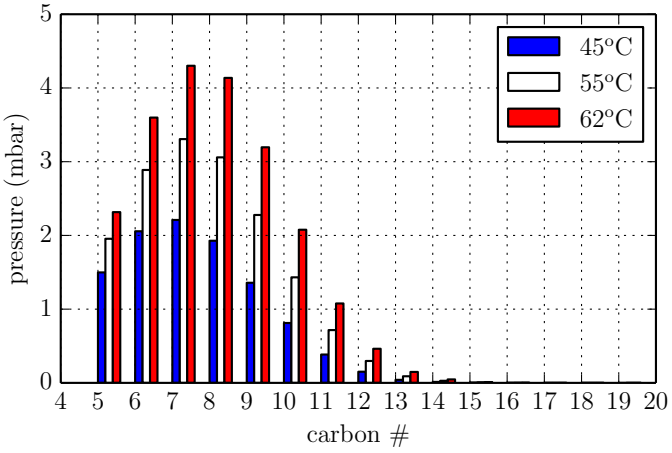

Figure A.4: Effect of temperature on vapor pressure of each n-alkane for a flash point of 42°C at a mass loading of 50 kg/m^3.

With increasing temperature, the saturation vapor pressure of each subsection increases so that the total fuel vapor pressure is always an increasing function of fuel temperature. In addition, the fuel vapor blend peaks at C_7, corresponding to heptane. Finally, Fig. A.5 shows the effect of flash point on the fuel vapor composition for a fixed fuel temperature and mass loading. As the flash point increases, the lighter hydrocarbons are fewer and the heavier hydrocarbons are dominant in the fuel vapor. This is attributed to the fact that the initial liquid composition for the higher flash

point contained fewer lighter hydrocarbons.

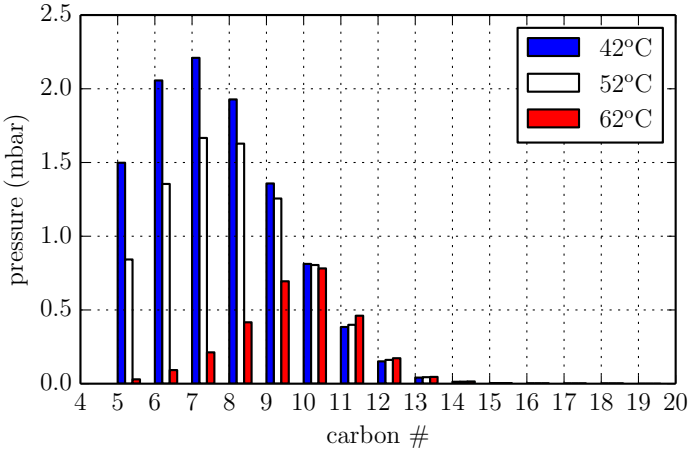

Figure A.5: Effect of flash point on vapor pressure of each n-alkane for a fuel temperature of 45°C at a mass loading of 50 kg/m^3.

Knowledge of the composition of the fuel vapor provides a better understanding on how a kerosene-based fuel compares with a simple hydrocarbon or a binary mixture. The observations indicate that the fuel vapor blend is on average composed of heptane. The vapor composition predictions indicate that lighter mass hydrocarbons (hexane/heptane) are more appropriate for low temperature fuel vapor surrogates.

Appendix B

Optical Components

B.1 Pyrometer Components

Name	Part #	Manufacturer	Description
Fiber A	FT1000EMT	Thorlabs	2 m long with reinforced furcation tubing
Fiber B	FT1000EMT	Thorlabs	2 m long without tubing
Fiber A lens	LA4078	Thorlabs	50 mm diameter convex lens with 75 mm F/L
Fiber B lens	LA4078	Thorlabs	50 mm diameter convex lens with 75 mm F/L
50/50 beamsplitter	BSW23	Thorlabs	1 inch diameter 50:50 beamsplitter IR Fused Silica
Dichroic mirror	DMLP1800L	Thorlabs	2 inch longpass dichroic mirror
Red path lens	LA4078	Thorlabs	50 mm diameter convex lens with 75 mm F/L
Blue path lens	LA4078	Thorlabs	50 mm diameter convex lens with 75 mm F/L
F1	BP-1940-105-B	Infrared Optical Products	1 inch bandpass filter centered at 1940 nm with a full width half maximum of 105 nm
F2	BP-1705-097-B	Infrared Optical Products	1 inch bandpass filter centered at 1705 nm with a full width half maximum of 97 nm
Photodetectors	PDA10DT	Thorlabs	2 InGaAs Amplified Detectors with TEC, $0.9 - 2.57$ μm

Table B.1: List of pyrometer components shown in Fig. 2.17.

B.2 Interferometer Components

Name	Part #	Manufacturer	Description
Laser	Sapphire SF 532	Coherent	CW 532 nm single-frequency laser
Beam expander	BE05M-A	Thorlabs	5× Galilean optical beam expander
M_1, M_2, M_3, M_8	43-408-533	Edmund Optics	1 inch dia. enhanced aluminum, $\lambda/20$ Flat Fused Silica
P_1, A_2	47-215	Edmund Optics	12.5 mm dia. linear glass polarizer
L_1	LA4545	Thorlabs	50 mm dia. 100 mm F/L UV fused silica plano-convex lens
WP_1, WP_2	68-820	Edmund Optics	25.4 mm dia. Quartz Wollaston prism
M_4	32-067-533	Edmund Optics	4.25 inch dia. 34 inch F/L enhanced aluminum, $\lambda/8$ parabolic mirror
M_5, M_6	47-573-533	Edmund Optics	3 inch dia. enhanced aluminum, $\lambda/20$ Flat Fused Silica
M_7	43-416-533	Edmund Optics	2 inch dia. enhanced aluminum, $\lambda/20$ Flat Fused Silica

Table B.2: List of interferometer components shown in Fig. 2.23.

Appendix C

Pyrometer Calibration

Two methods were used for calibration of the two-color pyrometer against a source of known temeprature, a tungsten filament lamp (Philips lamp model E4-2DT W21W) designed to operate under a nominal voltage of 12 V for a power of 21 W and a blackbody calibration source (Process Sensors PSC-BBS1200) with a temperature range of $20 - 1200°C$, both are shown in Fig. C.1.

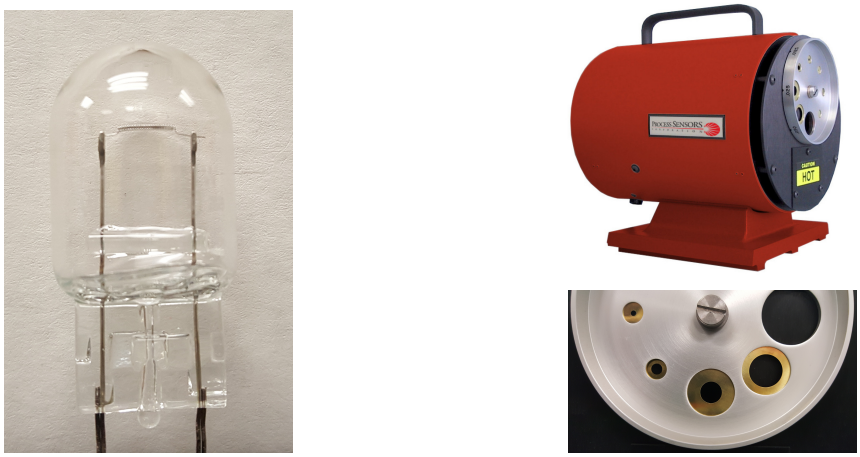

(a) Tungsten filament lamp (b) Blackbody calibration source

Figure C.1: Calibration sources: (a) Phillips lamp model E4-2DT W21W tungsten filament and (b) Process Sensors PSC-BBS1200 blackbody calibration source.

The tungsten filament lamp was first used since a blackbody calibration source was not available at the time. Before the calibration of the pyrometer could be performed against the filament, a calibration of the tungsten filament had to be completed. This appendix contains the procedure used to calibrate the tungsten filament and the

subsequent calibration of the pyrometer against this source. Additional details are provided on the reliability of the calibration procedure.

C.1 Calibration of Tungsten Filament Lamp

The approach used to calibrate a tungsten filament lamp is taken from de Izarra and Gitton (2010). A tungsten filament is used since it has a high melting temperature allowing giving it a wide range as a calibration source. The filament is heated by applying voltage from a DC power supply. The measured resistance of the filament can then be correlated to a temperature. The resistance of the filament, R, is given by,

$$R\left(T\right) = \frac{\rho_e\left(T\right) L\left(T\right)}{A\left(T\right)}, \tag{C.1}$$

where ρ_e is the electrical resistivity of tungsten, L is the length of the filament and A is the cross-sectional area. The geometric quantities L and A vary with temperature due to the thermal expansion of the material as it is heated. Rewriting Eq. C.1 in terms of a reference resistance R_0 at a temperature of $T_0 = 300$ K yields,

$$\frac{R\left(T\right)}{R_0} = \frac{\rho_e\left(T\right) L\left(T\right) A_0}{\rho_e\left(T_0\right) L_0 A\left(T\right)}. \tag{C.2}$$

Assuming a linear expansion of the filament as it is heated, L and d, the filament diameter, are given by,

$$\begin{aligned} L\left(T\right) &= L_0 + \frac{\beta\left(T\right)}{100} L_0 \\ d\left(T\right) &= d_0 + \frac{\beta\left(T\right)}{100} d_0, \end{aligned} \tag{C.3}$$

where d_0 and L_0 are the diameter and length of the filament at a temperature of 300 K, and β is the temperature dependent coefficient of thermal expansion. Combining Eqs.C.2 and C.3 results in,

$$\frac{R\left(T\right)}{R_0} = \frac{100\rho_e\left(T\right)}{\rho_e\left(T_0\right)\left(100 + \beta\left(T\right)\right)}. \tag{C.4}$$

Equation C.4 is a function of temperature only, values of ρ_e and β for tungsten, shown in Table C.1 (a), can be used to obtain Fig. C.2.

Temperature (K)	$\rho_e \times 10^8$ (Ω·m)	β (%)
300	5.65	0.003
400	8.06	0.044
500	10.56	0.086
600	13.23	0.13
700	16.09	0.175
800	19	0.222
900	21.94	0.27
1000	24.93	0.32
1100	27.94	0.371
1200	30.98	0.424
1300	34.08	0.479
1400	37.19	0.535
1500	40.36	0.593
1600	43.55	0.652
1700	46.78	0.713
1800	50.05	0.775
1900	53.35	0.839
2000	56.67	0.904
2100	60.06	0.971
2200	63.48	1.039
2300	66.91	1.109
2400	70.39	1.18
2500	73.91	1.253
2600	77.49	1.328
2700	81.04	1.404
2800	84.7	1.479
2900	88.33	1.561
3000	92.04	1.642
3100	95.76	1.724
3200	99.54	1.808
3300	103.3	1.893
3400	107.2	1.98
3500	111.1	2.068
3600	115	2.158
3655	117.1	2.209

Table C.1: Electrical resistivity and coefficient of thermal expansion of tungsten obtained from Lide (1991).

Figure C.2 (b) shows the residual of the quadratic fit of the data given by,

$$\frac{R}{R_0} = 2.842 \times 10^{-7} T^2 + 4.661 \times 10^{-3} T - 0.5243. \tag{C.5}$$

The maximum residuals correspond to temperatures below 500 K, in the region of interest for ignition, $1000 - 1300$ K, the residuals are less than 2%.

The resistance of the filament is calculated using Eq. C.6, where the voltage drop, V, is measured across the filament as the current I is varied on the power supply.

$$R = \frac{V}{I} \tag{C.6}$$

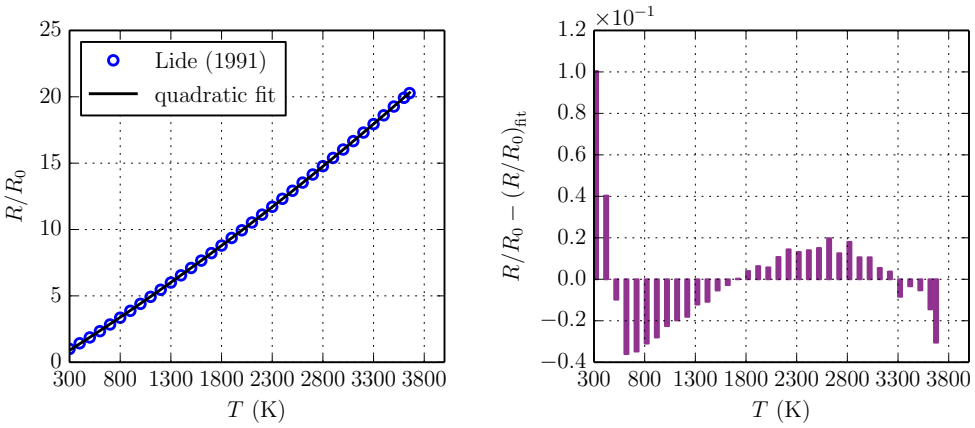

(a) R/R_0 vs. T (b) $R/R_0 - \left(R/R_0\right)_{\text{fit}}$ vs. T

Figure C.2: (a) Resistance ratio, R/R_0, as function of temperature, the open markers are data taken from Lide (1991) and the black line is a quadratic fit, (b)residuals of quadratic fit.

The calculated resistance of the filament as a function of the current is shown in Fig. C.3. The resistance at $I = 0$ is extrapolated from resistance values for $I > 0$ giving $R_0 = 0.52\,\Omega$. For a given value of I, the ratio R/R_0 is known, and using Eq. C.5, the temperature can be extracted. The temperature calibration of the filament is shown in Fig. C.4 as a function of the current. The two-color pyrometer can then be calibrated against the tungsten filament lamp using the results in Fig. C.4.

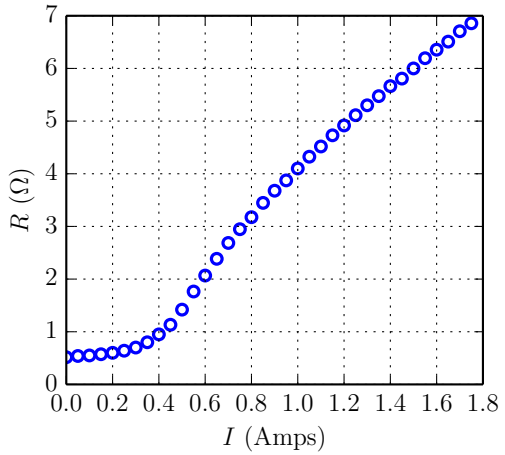

Figure C.3: Tungsten filament resistance as a function of the measured current I.

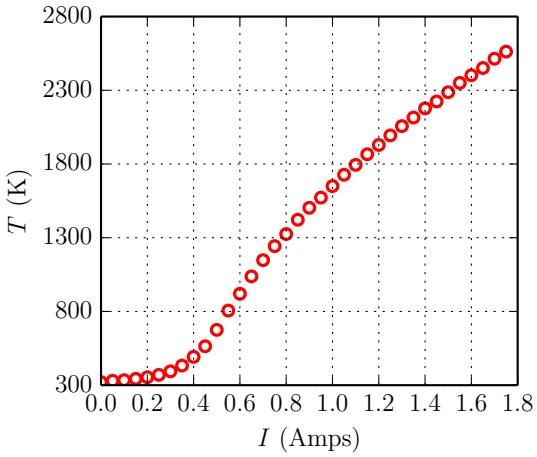

Figure C.4: Calibration of the tungsten filament as a function of the current I.

The calibration of the two-color pyrometer against the tungsten filament lamp is shown in the top figures of Fig. C.5. The bottom figures show the error calculated for each fiber using,

$$E_F = \frac{\ln\left(V_1/V_2\right) - f\left(T\right)}{\ln\left(V_1/V_2\right)}. \tag{C.7}$$

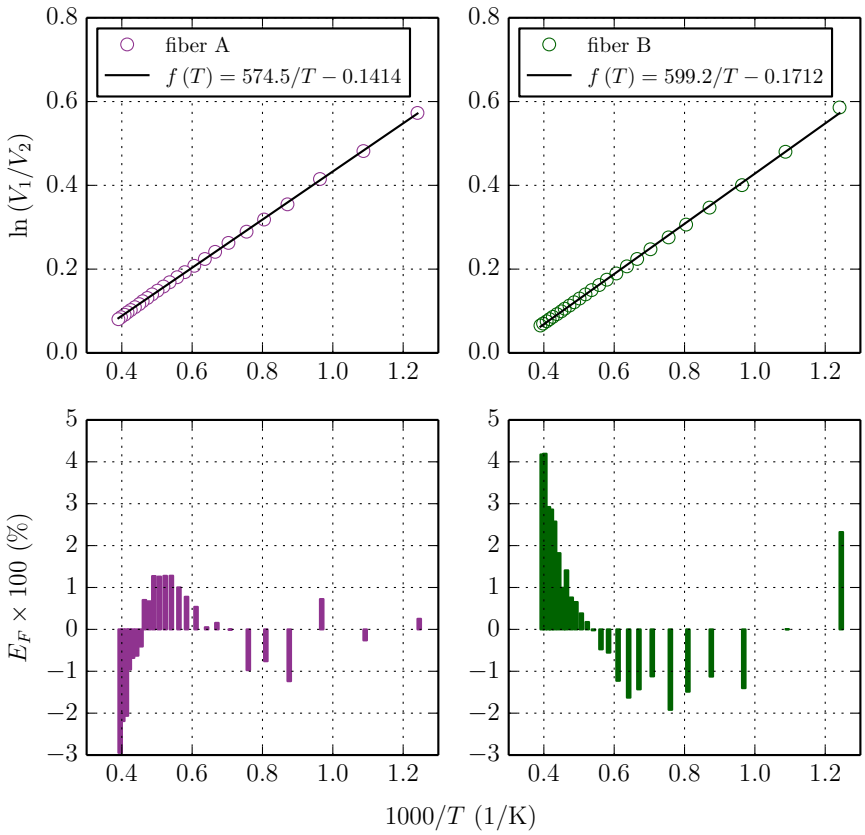

Figure C.5: Calibration curves for fiber A and fiber B using tungsten filament lamp.

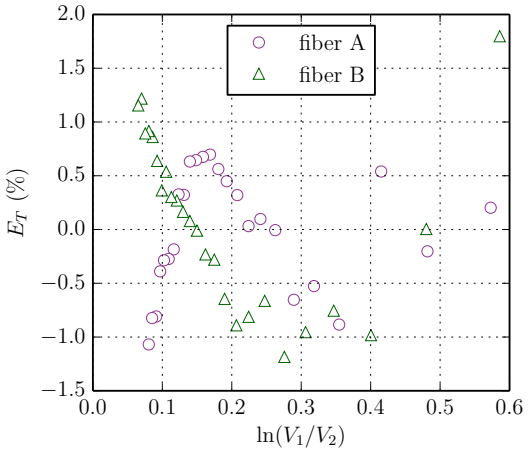

Figure C.6: Error in temperature for fiber A and fiber B as a function of $\ln\left(V_1/V_2\right)$.

At each temperature, the error in the calibration equation, f , is less than 5% of the measured ratio of voltages. This translates to an error in the temperature measurements, E_T , of less than 2%, shown in Fig. C.6. The corresponding calibration equations based on the tungsten filament lamp measurements are,

$$T_A = \frac{574.5}{\ln\left(V_1/V_2\right) + 0.1414} \tag{C.8}$$

$$T_A = \frac{599.2}{\ln\left(V_1/V_2\right) + 0.1712} \tag{C.9}$$

A blackbody calibration source was acquired after the two-color pyrometer had been calibrated against the tungsten filament lamp. The blackbody source in shown in Fig. C.1 (b), it consists of an enclosed cavity that can be heated up to 1200°; the bottom image of Fig. C.1 (b) shows the different apertures used over the heated cavity, they vary in diameter from 0.25 to 1 inch. An additional calibration of the pyrometer was performed with the blackbody source and new calibration equations, Eqs. C.10 and C.11, were obtained.

$$T_A = \frac{954.6}{\ln\left(V_1/V_2\right) + 0.2036} \tag{C.10}$$

$$T_A = \frac{1049.7}{\ln\left(V_1/V_2\right) + 0.4466} \tag{C.11}$$

The two calibrations are shown in in Fig. C.7, it appears that the use of different sources yields drastically different calibrations.

Figure C.8 shows the temperature obtained with the blackbody calibration equations plotted against the temperature obtained with the tungsten filament calibration equations. The dashed line corresponds to an ideal comparison in which the temperature sets are equal. Clearly, for a given $\ln\left(V_1/V_2\right)$, the blackbody calibration equations yield higher temperatures than the tungsten filament calibration equations. For example, for a temperature of 1200 K, values of 1300 K and close to 1800 K are obtained using the blackbody calibrations equations for fiber A and fiber B, respectively. That corresponds to an increase of 8 and 50%.

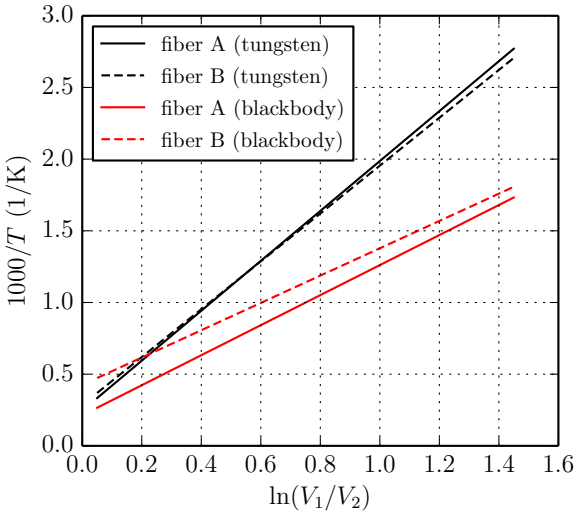

Figure C.7: Calibrations of fiber A (solid) and fiber B (dashed) using the tungsten filament lamp (black) and the blackbody calibration source (red).

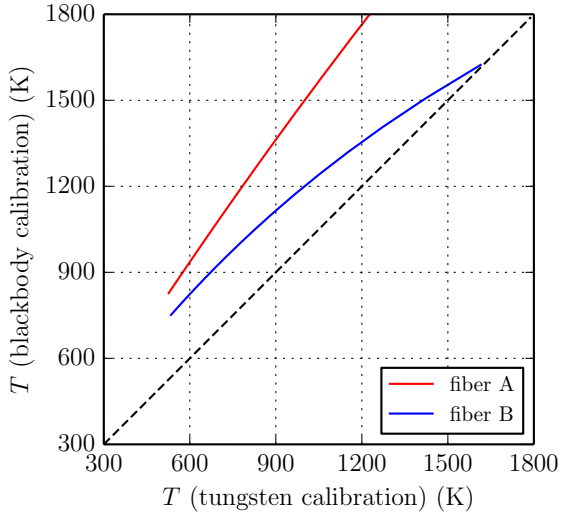

Figure C.8: Comparison of temperatures obtained with blackbody and tungsten filaments calibration equations. The fiber A and fiber B results are shown by the red blue lines, respectively.

C.2 Variation in Calibration Results

Several reasons can be given for why the tungsten calibration equations yield lower temperatures than the blackbody calibration equations. First, the temperature of

tungsten filament is not uniform due to the boundary conditions. The temperature distribution along the filament is illustrated in Fig. C.9, the temperature at the ends is lower due to heat losses from the filament to the rest of the lamp wiring. For a given current I, the lack of temperature uniformity leads to a wire resistance between $R(T_0)$ and $R(T_{\max})$, the temperature extracted from Eq. C.5 will therefore fall below $T_{\max}$. Given that the pyrometer collects light from the center of the filament were the temperature is highest, the tungsten filament calibration will systematically underpredict the temperature due to the non-uniform heating.

Additionally, extra care should be taken in interpreting the results from the blackbody calibration equations. A significant amount of time (+1 year) passed between the completion of the ignition experiments and the calibration of the pyrometer using the blackbody. During this void in time, the pyrometer remained untouched; however vibrations in the room could have led to minor misalignments of the pyrometer optical components.

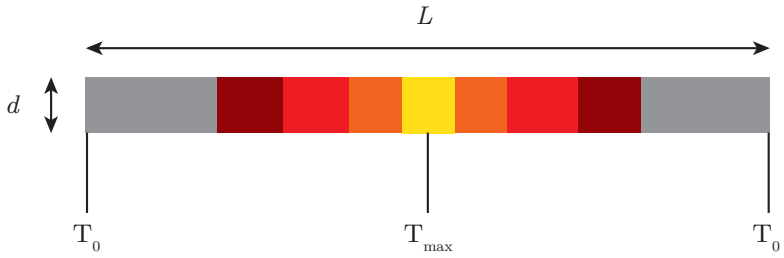

Figure C.9: Illustration of tungsten filament that is resistively heated, the temperature at the wire ends is T_0 and the maximum temperature, $T_{\max}$ occurs at the wire center; the wire has length L and diameter d.

Appendix D

Experimental Data

D.1 Hot Particle Ignition

Table D.1: Ignition experiments using 1.8, 3.5, and 6.0 mm alumina spheres traveling at 2.4 m/s, the spheres are heating using the laser heating configuration.

shot	Φ	$P_{C_6H_{14}}$ (kPa)	$P_{C_6H_{14}} + P_{N_2}$ (kPa)	$P_{C_6H_{14}} + P_{N_2} + P_{O_2}$ (kPa)	P_0 (kPa)	T_0 (K)	T_{sphere} (K)	d (mm)	No ignition (0)/ Ignition (1)
1	0.9	1.91	77.79	97.98	99.98	296	1229	6	1
2	0.9	1.92	78.37	98.66	100.03	296	1168	6	1
3	0.9	1.92	78.38	98.69	100.01	295	1153	6	1
4	0.9	1.92	78.37	98.62	100.01	296	1229	6	1
5	0.89	1.91	78.39	98.67	100.02	296	1109	6	1
6	0.89	1.91	78.37	98.7	99.99	296	1067	6	0
7	0.89	1.91	78.39	98.7	100.01	296	N/A	6	1
8	0.9	1.92	78.37	98.7	99.99	295	1165	6	0
9	0.9	1.92	78.38	98.69	99.99	296	1171	6	0
10	0.89	1.91	78.37	98.66	99.99	296	1193	6	1
11	0.89	1.91	78.37	98.7	99.99	296	1076	6	0
12	0.9	1.92	78.37	98.7	100.02	295	1118	6	0
13	0.9	1.92	78.38	98.71	100.01	296	1119	6	0
14	0.9	1.92	78.37	98.67	99.99	297	1038	6	0
15	0.9	1.92	78.43	98.71	100.01	296	1127	6	0
16	0.89	1.91	78.35	98.63	99.99	297	1196	6	0
17	0.9	1.92	78.38	98.73	100.03	297	1015	6	0
18	0.9	1.92	78.39	98.71	99.99	297	1185	6	1
19	0.9	1.92	78.38	98.69	100.05	296	1212	6	1
20	0.89	1.91	78.37	98.7	100.05	296	1193	6	1
21	0.9	1.92	78.38	98.74	100.05	296	1210	6	1
22	0.9	1.92	78.38	98.71	100.02	296	N/A	6	0
23	0.89	1.91	78.38	98.67	100.01	296	1238	6	1
24	0.9	1.92	78.38	98.66	100.05	297	N/A	6	0
25	0.89	1.91	78.38	98.69	100.05	296	1223	6	1

Table D.2: Ignition experiments using 1.8, 3.5, and 6.0 mm alumina spheres traveling at 2.4 m/s, the spheres are heating using the laser heating configuration [continued].

shot	Φ	$P_{C_6H_{14}}$ (kPa)	$P_{C_6H_{14}} + P_{N_2}$ (kPa)	$P_{C_6H_{14}} + P_{N_2} + P_{O_2}$ (kPa)	P_0 (kPa)	T_0 (K)	T_{sphere} (K)	d (mm)	No ignition (0)/ Ignition (1)
26	1.69	3.56	78.71	98.71	100.03	296	1068	6	0
27	1.7	3.57	78.73	98.73	100.05	296	1237	6	0
28	1.7	3.57	78.71	98.73	100.02	296	N/A	6	0
29	1.7	3.57	78.71	98.73	100.02	296	1233	6	0
30	1.7	3.57	78.73	98.71	100.03	296	N/A	6	0
31	1.7	3.57	78.71	98.69	100.02	296	N/A	6	0
32	1.7	3.57	78.73	98.69	100.01	296	1227	6	0
33	1	2.13	78.42	98.74	99.99	296	1225	6	1
34	1	2.13	78.41	98.63	100.02	296	1234	6	1
35	1	2.13	78.41	98.66	99.99	296	N/A	6	1
36	1	2.13	78.42	98.7	100.02	296	1276	6	1
37	1	2.13	78.42	98.71	100.03	296	1233	6	1
38	1	2.13	78.42	98.7	100.02	296	1196	6	0
39	1	2.13	78.41	98.63	100.02	296	N/A	6	0
40	1	2.13	78.42	98.67	100.02	296	1204	6	1
41	1	2.13	78.42	98.67	100.01	296	1247	6	1
42	1	2.13	78.41	98.71	100.02	296	1156	6	0
43	1	2.13	78.41	98.69	100.03	296	1245	6	1
44	1	2.13	78.41	98.65	100.02	297	1199	6	1
45	0.99	2.12	78.43	98.7	100.03	296	1217	6	0
46	1	2.13	78.42	98.7	100.01	297	1184	6	0
47	1.19	2.53	78.5	98.7	100.02	297	N/A	6	0
48	1.2	2.55	78.51	98.69	100.03	297	1189	6	0
49	1.2	2.55	78.53	98.73	100.02	296	1195	6	0
50	1.2	2.55	78.51	98.67	100.03	297	1181	6	0

Table D.3: Ignition experiments using 1.8, 3.5, and 6.0 mm alumina spheres traveling at 2.4 m/s, the spheres are heating using the laser heating configuration [continued].

shot	Φ	$P_{C_6H_{14}}$ (kPa)	$P_{C_6H_{14}} + P_{N_2}$ (kPa)	$P_{C_6H_{14}} + P_{N_2} + P_{O_2}$ (kPa)	P_0 (kPa)	T_0 (K)	T_{sphere} (K)	d (mm)	No ignition (0)/ Ignition (1)
51	1.2	2.55	78.51	98.69	100.03	296	1247	6	1
52	1.2	2.55	78.53	98.69	100.03	296	851	6	1
53	1.4	2.96	78.58	98.67	100.03	296	1145	6	0
54	1.69	3.56	78.74	98.7	100.03	296	1239	6	1
55	1.69	3.56	78.74	98.7	100.03	296	1201	6	0
56	2.49	5.16	79.07	98.74	100.03	296	1068	6	0
57	2.49	5.16	79.07	98.74	100.03	296	1245	6	1
58	0.7	1.51	78.29	98.73	100.05	296	1286	6	0
59	0.75	1.61	78.31	98.73	100.02	296	1185	6	1
60	0.75	1.61	78.31	98.73	100.01	296	1252	6	1
61	0.75	1.61	78.33	98.67	100.03	296	1293	6	1
62	0.75	1.61	78.31	98.71	100.03	296	N/A	6	1
63	0.75	1.61	78.31	98.67	100.02	296	N/A	6	0
64	0.75	1.61	78.31	98.71	100.01	296	1184	6	1
65	0.75	1.61	78.31	98.7	100.05	296	1381	6	1
66	0.75	1.61	78.31	98.71	100.05	296	1184	6	1
67	0.75	1.61	78.31	98.71	100.01	296	N/A	6	1
68	0.75	1.61	78.31	98.69	100.02	297	1310	6	1
69	0.75	1.61	78.31	98.74	100.03	296	1245	6	1
70	0.75	1.61	78.33	98.71	100.05	296	1207	6	1
71	0.75	1.61	78.31	98.73	99.99	296	1349	6	1
72	0.75	1.61	78.37	98.71	100.02	296	1267	6	0
73	0.75	1.61	78.31	98.71	100.03	296	1233	6	1
74	0.75	1.61	78.31	98.74	100.01	296	N/A	6	0
75	0.75	1.61	78.31	98.66	100.02	296	1249	6	1

Table D.4: Ignition experiments using 1.8, 3.5, and 6.0 mm alumina spheres traveling at 2.4 m/s, the spheres are heating using the laser heating configuration [continued].

shot	Φ	$P_{C_6H_{14}}$ (kPa)	$P_{C_6H_{14}} + P_{N_2}$ (kPa)	$P_{C_6H_{14}} + P_{N_2} + P_{O_2}$ (kPa)	P_0 (kPa)	T_0 (K)	T_{sphere} (K)	d (mm)	No ignition (0)/ Ignition (1)
76	0.75	1.61	78.31	98.73	100.02	296	N/A	6	0
77	0.75	1.61	78.31	98.7	99.99	296	1218	6	0
78	0.75	1.61	78.33	98.74	100.02	296	N/A	6	0
79	0.75	1.61	78.33	98.7	100.03	296	1077	6	0
80	0.75	1.61	78.31	98.71	100.05	296	N/A	6	0
81	0.75	1.6	78.3	98.7	100.05	296	1170	6	0
82	0.75	1.61	78.31	98.7	100.02	296	N/A	6	0
83	1.39	2.95	78.58	98.7	100.05	296	N/A	6	0
84	1.4	2.96	78.59	98.7	100.02	296	1194	6	1
85	1.4	2.96	78.59	98.73	100.05	296	N/A	6	0
86	1.4	2.96	78.58	98.66	100.03	297	1230	6	1
87	1.4	2.96	78.59	98.7	100.03	297	N/A	6	0
88	1.4	2.96	78.59	98.71	100.05	297	N/A	6	0
89	1.39	2.95	78.59	98.73	100.03	297	1181	6	1
90	1.4	2.96	78.59	98.74	100.05	297	1187	6	0
91	1.4	2.96	78.59	98.7	100.05	297	975	6	1
92	1.4	2.96	78.59	98.73	100.05	297	1025	6	1
93	1.39	2.95	78.59	98.73	100.05	297	1199	6	1
94	1.39	2.95	78.61	98.7	100.02	297	1147	6	1
95	1.8	3.77	78.77	98.71	100.06	297	1141	6	0
96	1.79	3.76	78.77	98.73	100.01	297	1148	6	1
97	1.79	3.76	78.77	98.7	100.02	297	1172	6	1
98	1.8	3.77	78.77	98.73	100.03	297	1172	6	0
99	1.8	3.77	78.78	98.71	100.03	297	1114	6	1
100	1.79	3.76	78.77	98.69	99.99	297	1069	6	0

Table D.5: Ignition experiments using 1.8, 3.5, and 6.0 mm alumina spheres traveling at 2.4 m/s, the spheres are heating using the laser heating configuration [continued].

shot	Φ	$P_{C_6H_{14}}$ (kPa)	$P_{C_6H_{14}} + P_{N_2}$ (kPa)	$P_{C_6H_{14}} + P_{N_2} + P_{O_2}$ (kPa)	P_0 (kPa)	T_0 (K)	T_{sphere} (K)	d (mm)	No ignition (0)/ Ignition (1)
101	1.8	3.77	78.77	98.73	99.98	297	1199	6	0
102	1.8	3.77	78.77	98.69	99.99	297	1217	6	1
103	1.8	3.77	78.77	98.67	100.01	297	1177	6	0
104	1.79	3.76	78.77	98.73	100.01	297	1190	6	0
105	1.8	3.77	78.77	98.69	99.99	297	1066	6	1
106	1.8	3.77	78.77	98.7	100.02	297	1220	6	1
107	2.2	4.56	78.98	98.69	99.99	297	1220	6	1
108	2.19	4.56	78.94	98.7	99.99	297	1217	6	1
109	2.19	4.56	78.93	98.69	99.99	297	1159	6	0
110	2.19	4.56	78.93	98.71	99.99	297	1186	6	0
111	2.19	4.56	78.93	98.73	100.02	297	1175	6	1
112	2.59	5.35	79.1	98.71	100.01	297	1038	6	0
113	2.6	5.36	79.1	98.7	100.01	297	N/A	6	0
114	2.6	5.36	79.11	98.7	99.99	297	1105	6	0
115	1	2.13	78.42	98.7	100.01	297	1215	6	1
116	1	2.13	78.42	98.7	100.01	297	N/A	6	0
117	1	2.13	78.42	98.7	100.01	297	N/A	6	0
118	1	2.13	78.42	98.73	100.01	297	1039	6	0
119	1	2.13	78.42	98.7	100.01	297	1080	6	0
120	1	2.13	78.42	98.7	99.99	297	1234	6	1
121	1	2.13	78.43	98.7	100.01	297	1180	6	1
122	1	2.15	78.42	98.71	100.02	297	N/A	3.5	0
123	1	2.13	78.42	98.67	99.99	297	N/A	3.5	0
124	1	2.13	78.43	98.7	99.99	297	1237	3.5	1
125	1	2.13	78.42	98.67	100.01	297	N/A	3.5	0

Table D.6: Ignition experiments using 1.8, 3.5, and 6.0 mm alumina spheres traveling at 2.4 m/s, the spheres are heating using the laser heating configuration [continued].

shot	Φ	$P_{C_6H_{14}}$ (kPa)	$P_{C_6H_{14}} + P_{N_2}$ (kPa)	$P_{C_6H_{14}} + P_{N_2} + P_{O_2}$ (kPa)	P_0 (kPa)	T_0 (K)	T_{sphere} (K)	d (mm)	No ignition (0)/ Ignition (1)
126	1	2.13	78.42	98.71	100.01	297	N/A	3.5	1
127	0.99	2.12	78.45	98.7	100.01	297	1251	3.5	1
128	1	2.13	78.42	98.65	100.01	297	1175	3.5	0
129	1	2.13	78.41	98.7	100.01	297	1191	3.5	1
130	0.9	1.92	78.38	98.71	99.99	297	1286	3.5	1
131	0.89	1.91	78.27	98.65	99.99	298	1254	3.5	1
132	0.9	1.92	78.39	98.73	100.01	299	1184	3.5	0
133	0.9	1.92	78.39	98.69	99.99	300	N/A	3.5	1
134	0.9	1.92	78.38	98.71	99.99	301	1215	3.5	1
135	0.9	1.92	78.38	98.7	100.01	302	N/A	3.5	1
136	0.89	1.91	78.39	98.71	100.01	303	1113	1.8	0
137	0.89	1.91	78.38	98.73	99.99	304	1258	1.8	0
138	0.89	1.92	78.26	98.7	100.02	305	N/A	1.8	1
139	0.9	1.92	78.38	98.7	100.01	306	N/A	1.8	1
140	0.9	1.92	78.38	98.65	99.99	307	1221	1.8	1
141	0.9	1.92	78.38	98.62	99.99	308	1270	1.8	1
142	0.9	1.92	78.39	98.74	99.99	309	1409	1.8	1
143	1	2.13	78.39	98.7	99.99	310	N/A	1.8	1
144	0.9	1.92	78.39	98.66	99.99	311	1338	1.8	1

Table D.7: Ignition experiments using a 4 mm titanium sphere traveling at 2.4 m/s, the spheres are heating using the electrial heating configuration.

shot	Φ	P_0 (kPa)	T_0 (K)	T_{sphere} (K)	No ignition (0)/ Ignition (1)
1	0.9	49.98	295.5	1297	1
3	0.9	100	295.2	1388	1
4	0.9	100	296.5	1464	1
6	0.9	100	295.3	1429	1
7	0.9	100	296.3	1356	1
8	0.9	100	297	1421	1
9	0.9	100	297.2	1071	0
10	0.9	100	295.3	1097	0
11	0.89	100	295.5	1150	0
12	0.9	100	296.5	1171	0
13	0.89	100	297.5	1175	0
14	0.9	100	298.5	1170	0
15	0.9	100	298.1	1167	0
16	0.89	100	299.1	1180	1
17	0.9	100	295.4	1195	1
18	0.9	100	296.5	1230	1
19	0.9	100	297.3	1163	1
20	0.9	100	295.5	1150	1
21	0.9	100	295.9	1199	1
22	0.9	100	295.4	1199	1
24	0.9	100	296.2	1071	0
25	0.9	100	295.3	1178	1
26	0.9	100	296.4	1156	1
27	0.89	100	296.1	1153	1
28	0.9	100	296.9	1083	0
29	0.9	100	296.7	1060	0
30	0.9	100	297.4	1167	0

D.2 Spherically Expanding Flames

Table D.8: Spherically expanding flame experiments performed in n-hexane-air, −L and −NL correspond to the results from the linear and non-linear extrapolation, respectively.

shot		$P_{C_6H_{14}}$ (kPa)	P_{N_2} (kPa)	P_{O_2} (kPa)	T_0 (K)	P_0 (kPa)	S_b^0−L (cm/s)	L_B−L (cm)	S_b^0−NL (cm/s)	L_b−NL (cm)	Comments
1	0.76	1.66	77.67	20.65	295	99.98	172.11	0.3619	164.17	0.2081	OK
2	0.83	1.8	77.57	20.58	295	99.95	217.2	0.2211	212.9	0.1528	OK
3	0.9	1.95	77.45	20.52	295	99.92	255.06	0.1564	251.97	0.1173	OK
4	0.98	2.12	77.32	20.53	295	99.97	278.41	0.1321	278.55	0.1147	OK
5	1.27	2.71	76.85	20.34	295	99.9	295.93	0.0691	296.66	0.0672	OK
6	1.43	3.07	76.51	20.37	295	99.95	221.55	-0.0184	220.23	-0.028	OK
7	0.96	1.15	37.44	11.41	295	50	N/A	N/A	N/A	N/A	N_2/O_2 too low
8	1.23	1.32	38.45	10.19	295	49.96	N/A	N/A	N/A	N/A	High flame speed
9	1.3	1.4	38.38	10.2	295	49.98	317.29	0.0492	315.99	0.0406	OK
10	1.4	1.5	38.3	10.2	295	50	N/A	N/A	N/A	N/A	Low flame speed
11	1.44	1.54	38.28	10.18	295	50	N/A	N/A	N/A	N/A	Low flame speed
12	1.5	1.6	38.23	10.16	295	49.99	N/A	N/A	N/A	N/A	Low flame speed
13	1.6	1.71	38.12	10.16	295	49.99	N/A	N/A	N/A	N/A	Low flame speed
14	0.99	1.2	37.35	11.46	295	50.01	N/A	N/A	N/A	N/A	N_2/O_2 too low
15	1.02	1.1	38.63	10.26	295	49.99	N/A	N/A	N/A	N/A	Oval flame
16	1.2	1.29	38.48	10.25	295	50.02	N/A	N/A	N/A	N/A	Oval flame
17	1.02	1.1	38.62	10.28	295	50	N/A	N/A	N/A	N/A	Two flames
18	1	1.08	38.65	10.27	295	50	319.2	0.2402	306.41	0.143	OK
19	0.91	0.98	38.72	10.27	295	49.97	N/A	N/A	N/A	N/A	Two flames
20	0.9	0.97	38.73	10.28	295	49.98	273.55	0.4329	253.14	0.2147	OK
21	0.62	0.87	35.8	13.33	295	50	N/A	N/A	N/A	N/A	N_2/O_2 too low
22	0.8	0.87	38.8	10.29	295	49.96	N/A	N/A	N/A	N/A	No ignition
23	0.85	0.92	38.77	10.3	295	49.99	N/A	N/A	N/A	N/A	Two flames
24	0.86	0.93	38.76	10.31	295	50	271.19	0.3136	259.66	0.1871	OK
25	1.11	2.38	77.11	20.45	295	99.94	N/A	N/A	N/A	N/A	Poor ignition

Table D.9: Spherically expanding flame experiments performed in n-hexane-air, −L and −NL correspond to the results from the linear and non-linear extrapolation, respectively [continued].

shot		$P_{C_6H_{14}}$ (kPa)	P_{N_2} (kPa)	P_{O_2} (kPa)	T_0 (K)	P_0 (kPa)	S_b^0−L (cm/s)	L_B−L (cm)	S_b^0−NL (cm/s)	L_b−NL (cm)	Comments
26	0.99	1.07	38.7	10.22	295	49.99	297.5	0.3446	279.34	0.1813	OK
27	1.1	1.19	38.55	10.29	295	50.03	348.36	0.2347	332.08	0.1318	OK
28	1.2	1.29	38.48	10.21	295	49.98	N/A	N/A	N/A	N/A	No video
29	1.2	1.29	38.46	10.24	295	49.99	324.05	0.1371	318.79	0.0982	OK
30	0.91	1.29	38.47	10.2	295	49.96	324.67	0.1417	318.69	0.099	OK
31	0.9	1.4	38.39	10.21	295	50	274.25	0.0334	274.67	0.0339	OK
32	0.88	1.5	38.33	10.16	295	49.99	217.8	-0.0677	218.28	-0.0696	OK
33	0.87	1.6	38.23	10.17	295	50	160.23	-0.166	152.39	-0.3003	OK
34	0.85	1.7	38.16	10.12	295	49.98	108.92	-0.2499	100.32	-0.5307	OK
35	0.84	0.97	38.72	10.28	295	49.97	N/A	N/A	N/A	N/A	No video
36	0.82	0.97	38.74	10.29	295	50	N/A	N/A	N/A	N/A	No video
37	0.81	1.08	38.64	10.26	295	49.98	N/A	N/A	N/A	N/A	No video
38	0.79	1.08	38.65	10.25	295	49.98	330.61	0.2824	312.42	0.1518	OK
39	0.78	1.19	38.56	10.23	295	49.98	336.84	0.1825	329.08	0.1233	OK
40	0.76	0.97	38.74	10.27	295	49.98	289.3	0.3325	273.7	0.1828	OK
41	0.75	1.44	38.36	10.2	295	50	249.56	-0.0112	251.71	0.0008	OK
42	0.73	1.8	38.09	10.11	295	50	78.22	-0.3432	64.26	-1.0968	OK
43	0.72	1.03	38.7	10.27	295	50	306.92	0.2417	297.19	0.1542	OK
44	0.7	0.93	38.79	10.26	295	49.98	267.07	0.2845	257.48	0.1772	OK
45	0.92	0.98	38.73	10.14	313	49.85	307.14	0.308	291.7	0.173	OK
46	1.11	1.19	38.56	10.21	312.4	49.96	346.06	0.1624	339.38	0.1133	OK
47	1.41	1.51	38.3	10.15	312.9	49.96	218.31	-0.0586	219.11	-0.0566	OK
48	0.89	0.97	38.72	10.36	332.7	50.05	300.78	0.3515	281.54	0.1836	OK
49	0.9	0.98	38.72	10.36	325.7	50.06	236.96	-0.0634	280.98	0.1677	OK
50	1.1	1.19	38.55	10.29	325.4	50.04	364.25	0.2344	349.21	0.1384	OK
51	1.4	1.5	38.3	10.2	325.3	50	242.73	-0.0079	244.77	0.0023	OK

Table D.10: Spherically expanding flame experiments performed in n-hexane-air, $-$L and $-$NL correspond to the results from the linear and non-linear extrapolation, respectively[continued].

shot		$P_{C_6H_{14}}$ (kPa)	P_{N_2} (kPa)	P_{O_2} (kPa)	T_0 (K)	P_0 (kPa)	S_b^0-L (cm/s)	L_B-L (cm)	S_b^0-NL (cm/s)	L_b-NL (cm)	Comments
52	0.9	0.98	38.71	10.37	357.4	50.06	328.8	0.2881	315	0.1706	OK
53	1.1	1.19	38.54	10.29	357.5	50.02	374.87	0.1834	364.65	0.1196	OK
54	1.4	1.5	38.31	10.2	357.6	50.01	249.71	-0.018	250.17	-0.0157	OK
55	0.9	0.98	38.72	10.36	380.2	50.06	338.52	0.2888	321.24	0.1615	OK
56	1.1	1.19	38.55	10.28	380.3	50.02	388.6	0.1634	380.6	0.1173	OK
57	1.4	1.5	38.32	10.19	380.1	50.01	273.82	0.0013	274.17	0.0032	OK
58	0.9	1.95	77.46	20.56	356.7	99.97	277.38	0.1079	273.89	0.0802	OK
59	0.89	1.56	61.97	16.71	356.8	80.23	282.47	0.1555	276.42	0.1061	OK
60	0.92	0.59	23.25	6.12	357	29.96	N/A	N/A	N/A	N/A	Strange flame
61	0.9	0.78	30.98	8.27	356.5	40.02	323.77	0.3161	307.01	0.1767	OK

Appendix E

Simplified Models of Ignition

The simple approach to predict the ignition behavior trend is based on a critical Damköhler number (Da). The Damköhler number is the ratio of the flow time scale to the chemical time scale, i.e.,

$$\mathrm{Da} = \frac{\tau_{\mathrm{res}}}{\tau_{\mathrm{ign}}}. \tag{E.1}$$

The chemical time scale or ignition delay time, τ_{ign}, is defined as the time required for chemical reactions to take place that will result in significant heat release which marks the ignition event. Ignoring the effects of thermal and species transport, the ignition delay time can be approximated using constant pressure zero dimensional reactor calculations using a chemical mechanism to represent the oxidation of *n*-hexane in air (Mével et al., 2014); the calculations are shown by the open markers in Fig. E.3. The flow time scale or residence time, which was first described in Chapter 1, is defined as the time needed for a fluid parcel to travel from the front stagnation point to the separation region (separated flow) or rear stagnation point (attached flow) of the sphere. For a fixed sphere diameter, the travel time depends on the location of the fluid parcel normal to the sphere wall; the fluid parcels closest to the wall will travel slowly as they have the lowest velocity (in the sphere reference frame) due to the no slip condition, and a fluid parcel that is at the edge of the momentum boundary layer will travel fast at a velocity comparable to the freestream velocity. The ignition threshold is defined by a critical Damköhler number, i.e. $\mathrm{Da} = \mathrm{Da}^*$; $\mathrm{Da}^* = 1$ is a typical critical value used in order of magnitude analysis.

E.1 Residence Time

The flow time scale or residence can be estimated using three models:

(a) Model I: assumes no variations in the edge velocity around sphere

(b) Model II: accounts for variations in edge velocity around sphere

(c) Model III: accounts for variations in velocity within momentum boundary layer

E.1.1 Model I: Neglecting Edge Velocity Variations

Assuming a constant freestream velocity, the travel time of the fluid parcel furthest from the wall is,

$$\tau_{\text{res}} = \frac{s_{\text{sep}}}{V_\infty}, \tag{E.2}$$

where s_{sep} is the arc length measured from the front stagnation point to the point of flow separation and V_∞ is the freestream velocity far from the sphere. To perform a first approximation, s_{sep} is approximated as s_{total}, which is the arc length from the front to the rear stagnation point, i.e. πR, where R is the radius of the sphere. For the three sphere diameters given in Section 4.3, s_{total} = 2.8, 5.5, and 9.4 mm for d = 1.8, 3.5, and 6.0 mm.

E.1.2 Model II: Accounting for Edge Velocity Variations

An improved residence time that accounts for variations in the flow velocity around the sphere can be calculated by assuming potential flow, i.e. the tangential velocity, u_θ, around the sphere is given by,

$$u_\theta = \frac{3}{2} V_\infty \sin\theta. \tag{E.3}$$

θ is shown Fig. E.1, where $\theta = 0$ corresponds to the front stagnation point, and $\theta = \pi$ corresponds to the rear stagnation point.

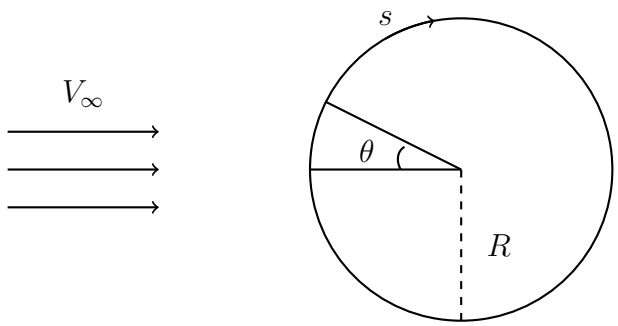

Figure E.1: Coordinate description of flow past a sphere.

The residence time is written as,

$$t_{\text{res}} = \int_0^\theta \frac{1}{u_\theta}\,\mathrm{d}s = \int_0^\theta \frac{R}{u_\theta}\,\mathrm{d}\theta', \tag{E.4}$$

Combining Eqs. E.3 and E.4 and integrating results in,

$$t_{\text{res}} = \frac{2R}{3V_\infty} \ln\left(\left|\tan\left(\theta/2\right)\right|\right)\Big|_0^\theta. \tag{E.5}$$

To satisfy the condition that the residence time at $\theta = 0$ is equal to 0,

$$t_{\text{res}} = \frac{2R}{3V_\infty} \ln\left(\left|\tan\left(\theta/2\right) + 1\right|\right). \tag{E.6}$$

Equation E.6 can be rewritten in terms of the residence time, τ_{res}, assuming a constant velocity V_∞ along the sphere surface,

$$\tau = \frac{\pi R}{V_\infty}. \tag{E.7}$$

Equation E.6 becomes,

$$t_{\text{res}} = \tau_{\text{res}} C \quad \text{and} \quad C = \frac{2}{3\pi} \ln\left(\left|\tan\left(\theta/2\right) + 1\right|\right). \tag{E.8}$$

Figure E.2 shows the constant C plotted as a function of θ; for separation angles of 136°, 125°, and 116° corresponding to sphere diameters of 1.8, 3.5, and 6.0 mm,

respectively, with a surface temperature of 1200 K and velocity of 2.4 m/s, $C = 0.2 - 0.3$. The residence times are shorter than τ_{res} obtained using Eq. E.2. The effect of the velocity gradient in the boundary layer, discussed in the next chapter, is even more significant and leads to substantially longer residence times.

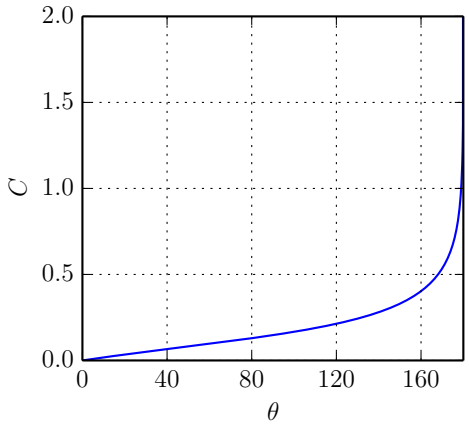

Figure E.2: Constant C from Eq. E.8 as a function of θ.

E.1.3 Model III: Accounting for Velocity Variations within Momentum Boundary Layer

A detailed description of the residence time within a momentum boundary layer is given in Section 5.7. The residence time calculation takes into account the variations in velocity within the momentum boundary layer and neglects edge velocity variations. The analysis indicates that there are very large variations in the residence time within boundary layers. To use Model III for making ignition estimates requires prior knowledge of the location of the igniting fluid parcel relative to the sphere wall; however, this is not possible without running a full reactive simulation of flow over a sphere.

E.2 Ignition Trend Estimates

Given that all three spheres tested experimentally are traveling at 2.4 m/s when ignition occurs, Model I yields $\tau_{\text{res}} = 1.2$, 2.3, and 3.9 ms. The gas temperature defined by using a critical Damköhler number, $\text{Da}^* = 1$, is shown in Fig. E.3 for the three sphere diameters ($d = 1.8$, 3.5, and 6.0 mm), and a comparison with the experimental trend (Fig. 4.18) is shown in Fig. E.4. In general, the trend observed experimentally is reproduced with this simple Damköhler number approach that uses Model I to estimate the flow time scale. Differences of $3.9-4.3\,\%$ are observed between the two trends, with the predicted values being slightly lower than the experimental results.

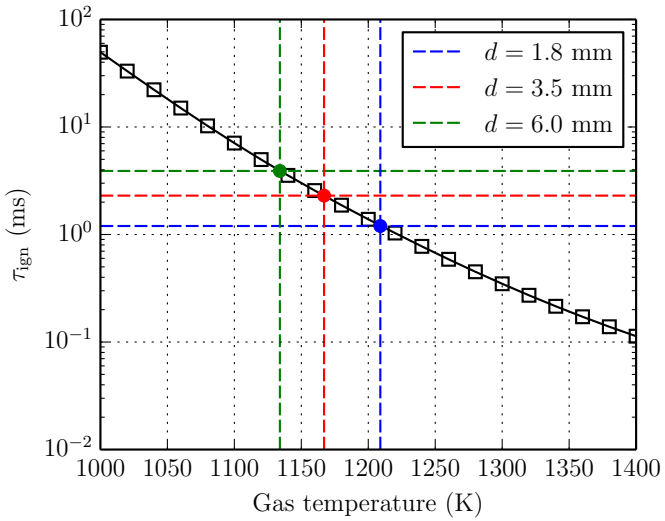

Figure E.3: Ignition delay time calculated using a zero-dimensional constant-pressure reactor implemented with Cantera Goodwin (2003) with the reduced mechanism of Mével et al. (2014) for n-hexane-air at $= 0.9$; the black open squares are the delay time calculations and the filled circles show the temperatures at which the $\text{Da} = 1$.

E.3 Issues with Simplified Model

Although the Damköhler number approach is simple and useful for estimating the general trend of the ignition threshold as a function of the sphere diameter, it is only

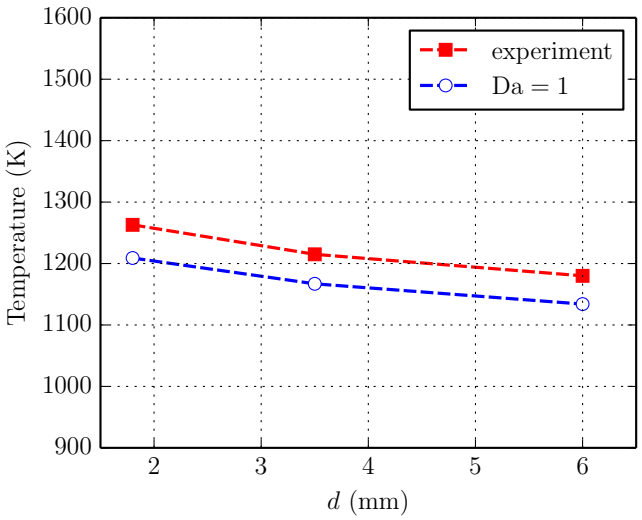

Figure E.4: Comparison of experimental ignition threshold as a function of diameter with ignition threshold estimates obtained by using a Damköhler number approach.

a rough guide that fails to account for several significant issues, including:

1. The residence time is based on a fluid parcel traveling at the freestream velocity of the sphere; however, based on numerical modeling presented in Chapter 5 and by Melguizo-Gavilanes et al. (2016b), it is a fluid parcel that is close to the wall that leads to ignition.

2. A fluid parcel that is closer to the wall will have a longer residence time than parcels further away; using the $\mathrm{Da}^* = 1$ criterion, the ignition thresholds will be lower than the predicted values shown in Fig. E.4.

3. For the sphere diameters presented, the flow actually separates since $\mathrm{Re} > 20$ (Clift et al., 2005), and this results in smaller residence times since a fluid parcel travels a shorter distance when compared to the s_{total} values given in Section E.1.1.

4. The velocity at the edge of the momentum boundary layer around a sphere is not constant, it is zero at the front stagnation point and increases to a maximum halfway between the front and rear stagnation points and then begins

to decrease until an adverse pressure gradient leads to flow separation (White, 1991).

5. A fluid parcel quickly reaches a nearly constant temperature when close to the wall; however, far from the wall the gas temperature is lower than the wall temperature for an extended time. As a consequence, the gas parcel that ignites experiences a very different temperature history than for parcels close to the wall.

6. Transport of thermal energy and species by diffusion is not accounted for.

7. Surface chemistry that might accelerate or mitigate ignition is not accounted for.

Appendix F

Performance of Nonlinear Methodology

F.1 Effect of Data Set Size: $|R_f|$

F.1.1 Variance of S_b^0

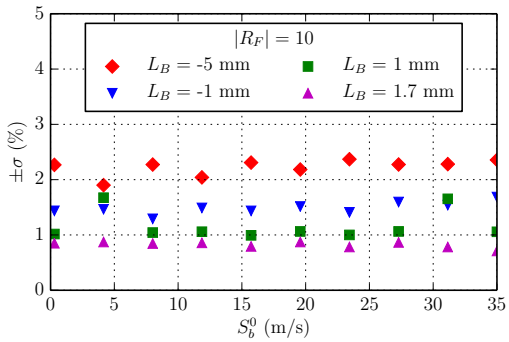

Figure F.1: $|R_f| = 10$: Effect of L_B on variance of S_b^0 for $R_f = [10, 58]$ mm, 1% Gaussian noise

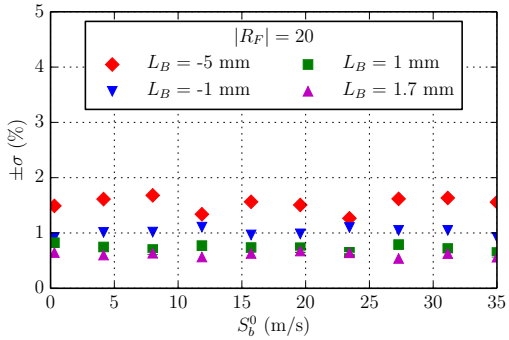

Figure F.2: $|R_f| = 20$: Effect of L_B on variance of S_b^0 for $R_f = [10, 58]$ mm, 1% Gaussian noise

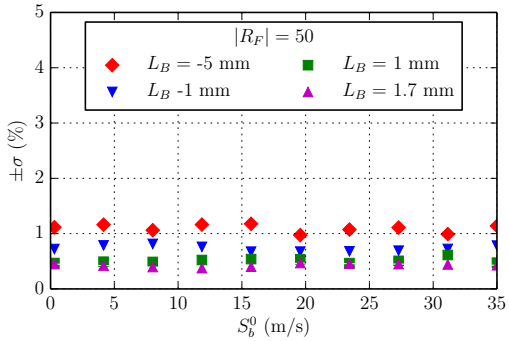

Figure F.3: $|R_f| = 50$: Effect of L_B on variance of S_b^0 for $R_f = [10, 58]$ mm, 1% Gaussian noise

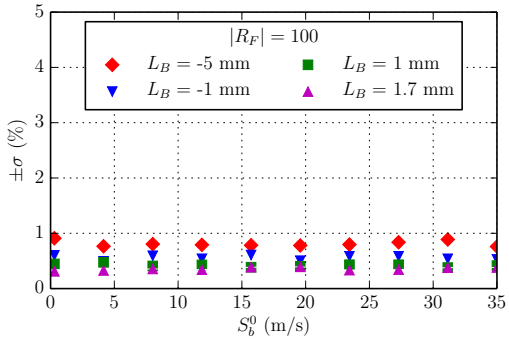

Figure F.4: $|R_f| = 100$: Effect of L_B on variance of S_b^0 for $R_f = [10, 58]$ mm, 1% Gaussian noise

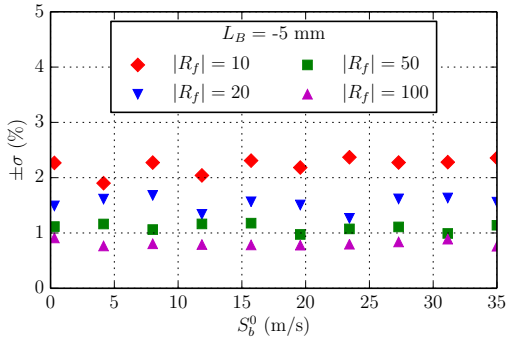

Figure F.5: $L_B = -5$ **mm**: Effect of $|R_f|$ on variance of S_b^0 for $R_f = [10, 58]$ mm, 1% Gaussian noise

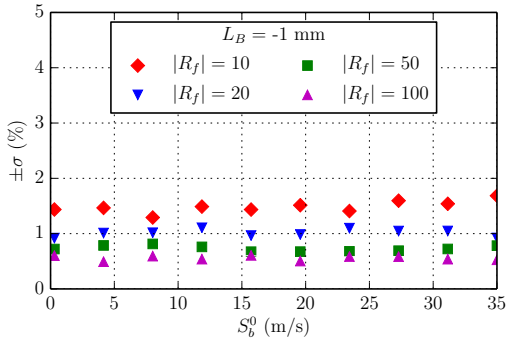

Figure F.6: $L_B = -1$ **mm**: Effect of $|R_f|$ on variance of S_b^0 for $R_f = [10, 58]$ mm, 1% Gaussian noise

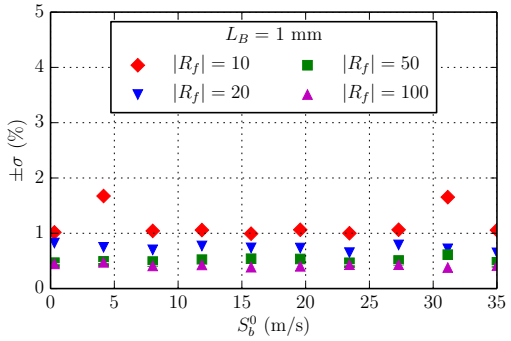

Figure F.7: $L_B = 1$ **mm**: Effect of $|R_f|$ on variance of S_b^0 for $R_f = [10, 58]$ mm, 1% Gaussian noise

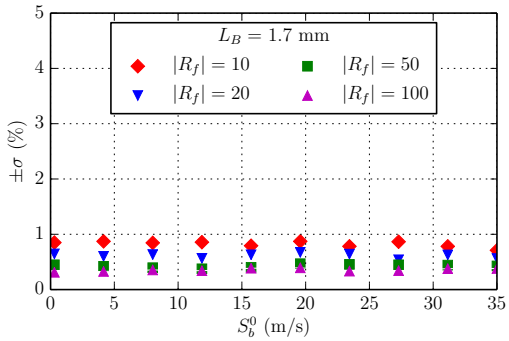

Figure F.8: $L_B = 1.7$ **mm**: Effect of $|R_f|$ on variance of S_b^0 for $R_f = [10, 58]$ mm, 1% Gaussian noise

F.1.2 Variance of L_B

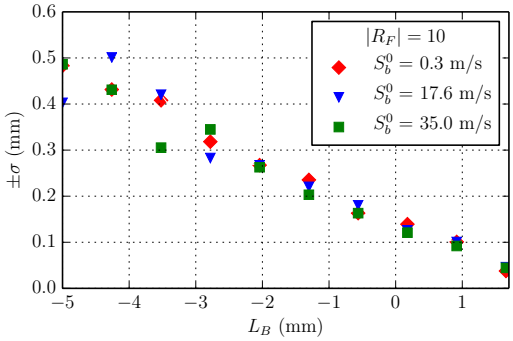

Figure F.9: $|R_f| = 10$: Effect of S_b^0 on variance of L_B for $R_f = [10, 58]$ mm, 1% Gaussian noise

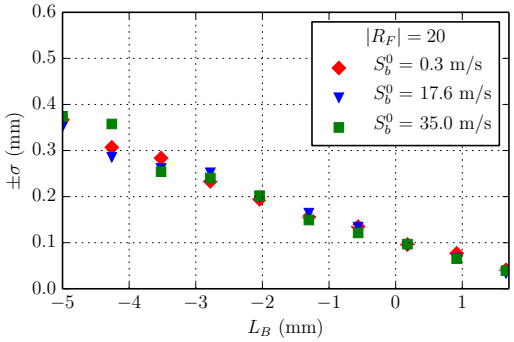

Figure F.10: $|R_f| = 20$: Effect of S_b^0 on variance of L_B for $R_f = [10, 58]$ mm, 1% Gaussian noise

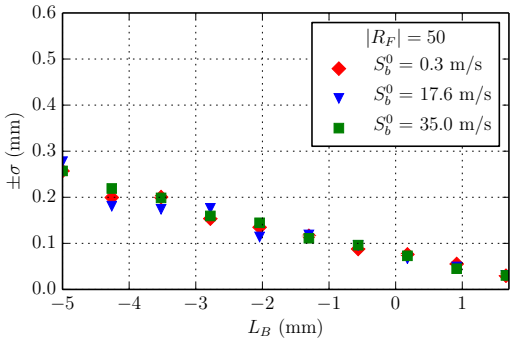

Figure F.11: $|R_f| = 50$: Effect of S_b^0 on variance of L_B for $R_f = [10, 58]$ mm, 1% Gaussian noise

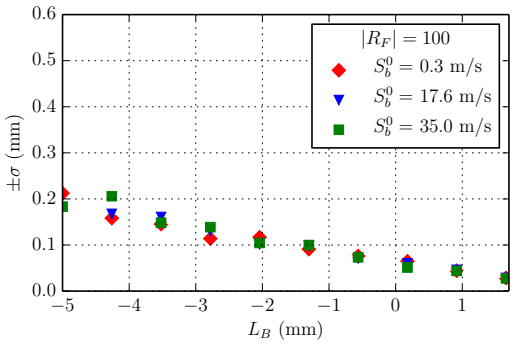

Figure F.12: $|R_f| = 100$: Effect of S_b^0 on variance of L_B for $R_f = [10, 58]$ mm, 1% Gaussian noise

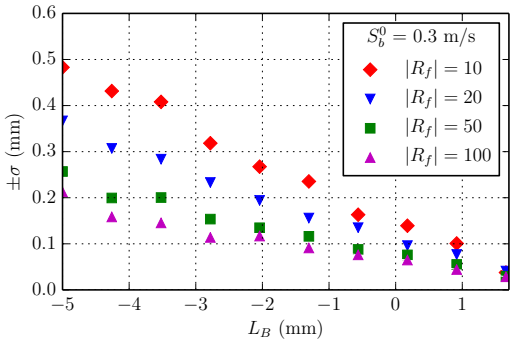

Figure F.13: $S_b^0 = 0.3$ m/s: Effect of $|R_f|$ on variance of L_B for $R_f = [10, 58]$ mm, 1% Gaussian noise

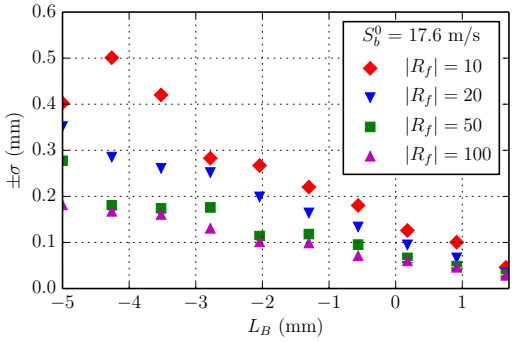

Figure F.14: $S_b^0 = 17.6$ m/s: Effect of $|R_f|$ on variance of L_B for $R_f = [10, 58]$ mm, 1% Gaussian noise

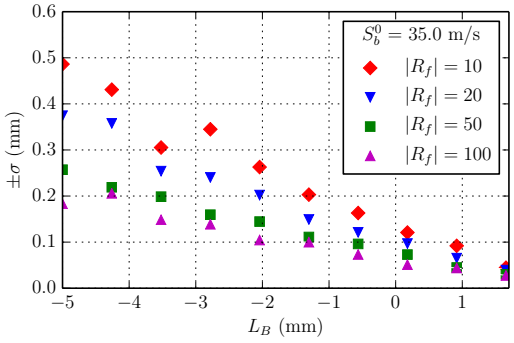

Figure F.15: $S_b^0 = 35.0$ m/s: Effect of $|R_f|$ on variance of L_B for $R_f = [10, 58]$ mm, 1% Gaussian noise

F.1.3 Uncertainty of S_b^0

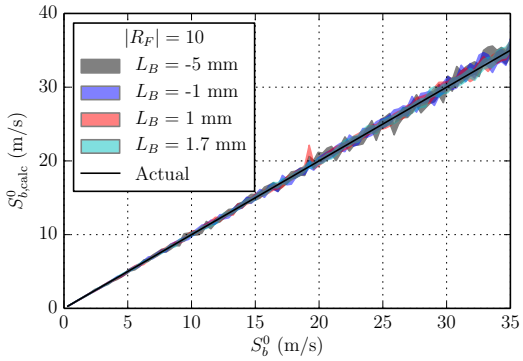

Figure F.16: $|R_f| = 10$: Effect of L_B on uncertainty of S_b^0 for $R_f = [10, 58]$ mm, 1% Gaussian noise

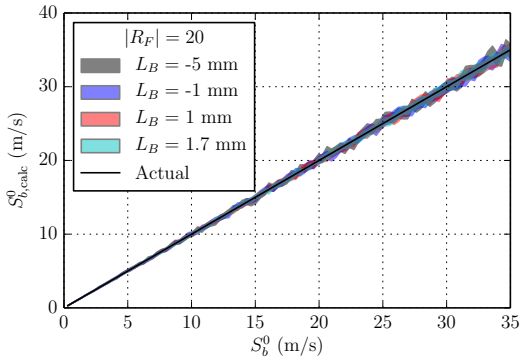

Figure F.17: $|R_f| = 20$: Effect of L_B on uncertainty of S_b^0 for $R_f = [10, 58]$ mm, 1% Gaussian noise

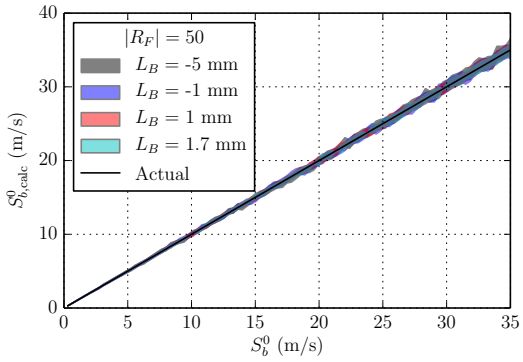

Figure F.18: $|R_f| = 50$: Effect of L_B on uncertainty of S_b^0 for $R_f = [10, 58]$ mm, 1% Gaussian noise

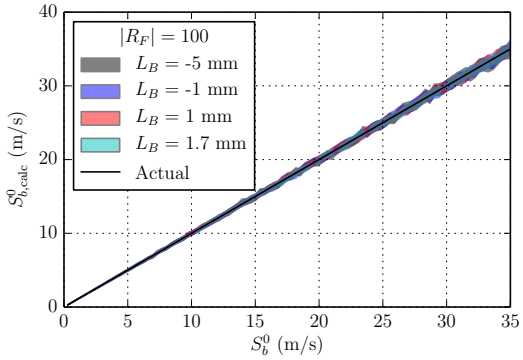

Figure F.19: $|R_f| = 100$: Effect of L_B on uncertainty of S_b^0 for $R_f = [10, 58]$ mm, 1% Gaussian noise

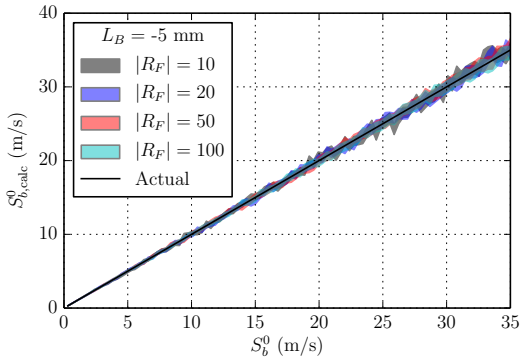

Figure F.20: $L_B = -5$ mm: Effect of $|R_f|$ on uncertainty of S_b^0 for $R_f = [10, 58]$ mm, 1% Gaussian noise

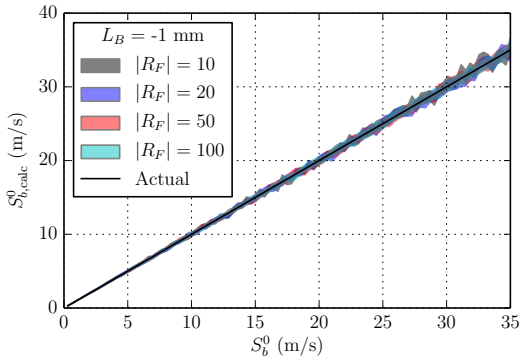

Figure F.21: $L_B = -1$ mm: Effect of $|R_f|$ on uncertaintyof S_b^0 for $R_f = [10, 58]$ mm, 1% Gaussian noise

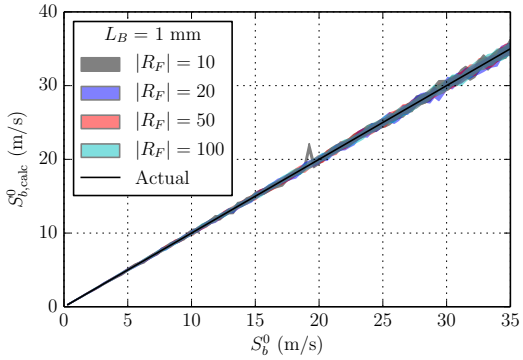

Figure F.22: $L_B = 1$ mm: Effect of $|R_f|$ on uncertainty of S_b^0 for $R_f = [10, 58]$ mm, 1% Gaussian noise

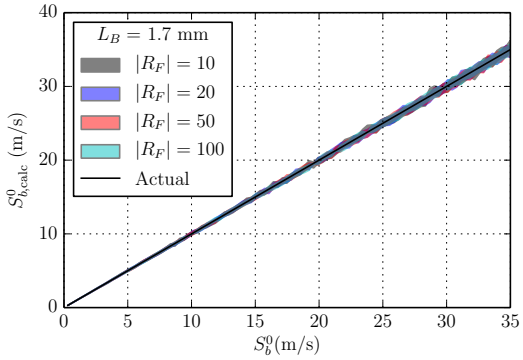

Figure F.23: $L_B = 1.7$ mm: Effect of $|R_f|$ on uncertainty of S_b^0 for $R_f = [10, 58]$ mm, 1% Gaussian noise

F.1.4 Uncertainty of L_B

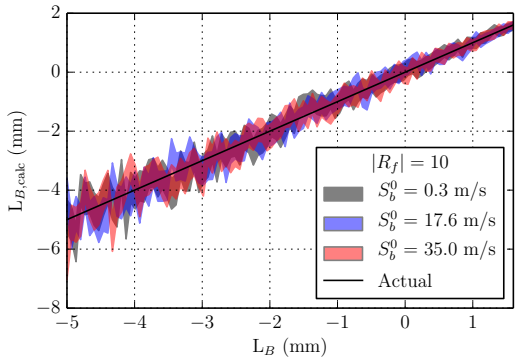

Figure F.24: $|R_f| = 10$: Effect of S_b^0 on uncertainty of L_B for $R_f = [10, 58]$ mm, 1% Gaussian noise

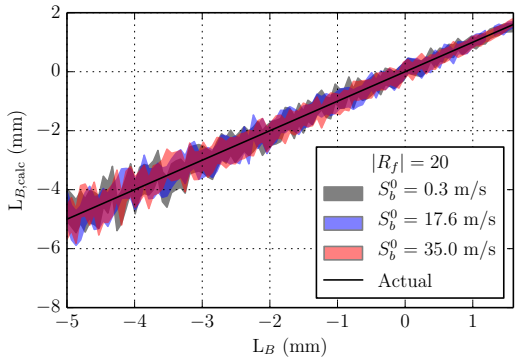

Figure F.25: $|R_f| = 20$: Effect of S_b^0 on uncertainty of L_B for $R_f = [10, 58]$ mm, 1% Gaussian noise

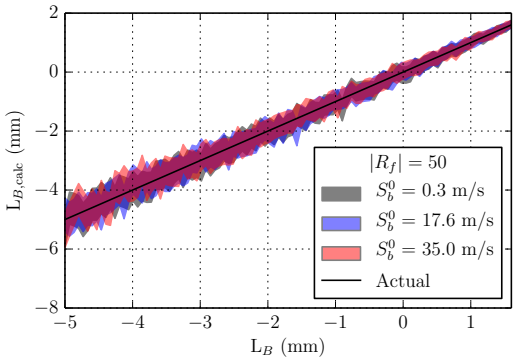

Figure F.26: $|R_f| = 50$: Effect of S_b^0 on uncertainty of L_B for $R_f = [10, 58]$ mm, 1% Gaussian noise

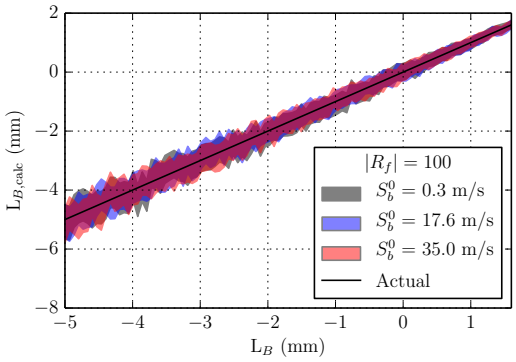

Figure F.27: $|R_f| = 100$: Effect of S_b^0 on uncertainty of L_B for $R_f = [10, 58]$ mm, 1% Gaussian noise

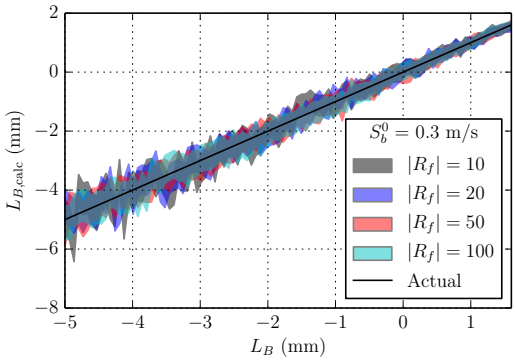

Figure F.28: $S_b^0 = 0.3$ m/s: Effect of $|R_f|$ on uncertainty of L_B for $R_f = [10, 58]$ mm, 1% Gaussian noise

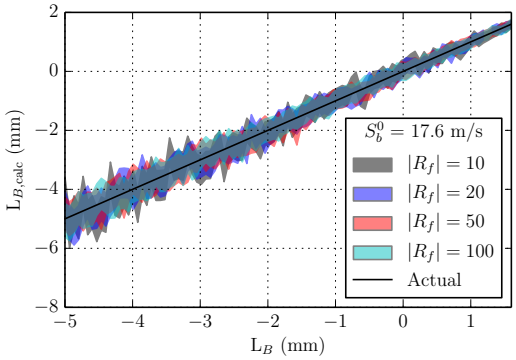

Figure F.29: $S_b^0 = 17.6$ m/s: Effect of $|R_f|$ on uncertainty of L_B for $R_f = [10, 58]$ mm, 1% Gaussian noise

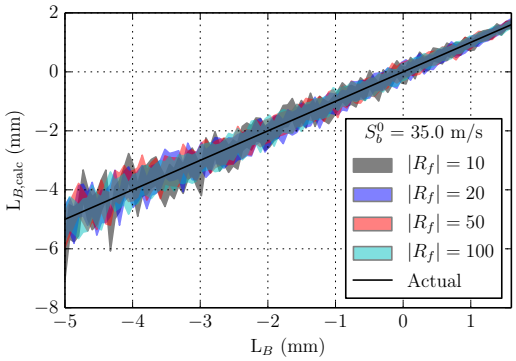

Figure F.30: $S_b^0 = 35.0$ m/s: Effect of $|R_f|$ on uncertainty of L_B for $R_f = [10, 58]$ mm, 1% Gaussian noise

F.2 Effect of Data Set Range: $R_f = \left[R_f^0, R_f^{\textbf{final}}\right]$

F.2.1 Variance of S_b^0

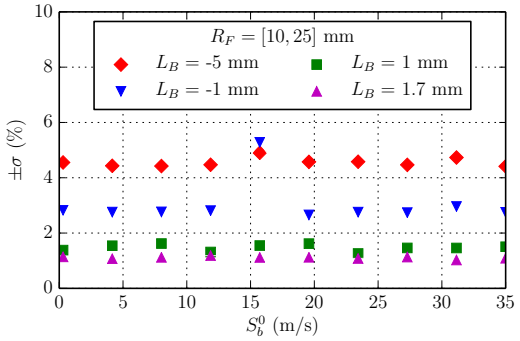

Figure F.31: $R_f = [10, 25]$ mm: Effect of L_B on variance of S_b^0 for $|R_f| = 100$, 1% Gaussian noise

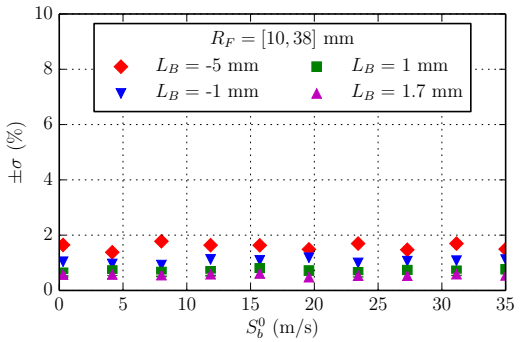

Figure F.32: $R_f = [10, 38]$ mm: Effect of L_B on variance of S_b^0 for $|R_f| = 100$, 1% Gaussian noise

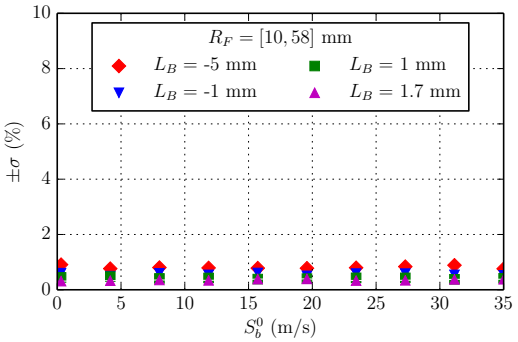

Figure F.33: $R_f = [10, 58]$ mm: Effect of L_B on variance of S_b^0 for $|R_f| = 100$, 1% Gaussian noise

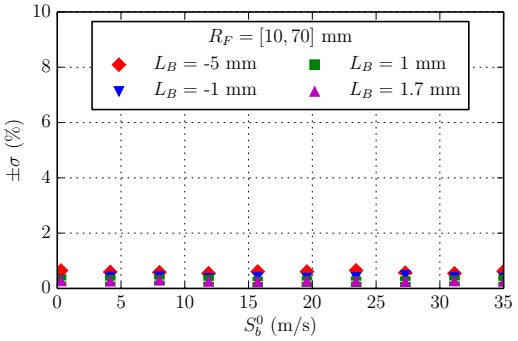

Figure F.34: $R_f = [10, 25]$ mm: Effect of L_B on variance of S_b^0 for $|R_f| = 100$, 1% Gaussian noise

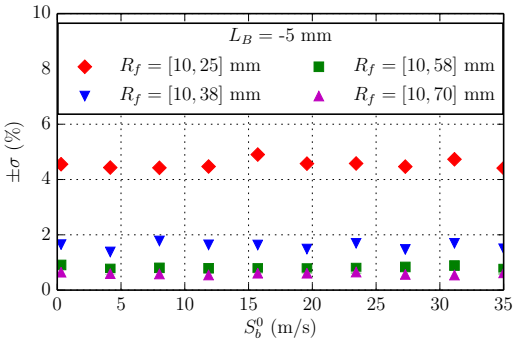

Figure F.35: $L_B = -5$ mm: Effect of $R_f = \left[R_f^0, R_f^{\text{final}}\right]$ on variance of S_b^0 for $|R_f| = 100$, 1% Gaussian noise

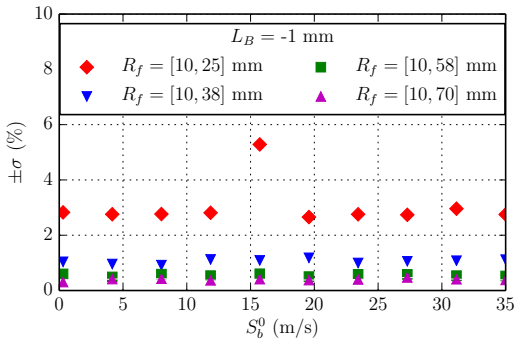

Figure F.36: $L_B = -1$ mm: Effect of $R_f = \left[R_f^0, R_f^{\text{final}}\right]$ on variance of S_b^0 for $|R_f| = 100$, 1% Gaussian noise

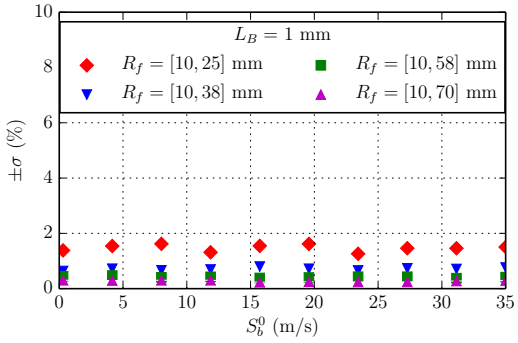

Figure F.37: $L_B = 1$ mm: Effect of $R_f = \left[R_f^0, R_f^{\text{final}}\right]$ on variance of S_b^0 for $|R_f| = 100$, 1% Gaussian noise

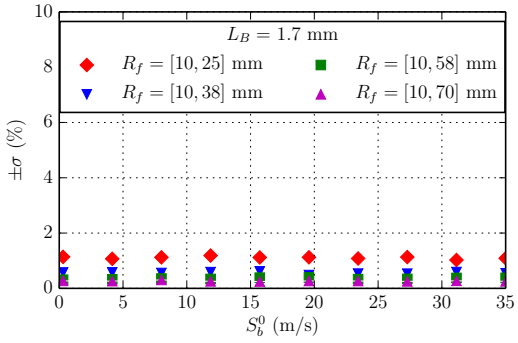

Figure F.38: $L_B = 1.7$ mm: Effect of $R_f = \left[R_f^0, R_f^{\text{final}}\right]$ on variance of S_b^0 for $|R_f| = 100$, 1% Gaussian noise

F.2.2 Variance of L_B

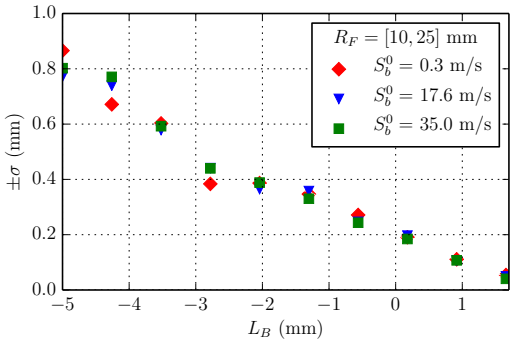

Figure F.39: $R_f = [10, 25]$ mm: Effect of S_b^0 on variance of L_B for $|R_f| = 100$, 1% Gaussian noise

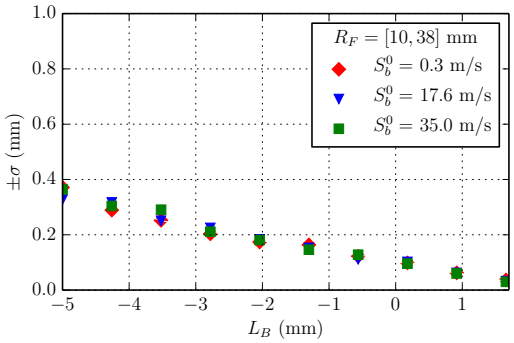

Figure F.40: $R_f = [10, 38]$ mm: Effect of S_b^0 on variance of L_B for $|R_f| = 100$, 1% Gaussian noise

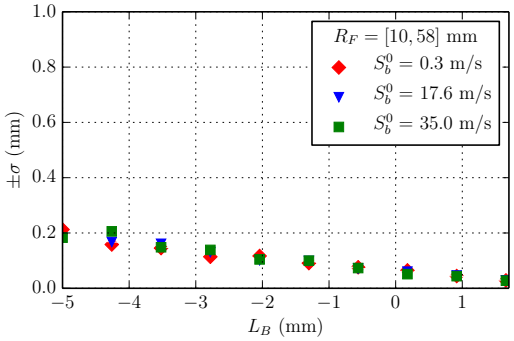

Figure F.41: $R_f = [10, 58]$ mm: Effect of S_b^0 on variance of L_B for $|R_f| = 100$, 1% Gaussian noise

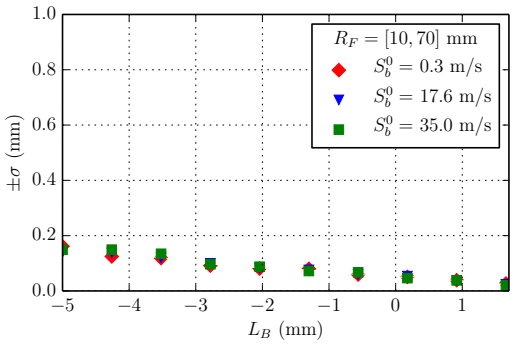

Figure F.42: $R_f = [10, 70]$ mm: Effect of S_b^0 on variance of L_B for $|R_f| = 100$, 1% Gaussian noise

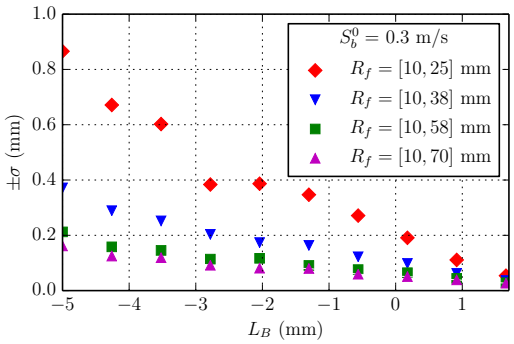

Figure F.43: $S_b^0 = 0.3$ m/s: Effect of $R_f = \left[R_f^0, R_f^{\text{final}}\right]$ on variance of L_B for $|R_f| = 100$, 1% Gaussian noise

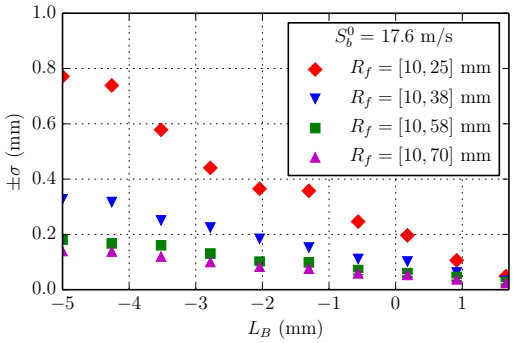

Figure F.44: $S_b^0 = 17.6$ m/s: Effect of $R_f = \left[R_f^0, R_f^{\text{final}}\right]$ on variance of L_B for $|R_f| = 100$, 1% Gaussian noise

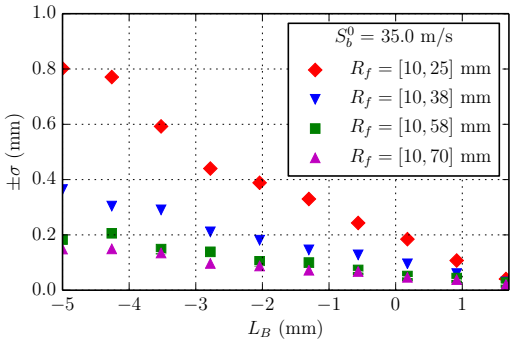

Figure F.45: $S_b^0 = 35.0$ m/s: Effect of $R_f = \left[R_f^0, R_f^{\text{final}}\right]$ on variance of L_B for $|R_f| = 100$, 1% Gaussian noise

F.2.3 Uncertainty of S_b^0

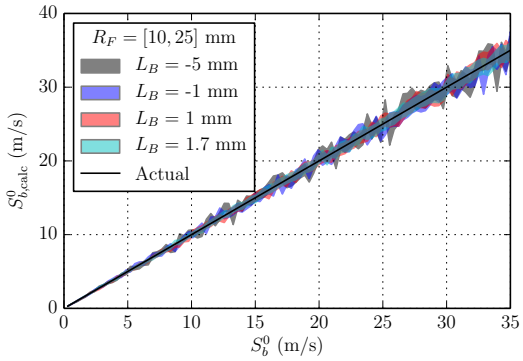

Figure F.46: $R_f = [10, 25]$ mm: Effect of L_B on uncertainty of S_b^0 for $|R_f| = 100$, 1% Gaussian noise

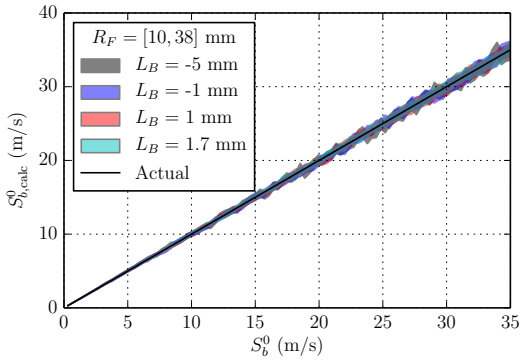

Figure F.47: $R_f = [10, 38]$ mm: Effect of L_B on uncertainty of S_b^0 for $|R_f| = 100$, 1% Gaussian noise

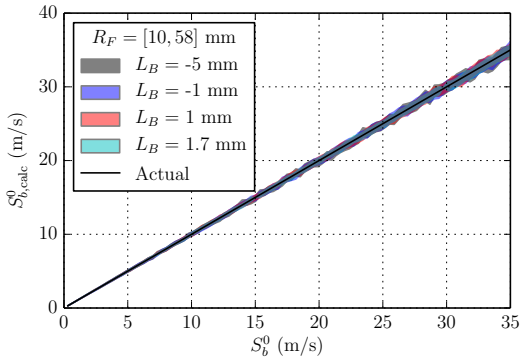

Figure F.48: $R_f = [10, 58]$ mm: Effect of L_B on uncertainty of S_b^0 for $|R_f| = 100$, 1% Gaussian noise

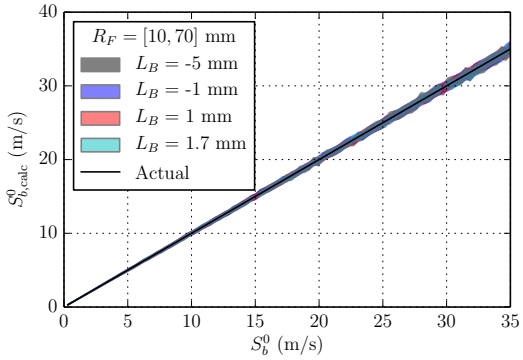

Figure F.49: $R_f = [10, 70]$ mm: Effect of L_B on uncertainty of S_b^0 for $|R_f| = 100$, 1% Gaussian noise

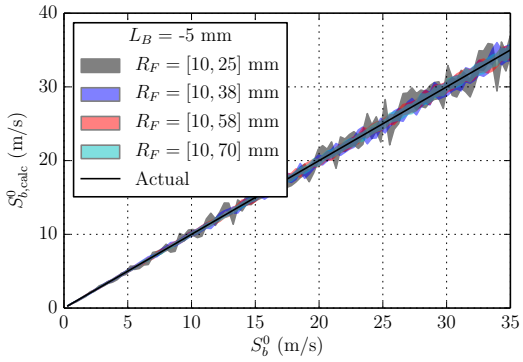

Figure F.50: $L_B = -5$ mm: Effect of $R_f = \left[R_f^0, R_f^{\text{final}}\right]$ on uncertainty of S_b^0 for $|R_f| = 100$, 1% Gaussian noise

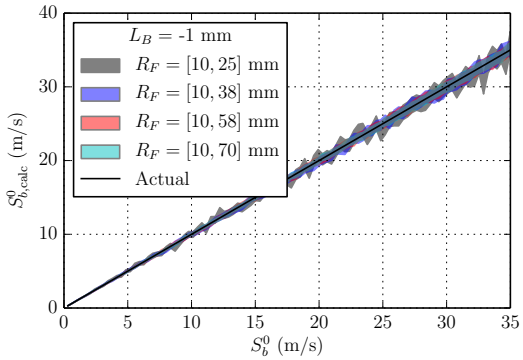

Figure F.51: $L_B = -1$ mm: Effect of $R_f = \left[R_f^0, R_f^{\text{final}}\right]$ on uncertainty of S_b^0 for $|R_f| = 100$, 1% Gaussian noise

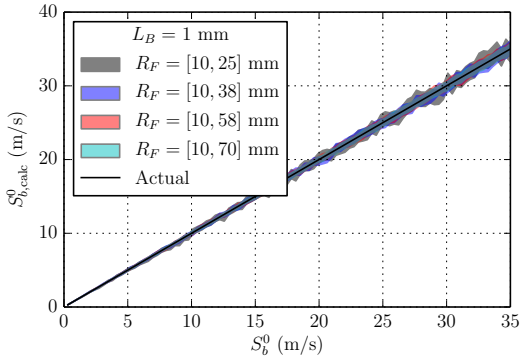

Figure F.52: $L_B = 1$ mm: Effect of $R_f = \left[R_f^0, R_f^{\text{final}}\right]$ on uncertainty of S_b^0 for $|R_f| = 100$, 1% Gaussian noise

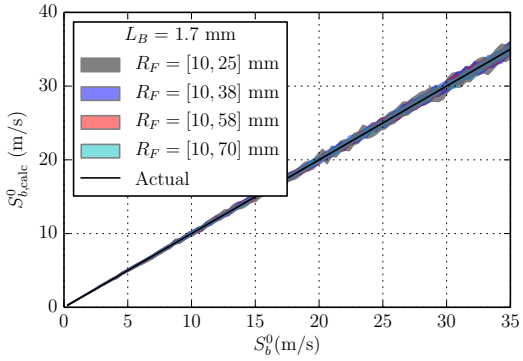

Figure F.53: $L_B = 1.7$ mm: Effect of $R_f = \left[R_f^0, R_f^{\text{final}}\right]$ on uncertainty of S_b^0 for $|R_f| = 100$, 1% Gaussian noise

F.2.4 Uncertainty of L_B

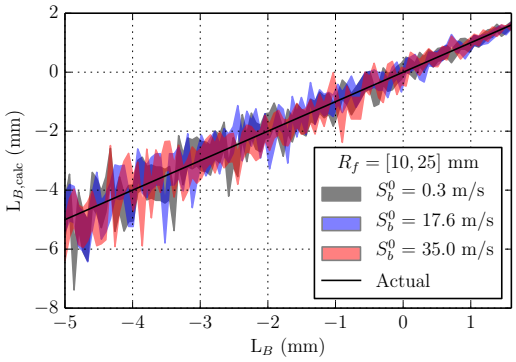

Figure F.54: $R_f = [10, 25]$ mm: Effect of S_b^0 on uncertainty of L_B for $|R_f| = 100$, 1% Gaussian noise

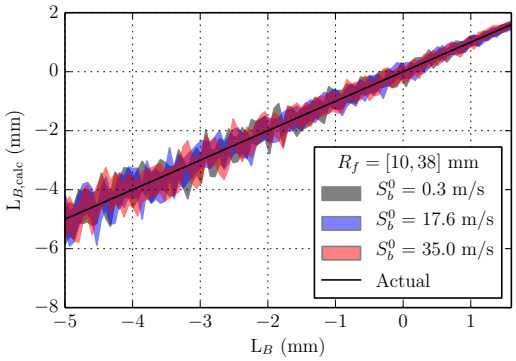

Figure F.55: $R_f = [10, 38]$ mm: Effect of S_b^0 on uncertainty of L_B for $|R_f| = 100$, 1% Gaussian noise

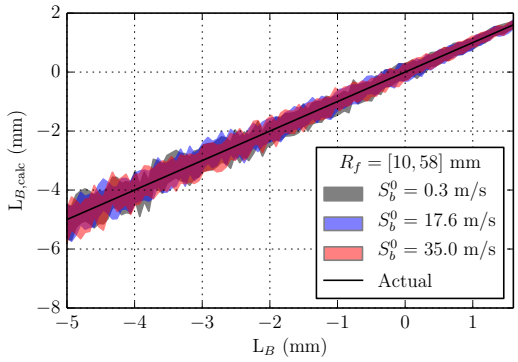

Figure F.56: $R_f = [10, 58]$ mm: Effect of S_b^0 on uncertainty of L_B for $|R_f| = 100$, 1% Gaussian noise

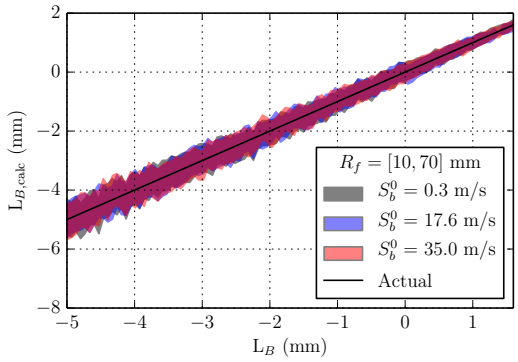

Figure F.57: $R_f = [10, 70]$ mm: Effect of S_b^0 on uncertainty of L_B for $|R_f| = 100$, 1% Gaussian noise

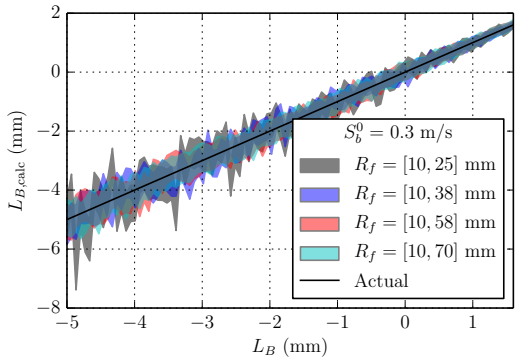

Figure F.58: $S_b^0 = 0.3$ m/s: Effect of $R_f = \left[R_f^0, R_f^{\text{final}}\right]$ on uncertainty of L_B for $|R_f| = 100$, 1% Gaussian noise

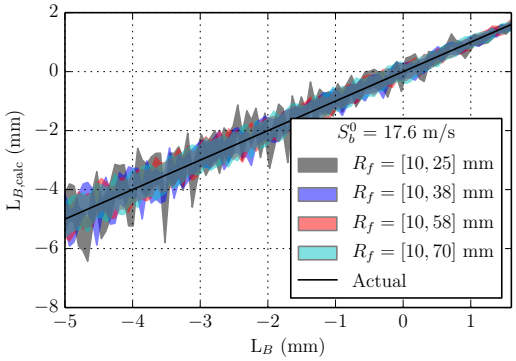

Figure F.59: $S_b^0 = 17.6$ m/s: Effect of $R_f = \left[R_f^0, R_f^{\text{final}}\right]$ on uncertainty of L_B for $|R_f| = 100$, 1% Gaussian noise

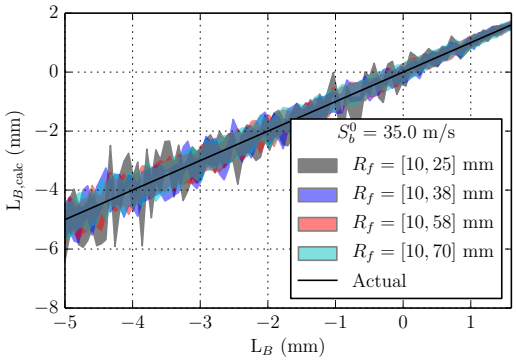

Figure F.60: $S_b^0 = 35.0$ m/s: Effect of $R_f = \left[R_f^0, R_f^{\text{final}}\right]$ on uncertainty of L_B for $|R_f| = 100$, 1% Gaussian noise

F.3 Effect of Gaussian Noise Addition

F.3.1 Variance of S_b^0

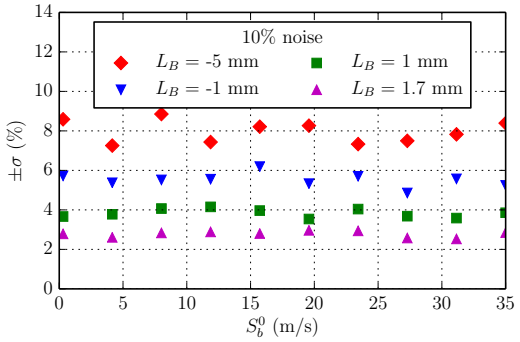

Figure F.61: 10% Gaussian noise: Effect of L_B on variance of S_b^0 for $|R_f| = 100$, $R_f = [10, 58]$ mm

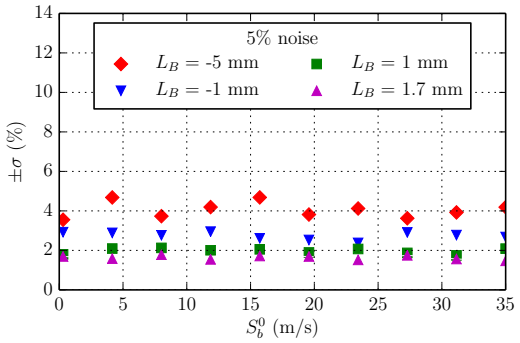

Figure F.62: 5% Gaussian noise: Effect of L_B on variance of S_b^0 for $|R_f| = 100$, $R_f = [10, 58]$ mm

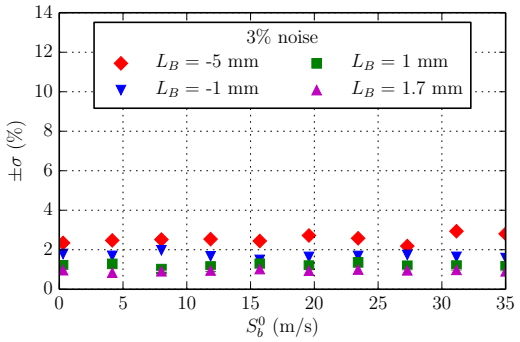

Figure F.63: 3% Gaussian noise: Effect of L_B on variance of S_b^0 for $|R_f| = 100$, $R_f = [10, 58]$ mm

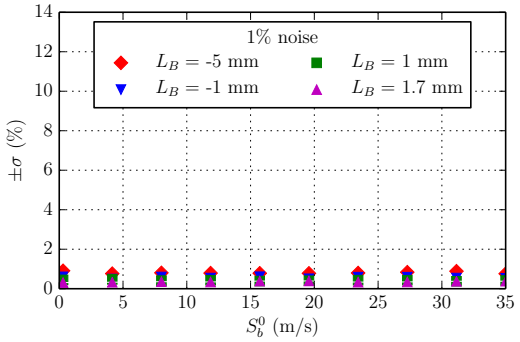

Figure F.64: 1% Gaussian noise: Effect of L_B on variance of S_b^0 for $|R_f| = 100$, $R_f = [10, 58]$ mm

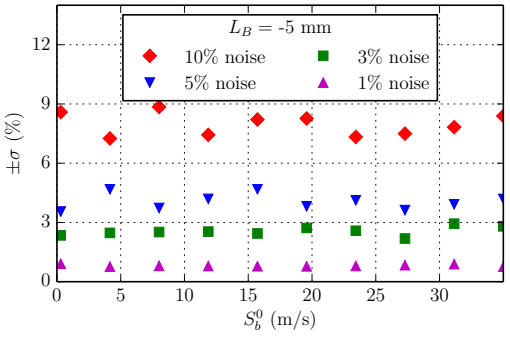

Figure F.65: $L_B = -5$ mm: Effect of Gaussian noise on variance of S_b^0 for $|R_f| = 100$, $R_f = [10, 58]$ mm

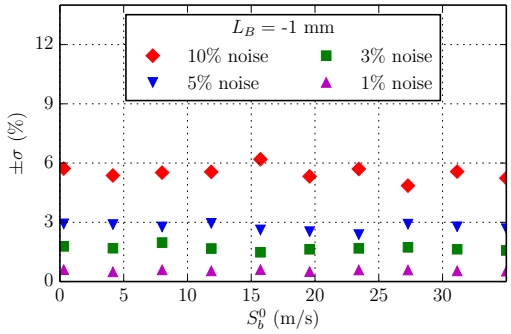

Figure F.66: $L_B = -1$ mm: Effect of Gaussian noise on variance of S_b^0 for $|R_f| = 100$, $R_f = [10, 58]$ mm

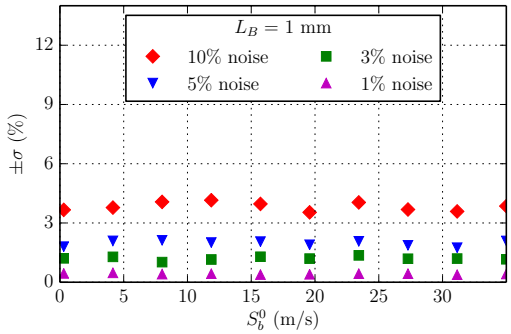

Figure F.67: $L_B = 1$ mm: Effect of Gaussian noise on variance of S_b^0 for $|R_f| = 100$, $R_f = [10, 58]$ mm

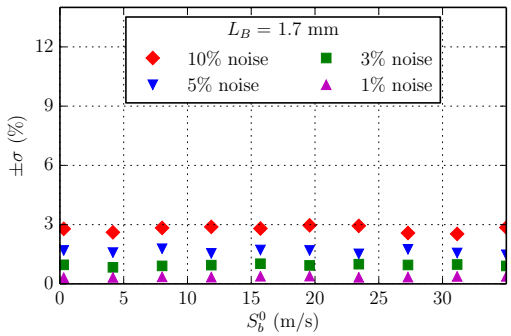

Figure F.68: $L_B = 1.7$ mm: Effect of Gaussian noise on variance of S_b^0 for $|R_f| = 100$, $R_f = [10, 58]$ mm

F.3.2 Variance of L_B

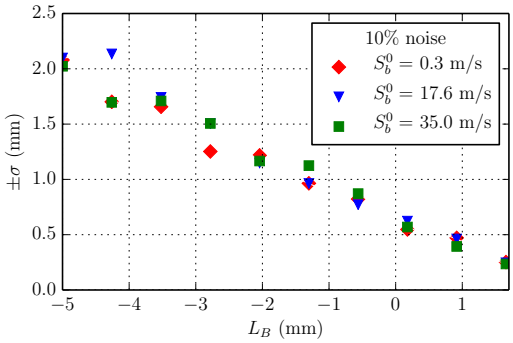

Figure F.69: 10% Gaussian noise: Effect of S_b^0 on variance of L_B for $|R_f| = 100$, $R_f = [10, 58]$ mm

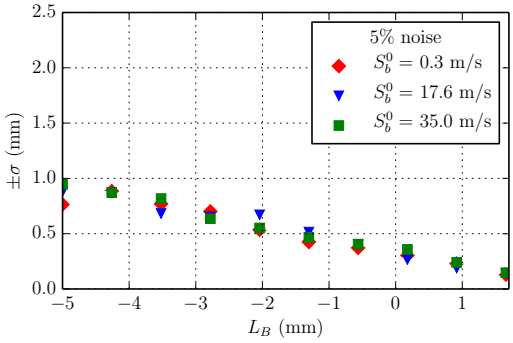

Figure F.70: 5% Gaussian noise: Effect of S_b^0 on variance of L_B for $|R_f| = 100$, $R_f = [10, 58]$ mm

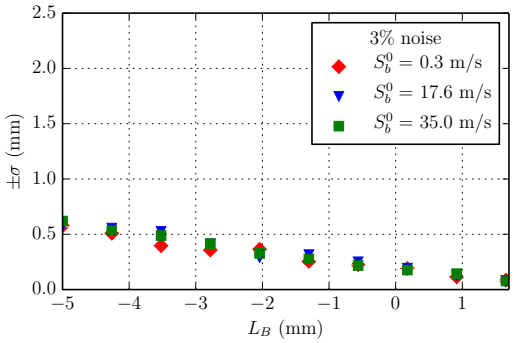

Figure F.71: 3% Gaussian noise: Effect of S_b^0 on variance of L_B for $|R_f| = 100$, $R_f = [10, 58]$ mm

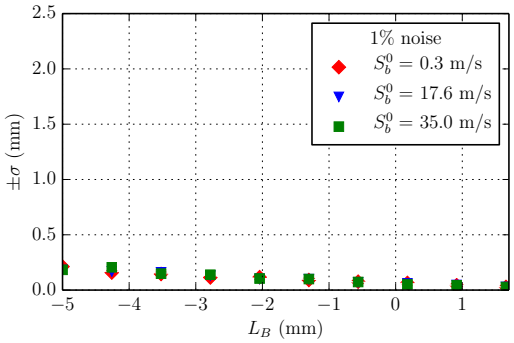

Figure F.72: 1% Gaussian noise: Effect of S_b^0 on variance of L_B for $|R_f| = 100$, $R_f = [10, 58]$ mm

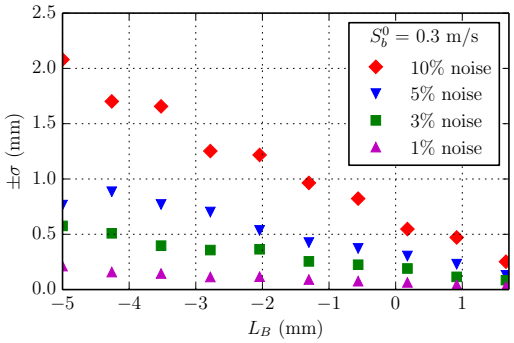

Figure F.73: $S_b^0 = 0.3$ m/s: Effect of Gaussian noise on variance of L_B for $|R_f| = 100$, $R_f = [10, 58]$ mm

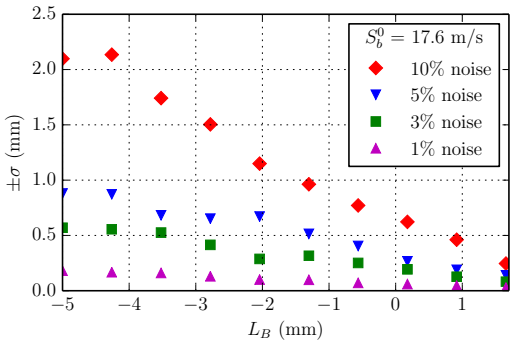

Figure F.74: $S_b^0 = 17.6$ m/s: Effect of Gaussian noise on variance of L_B for $|R_f| = 100$, $R_f = [10, 58]$ mm

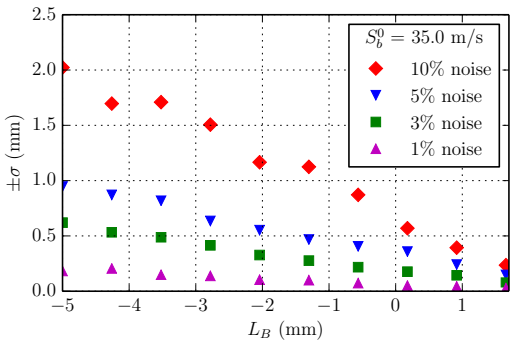

Figure F.75: $S_b^0 = 35.0$ m/s: Effect of Gaussian noise on variance of L_B for $|R_f| = 100$, $R_f = [10, 58]$ mm

F.3.3 Uncertainty of S_b^0

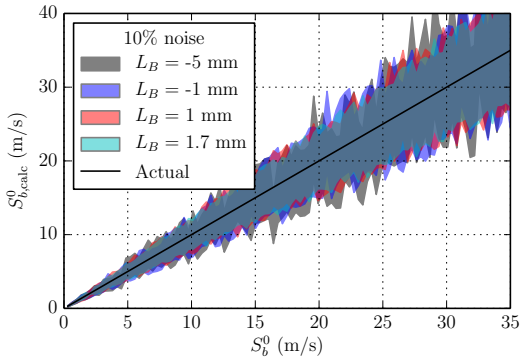

Figure F.76: 10% Gaussian noise: Effect of L_B on uncertainty of S_b^0 for $|R_f| = 100$, $R_f = [10, 58]$ mm

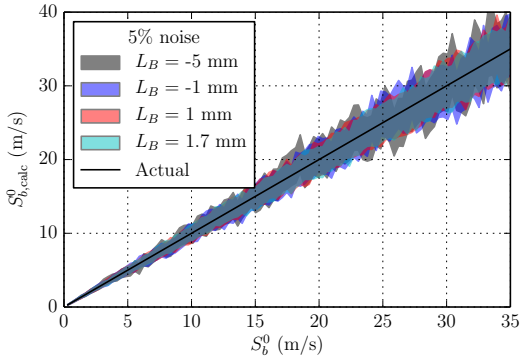

Figure F.77: 5% Gaussian noise: Effect of L_B on uncertainty of S_b^0 for $|R_f| = 100$, $R_f = [10, 58]$ mm

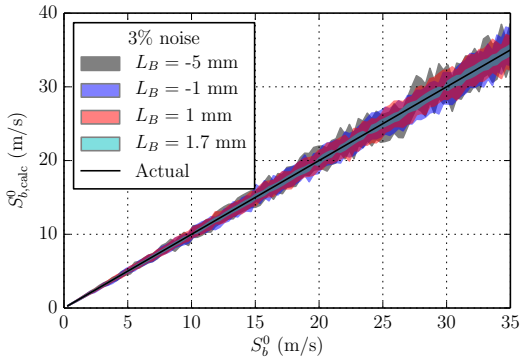

Figure F.78: 3% Gaussian noise: Effect of L_B on uncertainty of S_b^0 for $|R_f| = 100$, $R_f = [10, 58]$ mm

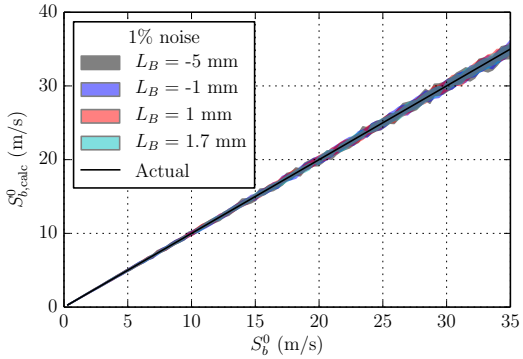

Figure F.79: 1% Gaussian noise: Effect of L_B on uncertainty of S_b^0 for $|R_f| = 100$, $R_f = [10, 58]$ mm

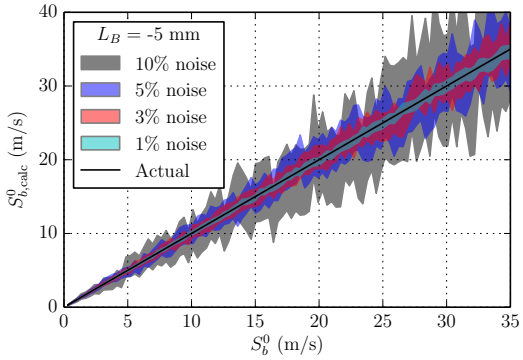

Figure F.80: $L_B = -5$ mm: Effect of Gaussian noise on uncertainty of S_b^0 for $|R_f| = 100$, $R_f = [10, 58]$ mm

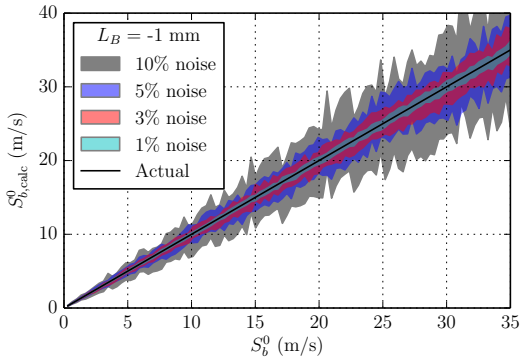

Figure F.81: $L_B = -1$ mm: Effect of Gaussian noise on uncertaintyof S_b^0 for $|R_f| = 100$, $R_f = [10, 58]$ mm

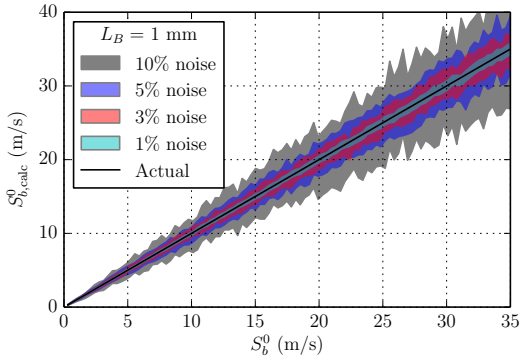

Figure F.82: $L_B = 1$ mm: Effect of Gaussian noise on uncertainty of S_b^0 for $|R_f| = 100$, $R_f = [10, 58]$ mm

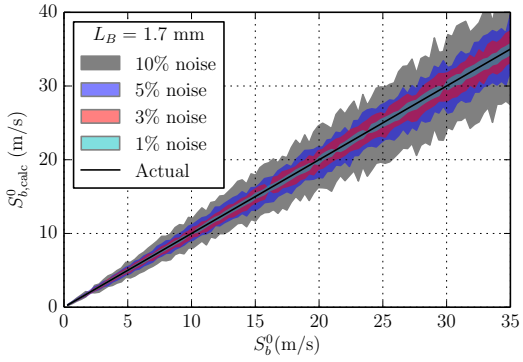

Figure F.83: $L_B = 1.7$ mm: Effect of Gaussian noise on uncertainty of S_b^0 for $|R_f| = 100$, $R_f = [10, 58]$ mm

F.3.4 Uncertainty of L_B

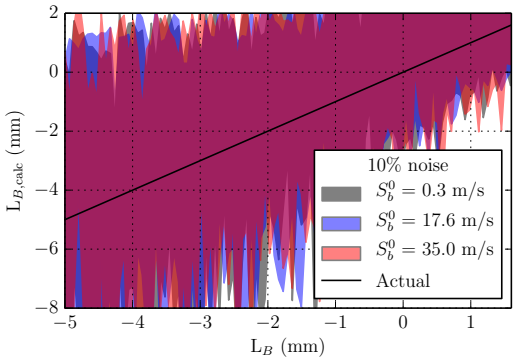

Figure F.84: 10% Gaussian noise: Effect of S_b^0 on uncertainty of L_B for $|R_f| = 100$, $R_f = [10, 58]$ mm

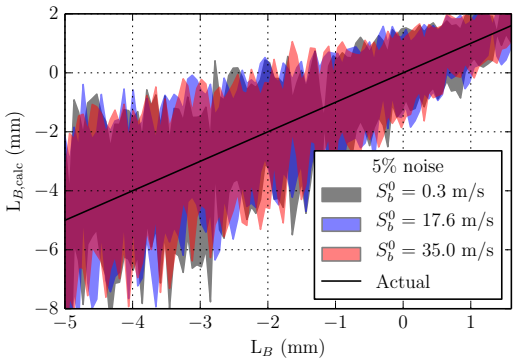

Figure F.85: 5% Gaussian noise: Effect of S_b^0 on uncertainty of L_B for $|R_f| = 100$, $R_f = [10, 58]$ mm

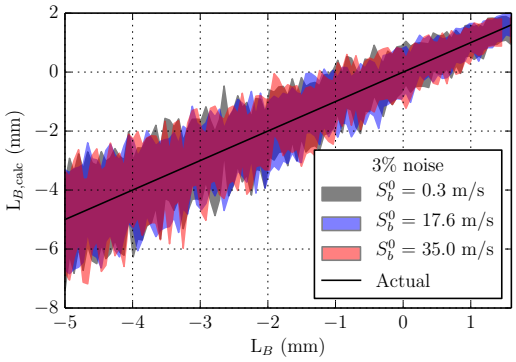

Figure F.86: 3% Gaussian noise: Effect of S_b^0 on uncertainty of L_B for $|R_f| = 100$, $R_f = [10, 58]$ mm

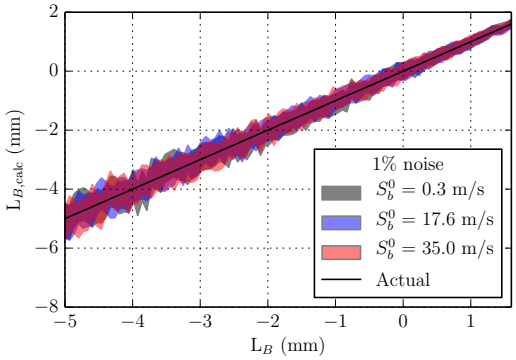

Figure F.87: 1% Gaussian noise: Effect of S_b^0 on uncertainty of L_B for $|R_f| = 100$, $R_f = [10, 58]$ mm

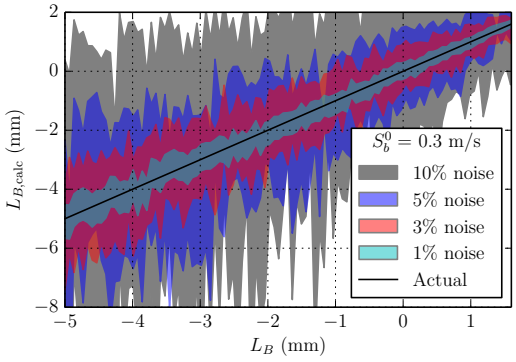

Figure F.88: $S_b^0 = 0.3$ m/s: Effect of Gaussian noise on uncertainty of L_B for $|R_f| = 100$, $R_f = [10, 58]$ mm

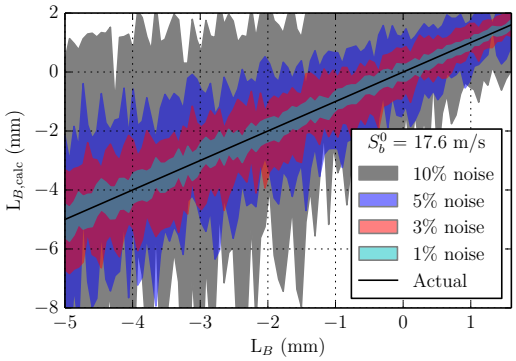

Figure F.89: $S_b^0 = 17.6$ m/s: Effect of Gaussian noise on uncertainty of L_B for $|R_f| = 100$, $R_f = [10, 58]$ mm

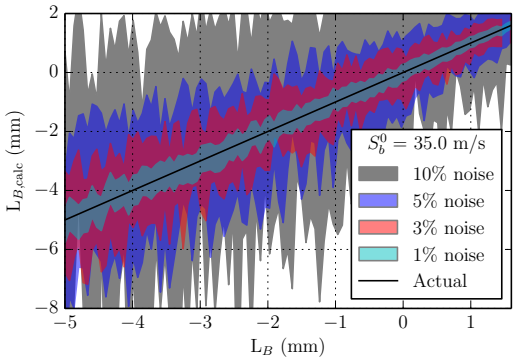

Figure F.90: $S_b^0 = 35.0$ m/s: Effect of Gaussian noise on uncertainty of L_B for $|R_f| = 100$, $R_f = [10, 58]$ mm